Title

Transition Metal Oxides Deposited on Rhodium and Platinum: Surface Chemistry and Catalysis

Author

Boffa, A.B.

Publication Date

1994-07-29

LBL-35954
UC-401

Center for Advanced Materials

CAM

Transition Metal Oxides Deposited on Rhodium and Platinum: Surface Chemistry and Catalysis

A.B. Boffa
(Ph.D. Thesis)

July 1994

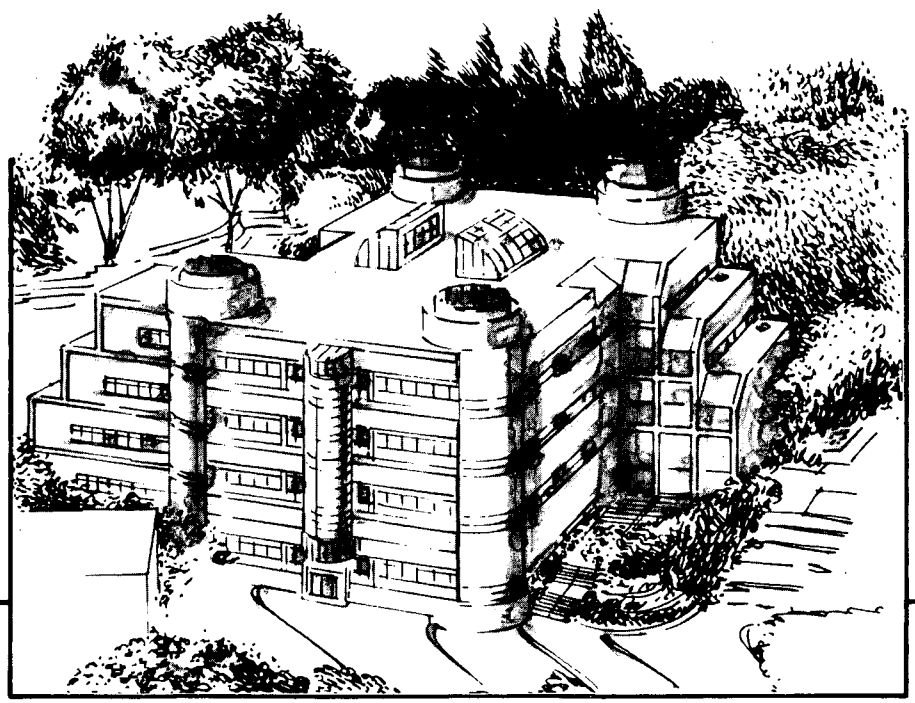

Materials and Chemical Sciences Division

Lawrence Berkeley Laboratory • University of California

ONE CYCLOTRON ROAD, BERKELEY, CA 94720 • (415) 486-4755

Prepared for the U.S. Department of Energy under Contract DE-AC03-76SF00098

DISCLAIMER

LBL-35954
UC-401

TRANSITION METAL OXIDES DEPOSITED ON RHODIUM AND PLATINUM: SURFACE CHEMISTRY AND CATALYSIS

ALEXANDER BOWMAN BOFFA
Ph.D. Thesis

DEPARTMENT OF CHEMISTRY
University of California

and

MATERIALS SCIENCES DIVISION
Lawrence Berkeley Laboratory
University of California
Berkeley CA 94720

JULY 1994

This work was supported by the Director, Office of Energy Research, Office of Basic Energy Sciences, Materials Sciences Division, of the U.S. Department of Energy under Contract No. DE-AC03-76SF00098

Transition Metal Oxides Deposited on Rhodium and Platinum: Surface Chemistry and Catalysis

by

Alexander Bowman Boffa

B.S. (University of Texas at Austin) 1988

A dissertation submitted in partial satisfaction of the

requirements for the degree of

Doctor of Philosophy

in

Chemistry

in the

GRADUATE DIVISION

of the

UNIVERSITY of CALIFORNIA at BERKELEY

Committee in charge:

Professor Gabor A. Somorjai
Professor Alexis T. Bell
Professor Angelica M. Stacy

1994

The dissertation of Alexander Bowman Boffa is approved:

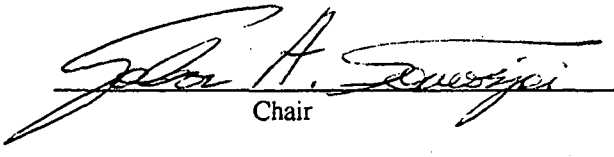

Chair 7/19/94
Date

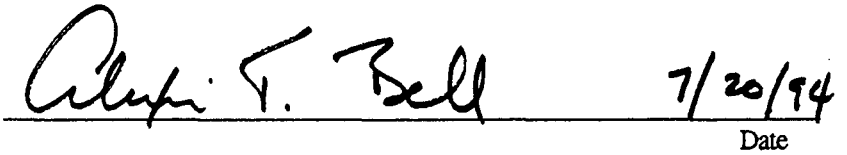

7/20/94
Date

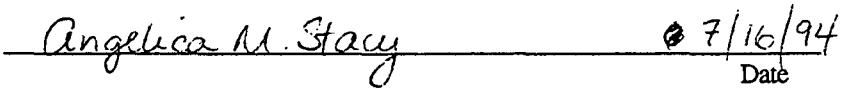

7/16/94
Date

University of California at Berkeley

1994

Abstract

Transition Metal Oxides Deposited on Rhodium and Platinum Surfaces:

Surface Chemistry and Catalysis

by

Alexander Bowman Boffa

Doctor of Philosophy in Chemistry

University of California at Berkeley

Professor Gabor A. Somorjai, Chair

The surface chemistry and catalytic reactivity of transition metal oxides deposited on rhodium (Rh) and platinum (Pt) substrates has been examined in order to establish the role of oxide - metal interactions in influencing catalytic activity. The oxides investigated included titanium oxide (TiOx), vanadium oxide (VOx), iron oxide (FeOx), zirconium oxide (ZrOx), niobium oxide (NbOx), tantalum oxide (TaOx), and tungsten oxide (WOx). The oxide overlayers were prepared in an ultra - high vacuum (UHV) apparatus by vapor phase deposition of the base metal followed by oxidation at elevated temperatures in an oxygen environment. Controlled oxide deposition on a planar metal substrate allowed differences in activity, as compared to the activtiy of the pure metal surface, to be ascribed to the direct chemical interaction between oxide, metal, and reactants. The techniques used to characterize the sample included Auger electron spectroscopy (AES), x - ray photoelectron spectroscopy (XPS), low energy electron diffraction (LEED), temperature programmed desorption (TPD), ion scattering spectroscopy (ISS), and scanning tunneling microscopy (STM). For titanium oxide films on Pt(111), a detailed compositional and

structural characterization was performed. Two ordered titanium oxide structures were identified with LEED and STM. For the oxides deposited on Rh foil (including TiOx, VOx, FeOx, ZrOx, NbOx, TaOx, and WOx), the samples were characterized with AES, TPD, and XPS, and kinetic measurements were made for CO and CO_2 hydrogenation. Each oxide exhibited a layer - by - layer growth mode and a non - stoichiometric composition with multiple oxidation states. After characterization of the surface in UHV, the sample was enclosed in an atmospheric reaction cell to measure the influence of the oxide deposits on the catalytic activity of the pure metal for CO and CO_2 hydrogenation. The oxide deposits were found to strongly enhance the reactivity of the Rh foil. The rates of methane formation were promoted by up to 15 fold with the maximum in rate enhancement occurring at oxide coverages of approximately 0.5 ML. Titanium oxide, tantalum oxide, and niobium oxide were the most effective promoters and were stable in the highest oxidation states during both reactions (compared to VOx, WOx, and FeOx). The trend in promoter effectiveness was attributed to the direct relationship between oxidation state and Lewis acidity. Bonding at the metal oxide / metal interface between the oxygen end of adsorbed CO and the Lewis acidic oxide was postulated to facilitate C - O bond dissociation and subsequent hydrogenation.

Contents

List of Figures

List of Tables

Acknowledgments

There is a large group of collaborators, associates, and friends without whose guidance and support this work would never have been completed. I would like to start by expressing appreciation to Dr. Kevin Williams. Kevin's patience in introducing me to the equipment allowed me to start doing science from the beginning, and his friendship helped me cope with the difficult first two years of the chemistry Ph.D. program. Next, I would like to acknowledge the support of Professors Alex Bell and Gabor Somorjai. Their stimulating ideas and comments always kept this research moving forward. Somorjai group members through the years have each contributed in some way to my understanding of surface science and catalysis. In particular, I would like to thank Michael Quinlan who took time out to help me think through dozens of problems and James Batteas who was office mate, sounding board, and basketball victim (just kidding). For Chapter 4, I would like to thank Heather Galloway and Dr. Miquel Salmeron for their STM expertise and Pete Jacobs for his help in collecting and analyzing the LEED data. Chin Lin has to be acknowledged for his hard work in learning the system and contributing within the confines of a busy schedule of classes. And lastly, Lisa Boffa has to be congratulated for surviving my daily explanations of discoveries and setbacks while still being able to give many helpful suggestions.

This work was supported by the Director, Office of Energy Research, Office of Basic Energy Sciences, Materials Sciences Division of the U.S. Department of Energy under Contract DE-AC03-SF00098.

Chapter 1

Introduction

1.1 The Oxide - Metal Interface

Multiphase materials consisting of oxide and metal components are utilized in a variety of technological applications: oxide supported, metal heterogeneous catalysts are an essential element in nearly all large scale chemical processes (1); metal - oxide - semiconductor (MOS) field effect transistors are used as chemical solid state sensors (2); oxide passivation layers are used to protect corrosion sensitive metals (3); and oxide binders are commonly used in coatings particularly as pigments in paints and as magnetic active media in recording tapes and computer data storage disks (4). In each material, the interface generated at the contact between the oxide and metal component plays a vital role in determining its properties. This work attempts to elucidate the nature of chemical interaction occurring at the oxide - metal interface, in particular, the role of oxide - metal interactions in catalysis.

1.2 Metal - Support Interactions in Catalysis

Heterogeneous catalysts generally consist of small (10 - 100 Å) metal particles dispersed on a porous oxide. Since catalytic reactions occur at surfaces, dispersion of the metal on a high surface area oxide support (~ 200 m^2/g) maximizes the surface to volume ratio of the metal and the utilization of the catalyst on a per gram basis. Consequently, in a typical heterogeneous catalyst the oxide and metal phases are in intimate contact, and chemical interactions between oxide and metal can potentially dramatically influence behavior (5-11).

In an article appearing in 1957, Schwab and coworkers were the first to report a dependence of catalytic activity on the nature of the support (12). To rationalize the observed changes in catalytic activities and activation energies, Schwab et al. (12-14), and later Solymosi et al. (15,16), postulated a bulk electronic semiconductor / metal interaction between the oxide support and catalyst particles. The next major contribution in the study of metal - support effects was nearly two decades later by Tauster and coworkers (17). These investigators found a near complete suppression in H_2 and CO chemisorption for Group 8 metals supported on reducible oxides after hydrogen reduction at 500 °C. (The term strong metal - support interaction (SMSI), originally coined by Tauster et al. (5,17), has since been used to describe all manner of metal - support interactions. Consequently, the acronym SMSI no longer has a well defined meaning and will not be further referred to in this work.) This publication was soon followed by a report by Vannice and coworkers (18) of a ten fold enhancement of activity for CO hydrogenation over Ni/TiO_2 compared to Ni/SiO_2. The intriguing findings of Tauster et al. and Vannice et al. have stimulated an active research effort involving several research groups (5-11). In the next two sections, conclusions from these studies of the role of oxide - metal interactions in influencing

chemisorption properties and catalytic activity of Group 8 metals supported on transition metal oxides will be discussed.

1.2.1 Chemisorption Properties

Upon hydrogen reduction, catalysts consisting of the metals Fe, Ni, Ru, Rh, Pd, Os, Ir , Pt or the support TiO_2, V_2O_3, ZrO_2, Nb_2O_5, Ta_2O_5, and CeO_2 have a greatly reduced capacity for both CO and H_2 chemisorption (5-11). Although the decreased chemisorption capacity of these catalyst systems has been rather convincingly demonstrated to be the result of geometric site blocking by reduced oxide deposits which migrate from the support during hydrogen treatment (5-11), the mechanism by which oxide material is transported from the support to the surface of the metal particle has not been fully elucidated. The bulk phases of the oxides listed above require temperatures in excess of 1000 °C before appreciable reduction is observed (5). However, in the presence of Group 8 metals, reduction is observed at temperatures as low as 200 °C (19-21). Because Group 8 metals dissociatively adsorb H_2, the metal component of the catalyst has been postulated to catalyze reduction of the support by providing hydrogen atoms via spillover (22-24). As a test of this hypothesis, Baker et al. (25) studied the reduction of TiO_2 in the presence of Ag, a metal in which hydrogen adsorption is non - dissociative. No migration or reduction of TiO_2 was observed with TEM and XPS after high temperature hydrogen treatment in the presence of Ag. Similarly, no reduction has been observed for TiO_2 in the presence of Au (26).

Reduction alone does not lead to oxide migration. Munuera et al. (22,23) reduced Rh/TiO_2 by ion bombardment and then annealed the catalyst to 500 °C in vacuum. Although the XPS measurement of a Ti^{3+} oxidation state indicated that the oxide remained reduced, no migration of the support was observed after annealing. When this experiment

was repeated in the presence of hydrogen, a migrating H-TiOx species was identified using XPS, EPR, and NMR. In the original work of Tauster et al. (5), SMSI behavior was only reported for "reducible" oxides. However, more recent studies have demonstrated that ZrO_2 (considered non - reducible (5)) also exhibits SMSI properties in the presence of Rh and Pt (27-28). After high temperature reduction of a ZrO_2 supported Rh catalyst, Zr^{3+} is observed with XPS and EPR, and H_2 chemisorption is suppressed (27). Rh/Zr and Pt/Zr are known to form particularly stable alloys (29), and ZrO_2 has been shown to display unusual redox behavior in the presence of these metals (30). Consequently, the driving force for interaction of ZrO_2 supports with metals such as Pt and Rh is attributed to a bonding similar to found in the alloys. Given these considerations, the mechanism of oxide migration appears to involve dissociative hydrogen adsorption over M followed by H(a) spillover and reduction of M´Ox to form an alloy like M-H-M´O_x migrating species.

1.2.2 Catalytic Behavior

The interest in metal - support interactions would likely have quickly diminished if chemisorption suppression was the primary characteristic; however, the choice of support was also found to dramatically influence activity and selectivity for certain reactions. Vannice et al. (18) were the first to report a dependence of catalytic behavior on the support. These authors found a tenfold greater activity for CO hydrogenation over Ni/TiO_2 than over Ni/Al_2O_3, Ni/SiO_2, and Ni/C. Further investigations have lead to reports of enhanced CO hydrogenation activity for Fe, CO, Ni, Ru, Rh, Pd, Os, Ir, and Pt supported on oxides such as TiO_2, V_2O_3, MnO_2, ZrO_2, Nb_2O_5, HfO_2, Ta_2O_5, La_2O_3, and CeO_2 compared to an inert carrier such as SiO_2 (5-11). In addition to enhanced activity, selectivity is observed to shift toward production of higher weight hydrocarbons. Some of these systems also have enhanced activity for CO_2 hydrogenation (31-34), acetone

hydrogenation (35), crotonaldehyde hydrogenation (36), and the reduction of NO with H_2 or CO (37). Enhanced activity in these catalysts is found to be independent of reduction pretreatment.

For reactions such as hydrocarbon hydrogenation and hydrogenolysis, the oxides listed above inhibit activity (5-11). In contrast to the reactions which are positively influenced by the support, the activity of hydrocarbon hydrogenation and hydrogenolysis depends on the catalyst pretreatment. After high temperature reduction (>500 °C), the extent of catalyst deactivation is greater than that after low temperature reduction. Given that only minor changes are observed in activation energies, the structure sensitive hydrogenolysis reactions are effected to a greater degree than are the structure insensitive hydrogenation reactions, and the amount of activity decline scales with the extent of H_2 and CO chemisorption suppression, the inhibition of hydrocarbon hydrogenation and hydrogenolysis is attributed to loss of catalytic metal sites due to support migration and encapsulation (5-11).

The relative distribution of oxide and metal in the active catalyst during CO hydrogenation is unknown. For catalysts which have been pretreated by high temperature reduction, oxide encapsulation of the supported metal crystallites is reversed during CO hydrogenation (38), due to reoxidation and agglomeration of the oxide support by H_2O produced during the reaction This support agglomeration results in an insensitivity to catalyst pretreatment. However, XPS measurements after CO hydrogenation demonstrate that the reoxidation and agglomeration of the oxide support is incomplete.

Recent work by Komaya et al. (40,41) has shown that titanium salts precipitate to form a decoration of titanium oxide deposits on Ru metal crystallites during catalyst preparation. The oxide deposits are found to remain on the Ru catalyst particle during CO hydrogenation, resulting in a promotion of activity. Van Santen et al. (39) studied Rh/SiO_2 catalysts promoted by deposits of V_2O_3. With a decoration of V_2O_3 on the Rh/SiO_2 of

0.5 ML as measured by a 50 % decrease in CO chemisorption capacity, the rate and selectivity was nearly identical to that measured over V_2O_3 - supported Rh. Since the catalyst preparation of Van Santen et al. was similar to that used by Komaya et al. (40,41), precipitation of oxide support material would also be expected to have occurred, which would account for the near identical behavior of the V_2O_3 - supported Rh catalyst compared to that of the V_2O_3 - promoted Rh/SiO_2 catalyst. These considerations suggest that during CO hydrogenation the metal particles are decorated by promoting oxide moieties which are deposited from the support during catalyst preparation.

The mechanism of CO hydrogenation proceeds through adsorption and dissociation of CO followed by hydrogenation of the resulting carbon deposit by adsorbed hydrogen atoms. For Ni, Rh, Pd, Ir, and Pt, CO adsorbs nondissociatively (42), and CO dissociation is considered to be the rate limiting step. These are the metals for which the greatest rate enhancements are observed when supported or promoted by active oxides. In temperature programmed reduction (TPR) measurements, Sachtler and Ichikawa (43) report the simultaneous production of CH_4 and H_2O while annealing Rh/SiO_2 catalyst with a saturation coverage of CO in the presence of hydrogen. When the sample was promoted with MnOx, again CH_4 and H_2O were produced simultaneously during TPR but at a significantly lower temperature. These observations indicate that the MnOx promotes the rate limiting CO dissociation step of CO hydrogenation. The rate of CO dissociation has been shown to be enhanced in similar TPD and TPR studies of $VOx/Rh/SiO_2$ (39), Pd/TiO_2 and $TiO_2/Pd/SiO_2$ (44-48), Pt/TiO_2 (48), Rh/TiO_2 (49), and $Ni/Ga/SiO_2$ (50).

The question remains, though, by what mechanism do active oxide promoters and supports enhance CO dissociation. Two primary proposals have emerged from the considerable debate in the literature (5-11): 1) an electronic perturbation of the metal catalyst particles by charge transfer from the reduced oxide leading to an increase in metal back - bonding and a weakening of the CO bond, and 2) formation of an active site at the

oxide - metal interface in which the C-O bond of adsorbed CO is weakened through simultaneous interaction with the metal and defect sites of the oxide. The original reports of measurements of charge transfer were interpreted to represent an electronic exchange from the oxide to the metal producing a negatively charged particle (6). However, in more recent investigations, no significant charge transfer has been observed, and the reports of charge transfer in the original studies have been attributed to the difficulty in determining corrections for relaxation effects, sample charging, particle size variations, and final state effects (6-11).

The proposal of active site formation at the oxide - metal interface was first suggested by Burch and Flambard (51) and has since been invoked to explain oxide induced rate enhancement by several authors (52-54), although the evidence for unique active site formation at the oxide - metal interface is for the most part circumstantial. The primary argument as first expressed by Sachtler et al. for active site formation at the oxide - metal interface is an analogy to bonding observed in C and O bonded organo - metallic compounds. In these compounds, the carbon - end of the carbonyl is bound to a middle or late transition metal while the oxygen - end is bound to an early transition metal in a high oxidation state (56). The vibrational frequencies of the carbonyl group in these compounds (56) are similar to those reported in studies by Sachtler and Ichikawa (43) as well as others (50,57-60).

1.3 Surface Science and Model (Planar) Catalysts

The complexity of the multi - component, multi - phase heterogeneous catalysts makes indirect, geometric, oxide - metal interactions such as variations in particle size and dispersion, bifuctionallity, and surface species spillover often impossible to distinguish from the direct chemical interaction of metal and oxide. For catalysts in which support migration is observed during reduction, an additional uncontrolled parameter is the coverage of decorating oxide moieties. An alternative approach, to aid in determining molecular processes, is to design a model catalyst containing the essential elements of the supported system yet which allows catalyst composition and structure to be rigorously defined and characterized using the techniques of surface science.

The most common model heterogeneous catalyst consists of a planar substrate on to which metals, oxides, and/or promoters and poisons (such as K, Cl, and S) can be deposited. Planar samples can be mounted in an ultra - high vacuum (UHV) apparatus and characterized using modern surface science techniques. The primary surface science techniques are Auger electron spectroscopy (AES) for measuring atomic composition, low energy electron diffraction (LEED) for determining surface structure and crystallinity, x - ray photoelectron spectroscopy (XPS) for determining the chemical state or environment, and temperature programmed desorption (TPD) for measuring adsorption energies of desorbing surface species. In heterogeneous catalysis, surface characterization is of vital importance since catalytic reactions occur primarily at surfaces; however, most industrial processes of interest are run at atmospheric pressures. Consequently, the development by Somorjai et al. (61) of a high pressure reaction cell incorporated within a UHV apparatus further increased the usefulness of surface science as a tool for studying catalytic processes. A model catalyst can be configured with the oxide component as the substrate on to which a metal is deposited or in the reverse arrangement with the oxide deposited on a

metal substrate. For the study of metal - oxide interactions both types of model catalysts have been utilized.

The study of oxide substrates with overlayers of the catalyst metals has provided convincing evidence for oxide migration and oxide/metal alloy formation during high temperature reduction. Takatani and Chung (62) monitored a 120 Å Ni film deposited on a TiO_2 substrate. After annealing at 425 °C in hydrogen, the Ti AES signal was substantially increased due to oxide migration through the Ni film. Similar behavior was observed for Pt films on TiO_2 by Tamura et al. (63), and for Rh films deposited on TiO_2 by Belton et al. (19) and Sadeghi and Henrich (64). Seng et al. (65) used TEM, AES depth profiling, and XPS to study Pt films on TiO_2. After annealing at 700 °C in vacuum, the Pt AES signal initially increased with ion sputter time indicating removal of a surface layer of TiOx. As the depth profile proceeded, a region of the sample was revealed in which the ratio of Pt to Ti AES signals remained relatively constant suggesting the formation of an intermetallic of Pt and Ti. TEM measurements of atomic layer spacings within this region matched well with those of Pt_3Ti (66). Pt_3Ti alloy formation was also reported in an EXAFS study of the reduction of titania impregnated Pt samples by Beard and Ross (66). Further ion sputtering by Seng and coworkers eventually led to the complete removal of Pt from the TiO_2 substrate.

Metal - oxide interactions have also been studied in reverse configuration in which oxide is deposited on a metal substrate. The primary advantage of this approach is that oxide coverage on the metal can be controlled and calibrated. The effect of oxide deposits on the CO hydrogenation activity of metal substrates has been established for TiOx deposits on Ni(111) (67), TiOx and NbOx and Pt foil (68-70), and TiOx and AlOx on Rh (71-73). For each of these systems, addition of oxide deposits led to an increase in the rate of CO hydrogenation similar to that observed in the supported catalysts, suggesting that the planar catalysts effectively model the behavior of the high surface area working catalysts.

Titanium oxide overlayers on Rh foil have been the most extensively studied of the model catalyst systems. The series of investigations of TiOx on Rh was initiated by Levin, Bell, and Somorjai (74) and continued by Williams, Bell, and Somorjai (75). Levin et al. (71-73) determined the dependence of the kinetics of CO hydrogenation over Rh foil on titanium oxide coverage. Using a correction to the oxide coverage calibration determined by Williams et al. (76), the data of Levin et al. (71-73) shows a maximum in the rate of methane formation over Rh foil at a titanium oxide coverage of 0.5 ML. The rate at this oxide coverage was three times greater than that measured on clean Rh. A computer simulation of island growth developed by Levin and Williams (74,75) showed that oxide perimeter maximizes at 0.5 ML regardless of the initial nucleation site density, and XPS measurements by Levin et al. (77) indicated the presence of reduced Ti^{3+} defect sites in the overlayer during reaction. These observations led Levin to postulate an enhancement of CO dissociation and subsequent hydrogenation through bonding with defect sites located at the oxide perimeter (74).

Williams et al. extended the measurement of the influence of titanium oxide deposits on activity of Rh foil to include CO_2 hydrogenation (78-79), acetone hydrogenation (78), ethylene hydroformylation (80), ethylene hydrogenation (81), and ethane hydrogenolysis (81). The reactions involving hydrogenation of C - O bonds (CO_2 hydrogenation and acetone hydrogenation) were promoted by the deposits of titanium oxide. The coverage at which the rates of CO_2 and acetone hydrogenation were maximized was again 0.5 ML, providing further support for the importance of interface sites. For ethylene hydrogenation and ethane hydrogenolysis, no promotion was found as the activity declined linearly with the addition of TiOx deposits, consistent with geometric site blocking of the Rh foil. For ethylene hydroformylation, while no promotional effect was observed on the rate of CO insertion, the formation of 1 - propanol was enhanced relative to 1 - propanal.

1.4 Scope of the Present Work

The influence of oxide - metal interaction in CO and CO_2 hydrogenation over Rh and Pt has been determined for several oxide deposits (TiOx, VOx, FeOx, ZrOx, NbOx, TaOx, and WOx). In order to isolate the oxide - metal interface, a model catalyst has been designed in which sub - monolayer metal oxide overlayers are deposited on a metal substrate. The controlled deposition of oxide deposits on a planar substrate allows differences in activity to be ascribed to the direct chemical interaction between oxide, metal, and reactants. The model catalyst is analyzed and prepared in a UHV environment and then subsequently enclosed within an atmospheric reaction cell enabling kinetic measurements to be made.

Chapters 2 and 3 give a detailed description of the experimental apparatus and procedures. The UHV characterization of the samples includes Auger electron spectroscopy (AES), x - ray photoelectron spectroscopy (XPS), low energy electron diffraction (LEED), temperature programmed desorption (TPD), and ion scattering spectroscopy (ISS). After UHV characterization, activity measurements have been made for CO and CO_2 hydrogenation. Chapter 4 describes a detailed characterization of sub - monolayer to 5 ML thick deposits of titanium oxide on Pt(111), using LEED, AES, XPS, ISS, and scanning tunneling spectroscopy (STM). Annealing to temperatures greater than 500 °C leads to formation of ordered overlayer structures of the titanium oxide overlayer. XPS measurements indicate that the deposits are non - stoichiometric with the reduced Ti^{3+} component of the oxide concentrated at the oxide/Pt(111) interface. The behavior of the titanium oxide deposits after annealing in reducing environments at elevated temperatures is consistent with oxide migration and alloy formation reported in other studies. In Chapter 5, the influence of titanium oxide overlayers on CO and CO_2 hydrogenation over Pt foil is

presented. Although the qualitative effect is similar to that observed by Levin et al. and Williams et al. (71-81) on Rh foil, the relative rate enhancement by titanium oxide deposits is greater for Pt than for Rh. Chapter 6 describes the influence of vanadium oxide on CO and CO_2 hydrogenation over Rh foil. XPS measurements of the reducibility of the oxide deposits are compared with the observed activity enhancements. In Chapters 7 and 8, the investigation of oxide deposits on Rh foil is expanded to include zirconium oxide, iron oxide, niobium oxide, tantalum oxide, and tungsten oxide. The details of the XPS measurements of these oxide deposits before and after reaction are presented in Chapter 7. The sub - monolayer oxide deposits are observed in lower oxidation states than expected based on behavior of the bulk oxides which is attributed to the influence of the Rh substrate. Chapter 8 reports on the influence of these oxide overlayers on the rate of methane formation from CO and CO_2 hydrogenation over Rh foil. A trend is found relating oxidation state with promoter effectiveness. The implications of these results are discussed relative to possible mechanisms for oxide promotion.

Chapter 2

Experimental Apparatus

2.1 Introduction

Over the past few decades, a powerful array of surface sensitive analytical tools have been developed. These techniques are used in this work to characterize the structure and composition of oxide deposits on Rh and Pt substrates. Electron spectroscopes are widely prevalent in surface science due to the short mean free path of electrons (~ 5 at 50 eV) in solids. Electron and ion based spectroscopies require an ultra-high vacuum (UHV) atmosphere, which also aids in keeping the surface free of contamination originating from adsorption of background gases. At a pressure of $1x10^{-6}$ Torr, a monolayer of adsorbates will contaminate the 1 cm^2 surface in 1 s, assuming a sticking probability of unity. For the purposes of this study, UHV is also required for the controlled preparation of the oxide overlayers.

Three separate UHV apparatus have been used. One of these is a Varian 240 model 981 - 0030 UHV chamber which has an incorporated atmospheric reaction cell. A diagram

of this apparatus is shown in Fig. 2.1. Oxide promoter deposits can be prepared and characterized in an UHV environment. Then, by enclosing the sample within the reaction cell, the effect of the promoters on catalytic activity can be measured. In addition to the reaction cell, this chamber is equipped with an Auger electron spectrometer (AES), a mass spectrometer (MS), and a metal deposition source. For performing x-ray photoelectron spectroscopy (XPS) and ion scattering spectroscopy (ISS), a commercial PHI 5300 ESCA system has been utilized as diagrammed in Fig. 2.2. Adjacent to the primary analysis XPS/ISS chamber is a preparation chamber (Fig. 2.2) in which the oxide overlayers were deposited and a environmental treatment cell (Fig. 2.3) in which the sample could be exposed to gases at pressures of up to 1 atm. The sample was moved between the primary analysis, preparation, and environmental chambers without leaving vacuum using two transfer rods. In a third chamber, low energy electron diffraction (LEED) measurements were made.

In Chapters 2 and 3 a detailed description of the apparatus and procedures will be given along with a brief discussion of the techniques. The focus will be on those aspects of the apparatus and procedures that are unique to this study. It is not intended to give a comprehensive discussion of modern surface science techniques for which many excellent reviews have been published (1,82-84).

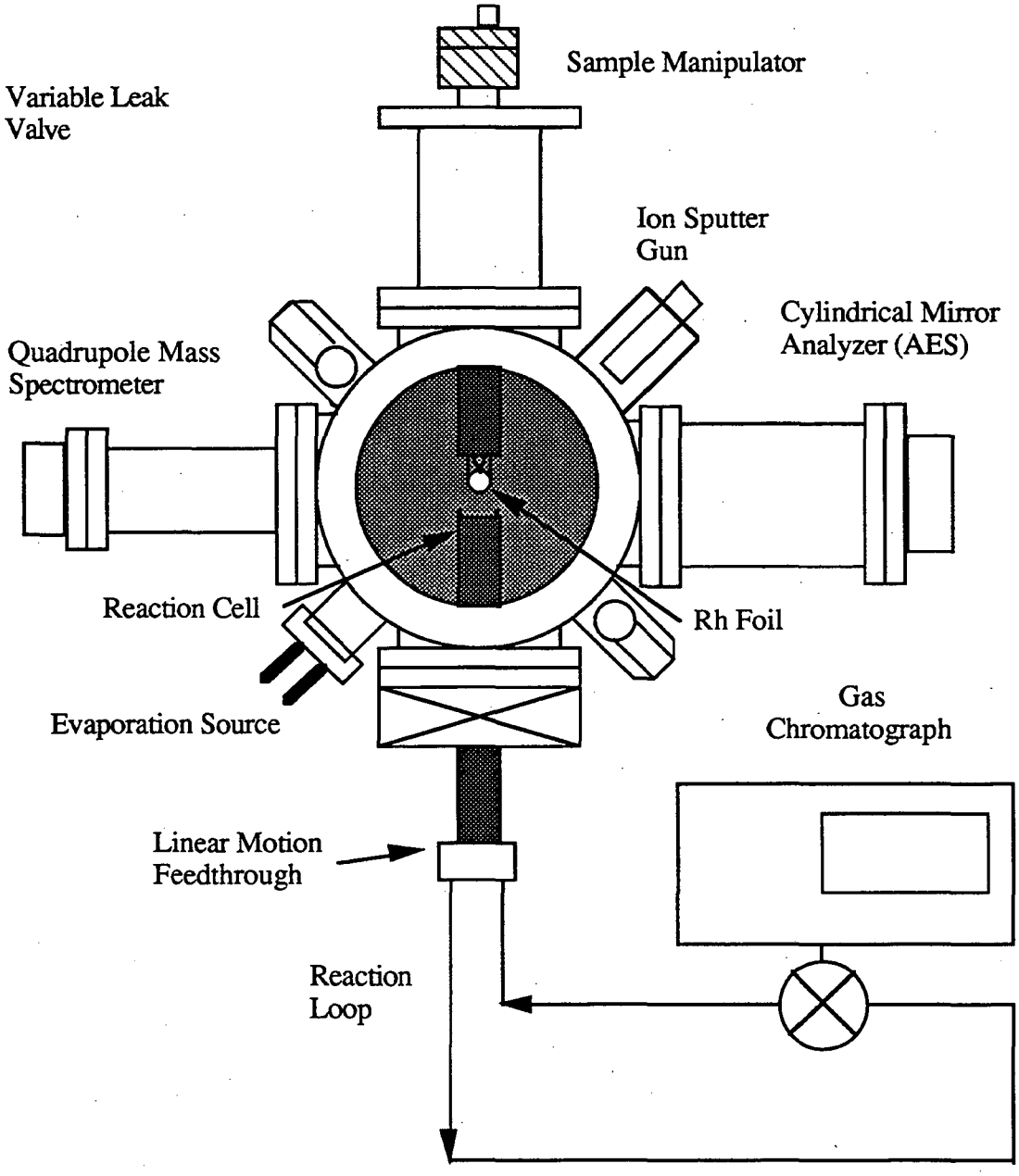

Figure 2.1: Varian ultra - high vacuum / reaction cell apparatus.

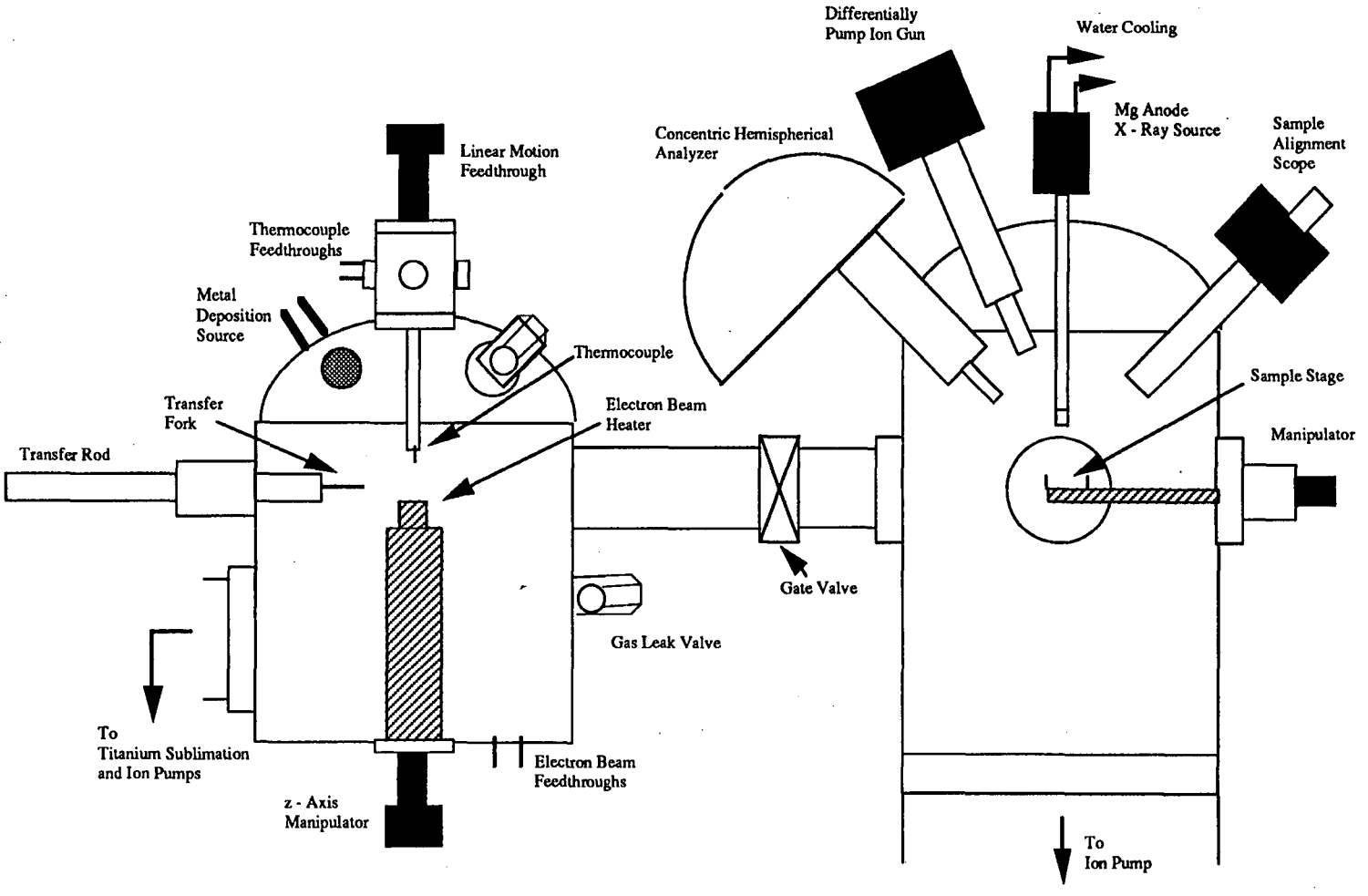

Figure 2.2: PHI 5300 ESCA XPS/ISS analysis and preparation chambers.

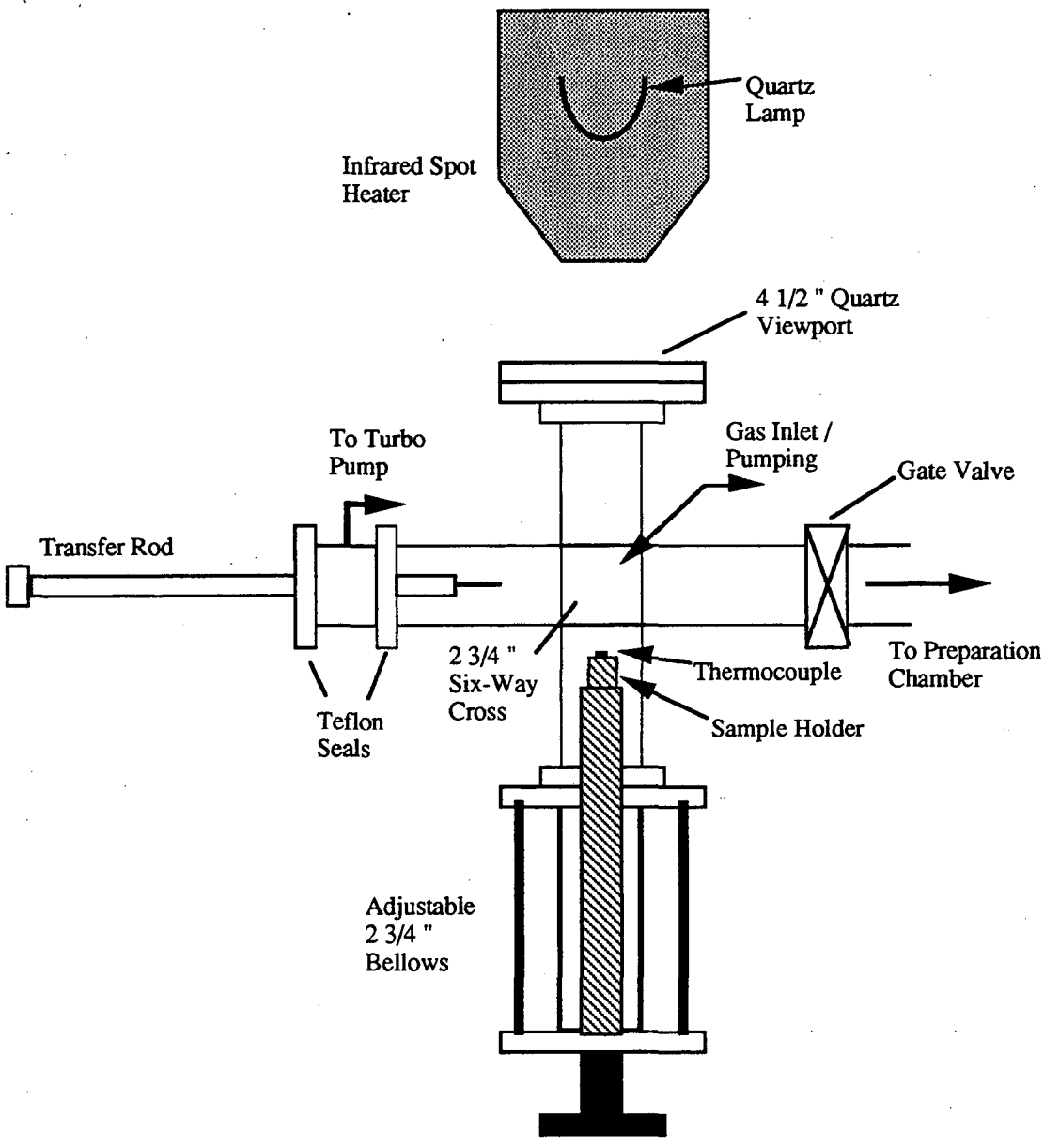

Figure 2.3: PHI 5300 ESCA environmental cell.

2.2 Surface Science/Reaction Cell Apparatus

2.2.1 Sample Manipulator and Heating

The sample used in the kinetic studies is a 1 cm^2, 0.002 in thick Rh or Pt foil. The foil is mounted in a UHV chamber to a sample holder, by support wires and barrel connectors, which in turn is held by a Varian manipulator (954 - 5031) with rotation; z - (2 in) translation; x- and y- (1 in) translation; and tilts. Cu braids make the electrical connection from feedthroughs on the manipulator flange to the sample holder. The support wires consist of 0.020 - in Au or Pt and are directly spot - welded to the sample. The advantage of Au over Pt is that it has less inherent catalytic activity; however, Au has a lower melting point than Pt and can only be used up to temperatures of ~ 1000 °C. Resistive heating accomplished by applying a current through the support wires gave a sample temperature of approximately 900 °C in vacuum and 250 °C under reaction conditions (H_2/CO_2 = 3, P = 1 atm) for a current of 30 A. "Hot spots" (areas where the sample temperature is significantly greater than the average) on the foil, which sometimes develop when resistively heating the sample, were virtually eliminated by improving the electrical connections of the support wires to the sample and by using a support wire material with low resistivity such as gold. The temperature was monitored with a 0.005 - in alumel - chromel thermocouple spot - welded directly to the sample and was calibrated by comparing the experimental equilibrium ratio of isobutene to isobutane to published thermodynamic data as outlined by Davis et al. (85). The heating was controlled using an LBL designed Crystal Heater 7S 3492 with a Eurotherm 808 PID Temperature Controller. The response of the crystal heater was particularly sensitive to the connection of the heating leads to the UHV electrical feedthroughs.

2.2.2 Auger Electron Spectroscopy (AES)

The primary characterization tool used in the Varian UHV chamber was AES. The production of Auger electrons is a two step process. In the first step, a core level (E_{L1}) electron is ejected upon excitation with an incident beam of electrons in the energy range 0.5 to 3.0 eV. In the second step, the hole created upon ejection of the first electron is filled by relaxation of an electron from an upper energy level (E_{L2}). The relaxation process provides the energy to eject a second electron (Auger electron) for which the measured kinetic energy (E_{AES}) is independent of the energy of the incident electron beam (84):

$$E_{AES} = E_{L1} - E_{L2} - \phi_S,$$

where ϕ_S is the work function of the sample. The components required for the AES experiment are an electron beam, electron energy analyzer, and a detector. The Varian UHV chamber was equipped with a 6 - in Varian single pass cylindrical mirror analyzer (CMA) model 981 - 2607 that had an integral electron gun and an electron multiplier detector. A CMA consists of two concentric cylinders. The outer cylinder is kept at negative potentials in order to deflect electrons toward the detector while the inner cylinder is held at ground potential. Depending on the voltage applied to the outer cylinder, only electrons of a particular energy will be focused on the exit aperture. An electron gun is located on the analyzer axis within the inner cylinder. The electron filament used was a Varian W / Ir ribbon model 981 - 0248 that was mounted within a can (cathode housing). A typical filament current of 3 A gave an emission of approximately 1.5 mA and a crystal current of approximately 5 μA. The filament emission was regulated using an LBL designed Auger Incident Electron Beam Control Power Supply 7S 1083. The electron detector was a channeltron Galelao 4731.

In AES secondary electron emission leads to a high background intensity. To aid in distinguishing the Auger peaks from the background, the AES spectrum was differentiated by adding a modulation voltage ($V_m\sin(wt)$) to the ramp voltage (V_r) on the outer CMA cylinder. A Taylor expansion of the collector current $i(V_r + V_m\sin(wt))$ gives (82):

$$i(V_r + V_m\sin(wt)) = i(V_r) + i'(V_r)*V_m\sin(wt) + \ldots$$

where the prime (') refers to differentiation with respect to V_r. Consequently, the collector current with frequency w was proportional to the first derivative of the electron energy distribution. The frequency w of the modulation voltage was generated and selected from the collector current using a Brookdeal 9503 Lock - in Amplifier. A typical reference frequency was 500 Hz. The voltage applied to the CMA outer cylinder was generated by a Varian Cylindrical Analyzer Control Unit 981 - 2601. V_r ranged from 20 to 1000 V, and V_m ranged from 2 to 5 V peak to peak. Larger values of V_m gave increased sensitivity but decreased resolution. The Auger spectra were recorded on a Hewlett - Packard (HP) 7035B x- y recorder. A typical AES spectrum is shown in Fig. 2.4 for a 0.5 ML VOx on a Rh foil.

2.2.3 Temperature Programmed Desorption (TPD)

The sample was characterized using TPD by monitoring the desorption of adsorbates with a mass spectrometer as a function of sample temperature. An Electronic Associates, Inc. (EAI) 200 Series quadrupole mass spectrometer was used to measure the desorbed gas products. The EAI Ionizer Controller was operated at 1 mA emission current and 70 eV electron energy, and the electron multiplier was biased at 2 kV. The sweep on the RF - DC generator was tuned to the mass of the desorbing species. The spectrometer

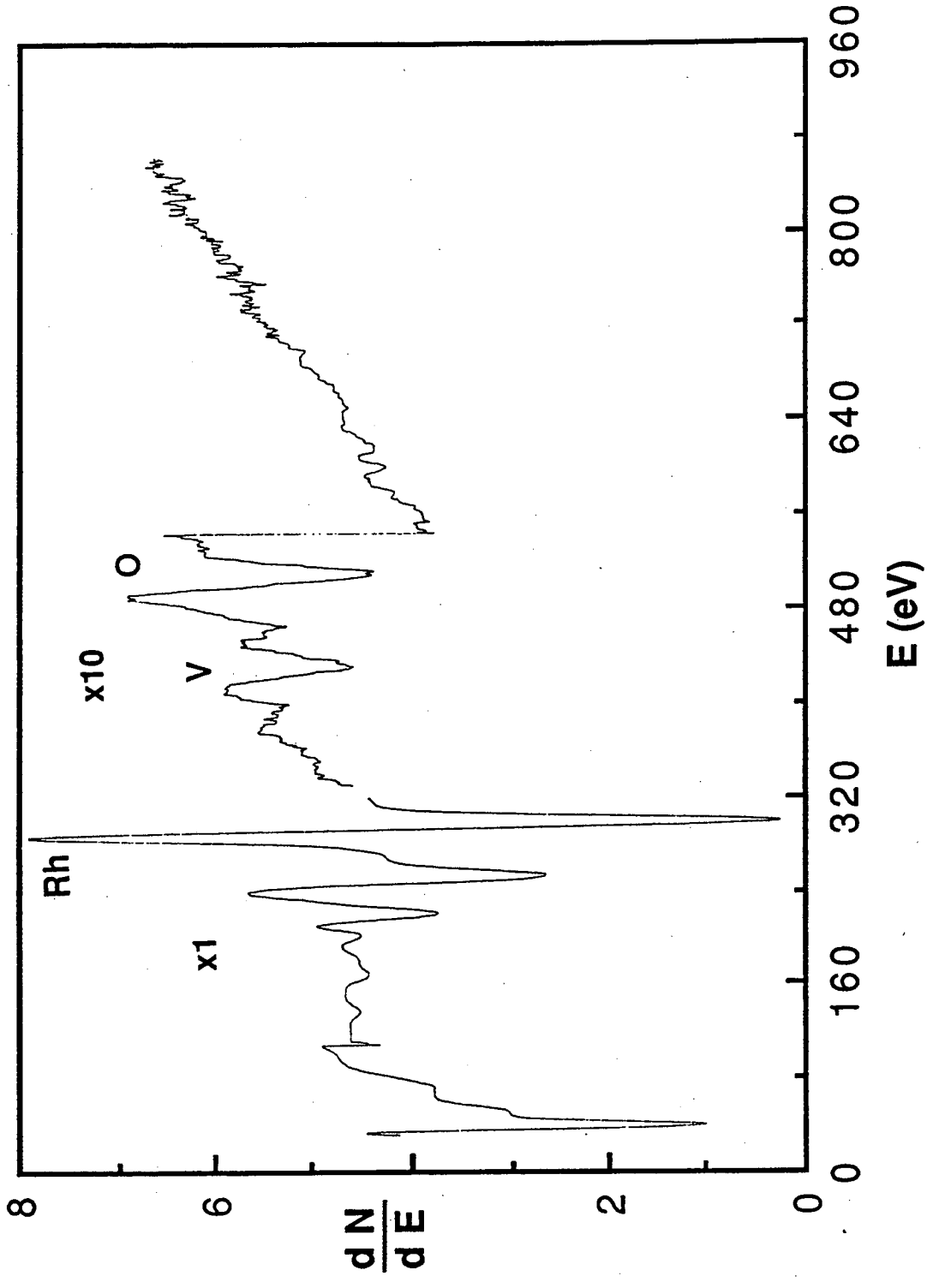

Figure 2.4: An AES spectrum for a 0.5 ML VOx deposit on Rh foil.

only had the capability of monitoring one mass range for each TPD experiment. The ramp rate of the temperature ramp controller, which was built in the U.C. Chemistry Electronic Shop (1058 A1), was approximately linear and determined by plotting temperature rise as a function of time using the HP x - y chart recorder. Ramp rates of approximately 15 °C/s were used. For quantitative TPD measurements the mass spectrometer signal was calibrated by introducing a known amount of calibration gas (measured with the ionization gauge) into the chamber with a leak valve.

2.2.4 Ion Sputter Gun

A Varian 981 - 2043 Ion Sputter Gun was used to clean the sample. Ar^+, ionized by electrons emmitted from the filament, was extracted from the sputter gun and focused on the sample. Surface species were removed upon collision with the ion beam. The LBL Sputter Ion Gun Controller 7S 1773 - A was operated at 30 mA emission with a 2 kV bias giving a crystal current of approximately 30 μA. The angle between the sample surface and the ion beam was approximately 60 °.

2.2.5 Metal Deposition Source

The deposition source consisted of a filament of the material to be evaporated surrounded by a tantalum and stainless steel shield to prevent metal contamination of ceramic parts within the chamber. The aperture at the end of the shield was approximately 1 cm in diameter and was designed to be approximately the dimensions of the sample, to promote uniform metal deposition. A shutter mounted on a rotatable feedthrough could be positioned to cover the evaporator aperture. Using a linear motion feedthrough, the deposition source could be positioned to within 2 cm of the sample. Two types of

filaments were used. For Ti, V, and Fe the wire (>99 % purity) of the metal to be evaporator was wrapped around 0.030 - in W wire (>99 % purity) which was resistively heated with a current of approximately 30 A (~ 1500 °C). Because higher temperatures were required to evaporate Zr, Nb, Ta, and W, a wire of these metals was heated directly to temperatures necessary for evaporation. Each metal source was degassed at a temperature above that used for deposition for approximately 12 hr to remove impurities from the filament.

2.2.6 Pumps

The vacuum within the chamber was obtained using a Varian 4 - in diffusion pump (DP) containing SantoVac 5 oil. The diffusion pump was equipped with a foreline mechanical pump, a liquid nitrogen trap, and cooling water line. An electrical interlock shut down the DP if the cooling water or foreline pumping were interrupted, and the liquid nitrogen trap was filled using an automatic valve and actuator. The chamber was also equipped with an ion pump that was used primarily as a back - up for the diffusion pump. After bake - out and opening the reaction cell, a Varian titanium sublimation pump (TSP) was used to aid in the removal of background $H_2O(g)$. Use of the TSP, lead to improvement in the base pressure of up to an order of magnitude. A base pressure of 5 x 10^{-10} Torr could be obtained when using the diffusion pump in combination with the TSP as measured by a Varian Bayard - Alpert nude ionization gauge.

2.2.7 Reaction Cell

The reaction cell consisted of a Au plated stainless steal cylinder of 1.5 - in diameter. The top portion of the cell which also served as the sample holder was welded to

the manipulator. The bottom half was part of a 4 - in linear motion feedthrough (see Fig. 2.1). The seal of the top and bottom portions of the cell was made with a Viton O - ring by translating the bottom half into alignment with the top. This enclosed the sample within the reaction cell. The linear motion feedthrough was designed to apply a load against the O - ring to ensure a proper seal and could be adjusted laterally to facilitate alignment with the top part of the cell. With an atmosphere of reaction gas, the leak in the seal was 1×10^{-8} Torr to 1×10^{-6} Torr depending on the condition of the O - ring. After an average of 15 reactions, the O - ring deteriorated to the extent that it was replaced. The better the alignment of the two halves of the cell the less damage was done to the O - ring.

2.2.8 Reaction Loop and Gas Manifold

At the bottom of the reaction cell were inlet and outlet lines which led with flexible tubing to Nupro valves labeled HPC (high pressure cell) isolation. The inlet and outlet lines were part of the UHV system, and VCR fittings were used for tubing connections up to the HPC isolation Nupro valves. Tubing from the HPC isolation valves led to the gas chromatograph (GC) where the reaction mixture was analyzed, and from the GC, tubing led back to the reaction cell completing the reaction loop. Within the reaction loop was a metal bellows recycle pump that circulated the reaction gases at a rate of approximately 100 cm^3 / min. The volume of the reaction cell plus reaction loop was determined to be 118 cm^3.

The reactant gasses were introduced into the reaction cell and loop through a gas manifold. Details of the gas handling system for this apparatus are given by Levin (74). The manifold had inlets from H_2, CO, O_2, Ar, and CO_2 gas bottles and had outlets to the manifold pumping system, the reaction loop, and two leak valves mounted on the UHV chamber. The manifold was pumped by a mechanical pump and a molecular sieve, liquid

nitrogen - cooled, sorption pump. Both pumps were required since mechanical pumps poorly evacuate CO and sorption pumps can not handle H_2. Pressure was measured in the manifold with a Granville - Phillips Series 275 convectron gauge and in the reaction loop with a Wallace and Tiernan Pennwalt mechanical gauge that had a range from 1 to 800 Torr.

2.2.9 Gas Chromatograph

Product accumulation in the reaction loop was monitored with a Hewlett - Packard 5890 Series II Gas Chromatograph. Nitrogen was used as the carrier at a column head pressure of 60 psi. The flame ionization detector (FID) was operated with 40 psi compressed air mixed with 20 psi H_2. For the primary product of interest (CH_4) the FID is the most sensitive detector. The column was a Carbopak B 3 % SP 1500 and was held at a temperature of 30 ± 1 °C by the GC oven. The GC was equipped with an automatic sampling valve which was programmed to sample from the reaction loop at periodic intervals. A Hewlett - Packard 3396 Series II Integrator was used to record and analyze the product GC peaks.

2.3 X - Ray Photoelectron Spectroscopy (XPS) and Ion Scattering Spectroscopy (ISS) Apparatus

2.3.1 X - Ray Photoelectron Spectroscopy

A commercial PHI 5300 ESCA system, depicted in Fig. 2.2, was employed for XPS and ISS measurements. In x - ray photoelectron spectroscopy, incident x - ray

radiation (hv) leads to ejection of core level electrons. The binding energy of the core level (E_b) can be determined by measuring the kinetic energy of the ejected electron (E_k) using the expression (84):

$$E_b = hv - E_k - \phi_{sp} ;$$

where ϕ_{sp} is the work function of the spectrometer. The advantage of XPS is that the binding energy of the core level depends on the chemical environment of the atom and can be used to distinguish oxidation states. The PHI 5300 ESCA system was equipped with a Mg (1253.6 eV) anode x - ray source. X - rays were produced by impinging electrons on the target anode. The anode was used at 15 kV and 400 W power. The source was cooled with deionized water and positioned to within 1 cm of the sample during analysis. The energy of the ejected photoelectrons was analyzed with a concentric hemispherical analyzer (CHA) which had a variable pre - retarding potential with which the pass energy was choosen. The detector consisted of a series of channelplate multipliers. The angle between the source and detector was 54.7°. In the survey mode of acquisition, the full binding energy range was scanned (1200 to 0 eV) with a pass energy of 89.5 eV. In the multiplex mode particular energy regions were selected, and a pass energy of 8.95 eV was used. In XPS, smaller pass energies give increased resolution and decreased sensitivity. The spectra were recorded on an Applo computer which allowed for signal averaging of repeated scans and deconvolution of the resulting spectra.

2.3.2 Ion Scattering Spectroscopy

The PHI 5300 ESCA system was used to make ion scattering spectroscopy measurements. In ISS a beam of inert gas ions is accelerated at the target sample at

energies ranging from 500 eV to 3000 eV. Because the duration of the collision is short, the interaction energy is large, and the local binding forces are small, the impact between the ion and the sample can be well described by a simple free atom two - body collision. Based on the laws of energy and momentum conservation, a relationship between the ratio (A) of the mass of the surface atom to that of the ion, the energy of the incident ion (E_O), the energy of the scattered ion (E_i), and the scattering angle θ can be developed. For θ = 90°, the expression relating the energy of the incident ion to that of the scattered ion is given by (84):

$$\frac{E_i}{E_o} = \frac{A-1}{A+1}.$$

Consequently, measuring the ratio of the scattered and incident ion energies gives the mass and atomic identity of the atoms in the outer most surface layer. This makes ISS unique compared to AES and XPS which sample several surface layers. The PHI 5300 was equipped with a differentially pumped ion gun for the source of ions, hemispherical concentric analyzer for ion energy analysis, and channelplate multiplier detector. The differential pumping of the ion gun allowed a two order of magnitude greater pressure to be present in the sputter gun compared to the UHV chamber during ion bombardment. He^4 cations were accelerated toward the sample at 500 eV giving a crystal current of 30 μA. The scattering angle was 123°, and the pass energy was 178.95 eV.

2.3.3 Preparation Chamber

Adjacent to the PHI 5300 ESCA analysis apparatus was a UHV preparation chamber where oxide deposits were grown (see Fig. 2.2). A base pressure of 5×10^{-10} Torr was maintained using a 200 L ion pump and a titanium sublimation pump. The sample was moved in vacuum between the preparation and analysis chambers using a

transfer rod with a fork clamp which fit the sample holder. On the bottom flange of the chamber was a z - motion manipulator that held an electron beam bombardment heater. When the sample rested on the manipulator, electrons evaporated from the electron beam heater filament were accelerated by a 2 kV bias to the back face of the grounded sample through an opening in the sample holder. Mounted above the manipulator was a 2 - in linear motion feedthrough with an alumel - chromel thermocouple probe. The heater was powered by an LBL 7S 2272 Electron Bombardment Supply. On a flange above the sample was mounted an evaporation deposition source identical to that described previously. The preparation chamber was also equipped with two leak valves and a PHI Bayard - Alpert nude ionization gauge.

2.3.4 Environmental Cell

Adjacent to the preparation chamber of the PHI 5300 ESCA system was an environmental treatment cell in which the sample was exposed to gas pressures of up to 800 Torr, as shown in Fig. 2.3. A transfer rod, which was differentially pumped and had Teflon seals, allowed the sample to be moved from the environmental cell to the preparation chamber where, in turn, it was placed in the analysis chamber. The environmental cell was constructed from a 2 3/4 - in six - way stainless steel cross. On the bottom flange of the cross, a sample holder with an alumel - chromel thermocouple was mounted to a z - motion feedthrough. When the sample was placed on this holder, it came in physical contact with the thermocouple. On the top flange of the six - way cross, a Research, Inc. model 4085 infrared radiative spot heater was focused through a 4 - in quartz viewport connected to the six - way cross by a 4 - in to 2 3/4 - in adapter flange. The lamp heater focused to a spot size of 0.25 - in with a focal point of 4 - in. Diffuse radiative heat from the lamp led to increases in the temperature of the viewport of approximately 100 °C for a sample

temperature of 300 °C. The thermal shock to the viewport required the use of quartz rather than glass and a coil of water cooled 3/8 - in Cu tubing to minimize the temperature changes. The two side flanges of the six - way cross that were on axis with the preparation chamber were used for sample transfer. On the other two side flanges were mounted a 2 3/4 - in glass viewport and the pumping / gas inlet line. The pumping / gas inlet line led to a gas manifold that was pumped by a mechanical and a turbo - molecular pump. The pressure in the environmental cell was measured with a Granville - Phillips Series 275 convectron gauge and a Baritron gauge with a range of 0.1 to 1000 Torr.

2.4 Low Energy Electron Diffraction (LEED) Apparatus

The apparatus used for LEED structure measurement was a Varian 240 model 981 - 0030 which is the same model of UHV chamber used for reactivity measurements; however, instead of being equipped with a reaction cell and a CMA, this chamber had a four - grid retarding field analyzer (RFA) for performing LEED. The details of this apparatus are presented by Jentz (86). In LEED, electrons impact the sample surface at energies of 30 to 250 eV and normal incidence and are elasticically back scattered into the four - grid LEED optics. For a surface that has periodic structure, electrons which are elastically scattered form a diffraction pattern on the phosphor LEED screen after being selected from the inelastically scattered electrons with the RFA. The LEED optics used were a Varian 981-0127. The RFA was also used to measure AES spectra by varying the voltages on the grids to select inelastically scattered Auger electrons. This chamber was also equipped with an evaporation deposition source and a UTI mass spectrometer.

Chapter 3

Experimental Procedures

3.1 Sample Cleaning

Fresh, unused Rh and Pt (>99 %) foils were found by AES to be contaminated with B, C, O, S, Si, and Cl. The sample was cleaned by cycles of annealing and Ar^+ ion sputtering. Annealing the sample was found to drive the impurities to the surface where it was removed by sputtering. The background pressure of gas present influenced diffusion of the impurity to the surface. Oxygen was the most effective in cleaning C, S, Si, and Cl. Hydrogen appeared to promote the removal of B and to some extent Si. After approximately two weeks of cycles of annealing and sputtering, C, S, Cl, and Si were no longer detected by AES. The amount of B was minimized by hydrogen annealing but not completely eliminated. Boron which originates within crucibles used to process rhodium metal is known to be difficult to completely removed (87). Once determined clean in UHV by AES, additional contamination, in particular S, was driven to the surface by exposure to the reaction atmosphere ($H_2/CO = 2$, P = 1 atm, and T = 280 °C) requiring further cleaning

with cycles of sputtering and treating at the conditions to be used for the reaction. For reactions involving CO (CO hydrogenation and ethylene hydroformylation), Ni was observed with AES after exposure to the reaction atmosphere. Originally, the Ni was considered to originate from the sample since traps were used to remove impurities from the reactant gases. However, the reaction of Ni and CO to form $Ni(CO)_6$ is highly favorable and the liquid nitrogen trap used on the CO line was not completely effective in removing $Ni(CO)_6$. An activated carbon trap was eventually used to purge the CO stream of nickel carbonyl. Contamination during reaction was also found to originate from outgassing of materials which were part of the reaction loop, such as the Viton O - ring of the reaction cell. Futhermore, for foils which had been used for a large number of experiments, gold was found by AES to be a contaminant. For reactivity measurements, both faces of the foil were used and therefore cleaned using ion sputtering. During ion bombardment, the ion beam struck not only the sample but also the Au support wires spot - welded to the sample face. Consequently, when sputtering one face, Au was sputter deposited on the opposite face. A remedy for this problem was to shorten the sputtering time for each side of the foil from 30 min to 5 min before turning to the other face. Another source of contamination was the oxide overlayers. After measurement of the influence on reactivity, the oxide overlayers were removed from the surface by cycles of annealing in oxygen and sputtering. This process did not completely remove the deposit due to diffusion into the bulk and alloy formation with the Rh or Pt. Eventually, a detectable residue of the metal from the oxide could be detected with AES, so a fresh Rh or Pt foil was introduced for each new metal oxide overlayer studied.

For surface studies the degree of sample cleanliness is only that which can be measured by the analytical techniques. For AES and XPS this is approximately 0.05 ML. This level of contamination may still strongly influence the reactivity of the Rh or Pt foil. The techniques AES, XPS, and TPD are all ex - situ characterizations. Upon exposure to

reactant gases, additional contamination can occur via segregation of contaminant species present in the sample bulk and via surface decomposion of impurities from the reaction mixture. Consequently, surface contamination is a major source of uncertainty in these studies and is likely to account for the approximate 10 % error in the rate measurements of the "clean" surface and the scatter in the measurements of the degree of promotion of the foils by the oxide deposits.

3.2 Preparation of Metal Oxide Overlayers

As shown in Fig. 3.1, the preparation of the oxide deposit was a two step process. In the first step the base metal of the oxide is evaporated on to the clean foil from the filament deposition source in a background of 2 x 10^{-7} Torr O_2. The presence of oxygen promotes oxidation of the overlayer and decreases the degree of carbon contamination. Typically the oxide was evaporated in steps of 0.5 ML or less with a rate of approximately 0.2 ML / min. Evaporation in steps greater than 1.0 ML or rates greater than 0.2 ML / min influences the chemical state of the resulting oxide overlayer. After evaporation in an oxygen background, the metal is partially oxidized to a reduced metal oxide. In the second step of the preparation further oxidation of the metal was accomplished by annealing in 1 x 10^{-6} Torr at 350 °C for 5 min. This annealing temperature is below the temperature at which the oxide deposits were found to diffuse into the bulk, above the temperature necessary to remove carbon contamination by formation of CO_2, and in the range of temperatures used for reaction.

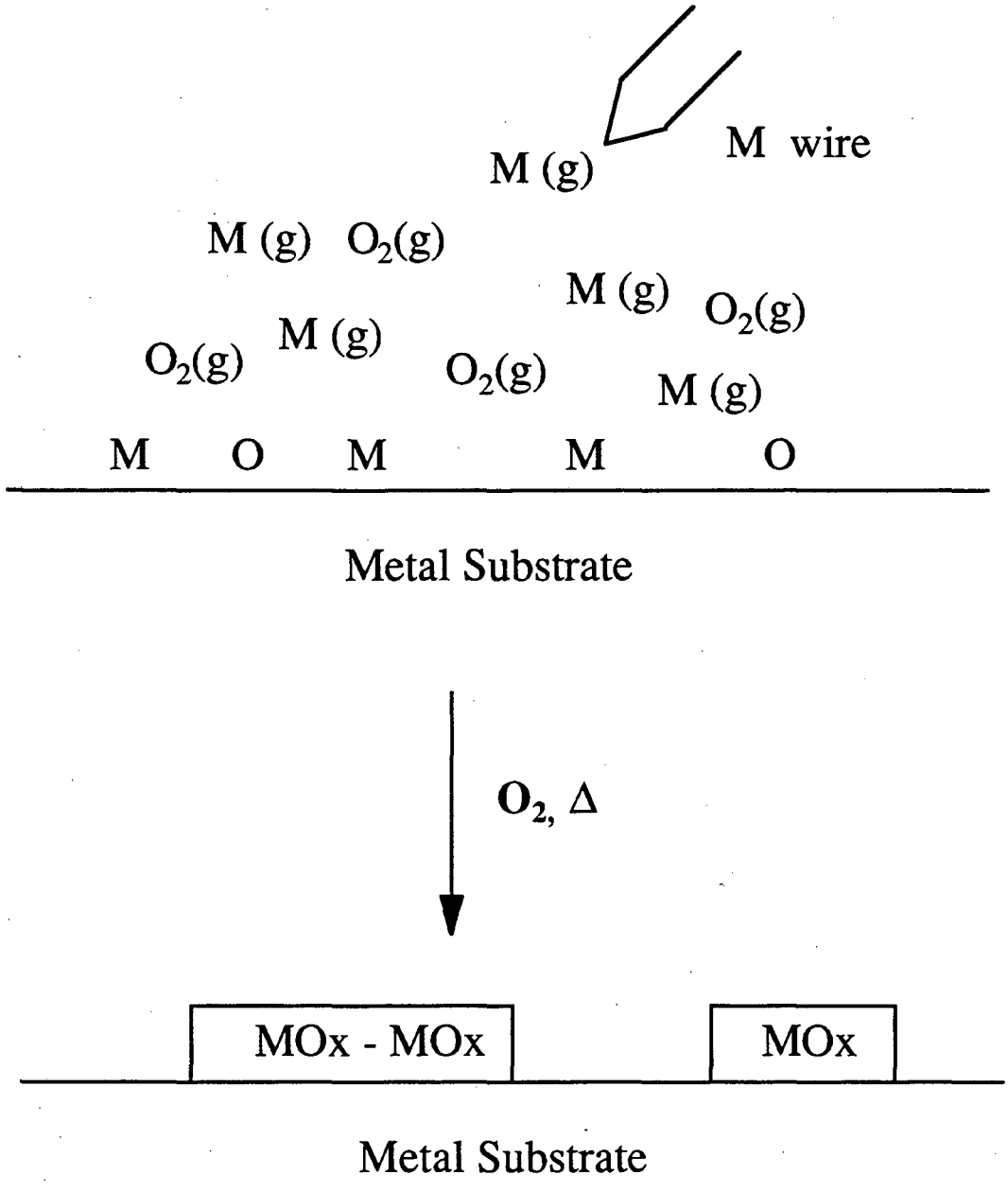

Figure 3.1: Preparation of oxide overlayers.

3.3 Coverage Determination

The coverage of the oxide deposits was determined using AES, ISS, and CO chemisorption uptake experiments. In an uptake experiment the intensity of the substrate and absorbate signals is measured as a function of deposition time. Figure 3.2 depicts schematically the possible modes of oxide growth. The three growth modes are layer - by - layer (Frank - van der Merwe) where the growth of each oxide layer is complete before the growth of subsequent layers, island growth (Volmer - Weber) where the oxide agglomerates into three - dimensional particles, and a combination of layer - by - layer and island growth (Stanski - Kranstanov) where the growth of first monolayer is complete before subsequent three - dimensional island growth (88). For layer - by - layer overlayer growth, a change (or break) in the slope of the uptake curve indicates the completion of a monolayer. The observation of multiple breaks in the AES uptake curve signifies Frank - van der Merwe growth, and the observation of a single break indicates Stranski - Kranstanov growth. After assignment of the coverage using the breaks in the uptake curve, a coverage calibration curve was generated by plotting coverage versus the ratio of the oxide overlayer and substrate AES signals. The ratio of intensities was used to correct for variations in the absolute AES signal from day - to - day operation.

Because of the difficulty in distinguishing breaks in AES uptake curves, other techniques are used to confirm the AES coverage assignment. For example, based on a coverage assignment determined from AES measurements, Levin et al. (74) postulated that titanium oxide deposits infuence CO chemisorption to neighboring Rh atoms. However, Williams et al.(76) performed the same coverage calibration but used ISS measurements to confirm the monolayer assignment. Their work showed that Levin et al. had underestimated the coverage of titanium oxide on Rh by 1/3. A coverage assigned by

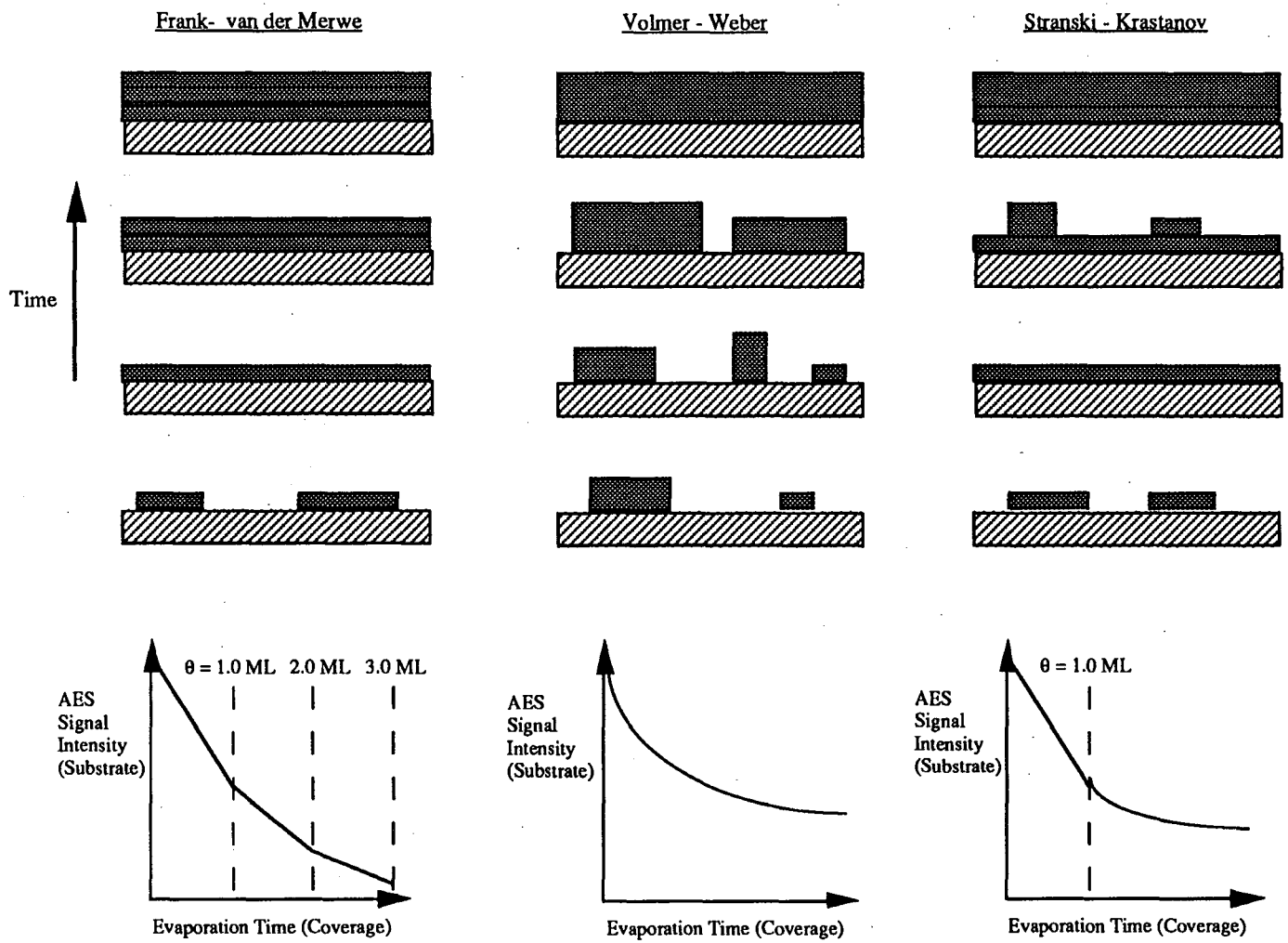

Figure 3.2: Overlayer growth modes.

Levin et al. to 0.33 ML was shown by Williams et al. to correspond to 1.0 ML. Based on the calibration of Williams et al. the decrease in CO chemisorption from the TiOx / Rh surface was attributed to geometric site blocking by the oxide. Consequently in this work, ISS and CO chemisorption uptake experiments were performed to confirm the coverage assignment based on AES. For layer growth, the ISS signal of the overlayer decreases linearly with oxide coverage and is completely suppressed upon completion of the first monolayer. Because none of the oxides studied are known to appreciably adsorb CO, the coverage calibration can be further confirmed by measuring the decrease in CO chemisorption to the Rh and Pt as a function of coverage.

3.4 Oxidation State Determination

The oxidation state of the oxide deposit was determined before and after reaction using XPS. The XPS spectra were a convolution of peaks from each oxidation state present, so the spectra were collected in the high resolution mode (8.95 eV pass energy) to aid in distinguishing the chemical states. The XPS envelope was deconvoluted using the PHI 5300 ESCA software curve fit routine. The routine allowed the peak position, height, width, and shape (Gaussian/Lorentzian) to be varied until the best least squares fit of the data was obtained. Peaks were added to the curve fit only when at least partially resolved in the experimental XPS curve. The binding energies of the fitted XPS peaks were assigned based on agreement with reported XPS data for reference compounds.

3.5 Rate Measurements

The effect of the UHV characterized metal oxide deposit on the reactivity of the Rh and Pt foils was measured after enclosing the sample within the high pressure reaction cell. Reactant gases were introduced while measuring the pressure with the Wallace and Tiernan Pennwalt mechanical pressure gauge. Each gas was passed through traps before introduction into the cell. CO was passed through an activated carbon trap and a liquid nitrogen cooled molecular sieve trap to eliminate iron and nickel carbonyls. Hydrogen was passed through a Pt catalyst (Deoxo hydrogen purifier) trap to eliminate oxygen and a Dri - rite trap to eliminate H_2O. After introduction into the cell, the reactant gases were mixed for approximately 5 min with the recirculation pump, and then the sample temperature was raised to the desired reaction temperature. The temperature controller held the sample within $\pm$ 2 °C of the reaction temperature. The GC sampling valve was programmed to monitor the accumulation of products every 4 min. After reaction, the temperature controller was turned off followed by evacuation of the reaction gases. Within 5 min the reaction cell was opened, and the sample was again within a UHV environment where further characterization was performed. The rate of reaction was determined from the slope of a plot of the product GC peak areas as a function of time. To determine the activation energy, the rate was measured at several reaction temperatures, and to determine partial pressure dependence, the rate was measured with varying reactant pressures.

For the PHI 5300 ESCA system, the environmental cell was used to prepare the sample under conditions identical to those during reaction. The primary difference between the treatment in the environmental and atmospheric reaction cells was that in the environmental cell the gases were not recirculated and the sample was heated by infrared radiation from the spot heater, rather than resistively. Using the environmental cell required moving the sample from the preparaion chamber with the transfer rod. In the

enviromental cell the sample was placed on the sample holder where physical contact was made with the thermocouple and was moved to within approximately 1 - in of the quartz viewport mounted on the top flange of the 2 3/4 - in six - way cross using the adjustable bellows (see Fig. 2.3). This put the sample at the focal point of the infrared spot heater. After introducing the reaction mixture, the sample was brought to reaction temperature and treated for 20 min. The cell was evacuated to 1 x 10^{-5} Torr using a turbo - molecular pump after cooling the sample to below 200 °C. For XPS and ISS analysis of the oxide deposits, the sample was transferred in vacuum directly to the analysis chamber.

Chapter 4

The Growth and Structure of Titanium Oxide Films on Pt(111) Investigated by LEED, XPS, ISS, and STM

Abstract

Titanium oxide films grown on Pt(111) have been investigated using LEED, XPS, ISS, and STM for coverages ranging from 1.0 to 5.0 ML. The oxide overlayers are prepared by vapor phase deposition of titanium metal followed by oxidation in 10^{-6} Torr O_2. Partial dissolution of the overlayer into the Pt substrate occurs upon annealing to temperatures in excess of 500 °C. Annealing in 1 x 10^{-6} Torr O_2 at temperatures ranging from 500 °C to 700 °C leads to a three - fold symmetric structure with a unit cell of 18.2 Å x 18.2 Å. This structure is observed at coverages ranging from 1.0 to 5.0 ML. XPS measurements of this phase show the stoichiometry of TiO_2. Heating in vacuum at 650 °C to 850 °C leads to a new structure with a unit cell of 18.2 Å x 13.9 Å which is observed at coverages of 1.0 to 1.5 ML. This oxide overlayer is shown by XPS to have the

stoichiometry of Ti_4O_7. Similarities are observed between the ordered overlayers and reported structures of stoichiometric and reduced rutile TiO_2 surfaces. Angle resolved XPS measurements of disordered titanium oxide films, formed by annealing at temperatures below 500 °C, indicate that reduced Ti^{3+} is concentrated at the oxide / Pt(111) interface.

4.1 Introduction

Over the past thirty years, studies of the structure of surfaces have focused on metals and semiconductors. The surfaces of oxides of transition metals have been explored to a much lesser extent, despite their important chemical and electronic properties and applications. This has been due in the past to the difficulty of controlling the stoichiometry of the oxides and the concentration of undesirable impurities at the surface. Recently, however, ordered iron oxide and zirconium oxide have been investigated as thin films grown by atomic beam epitaxy from the vapor phase on single crystal platinum substrate surfaces of (111) orientation (90-96).

In this study we report a structural and compositional characterization of titanium oxide thin films grown on the (111) crystal face of platinum. The films were analyzed by low energy electron diffraction (LEED), scanning tunneling microscopy (STM), X-ray photoelectron spectroscopy (XPS), and ion scattering spectroscopy (ISS). Two ordered titanium oxide structures on Pt(111) are observed depending on the sample pretreatment. A three - fold symmetric structure with a $\sqrt{43}x\sqrt{43}$ R 7.6° (18.2 Å x 18.2 Å) unit cell is formed after preparation in O_2 at temperatures between 500 °C to 700 °C. XPS measurements indicate a stoichiometry of TiO_2 . After preparation in vacuum (650 °C - 850 °C), a second ordered overlayer with a primitive cell of dimensions 18.2 Å x 13.9 Å is

found. The stoichiometry of this phase is Ti_4O_7. Because of partial dissolution of the overlayer into the Pt substrate at temperatures in excess of 500 °C, the coverage of titanium oxide after heating in vacuum at 650 °C - 850 °C is ~ 1.0 ML. STM measurements confirm the structures deduced from the LEED analysis for both oxide films. Angle resolved XPS measurements of disordered titanium oxide films indicate that reduced Ti^{3+} ions are concentrated at the oxide / Pt(111) interface. The similarities of the ordered titanium oxide films to structures of bulk titania are discussed.

4.2 Experimental

4.2.1 Titanium Oxide Thin Film Preparation

Titanium was deposited on the clean Pt(111) substrate at ambient temperatures in successive increments of approximately 0.5 ML. The Pt(111) single crystal was cleaned by repeated annealing in 1 x 10^{-6} Torr of O_2 at 600 °C and argon ion sputtering until no contamination could be detected by Auger electron spectroscopy (AES) and the crystal exhibited a (1x1) LEED pattern with a beam splitting indicative of terrace widths of ~ 40 Å. The deposition source consisted of a high purity, 0.020 in diameter, Ti wire wrapped around a 0.030 in diameter W wire filament that was resistively heated. To eliminate impurities the source was degassed for approximately 24 hr. During evaporation a 1 x 10^{-6} Torr background pressure of oxygen was present to promote oxide formation and eliminate carbon contamination. AES and CO chemisorption uptake experiments indicate that the overlayer growth at these conditions is layer - by - layer (8). After each 0.5 ML increment of TiOx deposition, the sample was oxidized at 300 °C in 1 x 10^{-6} Torr O_2. Deposits of 1.0 to 5.0 ML were ordered by raising the sample temperature to between 500

°C and 800 °C for 1 - 5 min. The structure of the ordered overlayer was dependent on the environment ($1x10^{-7}$ to $1x10^{-5}$ Torr O_2 or vacuum).

4.2.2 XPS, ISS, LEED, and STM Characterization

XPS and ion scattering spectroscopy (ISS) measurements were performed in a PHI 5300 ESCA system equipped with a hemispherical analyzer and a differentially pumped ion sputter gun. For XPS, a Mg anode (1253.5 eV) source was operated at 400 W power, and the hemispherical analyzer was operated at 8.75 eV pass energy. For ISS, an incident beam of He ions at an energy of 500 eV was scattered at an angle of 123.0° and analyzed by a hemispherical analyzer operated at 179 eV pass energy. Attached directly to the main chamber was a preparation chamber in which the oxide overlayers were grown. The base pressure in the preparation chamber was $5x10^{-10}$ Torr. This chamber contained an electron bombardment heater, an alumel-chromel thermocouple, and a titanium evaporation source identical to that used in the LEED apparatus. After deposition of the oxide overlayers, the sample was moved from the preparation chamber to the analysis chamber by means of a transfer rod. The coverage of the overlayer was calibrated from XPS and ISS uptake measurements.

The XPS envelope was deconvoluted using the PHI 5300 ESCA software curve fit routine. The routine allowed the peak position, height, width, and shape (Gaussian/Lorentzian) to be varied until the best least squares fit of the data was obtained. Based on a comparison with reported XPS data for reference compounds (see Chapter 7), the Ti 2p doublet observed at 458.4 eV and 464.1 eV is assigned to Ti^{4+} and that observed at 456.2 eV and 461.9 eV is assigned to Ti^{3+}.

The LEED surface structure measurements were performed in a separate ultra high vacuum (UHV) chamber equipped with an off-axis Varian four grid LEED optics, which

also functioned as an retarding field analyzer for AES analysis. Diffraction patterns were recorded from the LEED screen with a Dage MTI - SIT68 high sensitivity video camera, interfaced with a computer. This allowed the LEED patterns to be digitized and stored for subsequent analysis. The chamber was also equipped with a UTI mass spectrometer for temperature programmed desorption studies and a titanium deposition source. The oxide coverage was determined using AES and CO chemisorption. The Pt(111) single crystal was heated resistively while the temperature was monitored with an alumel-chromel thermocouple spot-welded to the back face of the crystal.

Scanning tunneling microscopy experiments were carried out in a separate UHV chamber using the same experimental procedures as described previously. Sample preparation was also carried out in situ, and the sample was transferred from the manipulator onto the STM. The STM head is of a double tube design and has been described in detail previously (97). The electronic control and software were designed in house (98). All STM images shown here are taken in the constant current mode where the tip moves up and down to keep the current constant, and this z-motion provides the contrast for the image. Sample bias voltages vary from -0.5 to +1.5 V and current values from 0.8 to 1.4 nA.

4.3 Results and Discussion

4.3.1 Disordered Titanium Oxide Films

Disordered titanium oxide films are formed after annealing at temperatures less than 500 °C or greater than 800 °C. The total Ti (Ti^{4+} + Ti^{3+}) and the partial Ti^{3+} XPS signal for successive 0.5 ML depositions up to a coverage of 5.0 ML is shown in Fig. 4.1. After

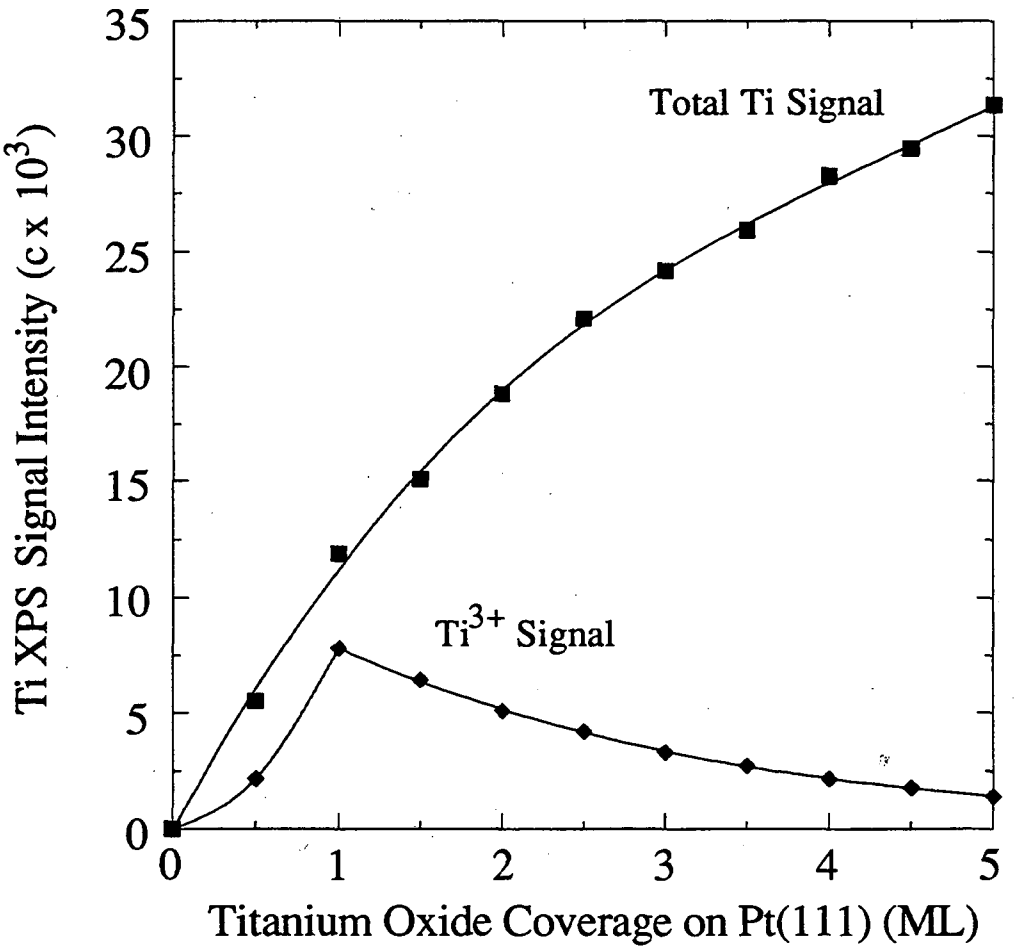

Figure 4.1: Total Ti XPS signal (Ti^{4+} + Ti^{3+}) from titanium oxide deposits on Pt(111) and the Ti^{3+} component plotted as a function of coverage. After each successive, 0.5 ML deposition the surface has been annealed in 1 x 10^{-6} Torr O_2 at 300 °C.

each 0.5 ML deposition, the sample was annealed at 300 °C in $1x10^{-6}$ Torr O_2 for 5 min. This is well below the temperature at which the Ti XPS signal begins to decrease due to loss of titanium oxide from the surface region (see 4.3.2.). Auger and CO chemisorption uptake measurements indicate that the oxide growth is mostly two - dimensional.

As the coverage of the titanium oxide is increased from 1.0 to 5.0 ML, the total Ti (Ti^{4+} + Ti^{3+}) XPS signal increases, and the fraction of Ti present as Ti^{3+} decreases. For the 3.0 ML deposit the XPS sampling depth was varied by orienting the sample at ~ 90° and 10° with respect to the detector as shown in Fig. 4.2. When the surface sensitivity is highest (10° sample orientation) only 3 % Ti^{3+} is observed compared to 17 % when the sensitivity is lowest (90°). This suggests that the Ti^{3+} is concentrated at the interface between the oxide layer and Pt(111) substrate. To further confirm the location of reduced titania within the film, a model for the overlayer was developed in which TiO_2 is assumed to grow upon a reduced 1.0 ML deposit. The model predicts that the decrease in Ti^{3+} XPS signal with increasing TiOx coverage results from attenuation of the Ti^{3+} signal in the first monolayer by subsequent layers of TiO_2. The attenuation factor (α) is derived from a fit to the total Ti intensity data in Fig. 4.1, resulting in a value of $\alpha = 0.66$. This attenuation factor was then used to determine the expected decrease in the Ti^{3+} signal after attenuation by subsequent deposits of TiO_2. Figure 4.3 shows the calculated Ti^{3+} signal versus oxide coverage compared with that found experimentally. The close agreement between the experimental and calculated attenuation of the Ti^{3+} signal provides further evidence that oxidized TiO_2 grows upon a reduced monolayer of titania. The decrease in the oxidation state for Ti atoms located at the titania/Pt(111) interface is attributed to bonding interactions with the Pt surface. This conclusion is consistent with a Hartree-Fock calculation of the bonding between titanium oxide and Pt by Horsely et al. (99) in which higher bonding energies are found when an oxygen atom is removed from the coordination sphere of TiO_2 so that direct bonding between Ti and Pt occurs.

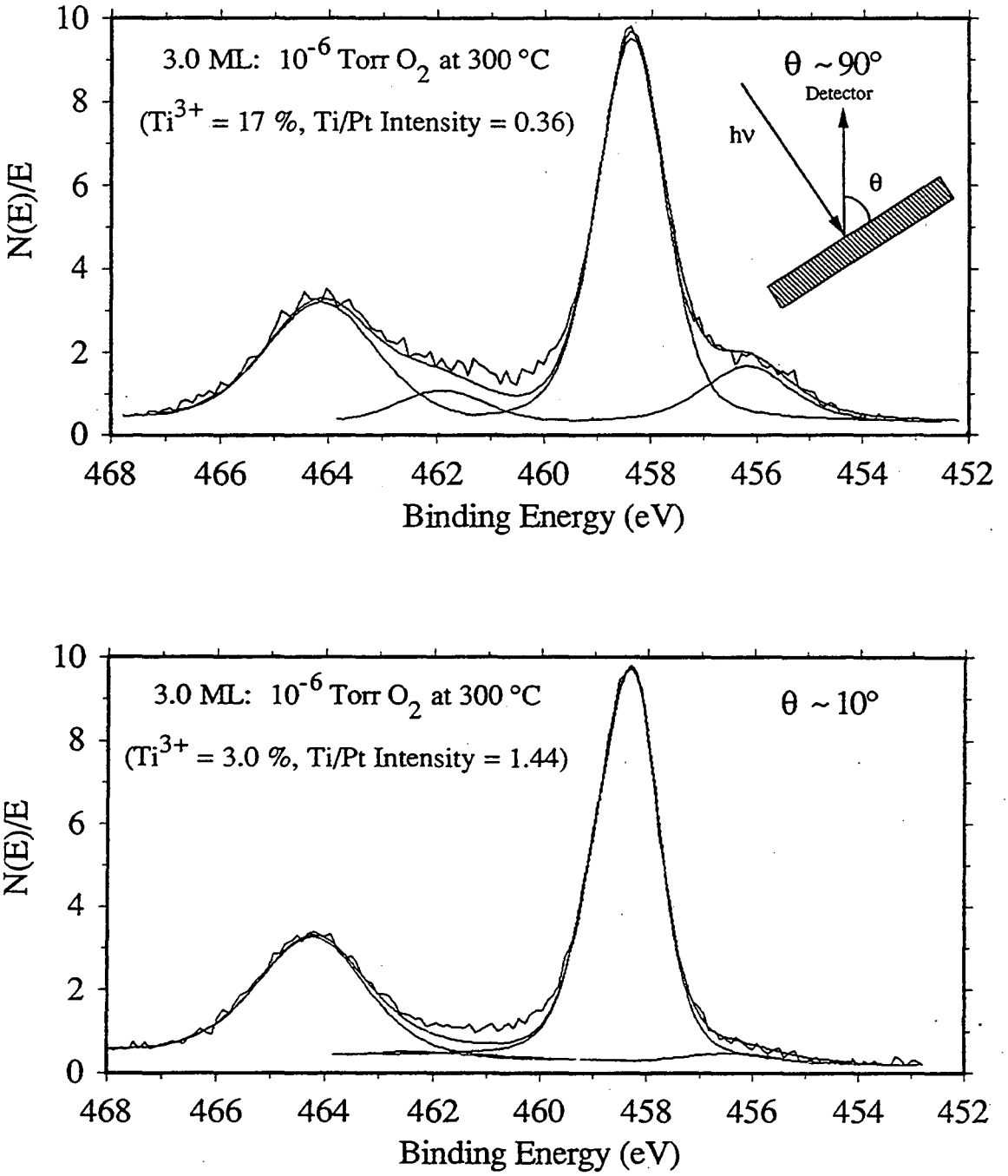

Figure 4.2: Ti 2p XPS spectra of a 3.0 ML titanium oxide deposit on Pt after annealing to 1 x 10^{-6} Torr O_2 at 300 °C collected with the angle between the surface and the detector at (a) 90 ° and (b) 10 °.

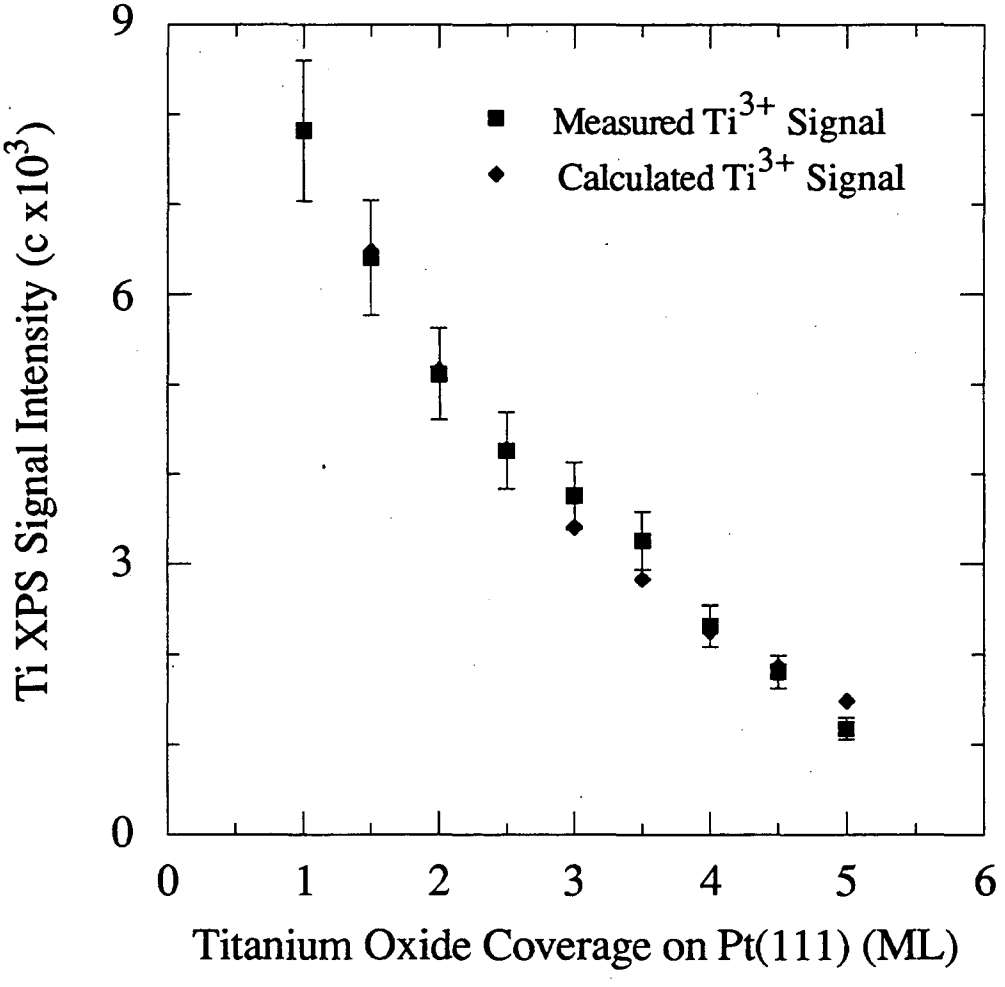

Figure 4.3: A comparison of the experimentally measured Ti^{3+} signal with that calculated assuming the Ti^{3+} is concentrated in the first monolayer at the oxide/metal interface.

4.3.2 Stoichiometric Ordered Titanium Oxide Films

Figure 4.4 shows the change in total (Ti^{4+} + Ti^{3+}) Ti XPS signal and the percentage of Ti^{3+} after annealing a 3.0 ML titanium oxide overlayer from 300 to 1000 °C in 10^{-6} Torr of O_2 for 5 min. Before the XPS spectra were taken, the sample was quenched to below 300 °C . The total Ti signal intensity remains more or less constant up to 500 °C, followed by a decrease in the signal intensity as the temperature is raised further. A similar decrease in titanium oxide signal has been reported in other studies of titanium oxide films on Pt (100-103). The decrease in Ti signal with increasing temperature above 500 °C is not linear. A change in slope is observed at 575 °C with a greater loss in Ti signal per degree rise in temperature observed between 500 °C and 575 °C than is observed from 575 °C to 1000 °C. This suggests that two mechanisms are responsible for the loss of titanium oxide signal. Since no titanium is detected in the gas phase with a mass spectrometer, the decrease in titanium XPS signal is due to either diffusion of titanium into the bulk of the Pt(111) (forming a Pt - Ti - O alloy) or overlayer agglomeration.

The variation in the percentage Ti^{3+} with increasing annealing temperature is also shown in Fig. 4.4. While from 300 °C to 500 °C the total Ti signal remains constant, the fraction of Ti^{3+} declines. Since angle resolved XPS measurements indicate that the Ti^{3+} is located at the interface between the oxide overlayer and the Pt(111) substrate (see Fig. 4.2), oxygen must diffuse through the 3.0 ML TiOx overlayer to react with Ti^{3+}. With further increase in temperature up to 600 °C, the percentage of Ti^{3+} declines to less than 2 %.

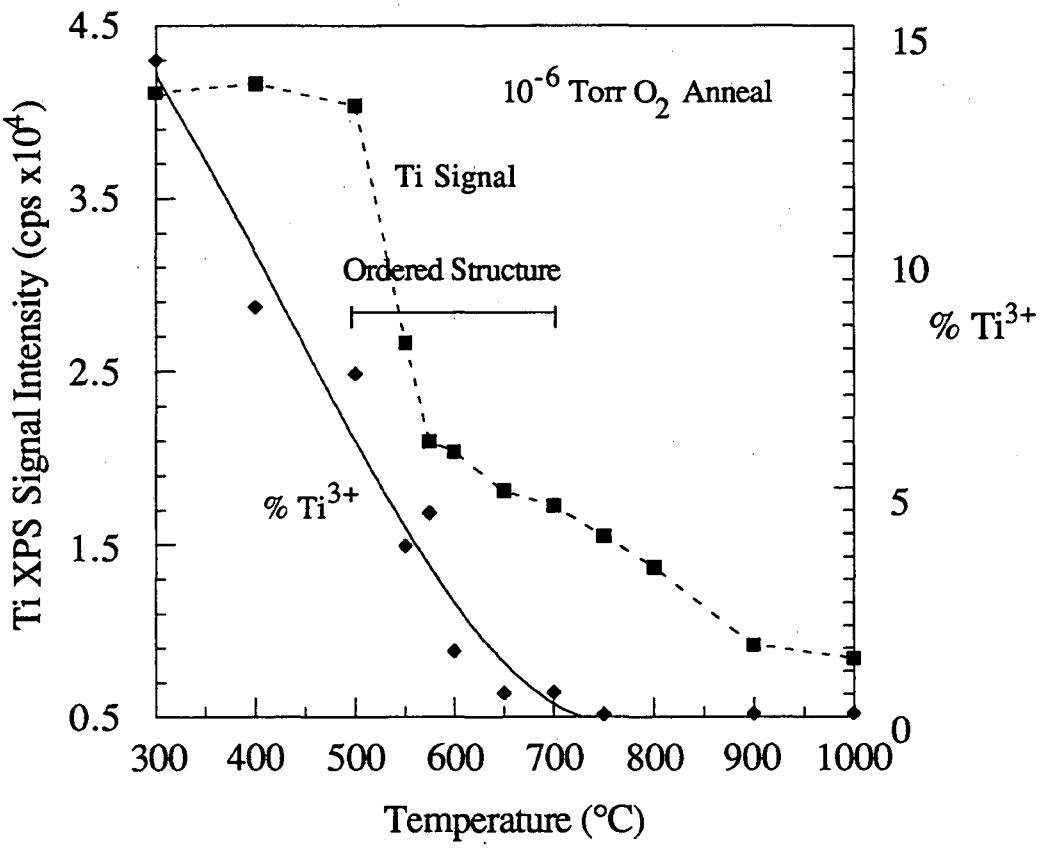

Figure 4.4: Ti 2p XPS signal from of a 3.0 ML titanium oxide film as a function of temperature in 1 x 10^{-6} Torr O_2. The temperature range is indicated for which an ordered overlayer is observed by LEED.

Figure 4.5 shows ISS spectra of a 3.0 ML titanium oxide deposit annealed in 10^{-6} Torr O_2 to 300 °C and 575 °C as well as of the clean Pt(111) for reference. After heating to 300 °C, a negligible Pt ISS signal indicates a coverage of the Pt(111) substrate by a contiguous layer of titanium oxide. However, when this sample was heated to 575 °C in O_2, a Pt ISS signal corresponding to approximately 0.3 ML of exposed Pt substrate is observed, despite a coverage of titanium oxide as determined from the ratio of Ti/Pt XPS intensity of 2.0 ML. Since STM measurements of this film indicate the presence of pits within the overlayer (see Fig 4.10), no titanium is detected in the gas phase, and no XPS features characteristic of Pt - Ti - O alloy formation (66) are found, the exposure of the Pt substrate as measured by ISS is attributed to partial overlayer agglomeration upon oxidation at temperatures above 500 °C. This conclusion is consistent with several studies which demonstrate that oxidation leads to de - wetting of oxide overlayers on metal substrates (104,105). This interpretation is also in agreement with the behavior of the Ti^{3+} signal. As the overlayer is oxidized, Ti^{3+} cations at the oxide/metal interface are oxidized to Ti^{4+}, thereby reducing the wetting of the Pt surface by the oxide. The decline in the Ti ISS signal intensity observed above 575 °C is attributed to dissolution into the Pt bulk. Consequently, two mechanisms are postulated for the loss of Ti XPS signal upon oxidation at elevated temperatures. From 500 to 575 °C, the decline in signal is attributed to overlayer agglomeration, and above 575 °C, the signal loss is attributed to diffusion of Ti into the bulk of the Pt substrate.

Figure 4.6a shows an XPS spectrum of the Ti $2p_{3/2}$ binding energy region obtained after annealing a 3.0 ML titanium oxide deposit in $1x10^{-6}$ Torr O_2 at 600 °C. This is within the range of temperatures (500 °C - 700 °C) where an ordered film is formed. The spectrum shows that titanium is all in the 4+ oxidation state, which along with the ratio of O/Ti XPS signal is consistent with an oxide stoichiometry of TiO_2.

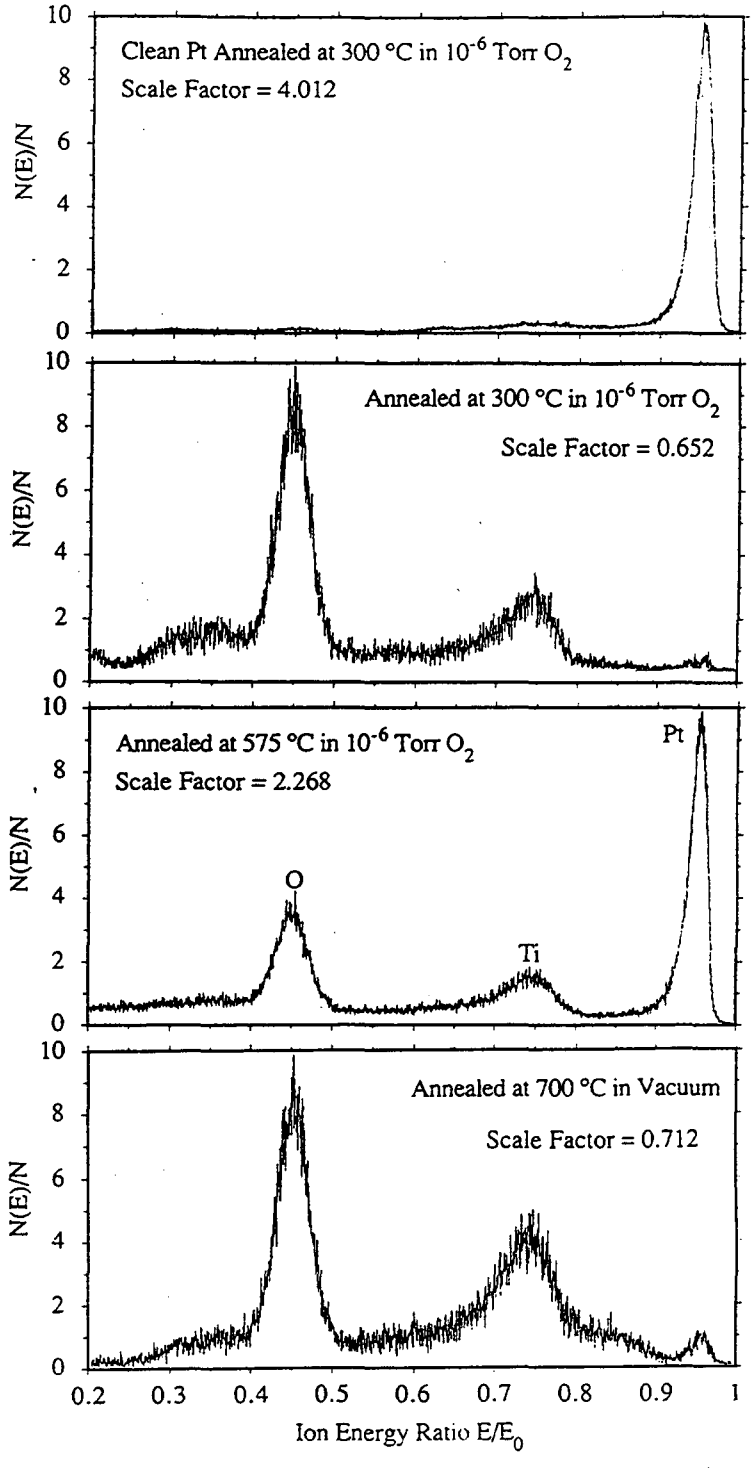

Fig. 4.5: ISS spectra of (a) clean Pt, (b) a 3.0 ML titanium oxide deposit of annealed at 300 °C in 1 x 10^{-6} Torr O_2, (c) a 3.0 ML deposit annealed at 575 °C in 1 x 10^{-6} Torr O_2, and (d) a 3.0 ML deposit annealed at 700 °C in vacuum.

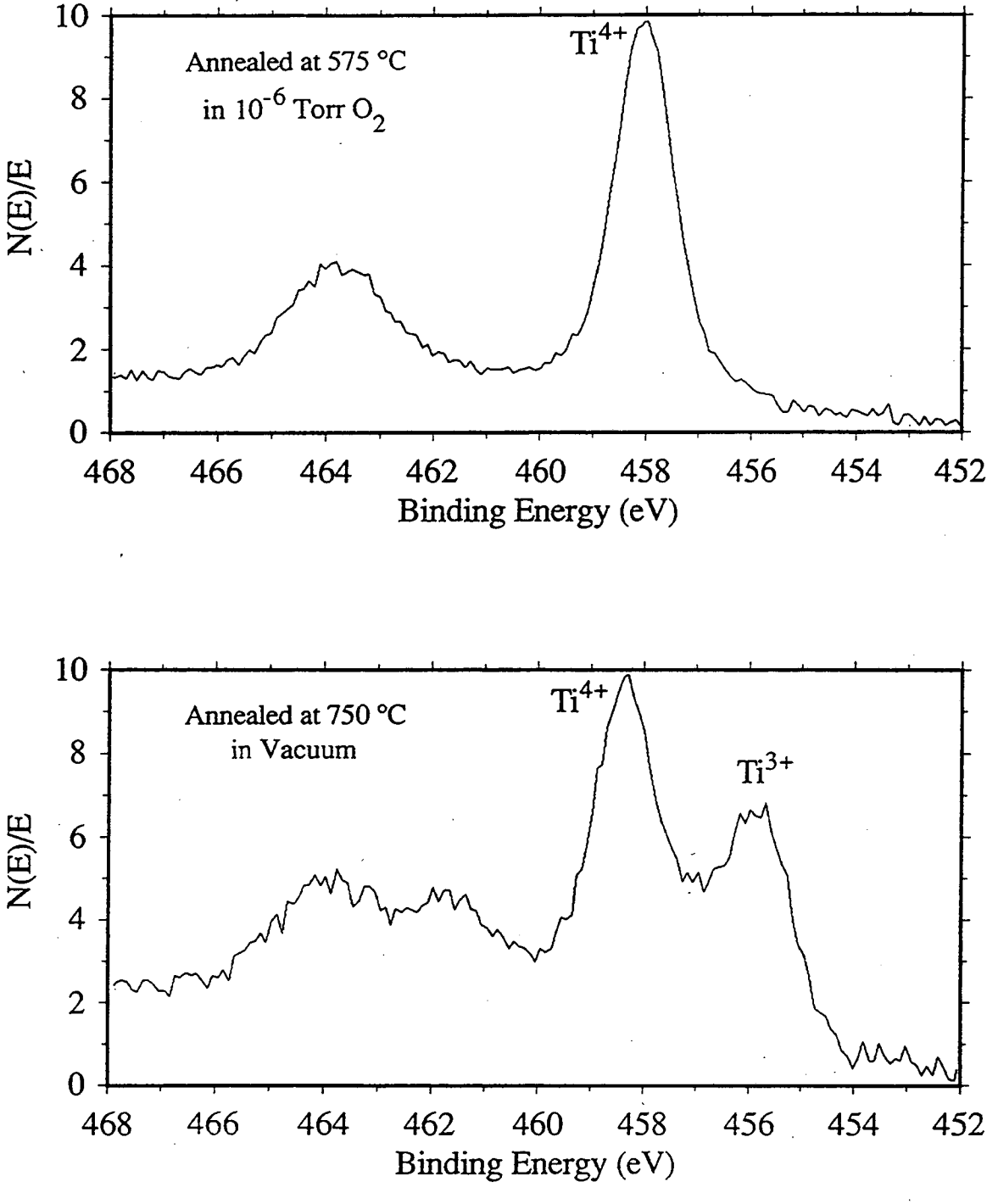

Fig. 4.6: Ti 2p XPS spectra of the ordered overlayer prepared by annealing at a) 575 °C in 1 x 10^{-6} Torr O_2 and b) 750 °C in vacuum.

The LEED pattern of the TiO_2 ordered overlayer is shown in Fig. 4.7 and 4.8. It exhibits six sets of diffraction beams with three - fold symmetry, each set consisting of six pairs of satellite beams surrounding a central beam. The central beam corresponds to a lattice spacing that is equivalent to that of Pt (2.77 Å); however, the most intense spots in the satellite group correspond to a spacing of 3.3 ± 0.2 Å. The pairing of diffraction beams is produced by overlap of the diffraction patterns of two overlayer domains. Repeating units of the primitive unit cell are outlined in the schematic diagram of Fig. 4.8. The dimensions of the unit cell are 18.2 Å x 18.2 Å which corresponds to a $(\sqrt{43} \times \sqrt{43})$ R 7.6° structure with respect to the Pt(111) substrate. This structure may also be described in matrix notation by:

$$\begin{bmatrix} 7 & 1 \\ -1 & 6 \end{bmatrix}$$

Illustrated in Fig. 4.9 is the real space representation of the unit cell superimposed on a Pt(111) substrate.

An 118 Å x 112 Å constant current mode STM image of a TiO_2 overlayer produced under identical preparation conditions is shown in Fig. 4.10. Rows are observed running in the direction marked by the cursor line (A). The spacing between these rows is 3.5 ± 0.3 Å, consistent with the spacing of the lattice producing the intense spots in the LEED pattern. Intersecting these rows is another set of rows like the one marked by a broken line. The intersection between the two features forms predominantly angles of $60° \pm 10°$ with the large error caused by thermal drift. 2D Fourier transforms of these images reveal distinct, 18 Å, periodicities in the directions perpendicular to the rows indicated by the broken line, which are not evident on visual inspection of the image. This is consistent with the spacing of the unit cell (18.2 Å x 18.2 Å) determined from the LEED analysis. The dark areas in the STM image are pits or defects within the overlayer.

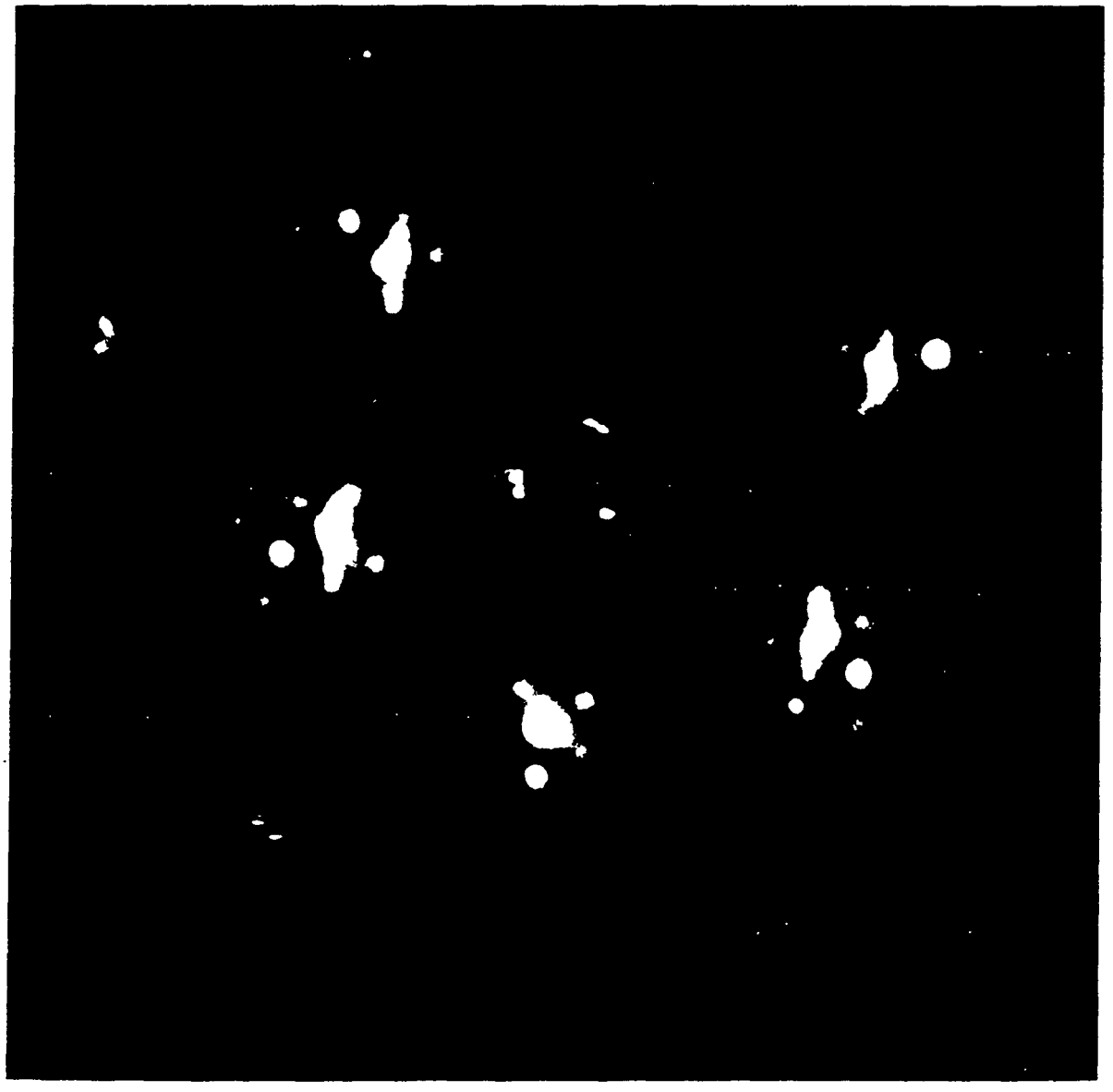

Figure 4.7: LEED pattern of the TiO_2 film measured with a 89 eV incident electron energy.

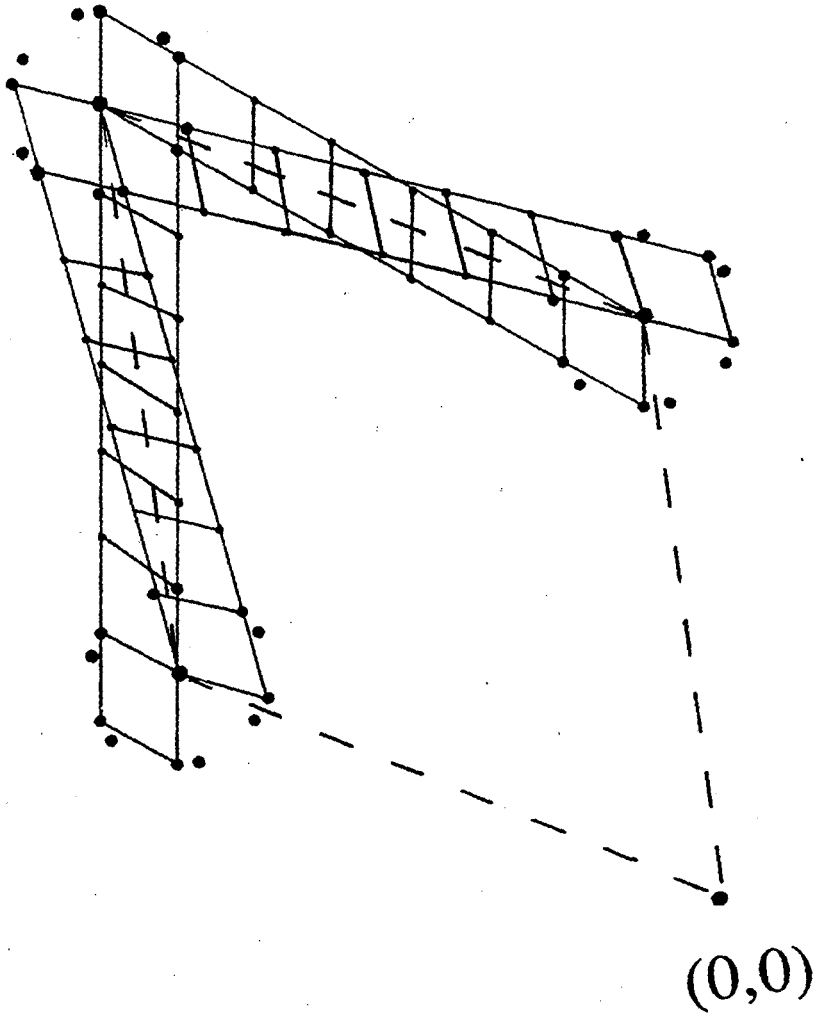

Figure 4.8: The schematic representation of the LEED pattern. The two domains of the structure are indicated.

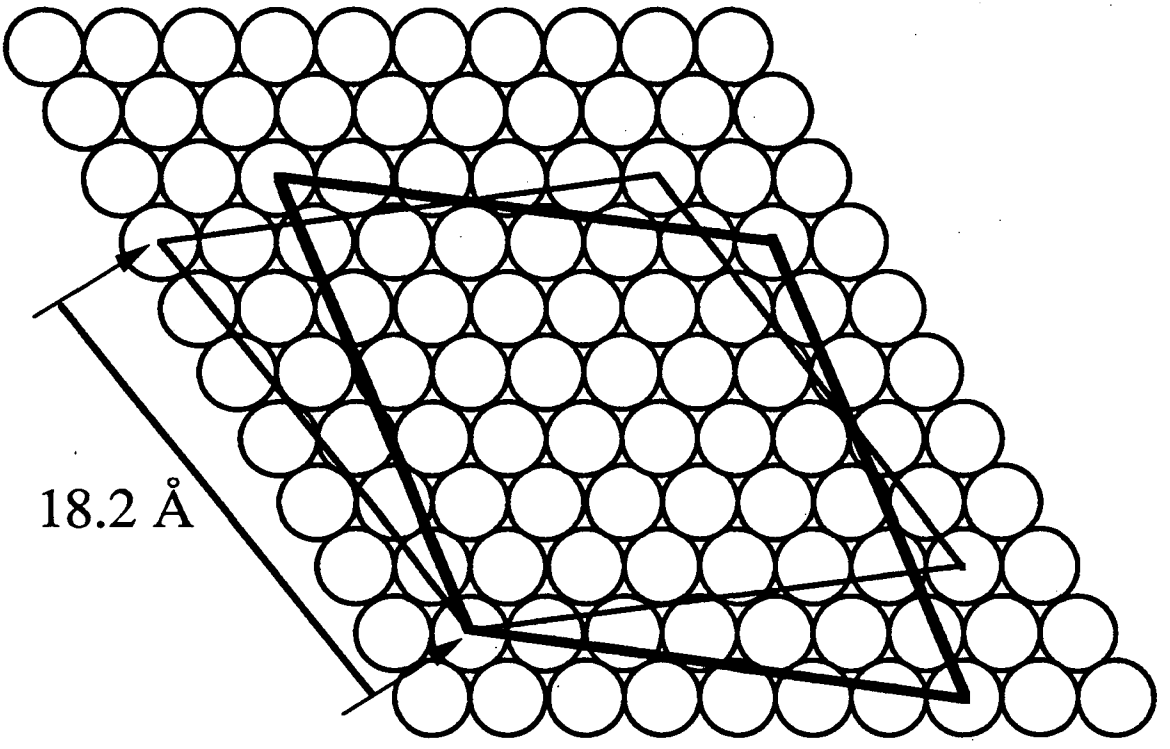

Figure 4.9. Real space representation of the TiO_2 unit cell superimposed on a Pt(111) substrate.

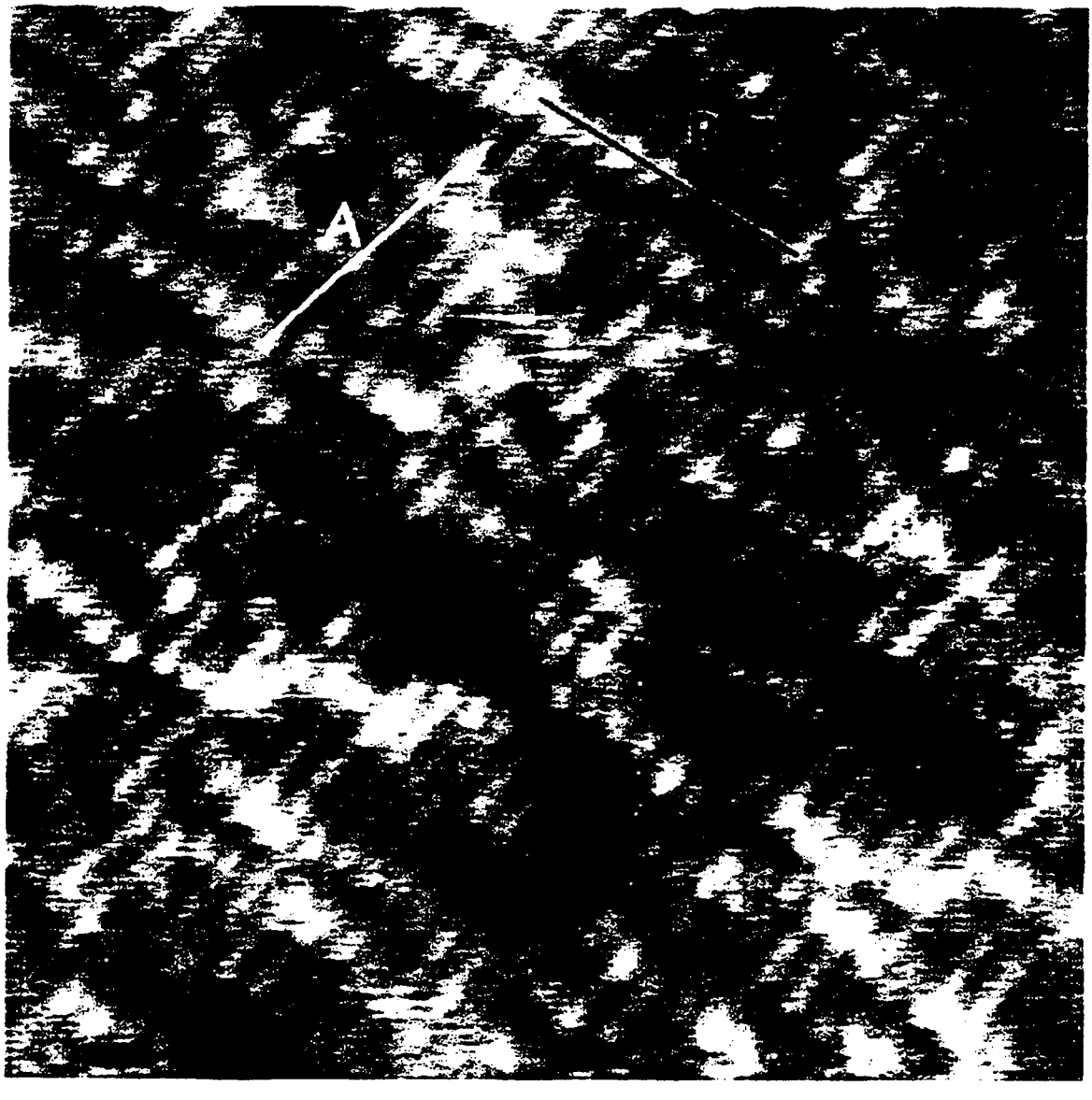

Figure 4.10. Constant current image of a 118 x 112 Å area taken at sample bias of 1.23 V and a current of 0.96 nA. Rows in the direction marked by a cursor labeled A are spaced by 3.5 ± 0.3 Å. Another set of rows (marked B) appear to be partially random, but a Fourier transform reveals a preference for an 18 Å spacing along the direction perpendicular to B.

The STM image was taken at a positive sample bias of 1.5 V, or tunneling into the unoccupied conduction band on the sample. UPS experiments on TiO_2 surfaces have shown that this band is primarily composed of Ti 3d states (106). Thus, it could be argued that primarily Ti atoms contribute to the tunneling current at this bias and produce the bright spots in the image (107). However, the geometry of the surface is unknown making the interpretation difficult. I-V tunneling spectra of this ordered overlayer show a band gap of approximately 4 eV, larger than the expected band gap of bulk TiO_2 (3.1 eV) but clearly indicating a well developed gap as expected from the stoichiometric oxide.

In the rutile structure as viewed from the (111) surface, oxygen anions form a nearly hexagonal close-packed array with half the octahedral holes filled with Ti^{4+} cations (106). While no studies have been reported for rutile TiO_2(111) surfaces, the (111) crystal face is postulated to be stable and has been observed as facets upon annealing a TiO_2(001) surface in vacuum (108). The O-O distances in rutile TiO_2 are 2.54 Å, 2.78 Å, and 2.96 Å (109) which are smaller than the 3.3 - 3.5 Å atomic spacing indicated by LEED and STM. This suggests that the spacing in the three fold symmetric TiO_2 film on Pt(111) is substantially expanded compared to bulk titania. An expanded oxygen spacing has also been reported for iron oxide on Pt(111) but only by 7% (from 3.04 Å to 3.2 Å) (95).

4.3.3 Reduced Ordered Titanium Oxide Films

Annealing in vacuum between 650 °C to 800 °C produces an ordered layer as shown by LEED and STM. Figure 4.6b shows an XPS spectrum of the 2p3/2 Ti region of a 3.0 ML deposit which has been annealed at 750 °C in vacuum. Deconvolution of this region indicates that 46 % of the Ti is in the 3+ oxidation state which corresponds to an oxide stoichiometry of $TiO_{1.77}$. This stoichiometry closely matches that reported for titania overlayers (Ti_4O_7) in TiO_2 - supported Pt which had been reduced at elevated temperatures (500 °C) (110).

Figure 4.11 shows the decrease in the Ti 2p XPS signal and the change in percentage of Ti^{3+} for a 3.0 ML titanium oxide deposit annealed at different temperatures in vacuum. Similar to the oxide film annealed in O_2 (see Fig. 4.4), the Ti signal remains approximately constant up to a temperature of 550 °C, after which a continuous decrease in signal is observed. In addition to this loss, a reduction of the Ti is observed. The percentage of Ti^{3+} increases from 10 % at 550 °C to 65 % at 1000°C.

The loss of Ti signal from a 3.0 ML titanium oxide overlayer was also observed after annealing in 1 $x10^{-6}$ Torr H_2. The decrease in Ti signal intensity and extent of oxide reduction in this case are similar to that observed in vacuum. However, whereas after annealing in vacuum to 1000 °C, a significant Ti signal is still observed, after annealing in H_2, the Ti XPS signal is negligible. This suggests that hydrogen promotes diffusion of TiOx ($x < 2$) or Ti metal into the Pt bulk.

The ISS spectrum after annealing to 700 °C in vacuum is shown in Fig. 4.5d. The surface coverage as determined from the Ti and Pt XPS signals is 1.2 ML. The O/Ti ISS peak ratio is smaller than that observed after oxidation in 10^{-6} Torr O_2 indicating that the amount of oxygen relative to titanium in the outer most surface layer has decreased. The Pt ISS signal is nearly completely suppressed, indicating that no Pt is now present in the

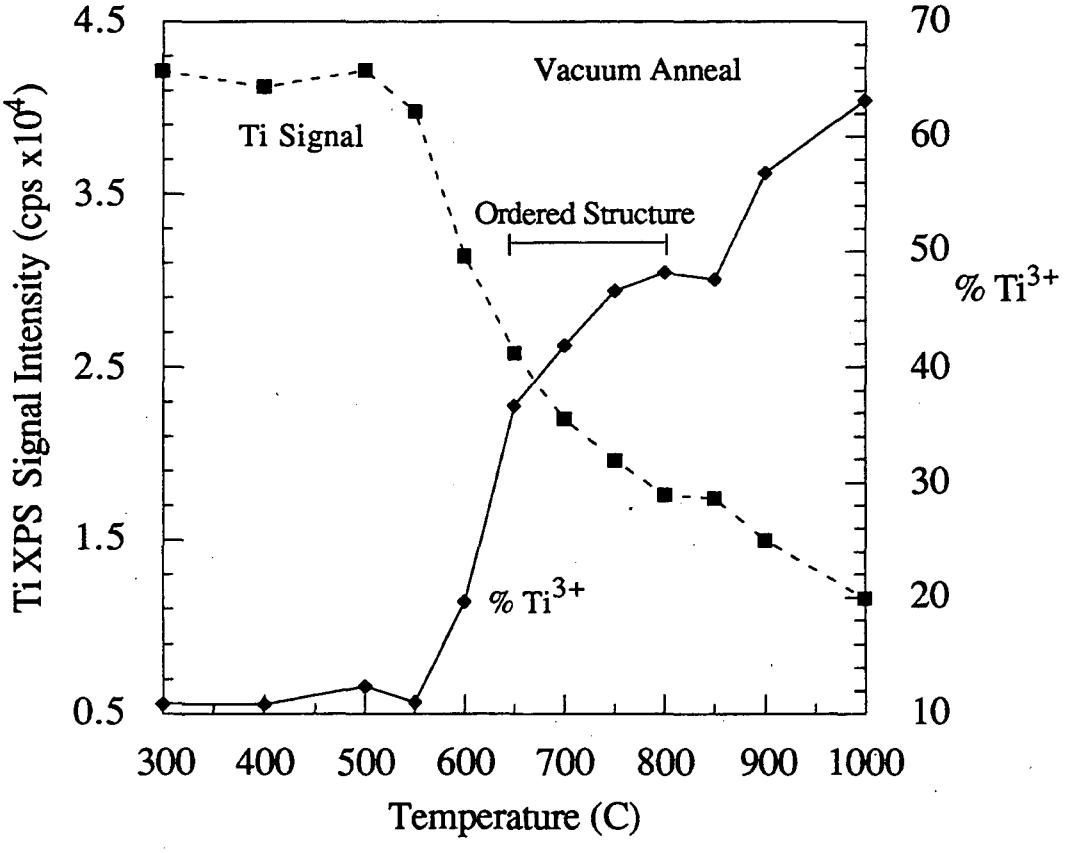

Figure 4.11: Ti 2p XPS signal from a 3.0 ML titanium oxide film as a function of temperature in vacuum. The temperature range for which an ordered structure is observed by LEED is indicated.

the outermost surface layer. This is in sharp contrast to the ISS spectrum observed after heating in 10^{-6} Torr O_2 to 575 °C in which a Pt ISS signal corresponding to ~ 0.3 ML of exposed Pt was measured. This indicates the different wetting properties of stoichiometric and reduced oxide films.

Figure 4.12 shows the LEED pattern of the ordered oxide film prepared in vacuum (650 °C - 850 °C). A schematic of the LEED pattern is presented in Fig. 4.13. The majority of the diffraction beams in the LEED pattern are weak and form a pattern with oblique symmetry as the primitive unit cell, given by the bold lines in the schematic representation in Fig. 4.13. The registry of the overlayer with the Pt(111) substrate may be described by the matrix notation:

$$\begin{bmatrix} 5 & 0 \\ 1 & 7 \end{bmatrix}$$

Figure 4.14 shows the real space representation of the monolayer structure superimposed on a Pt(111) substrate. The primitive cell, represented by bold lines in Fig. 4.14, has dimensions of 13.9 Å x 18.2 Å. The 18.2 Å spacing is identical to that observed in the unit cell of the TiO_2 film.

A modulation of the intensity of the diffracted beams gives rise to a more intense subset of spots that form a pattern with rectangular symmetry. This is shown by the thin lines in Figs. 4.13 and 4.14. The dimensions of this rectangular cell are 8.4 Å x 3.5 Å. A different choice of the unit cell with oblique symmetry is shown in broken lines. Missing pseudo 1/2 order diffraction beams from the rectangular cell, shown by open circles in Fig. 4.13, indicate the presence of glide planes.

STM images of a similarly prepared structure taken in the constant current mode are presented in Fig. 4.15 and Fig. 4.16. The 230 Å x 230 Å image in Fig. 4.15 shows several terraces separated by a step height of 2.4 ± 0.2 Å, consistent with the monatomic

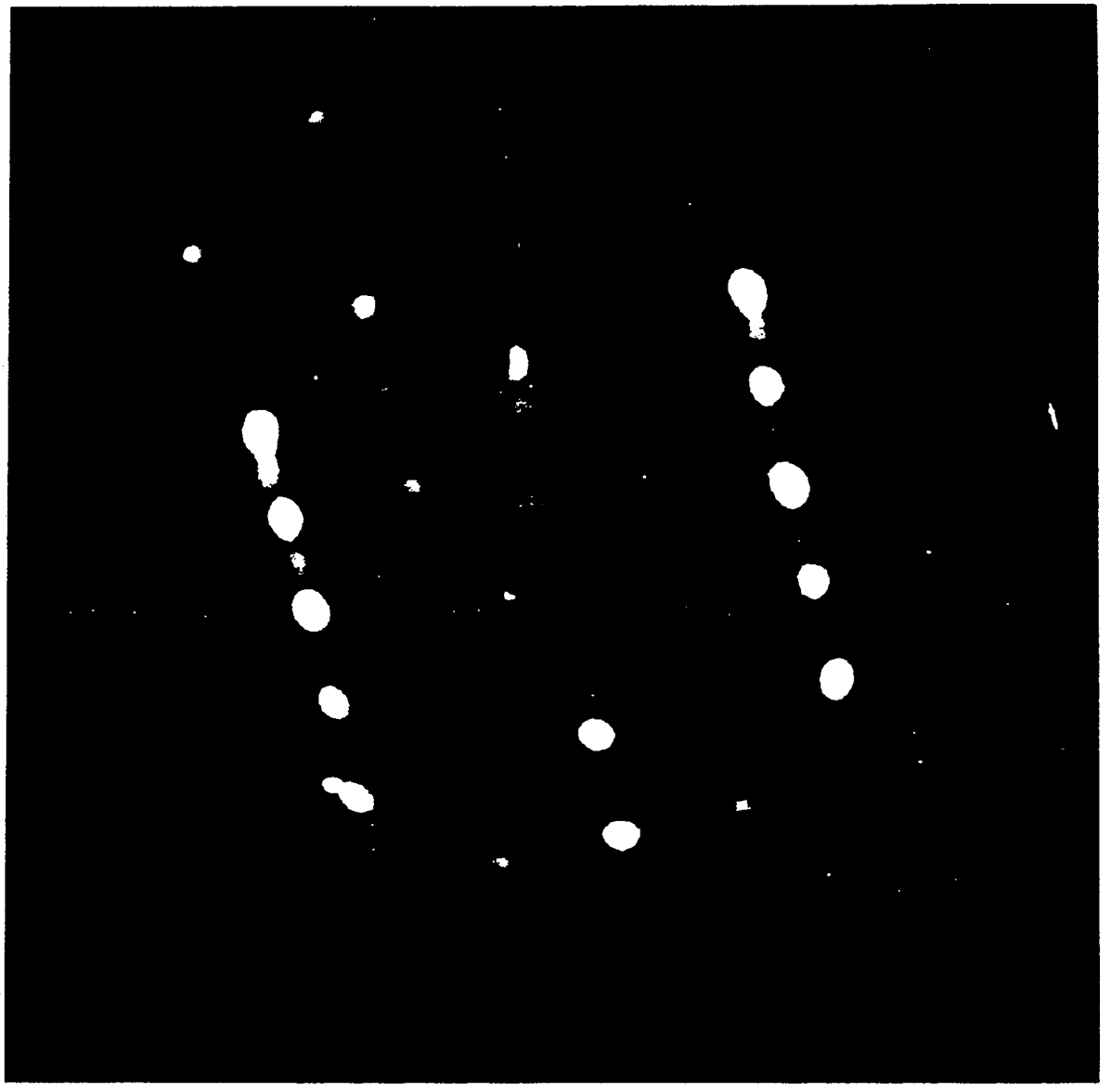

Figure 4.12: LEED pattern of the Ti_4O_7 overlayer structure measured with a 74 eV incident electron energy.

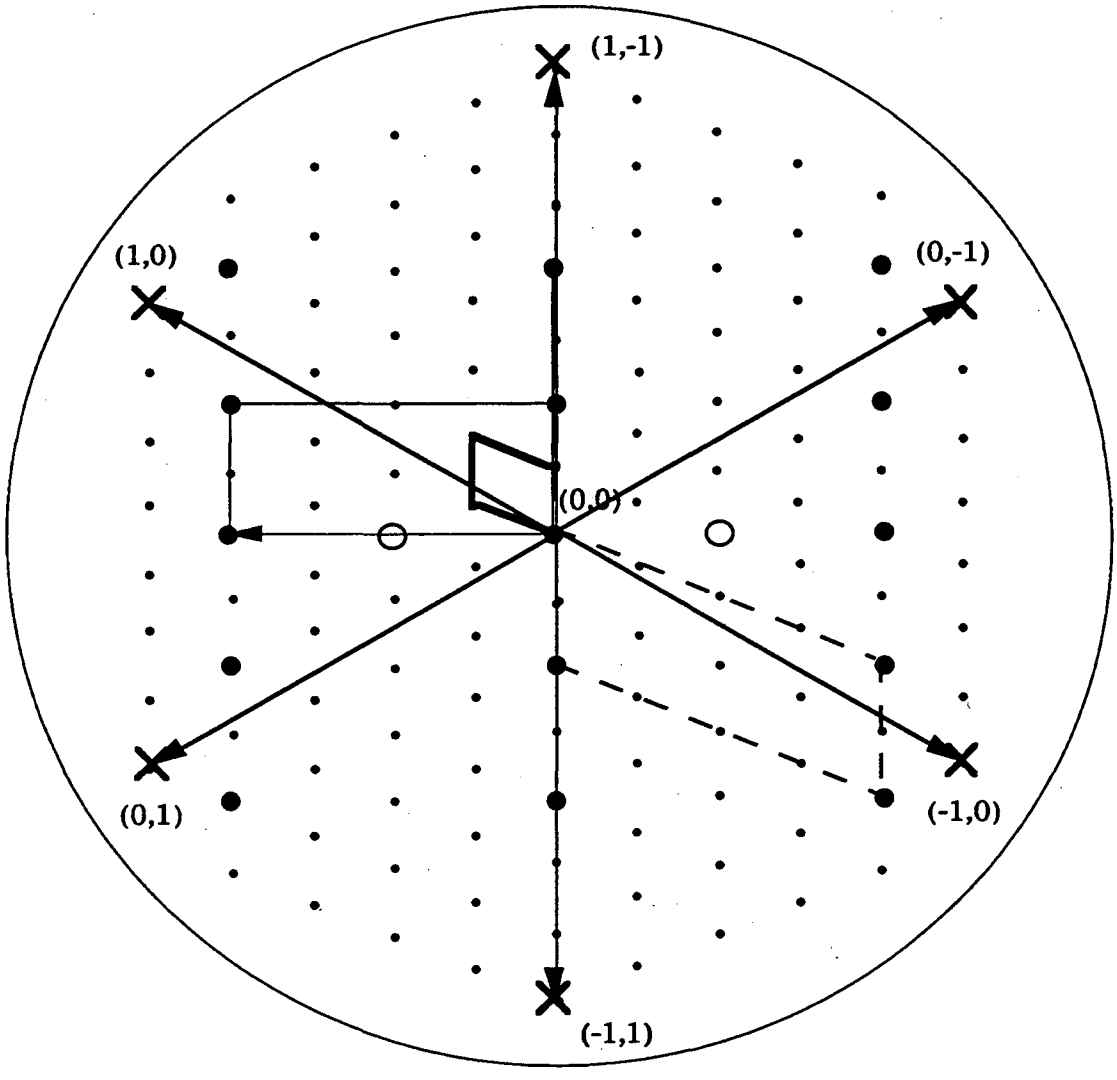

Figure 4.13: The schematic representation of the LEED pattern. The primitive cell is shown as the bold lines, the rectangular cell of the most intense diffracted beams is indicated by the thin lines, the unit cell observed by STM is indicated by the dashed lines, the missing diffracted beams attributed to the presence of glide planes are shown as the open circles, and the position of the underlying Pt(111) diffracted beams is indicated by the symbol **X**.

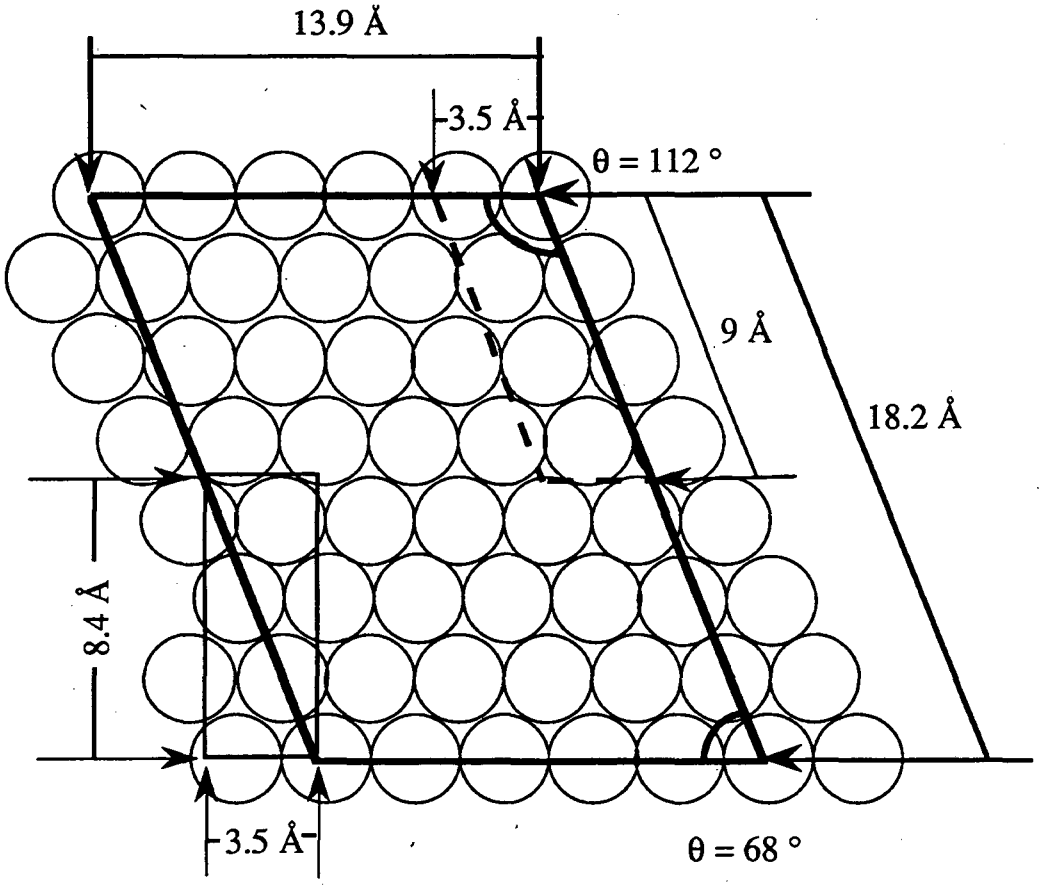

Figure 4.14: Real space representation of the Ti_4O_7 film superimposed on the Pt(111) substrate. The primitive cell is shown as the bold lines, and the rectangular cell is indicated by the thin lines. The unit cell found by STM is indicated by the dashed lines.

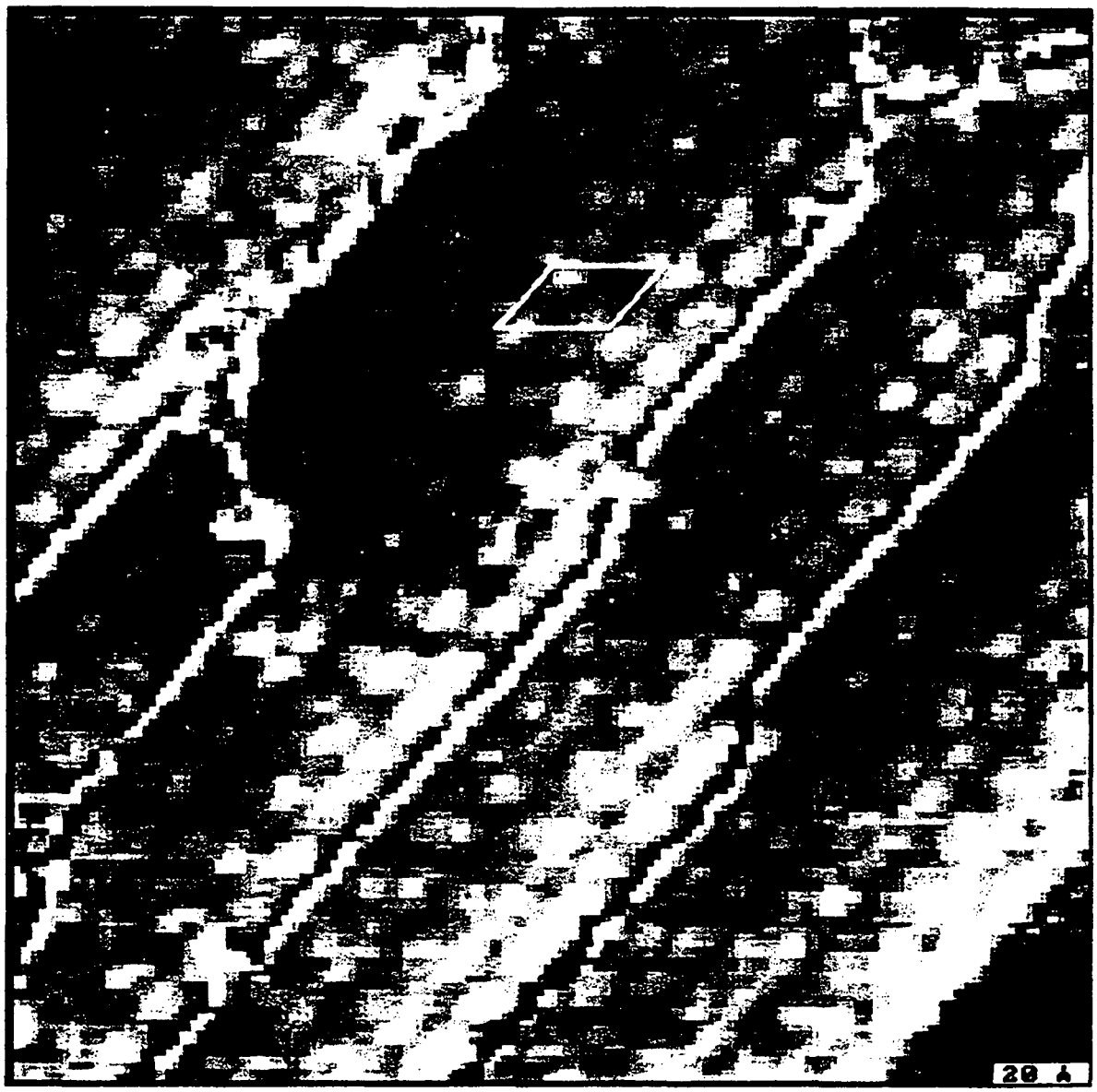

Figure 4.15: A 240 x 240 Å image taken at sample bias of - 0.29 V and a current of 1.26 nA. Several terraces are visible covered by Ti_4O_7 with a unit cell of approximately 18 x 14 Å. One unit cell is marked for visual reference. The height separation between terraces has been subtracted so that the contrast on the terraces would be clearly visible.

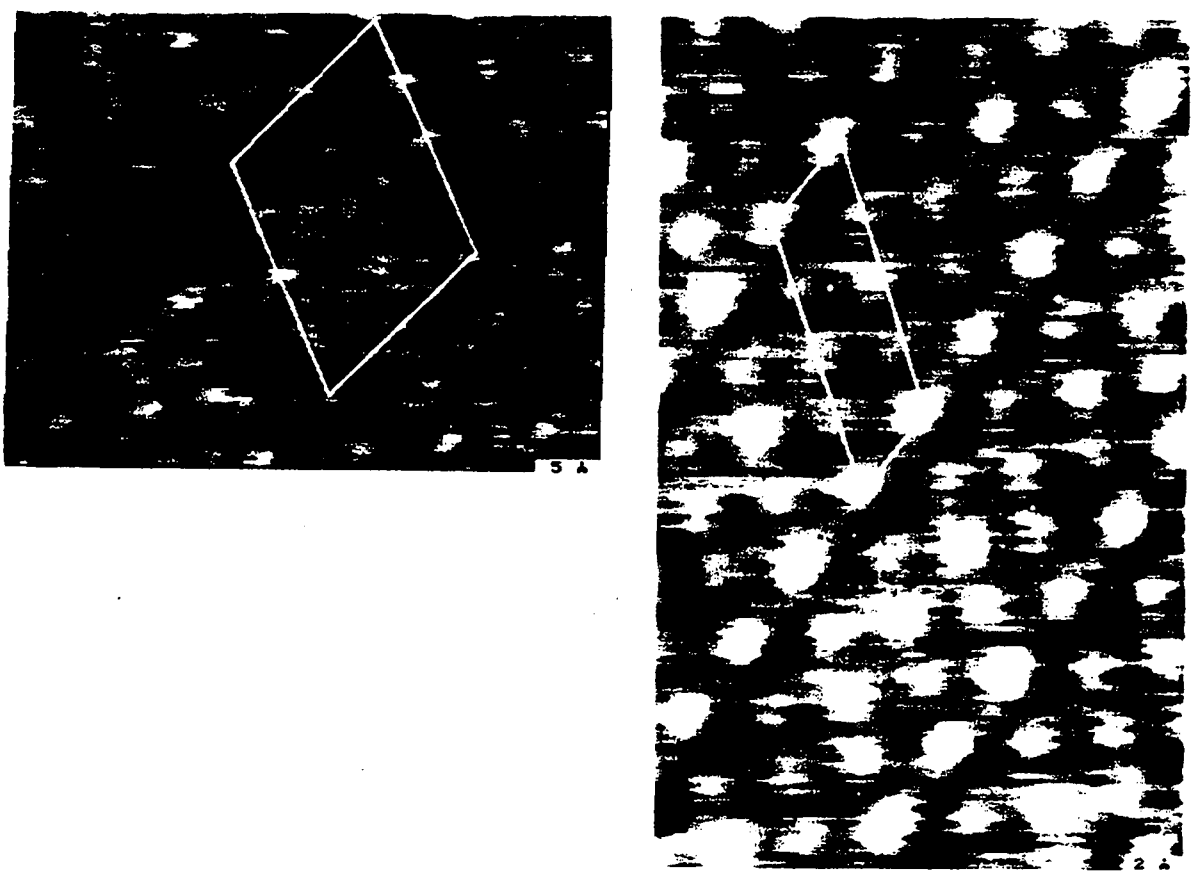

Figure 4.16: A smaller scale image of the same area as in Fig. 4.15 reveals fine details within the (18 Å x 14 Å) primitive cell, which is marked for reference. The image is 40 x 32 Å and is taken at a sample bias of - 0.271 V and a current of 1.25 nA. A 20 x 32 Å correlation averaged image reveals a 9 x 3.5 Å sub unit cell as outlined.

Pt(111) step height of 2.26 Å. The periodic structure imaged by STM consists of ordered rows of bright spots aligned with the step edges. The spacing is 14 Å along the rows and 18 Å between the rows, giving a cell of approximately 18 Å x 14 Å. The dimensions and symmetry of this cell are in agreement with the 18 Å x 14 Å, primitive cell determined from LEED analysis. The smaller scale, 40 Å x 32 Å STM image in Fig. 4.16 reveals fine structure within the 18 Å x 14 Å cell, which is drawn on the image for reference. To understand the internal structure of the unit cell, a correlation algorithm is used to find the average unit cell over the image. This reduces the noise substantially but also removes possible point defects. The result of this analysis is a unit cell of 9.5 x 3.5 Å. This unit cell can also be constructed by the intense spots of the LEED pattern as is indicated by the dashed lines in Fig. 4.13 which has dimensions of 9.1 x 3.5 Å in agreement with the unit cell observed by STM.

The STM images in Figs. 4.15 and 4.16 have been taken at negative sample bias leading to a tunneling current from filled states of the sample to unoccupied states of the tip. UPS studies indicate that the filled state at the top of the band gap is localized on Ti atoms for reduced titanium oxide (106). In the STM images of the vacuum reduced titanium oxide overlayer in Figs. 4.15 and 4.16, enhanced contrast (or bright spots) is, therefore, attributed to tunneling from either O vacancies or Ti atoms. Similarly, image contrast has been attributed to tunneling from Ti atoms in STM studies of bulk titania surfaces (111). Tunneling spectra (I-V curves) reveal a band gap of 1.2 eV, which is significantly lower than the band gap from the overlayer annealed in oxygen (4 eV). This is consistent with measurements on bulk titania that show a lowering of the band gap upon reduction (106).

A sub - cell of the Ti_4O_7 structure found with LEED and STM can be chosen with rectangular symmetry (see thin lines in Fig. 4.13 and 4.14). This is also the symmetry of the most stable surface of rutile, (110) (106). Ordered regions of TiO_2(110) surfaces from bulk titania have been imaged with STM (111,112). In these studies, reduction by

annealing in vacuum gave rise to periodicities greater than the unreconstructed $TiO_2(110)$ (1x1) periodicities which was attributed to formation of ordered oxygen vacancies. Since the 3.5 Å spacing observed by LEED and STM for the titanium oxide films on Pt(111) is consistent with the 3.3 Å Ti-Ti distance along the $[1\bar{1}0]$ direction, the structure reduced in vacuum is also attributed to an ordered array of O^- ion defects within a $TiO_2(110)$ matrix.

4.5 Conclusions

Titanium oxide is found by LEED and STM to form disordered and ordered structures on Pt(111). After annealing a multilayer oxide deposit in 1 x 10^{-6} Torr O_2 at temperatures ranging from 500 °C to 700 °C a three - fold symmetric structure with a unit cell of 18.2 Å x 18.2 Å is formed. This structure is observed at coverages ranging from 1.0 to 5.0 ML. XPS measurements indicate a stoichiometry of TiO_2. The three - fold symmetry of this titanium oxide film is suggestive of a similarity to the $TiO_2(111)$ rutile surface plane of nearly close - packed O^- ions. Annealing in vacuum from 650 °C to 850 °C leads to a new structure with a unit cell of 18.2 Å x 13.9 Å which is observed at coverages of 1.0 to 1.5 ML. This oxide overlayer is shown by XPS to have a stoichiometry of Ti_4O_7. The structure is similar to that reported for reduced surfaces of $TiO_2(110)$. The loss in XPS signal for the oxide overlayers as a function of temperature indicates diffusion into the Pt substrate at temperatures greater than 550 °C. Angle resolved XPS measurements of the relative amounts of Ti^{3+} and Ti^{4+} after preparation in 1 x 10^{-6} Torr O_2 at 300 °C indicate that the Ti^{3+} component is concentrated at the oxide / Pt(111) interface.

Chapter 5

Comparison of the Effects of Titania on the CO and CO_2 Hydrogenation Reactivity of Pt and Rh Foils

Abstract

The effects of deposits of TiOx on the rate of methane formation from CO and CO_2 hydrogenation over Pt have been examined. The maximum CH_4 rate enhancement is 31 times at a TiOx coverage of 0.2 ML for CO_2 hydrogenation and 17 times at a TiOx coverage of 0.4 ML for CO hydrogenation. The promotion by titania of CO and CO_2 hydrogenation over Pt foil is greater than that observed previously for promotion by titania of Rh foil (71-81), for which the maximum CH_4 rate enhancement is 15 times at a TiOx coverage of 0.5 ML for CO_2 hydrogenation and 3.5 times at a TiOx coverage of 0.5 ML for CO hydrogenation. Due to the difference in the inherent activity of Rh and Pt, the overall methanation rate on the oxide covered Pt remains orders of magnitude less than the rate over Rh. A comparison to measurements made on supported catalysts finds that the

extents of CH_4 rate enhancement for CO hydrogenation by addition of TiOx to Pt and Rh foils are in good agreement with the difference in reactivity between TiO_2 and SiO_2 supported Pt and Rh catalysts. This indicates that the oxide / metal configuration that exists in the model catalyst is similar to that which is present in the supported catalyst during CO hydrogenation.

5.1 Introduction

Pt and Rh - supported on TiO_2 exhibit altered chemisorption characteristics and enhanced CO hydrogenation compared to when supported on SiO_2. In an effort to understand these phenomenon, Pt/TiO_2 and Rh/TiO_2 have been studied as supported catalysts (10-50 Å Pt and Rh particles dispersed on a high surface area TiO_2 support) and as a model catalysts with Pt and Rh deposited on a single crystal TiO_2 surface or, in the reverse configuration, with TiOx deposited on a Pt or Rh single crystal or foil (5-11).

In this study, an attempt has been made to isolate the factors contributing to enhanced activity for CO and CO_2 hydrogenation by depositing sub - monolayer films of titanium oxide on a Pt foil This allows the dependence of the rate on oxide coverage to be determined. This method has been used previously to determine the effects of titanium oxide deposits on CO and CO_2 hydrogenation over Rh foils (71-81). In this work we extend these investigations to include Pt. The influence of titanium oxide on CO hydrogenation over Pt foils has been studied by Gorte et al. (68); however, the specific dependence of methanation on oxide coverage was not reported. In this work, CO and CO_2 hydrogenation measurements are reported for coverages of TiOx ranging from 0.1 to 3.0 ML on a Pt foil. The oxide preparation and reaction conditions have been chosen to match those used in previous studies of TiOx deposited on Rh foils allowing for direct

comparison of Rh and Pt. Addition of titanium oxide to Pt foil leads to a maximum CH_4 rate enhancement of 31 times at an oxide coverage of 0.2 ML for CO_2 hydrogenation and 17 times at a TiOx coverage of 0.4 ML for CO hydrogenation. A comparison of these results with those of TiOx deposited on Rh foils and with measurements of supported Pt/TiO_2 catalysts leads to conclusions regarding the factors contributing to oxide promotion.

5.2 Experimental

Experiments were performed in a Varian UHV chamber equipped with a cylindrical mirror analyzer for Auger electron spectroscopy, an EAI quadrupole mass spectrometer, and an atmospheric-pressure isolation cell. It is evacuated by an oil diffusion pump and titanium sublimation pump to achieve a base pressure of 1×10^{-9} Torr. The sample, 1 cm^2 Pt polycrystalline foil 0.002-in thick, is attached to a manipulator through spot welds to 0.020-in gold support wires. An K type thermocouple is spot welded to the foil for temperature measurement. Prior to initiating a reaction, the foil is cleaned by several cycles of high temperature annealing and sputtering.

Titanium was deposited on the Pt surface using an evaporator. The evaporator consisted of a 0.030 in W wire around which was wound 0.020 in Ti wire. A current of 26 amp was necessary to give a deposition rate of approximately 1.0 ML/min. A back pressure of 5×10^{-7} Torr of oxygen was present during evaporation in order to reduce carbon contamination. After Ti deposition, the surface was oxidized at 3×10^{-6} Torr of O_2 at 350 °C for 5 min. To remove oxygen adsorbed on the exposed Pt surface, 2×10^{-7} Torr of CO was admitted into the chamber for 20 s, and the sample was then flashed to 400 °C. The preparation procedure is the same as that used in the studies of TiOx deposited on

a Rh foil (71-81). After preparation, an Auger spectrum was taken to determine the oxide coverage and to confirm the sample cleanliness. The bare Pt surface was subject to the same gas exposures before reaction to eliminate the possibility of ascribing rate enhancements to pretreatment effects. When necessary, the deposited oxide was removed by sputtering and annealing.

To perform a reaction, the sample was enclosed in a high-pressure cell, connected to a gas recirculation loop. The total volume of the reactor and recycle loop was 120 cm^3. H_2 and CO, or CO_2, purified through a trap maintained at 150 K, were introduced into the loop, and argon was added when necessary to give a total pressure of 760 Torr. For CO an activated carbon trap was used in addition to the liquid nitrogen cooled molecular - sieve to remove metal carbonyls. A metal-bellows pump was used to recirculate the gases at a flow rate of approximately 100 cm^3/min. The accumulation of reaction products in the loop was monitored with an HP 5890II gas chromatograph equipped with an FID. A stainless steel 10 - ft. x 1/8 in column packed with 80/120 Carbopak B coated with 3% SP1500 was used for product separation. All reactions were run at conversions of less than 5%. After reaction, approximately 10 min was required to return the UHV chamber to its base pressure.

5.3 Results and Discussion

To determine the coverage and growth mode of titanium oxide deposits on Pt foil, the Pt and Ti AES intensities, crystal current, and CO TPD intensity were measured as a function of evaporation time for sequential depositions of titanium oxide as plotted in Figs. 5.1 - 5.4. After each evaporation the sample was oxidized in 1 x 10^{-6} Torr O_2 for 5 min at 350 °C, which is below the temperature that diffusion of titanium into the Pt foil is

observed. The sample was then exposed to CO to remove adsorbed oxygen from the Pt. A change in the slope (or break) in the plot of intensity versus deposition time is observed after 6 min evaporation in each of the uptake curves, indicating the completion of the growth of a monolayer of oxide deposit. The plot of titanium oxide coverage versus the ratio of Ti(387eV) / Pt(237eV) AES intensity in Fig. 5.5 is based on the assignment of 1.0 ML to the film observed after 6 min evaporation and was used to calibrate the titanium oxide coverage before reaction. The coverage assignment based on the uptake curves in Figs. 5.1 - 5.3 are supported by the CO chemisorption measurements in Fig. 5.4. Since CO does not adsorb appreciably to titanium oxide, CO chemisorption is representative of the extent of exposed Rh. After 6 min of titanium evaporation the CO TPD intensity has decreased to within 15 % of the background CO intensity indicating approximately total oxide blockage of Rh CO chemisorption sites; however, the lack of compete attenuation of the CO TPD peak intensity suggests the presence of defects in the oxide overlayer. The breaks observed in the plots of Figs. 5.1 - 5.3 and the near linear decline in the CO TPD intensity is consistent with a layer - by - layer mode for the growth of titanium oxide on Pt foil. However, the tailing in the CO chemisorption measurements at 6 min evaporation indicates partial three - dimensional islanding as the oxide overlayer approaches a 1.0 ML coverage.

Figure 5.6 is a plot of the rate of methane formation over Pt and Rh foils from CO and CO_2 hydrogenation as a function of TiOx coverage. (The curves in Fig. 5.6 are added as a visual aid.) The turnover frequencies (TOF) (molecules of methane produced / s / total sites (oxide + metal)) for the clean and titanium oxide promoted surfaces are summarized in Table 1. Results given for titanium oxide deposited on Rh foil are taken from references (71-81). For CO hydrogenation, $P(H_2)$ = 506 Torr, P(CO) = 253 Torr, and T = 280 °C; and for CO_2 hydrogenation, $P(H_2)$ = 570 Torr, $P(CO_2)$ = 190 Torr, and T = 250 °C.

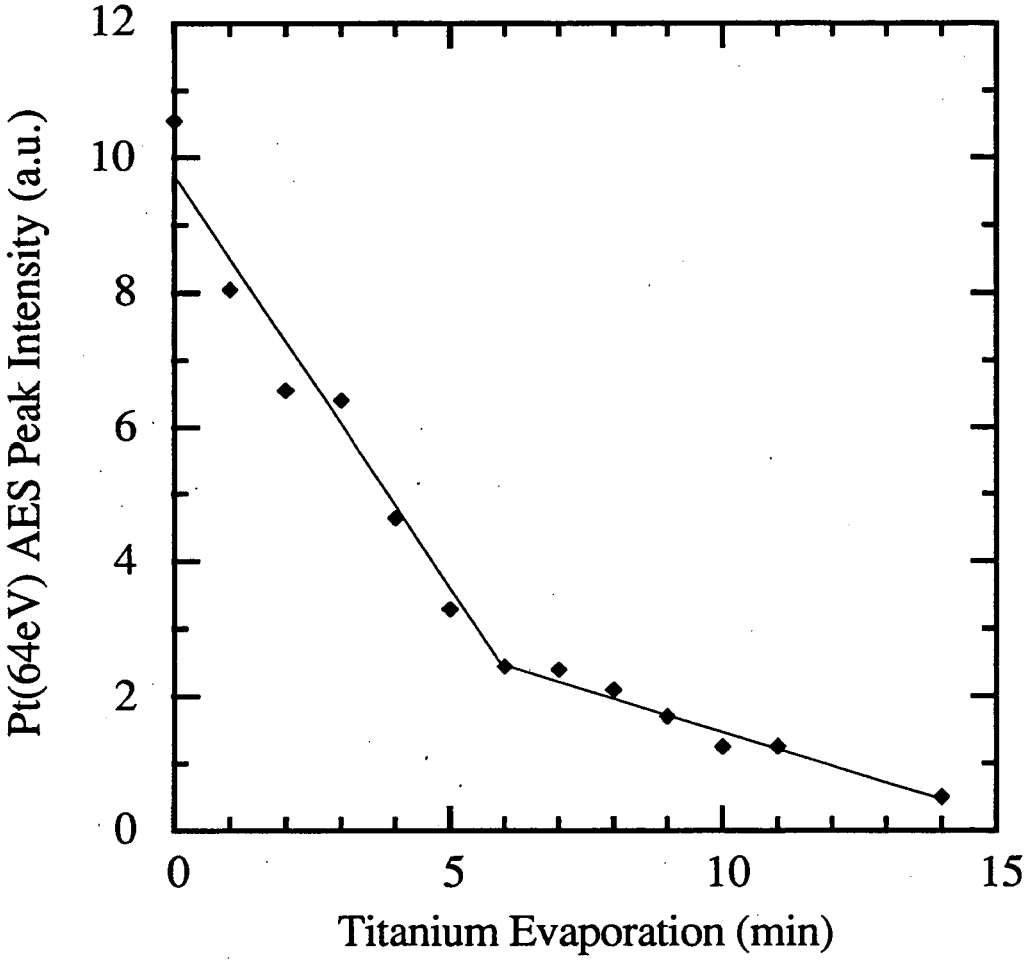

Figure 5.1: Pt(64 eV) AES peak intensity plotted as a function of titanium evaporation time on a Pt foil (r (goodness of fit) = 0.99).

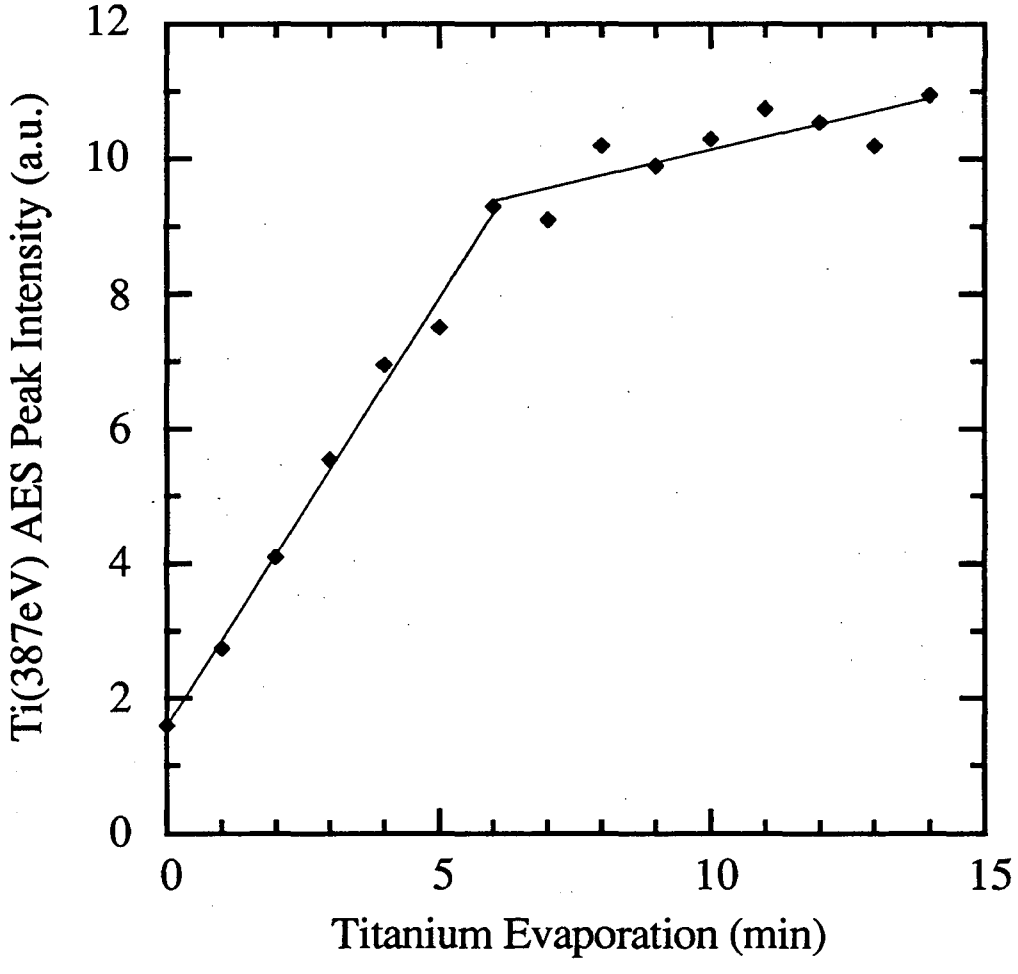

Figure 5.2: Ti(387 eV) AES peak intensity plotted as a function of titanium evaporation time on a Pt foil (r = 0.92).

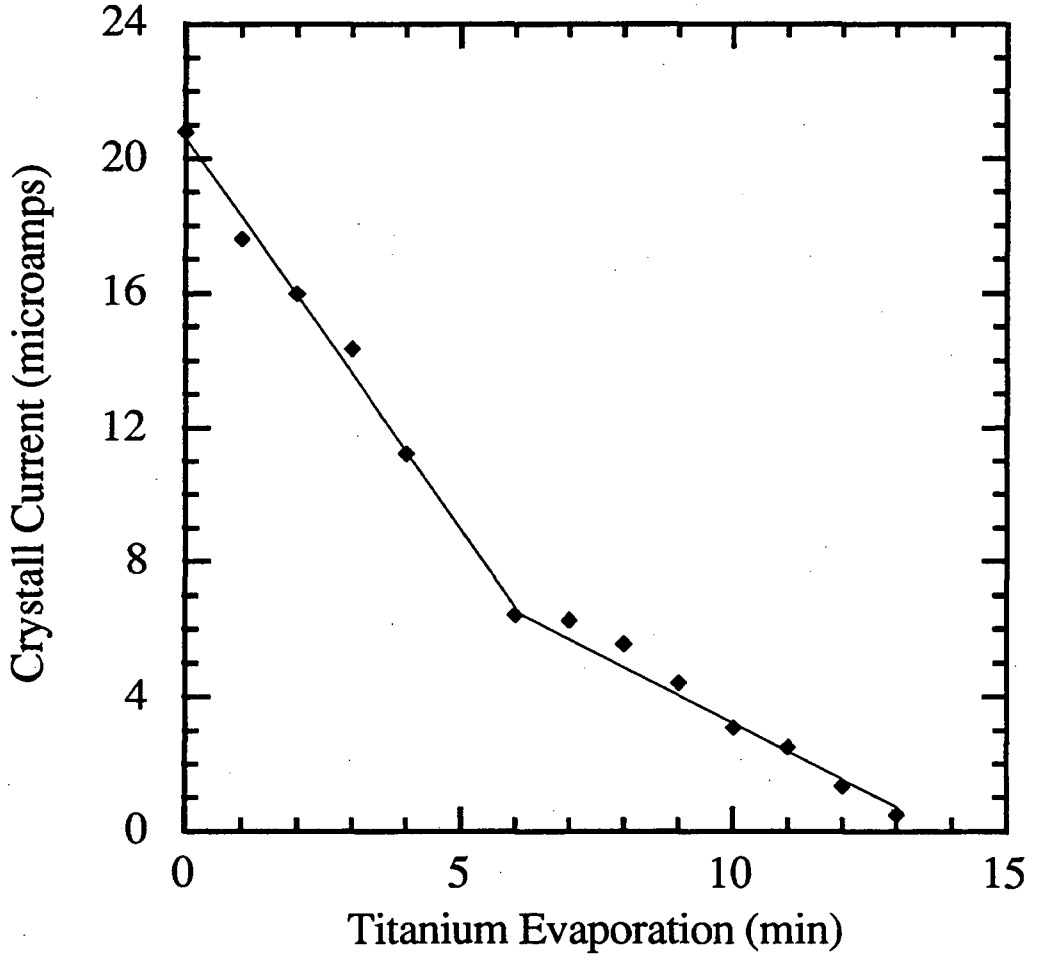

Figure 5.3: Crystal current plotted as a function of titanium evaporation time on a Pt foil (r = 0.99).

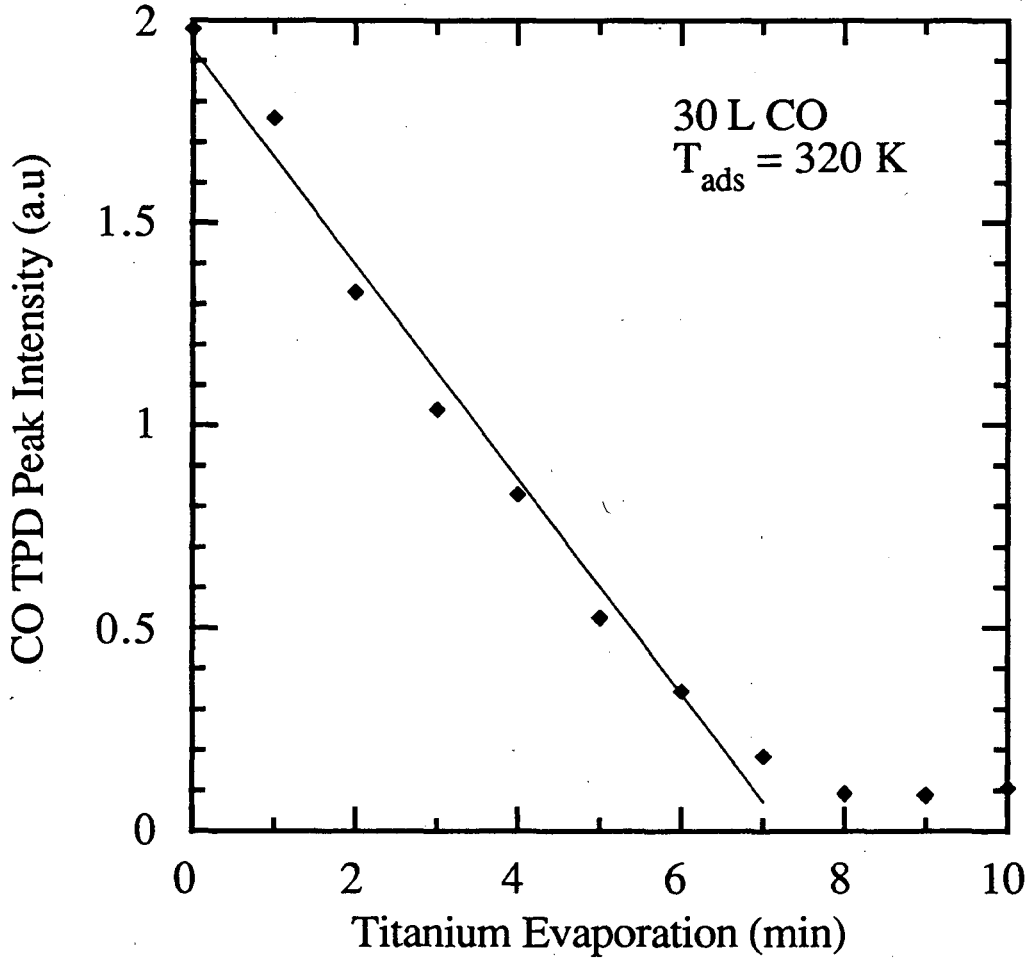

Figure 5.4: CO TPD intensity plotted as a function of titanium evaporation time on a Pt foil (r = 0.99).

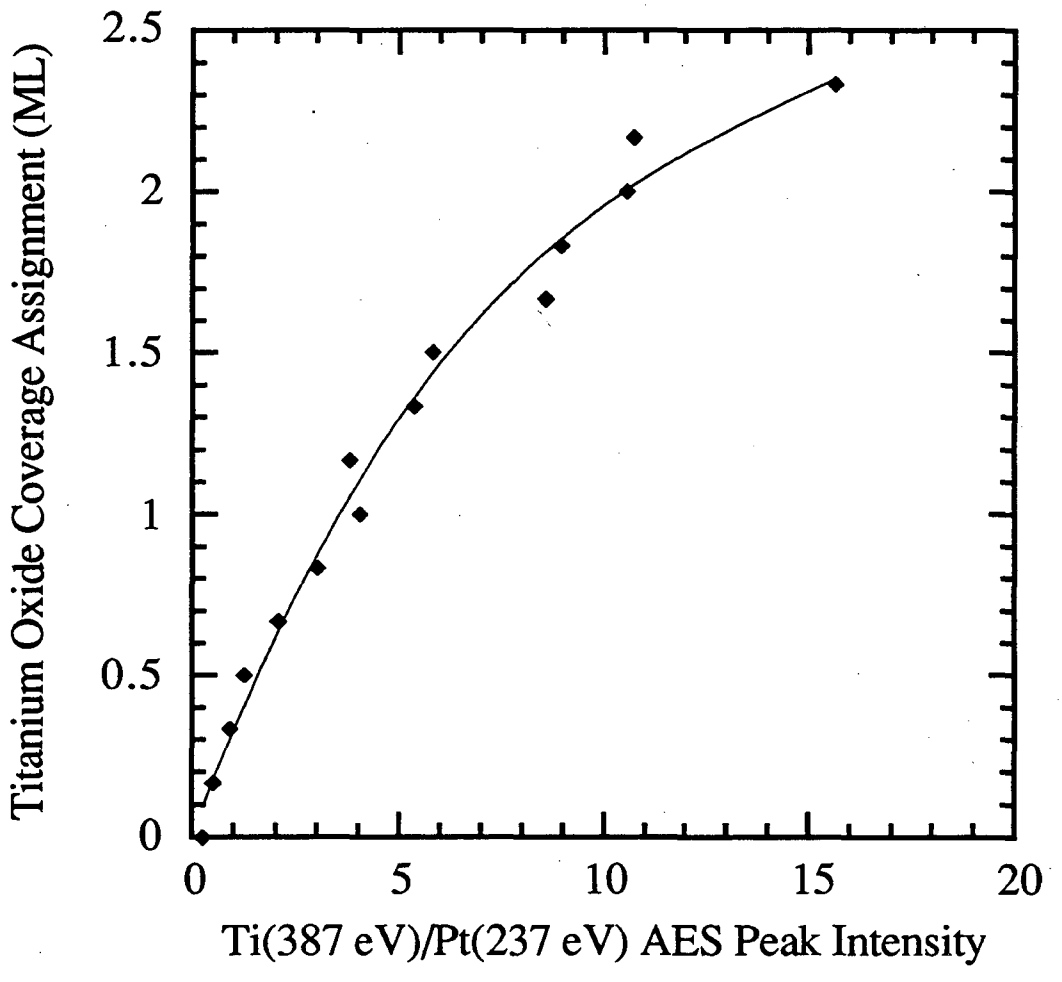

Figure 5.5: Titanium oxide coverage versus the ratio of Ti(387eV) / Pt(237eV) AES intensities (r = 0.99).

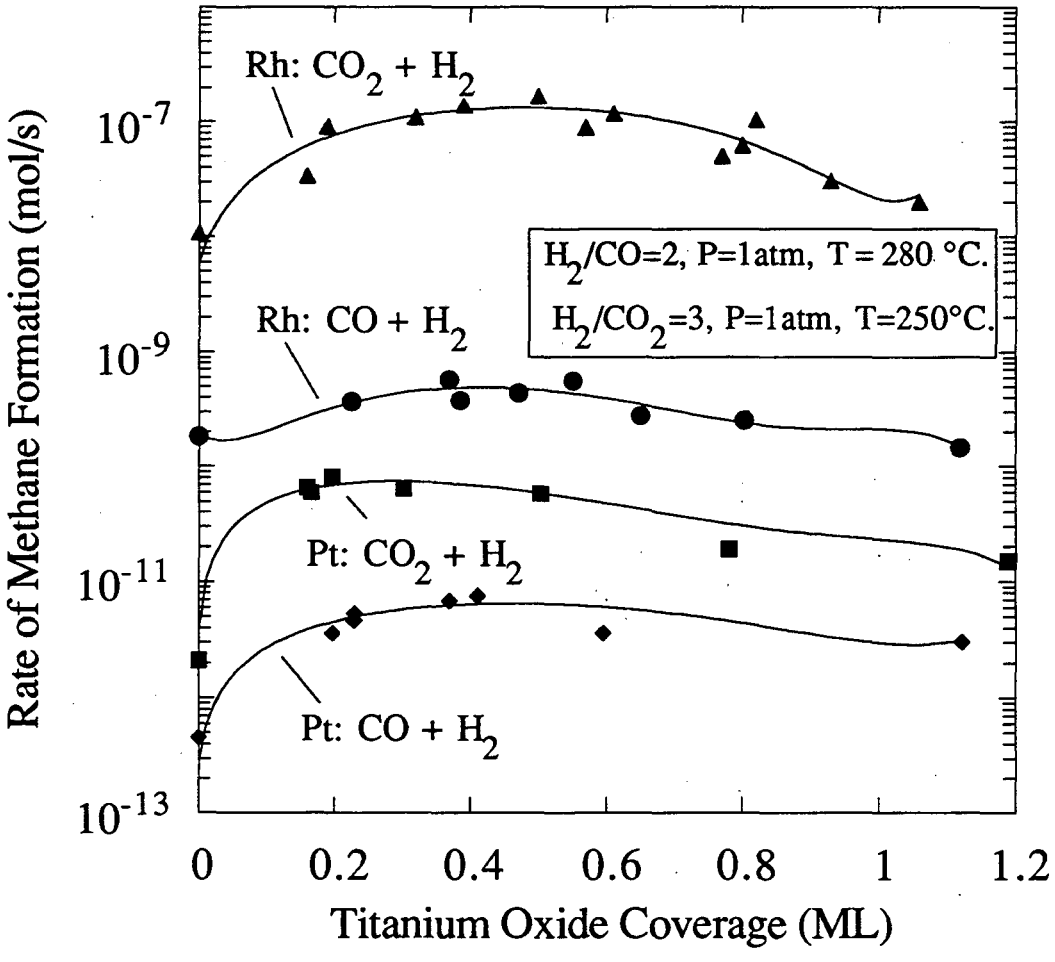

Figure 5.6: The rate of methane formation from CO and CO_2 hydrogenation plotted as a function of TiOx coverage on Pt and Rh foil.

Table 5.1: Comparison of the effect of deposits of TiOx on the CO and CO_2 hydrogenation reactivity of a Pt and Rh foil

	$CO + H_2$ (553K)			$CO_2 + H_2$ (523K)		
	CH_4 TOF (s^{-1}) Clean Metal	Maximum CH_4 TOF (s^{-1})[b] w/ Oxide	TiOx Coverage at Maximum	CH_4 TOF (s^{-1}) Clean Metal	Maximum CH_4 TOF (s^{-1})[b] w/ Oxide	TiOx Coverage at Maximum
Pt	1.2×10^{-4}	20×10^{-4} (17x)	0.4	0.57×10^{-3}	17×10^{-3} (31x)	0.2
Rh [a]	3.4×10^{-2}	10×10^{-2} (3.5x)	0.5	0.11	1.7 (15x)	0.5

Reaction conditions: P = 1 atm, $H_2/CO = 2$, $H_2/CO_2 = 3$.

[a] From ref.

[b] Based on the number of sites present on a clean Rh surface.

For CO hydrogenation over clean foil surfaces, the rate of methane formation is approximately 3 orders of magnitude less over Pt than over Rh foil, and for CO_2 hydrogenation, clean Pt is approximately 4 orders or magnitude less active than clean Rh. Consequently, although it is found that promotion by titania has a greater relative effect on Pt than on Rh, the overall methane rate on the oxide promoted Pt remains orders of magnitude less than the rate over clean or oxide promoted Rh. For CO hydrogenation, deposits of titania induce a CH_4 rate enhancement of 17 times on Pt and 3.5 times on Rh which gives TOF's for the oxide promoted foils of 2.0×10^{-3} s^{-1} and 0.10 s^{-1}, respectively. For CO_2 hydrogenation, deposits of TiOx lead to a CH_4 rate enhancement of 30 times on Pt (TOF = 1.7×10^{-2} s^{-1}) and 15 times on Rh (TOF = 1.7 s^{-1}) . Given these results, it is apparent that the metal remains the active component and that the oxide acts strictly as a promoter. If, as has been suggested by Dayte et al. (113,114), Falconer et al. (115-117), and Robbins et al. (118) the TiOx is the active component in the oxide / metal system with the metal simply providing H(a) via spillover, the overall reactivity of TiOx/Pt and TiOx/Rh should be at least roughly equivalent, since Pt and Rh both adsorb $H_2(g)$ dissociatively. It is also apparent, given the results shown in Fig. 5.6, that deposits of TiOx have a similar qualitative effect on CO and CO_2 hydrogenation reactivity of Pt and Rh, suggesting that the same general mechanism is involved in affecting promotion of both metals.

The titanium oxide coverage at the maximum rate enhancement is 0.5 ML for both CO and CO_2 hydrogenation over Rh foil. Over Pt, the maximum rate enhancement is observed at a TiOx coverage of 0.4 ML for CO hydrogenation and 0.2 ML for CO_2 hydrogenation. A computer simulation of island growth predicts that the oxide / metal interfacial adlineation will maximize at coverages of approximately 0.5 ML; therefore, the occurrence of rate maxima at coverages of approximately 0.5 ML is consistent with mechanisms that involve active site formation at the oxide / metal perimeter.

For oxide coverages greater than 3.0 ML, the TOF for methane formation falls to values less than that of the oxide free Pt and Rh surfaces. For coverages between 1.0 and 3.0 ML, the Pt surface retains an activity that is greater than that of the clean surface. This may be attributed to a greater extent of defect formation in the titanium oxide overlayer on Pt compared to on Rh. STM measurements indicate that defects exits in the oxide deposits grown on both Pt and Rh in vacuum (119,Chapter 4); however, the extent of the STM evidence is not sufficient to allow comparisons between Pt and Rh under reaction conditions.

Table 1 shows the maximum promotion for CO_2 hydrogenation is greater than that for CO hydrogenation for both Pt and Rh. For Rh the ratio of the maximum promotion for CO_2 hydrogenation (15x) to that for CO hydrogenation (3x) is 5. For Pt this ratio is 2. Because the oxide influences the activation energies, the degree of oxide promotion is dependent on the reaction temperature (120). The rate measurements for CO and CO_2 hydrogenation in Table 1 are for reaction temperatures of 280 °C and 250 °C, respectively. For Pt, measurements of the rate of CO hydrogenation have also been made at 250 °C to match the temperature of CO_2 hydrogenation. The maximum rate enhancement for CO hydrogenation at 250 °C for TiOx/Pt is 39 times, which is in good agreement with the 31 times enhancement observed for CO_2 hydrogenation over TiOx/Pt at 250 °C. For Rh, an estimate of the maximum CH_4 rate enhancement by TiOx at 250 °C using the activation energy reported in (79) gives a value of 5 times for CO hydrogenation, which is significantly less than the 15 times promotion observed for CO_2 hydrogenation at 250 °C.

The agreement in the rate enhancements observed for CO and CO_2 hydrogenation over Pt and the disagreement in degrees of promotion observed over Rh is consistent with arguments put forth by Williams et al (79). Due to the build - up of carbon containing surface species, Williams and coworkers postulated that the rate limiting step for CO hydrogenation over Rh shifted from CO(a) dissociation to hydrogenation of carbonaceous

intermediates ($CH_x(a) + H_{4-x}(a) = CH_4(g)$) upon promotion with titanium oxide. The change in the rate limiting step was used to account for the smaller degree of promotion for CO hydrogenation relative to CO_2 hydrogenation. Because Pt has less ability to adsorb and dissociate CO than Rh (43), promotion of C - O bond dissociation by deposits of TiOx is not expected to lead to a significant build - up of carbonaceous deposits that would induce a shift in the rate limiting step of CO hydrogenation, and the relative degrees of rate enhancement for CO hydrogenation and CO_2 hydrogenation over titanium oxide promoted Pt foil are comparable.

The TOF for a Rh catalyst supported on TiO_2 was found to be 15 times greater than that of a Rh/SiO_2 catalyst for the reaction of a 3:1 H_2 to CO mixture at 275 °C (125), and the TOF of Pt supported on TiO_2 was found to be 31 times greater than when supported on SiO_2 for the reaction of a 3:1 H_2 to CO mixture at 280 °C (120). The rate enhancements for the TiOx promoted Pt and Rh foils are shown in Table 1. The values in Table 1 are based on the total number of sites present (metal + oxide). Basing the TOF on only the number of metal sites and adjusting the rates to match the reaction conditions of the supported catalyst studies (125,120) using the kinetic parameters given in (78) results in a maximum rate enhancement for CO hydrogenation over TiOx/Pt foil of 29 times and over TiOx/Rh foil of 11 times relative to the clean foils. The adjusted extents of CH_4 rate enhancement for CO hydrogenation by addition of TiOx to Pt and Rh foils (29 and 11 times, respectively) are in good agreement with the relative reactivity of TiO_2 and SiO_2 supported Pt and Rh catalysts (31 and 15 times, respectively). This agreement indicates that the oxide / metal configuration that exists in the model catalyst is similar to that which is present in the supported catalyst during CO hydrogenation.

5.4 Conclusions

AES and CO uptake curves, indicating that the growth of titanium oxide on Pt foil is layer-by-layer, gave a measure of the oxide coverage. Deposition of titanium oxide to Pt foil leads to a 17 fold increase in the rate of CO hydrogenation and a 31 fold increase in the rate of CO_2 hydrogenation. The maximum rate enhancement occurred at a coverage of 0.4 and 0.2 ML for CO and CO_2 hydrogenation, respectively. Although the relative effect of titanium oxide is greater for Pt than for Rh (71-81), the absolute rates over Pt remain orders of magnitude less than over Rh due to the differences in the inherent activities of the clean metals. Titanium oxide deposits on Pt promote each reaction to a similar degree; however, over Rh, deposits of TiOx have a greater effect on CO_2 hydrogenation. The differences in effect on CO and CO_2 hydrogenation over the two metals is attributed to the difference in the ability of each metal to adsorb and dissociate CO. The behavior of the oxide promoted foils is shown to be similar to that observed in supported catalysts, indicating that the model planar catalysts effectively mimic the supported systems.

Chapter 6

Vanadium Oxide Deposited on an Rh Foil: CO and CO_2 Hydrogenation Reactivity

Abstract

The effects of sub-monolayer deposits of vanadium oxide on the rates of CO and CO_2 hydrogenation of a Rh foil have been examined. Auger electron spectroscopy (AES), ion scattering spectroscopy (ISS), and temperature programmed desorption (TPD) have been used to determine the oxide coverage, and x-ray photoelectron spectroscopy (XPS) has been used to determine the oxidation state for VOx deposits on a rhodium. After oxidation ($3x10^{-6}$ O_2 at 350 °C), the vanadium valence state is 3+, which corresponds to an oxide stoichiometry of V_2O_3. CO chemisorption reduces 34 % of the V^{3+} to V^{2+} at low oxide coverages. The absolute amount of V^{2+} in the oxide overlayer after CO titration is found to maximize at a coverage of 0.5 ML. The rates of CO and CO_2 hydrogenation increase upon addition of VOx to a Rh foil. For CO hydrogenation, the rate maximizes at two times that of the rate on the clean surface at an oxide coverage of 0.4 ML. For CO_2

hydrogenation, the rate maximizes at 6 times that of the clean surface rate at an oxide coverage of 0.6 ML. The oxide promoter also alters the activation energies, partial pressure dependences, and selectivities for the hydrogenation reactions. A comparison of the kinetic and spectroscopic data reveals a strong correlation between the degree of reducibility of the oxide overlayer and the amount of rate enhancement for CO and CO_2 hydrogenation.

6.1 Introduction

Numerous investigations have shown that interactions between small particles of Group VIII metal and metal oxide supports can result in a decoration of the metal particles by metal oxide moieties derived from the support (5-11). This phenomenon has been the object of intense research. There are two principal reasons for interest in metal - metal oxide interactions. The first is that such interactions can result in a decrease in chemisorption capacity due to blockage of metal sites. The second reason is that metal - metal oxide interactions can give rise to very significant increases in catalyst activity, particularly for reactions such as CO and CO_2 hydrogenation and NO reduction (5-11,31-34,37).

The study of effects of metal - metal oxide interactions on the catalytic activity of supported metal catalysts is encumbered by difficulties in defining and controlling the extent of metal particle decoration by moieties derived from the support. Not only the method of catalyst preparation, but also the method of pretreatment (e. g., calcination and reduction condition), can affect the extent of decoration. To obtain greater experimental control, it is possible to produce a planar model catalyst in which a single crystal or foil is partially covered by vapor deposition of an oxide. Such samples can readily be

characterized by a number of surface analytical techniques, and possess sufficient activity to enable studies of reaction kinetics. Experiments conducted with Rh, Pt, Ni, and Pd, decorated by several different oxides, have shown that planar model catalysts exhibit activities and selectivities very similar, and often identical, to those observed for metal oxide - supported metals (67-73). In one such study, the coverage dependence of the reactivity of a Rh foil promoted with deposits of TiOx for CO and CO_2 hydrogenation were investigated (79). It was found that addition of 0.5 ML of TiOx to the Rh foil caused a rate enhancement of three times for CO hydrogenation and fifteen times for CO_2 hydrogenation. The aim of the present investigation is to establish the effects of vanadia addition on the activity of Rh for CO and CO_2 hydrogenation. The observed changes in activity are correlated with measurements of oxide coverage and composition obtained by AES, ISS, TPD, and XPS.

6.2 Experimental

Experiments were performed in a Varian UHV chamber equipped with a cylindrical mirror analyzer for Auger electron spectroscopy, an EAI quadropole mass spectrometer, and an atmospheric-pressure isolation cell. Additional characterization of the catalyst samples were carried out in a PHI 5300 ESCA system equipped with x-ray photoelectron spectroscopy and ion scattering spectroscopy.

The Varian UHV chamber is evacuated by an oil diffusion pump and titanium sublimation pump to achieve a base pressure of 1×10^{-9} Torr. The sample, 1 cm^2 Rh polycrystalline foil 0.002-in thick, is attached to a manipulator through spot welds to 0.020-in gold support wires. An S type thermocouple is spot welded to the foil for

temperature measurement. Prior to initiating a reaction, the foil is cleaned by high temperature annealing and sputtering to remove B, S contamination.

Vanadium was deposited on the Rh surface using an evaporator. The evaporator consists of a 0.030 in W wire around which is wound 0.005 in V wire. A current of 38 amp was necessary to give a deposition rate of approximately 1.0 ML/min. A back pressure of 4×10^{-7} Torr of oxygen was present during evaporation in order to reduce carbon contamination. After V deposition, the surface was oxidized at 3×10^{-6} Torr of O_2 at 350 °C for 5 min. To remove oxygen adsorbed on the exposed Rh surface, 2×10^{-7} Torr of CO was admitted into the chamber for 20 s, and the sample was then flashed to 400 °C. After preparation, an Auger spectrum was taken to determine the oxide coverage and to confirm the sample cleanliness. The bare Rh surface was given the same gas exposures before reaction to eliminate the possibility of ascribing rate enhancements to pretreatment effects. When necessary, the deposited oxide was removed by sputtering and annealing.

To perform a reaction, the sample was enclosed in a high-pressure cell, connected to a gas recirculation loop. The total volume of the reactor and recycle loop is 120 cm^3. H_2 and CO, or CO_2, purified through a trap maintained at 150 K, were introduced into the loop, and argon was added when necessary to give a total pressure of 760 Torr. A metal-bellows pump was used to recirculate the gases at a flow rate of approximately 100 cm^3/min. The accumulation of reaction products in the loop was monitored with an HP 5720A gas chromatograph equipped with an FID. A stainless steel 10 - ft. x 1/8 in column packed with 80/120 Carbopak B coated with 3% SP1500 was used for product separation. All reactions were run at conversions of less than 5%. After reaction, approximately 10 min was required to return the UHV chamber to its base pressure.

The PHI ESCA 5300 was used for the XPS and ISS studies. It is equipped with a Mg and Al anode x-ray source, an He and Ar differentially pumped ion gun, a hemispherical analyzer, and a sample preparation cell. For XPS, the Mg anode (1253.6

eV) was used, and the hemispherical analyzer detector was operated at a 35.75 eV pass energy. For ISS, an incident beam of He ions at 500 eV was scattered at an angle of 123.0 degrees and detected with the hemispherical analyzer operated at a 179 eV pass energy. Before analysis, catalyst samples were prepared in an adjacent preparation chamber which was maintained at a base pressure of 1 x 10^{-9} Torr. A transfer rod was employed to move the sample between chambers in vacuo. An electron beam heater and a vanadium evaporation source were utilized to deposit vanadium oxide overlayers on a Rh foil surface in a similar manner as was described above for oxide preparation in the Varian UHV system.

6.3 Results and Discussion

6.3.1 Sample Characterization

The coverage and growth mode for VOx deposited on the Rh foil were determined by AES, ISS, and CO TPD, and the oxidation state of the vanadium was determined by XPS. Since all four techniques could not be carried out in one vacuum chamber, samples were produced in each of the two vacuum chambers, using identical procedures. The sample in the Varian UHV chamber was characterized by AES and CO TPD, whereas that in the PHI UHV chamber was characterized by ISS and XPS.

Figure 6.1 is a plot of the vanadium (435 eV) and rhodium (302 eV) AES peak intensities as a function of the vanadium evaporation time, in the Varian UHV chamber. Changes in the slopes of the plots of Rh and V peak intensity are observed after 80 s of V deposition.

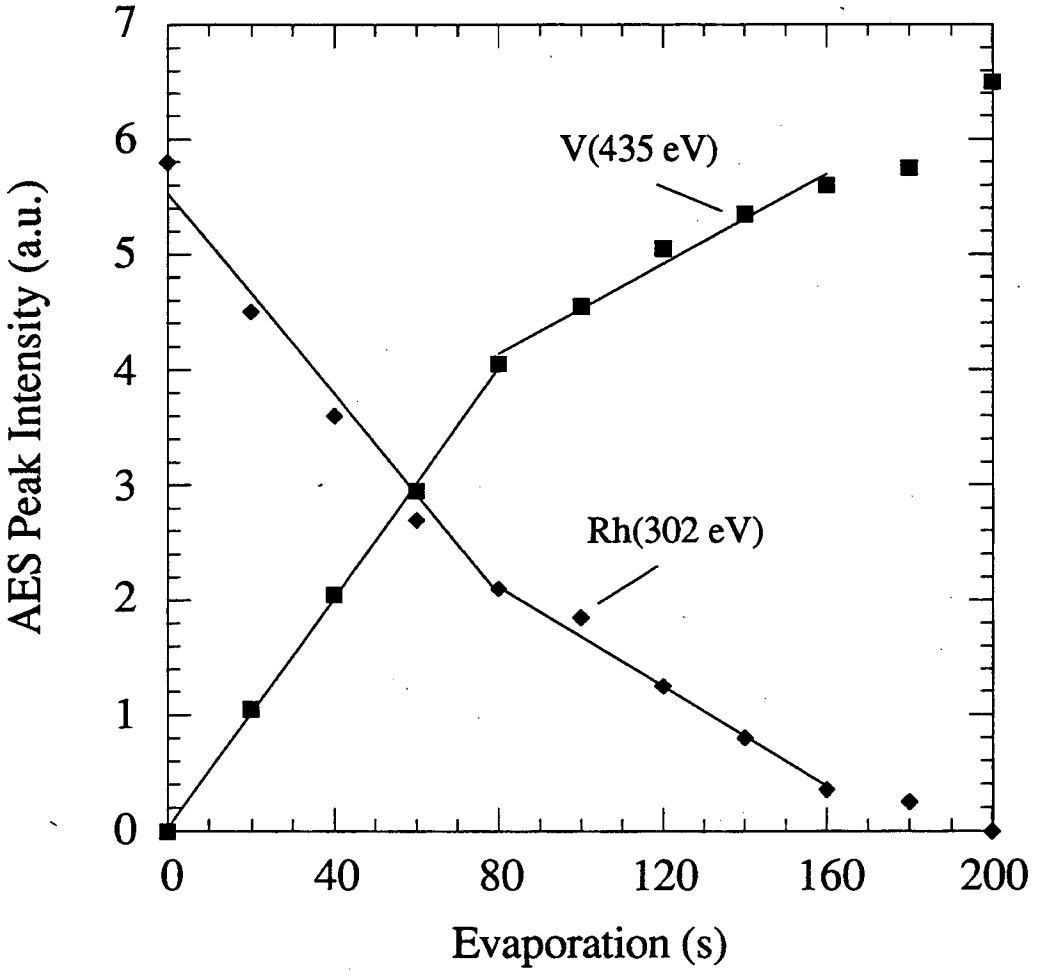

Figure 6.1: V(435 eV) and Rh(302 eV) AES peak intensities plotted as a function of vanadium evaporation time on a Rh foil (r = 0.99).

Figure 6.2 shows a plot of CO TPD peak intensity as a function of VOx coverage. The VOx coverage has been determined using the coverage calibration derived from the AES uptake curve in Fig. 6.1. The plot of TPD intensities measured up to 1.0 ML have been subject to a linear fit. The addition of vanadium oxide to Rh causes a linear decline in CO TPD intensity with complete suppression at coverages of 1.0 ML or greater. Since CO does not adsorb appreciably on vanadia, the linear decline and complete suppression of the TPD peak intensity indicates that the amount of vanadium oxide on the surface can be determined accurately by AES.

Figure 6.3 shows a plot of Rh ISS intensity as a function of vanadium evaporation time in the PHI UHV chamber. The plot of ISS intensities measured from 0 - 7 min evaporation time have been subject to a linear fit. The Rh ISS peak intensity decreases linearly with V evaporation time consistent with the growth of a two-dimensional film. A small degree of tailing occurs near 1.0 ML vanadium oxide coverage indicating that a second layer of vanadium oxide starts to form before completion of the first layer. After 7 min of vanadium evaporation, the relative Rh ISS intensity is less then 10 % and the uptake curve begins to level off. Consequently, 7 min evaporation time is considered to be the point at which the Rh surface is covered by 1.0 ML. To determine the similarity of the VOx overlayers produced in the PHI and Varian chambers, an AES measurement was made in the PHI chamber using the XPS spectrometer. For a V deposition time corresponding to 1.0 ML in both chambers, the Rh AES signal attenuation is 0.734 in the PHI chamber and 0.726 in the Varian chamber. The close agreement between these two values indicates that the two samples are similar.

An XPS spectrum of the 540 to 510 eV binding energy region for a 1.0 ML deposit of vanadium oxide on a Rh foil is shown in Fig. 6.4 (solid curve). The dominant features are the O(1s) peak at 529.8 eV and the Rh(3p1/2) peak at 523.0 eV. The V(2p3/2) at approximately 515 eV appears as a shoulder on the Rh(3p1/2) peak. The dashed curve in

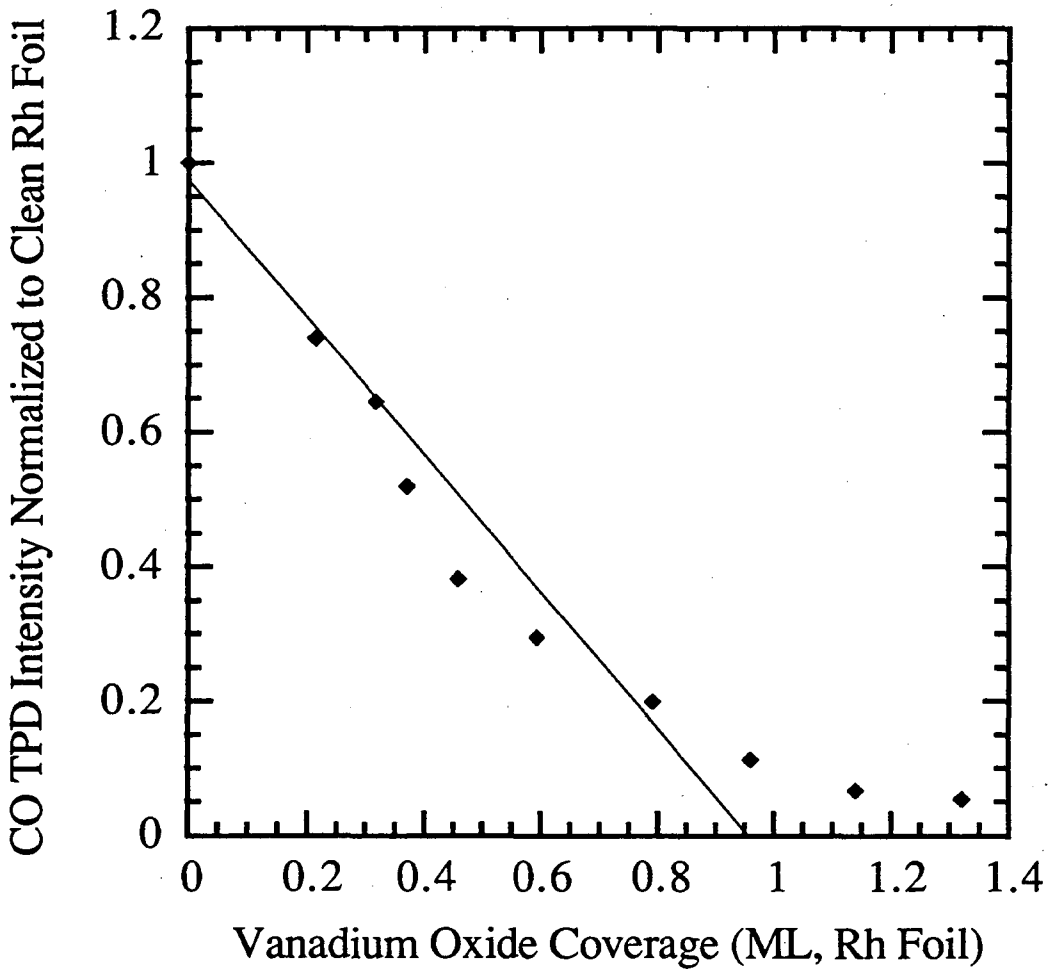

Figure 6.2: CO TPD intensity plotted as a function of vanadium oxide coverage on Rh foil (r = 0.98).

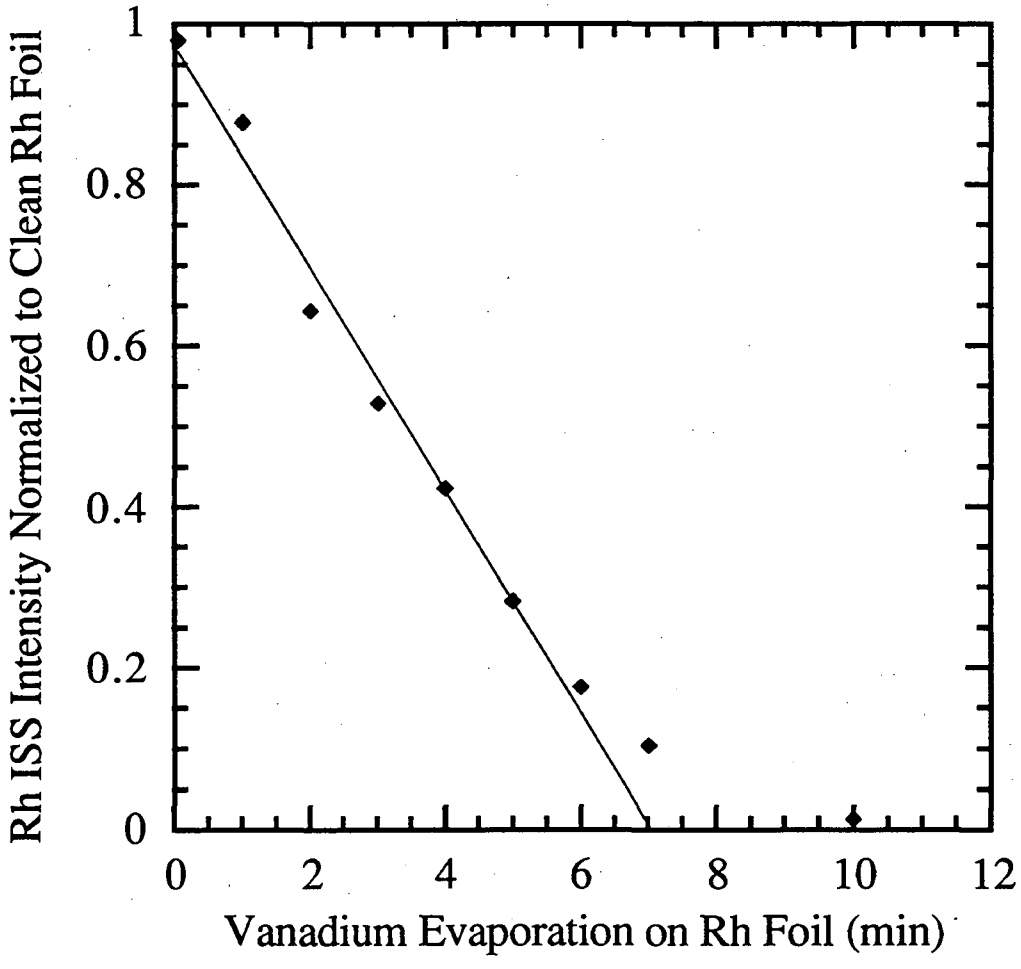

Figure 6.3: Rh ISS intensity plotted as a function of vanadium evaporation time on Rh foil ($r = 0.99$).

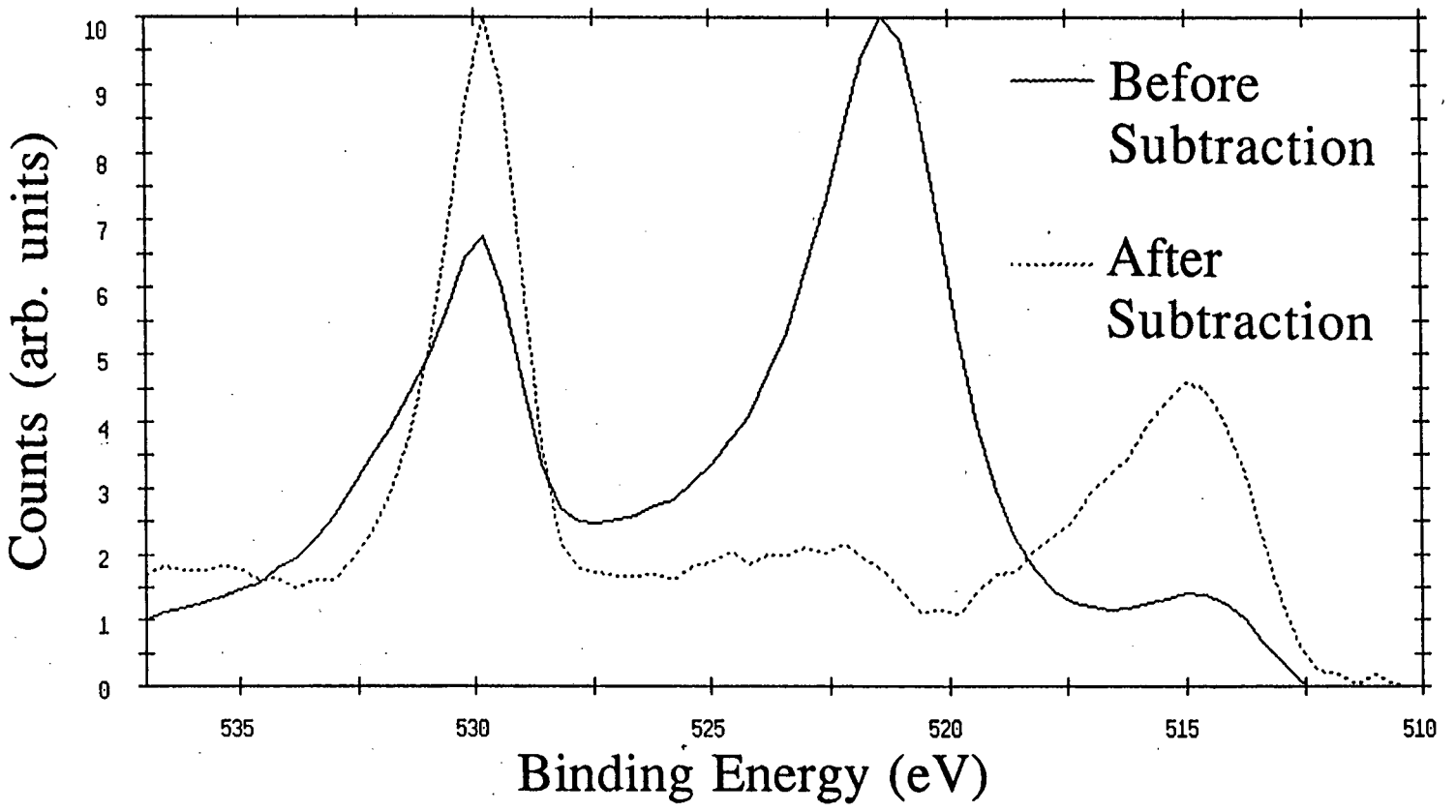

Figure 6.4: XPS spectrum of 1.0 ML vanadium oxide deposit on Rh.

Fig. 6.4 is a plot of the difference between the XPS spectra of a Rh surface covered by 1.0 ML of VOx and a clean Rh surface.

XPS spectra were obtained at several different vanadium oxide coverages. At each coverage, the surface was oxidized with 3 x 10^{-6} Torr O_2 at 350 °C for 5 min after which an XPS spectrum was recorded. The vanadium binding energy after the oxidation step remains the same, 515.6 eV, for all coverages. The measured V(2p3/2) B.E. of 515.6 eV is identical to that measured for a sample of polycrystalline V_2O_3 pressed into a Ta mesh and is consistent with the B.E. reported in the literature for V_2O_3 (126,127), indicating that V in the oxidized overlayer is in the V^{3+} valence state.

After oxidation, the same sample was titrated with a saturation dose (10 L) of CO, and a second XPS spectrum was taken. The vanadium B.E. after CO titration varies as a function of coverage. Figure 6.5 shows the percentage of the VOx overlayer that is reduced from V^{3+} to V^{2+} after CO titration. (The curve in Fig. 6.5 is added as a visual aid). The amount of V^{2+} was determined by subtracting the XPS spectrum of the oxidized V_2O_3 overlayer from that of overlayer reduced by CO titration. The resulting difference spectrum has a peak centered at 513.8 eV which is taken to correspond to vanadium in the 2+ valence state (127). The percentage of V^{2+} in the overlayer decreases from 34% at 0.2 ML to less than 5% at coverages greater than 1.0 ML. This trend is similar to that reported by Levin et al. (77) for TiOx deposited on a Rh foil. These authors found that CO titration reduced 40 % of the titanium from Ti^{4+} to Ti^{3+} at low coverages, whereas at higher coverages, CO titration had almost no effect. Figure 6.6 shows the absolute amount of V^{2+} in the overlayer after CO titration plotted as a function of coverage. The curve in the Fig. 6.6 is derived from a polynomial fit of the data with r = 0.97. The amount of V^{2+} is shown to maximize at coverages of VOx of approximately 0.5 ML.

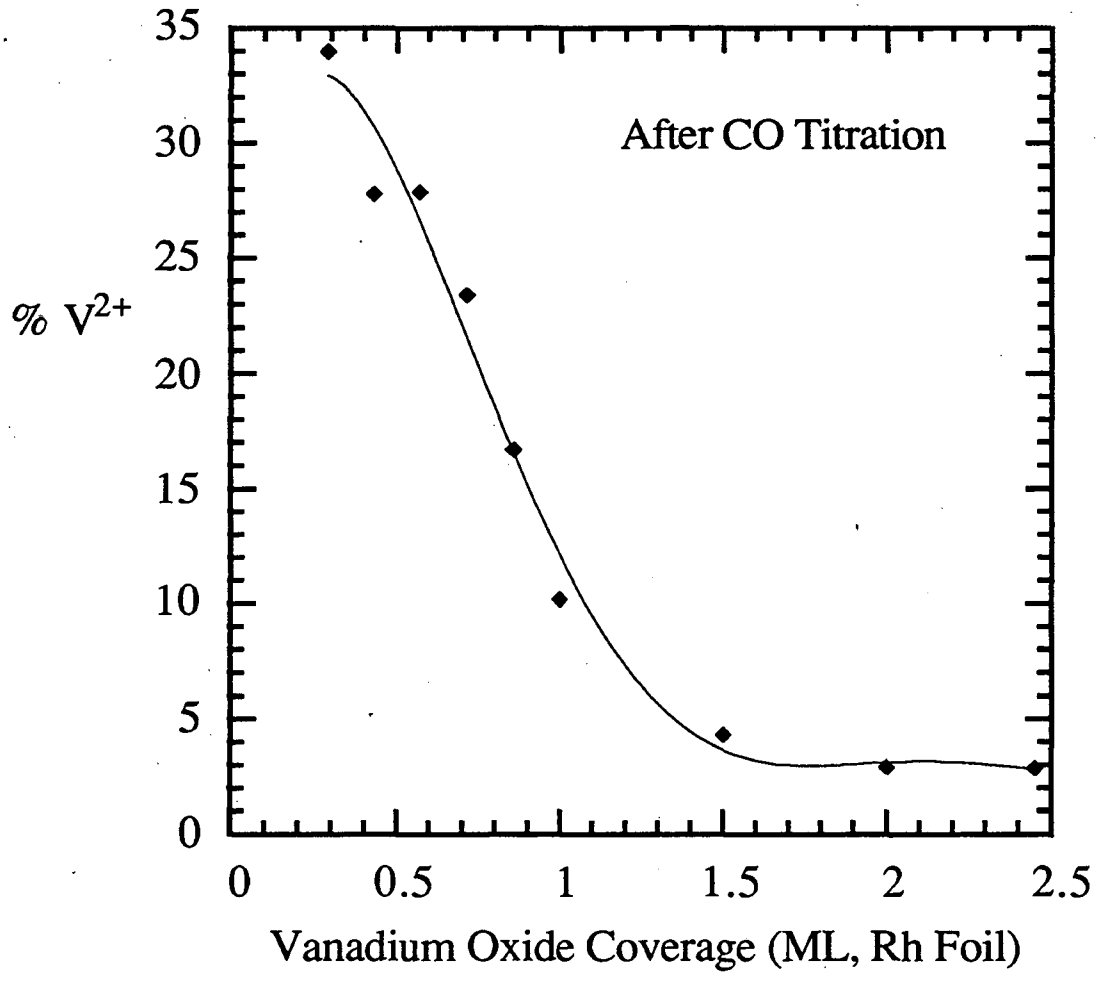

Figure 6.5: V^{2+}% after CO titration as a function of vanadium oxide coverage on Rh Foil.

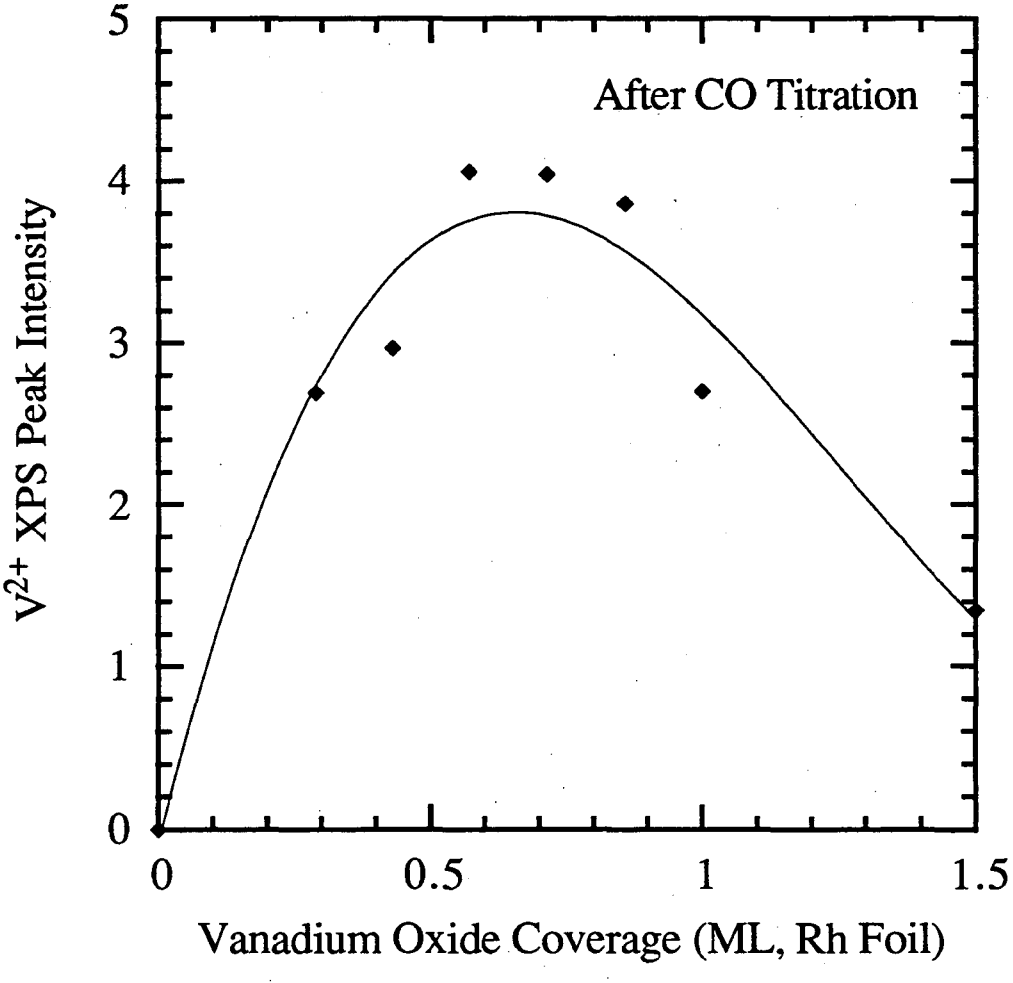

Figure 6.6: Area of V^{2+} XPS (513.8 eV) peak as a function of vanadium oxide coverage.

An explanation for the observation that the degree of reduction of the oxide overlayer decreases with increasing coverage becomes apparent when the CO uptake curve is considered. Figure 6.2 shows that CO does not adsorb appreciably to the vanadium oxide overlayer; therefore, at coverages greater than 1.0 ML, Rh adsorption sites are completely blocked, and the oxide overlayer is unaffected by CO titration. However, as the coverage decreases, more Rh adsorption sites are exposed, and the oxide is readily reduced. These results suggest that reduction of the vanadia overlayer occurs via diffusion of CO adsorbed on the exposed Rh sites to the perimeter of the vanadia islands comprising the overlayers.

6.3.2 Catalytic Activity

The rate of methane formation over the unpromoted Rh foil is 0.034 s^{-1} for CO hydrogenation at 280 °C in the presence of 253 Torr CO and 506 Torr H_2, and 0.19 s^{-1} for CO_2 hydrogenation at 280 °C in the presence of 190 Torr CO_2 and 570 Torr H_2. As shown in Figs. 6.7 and 6.8, promotion with VOx has a significant effect on the rate of CH_4 formation from both CO and CO_2. The curves in the Figs. 6.7 and Fig. 6.8 are derived from a polynomial fit of the data with r = 0.98 and 0.93, respectively. For CO hydrogenation, the rate increases to a maximum of twice that for clean surface, for a VOx coverage of 0.4 ± 0.2 ML, whereas for CO_2 hydrogenation, the rate increases to six times that for the clean surface, for a VOx coverage of 0.6 ± 0.2 ML. AES and XPS characterization of the catalyst after CO or CO_2 hydrogenation indicate the presence of carbon on the surface, the amount being two-fold greater for CO hydrogenation than for CO_2 hydrogenation. For both reactions, though, promotion of Rh with 0.5 ML VOx increases the amount of carbon deposited.

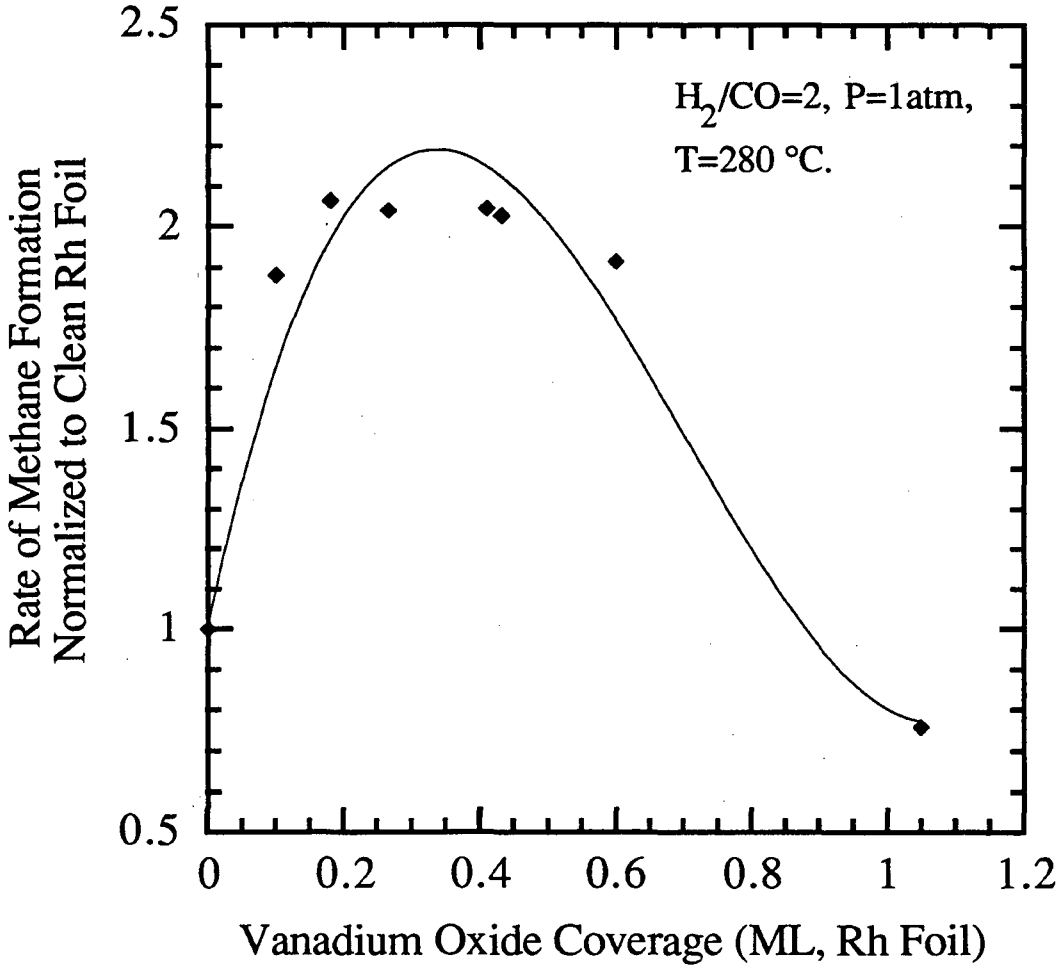

Figure 6.7: Rate of methane formation of a Rh foil as a function of vanadium oxide coverage for CO hydrogenation.

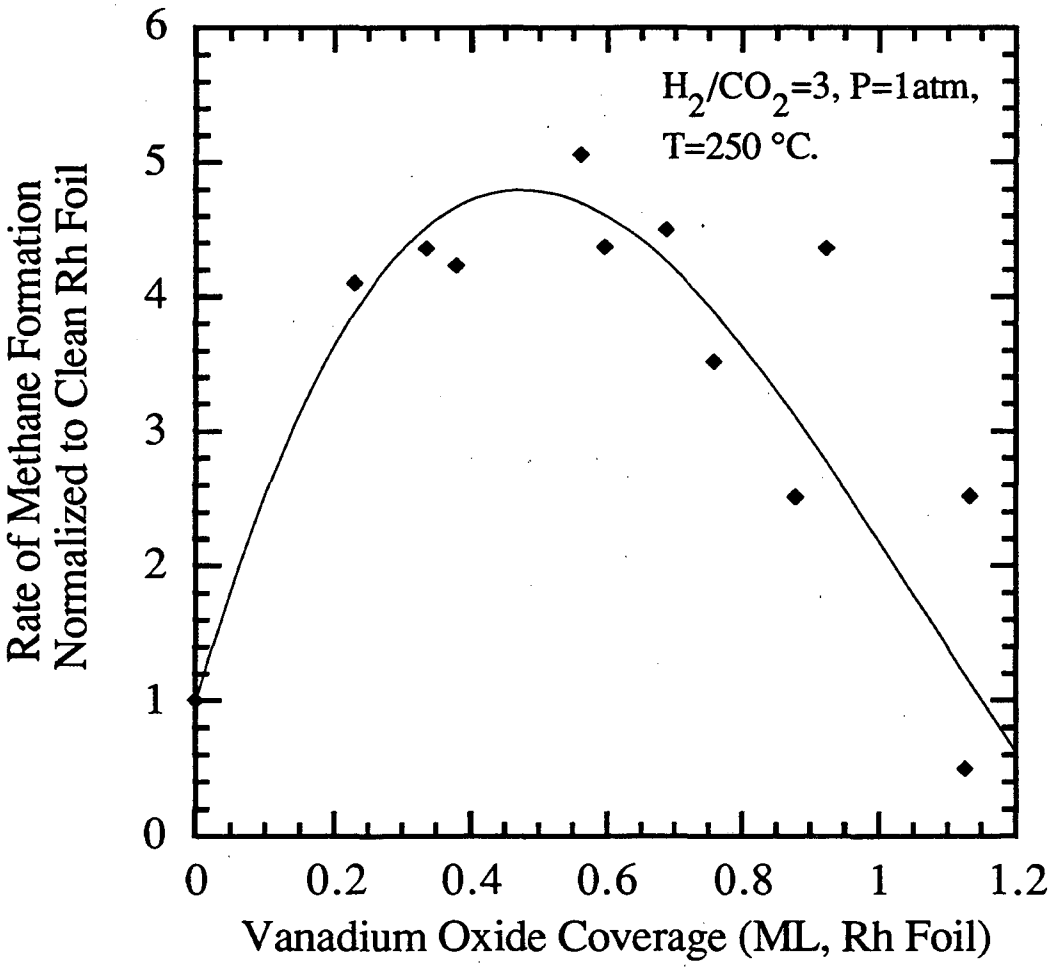

Figure 6.8: Rate of methane formation of a Rh foil as a function of vanadium oxide coverage for CO_2 hydrogenation.

Table 6.1: Percentage of V^{2+} in the VOx overlayer following CO titration, and CO and CO_2 hydrogenation

Treatment	1 X 10^{-6} Torr O_2 at 350 °C and 5 X 10^{-7} Torr CO at 250 °C	200 Torr H_2 and 50 Torr CO at 250 °C for 60 min	200 Torr H_2 and 50 Torr CO_2 at 250 °C for 60 min
VOx coverage (ML)	0.5	0.5	0.5
% V^{2+}	28	54	98

The rate parameters for CH_4 formation from CO and CO_2 hydrogenation over clean and VOx covered Rh are presented in Table 6.2. The rate of CH_4 formation is assumed to be given by a power-law expression of the form:

$$r_{CH_4} = k_0 \exp(-E_a/RT)\, P^a_{H_2}\, P^b_{CO(CO_2)}$$

where Ea, a, and b represent the activation energy, hydrogen partial pressure dependence, and CO or CO_2 partial pressure dependence, respectively. For the E_a determination, four rate measurements were made over a range of temperatures from 250 to 400 °C. For the parameter a determination, three measurements were made over a range of pressures from 169 to 590 Torr, and for the parameter b, three measurements were made over a range of pressures from 63 to 253 Torr. For CO hydrogenation, $E_a = 24 \pm 2$ kcal/mol over the clean Rh surface. Upon promotion with vanadium oxide, E_a decreases to 13 ± 2 kcal/mol. The values of a and b for the clean surface are 1.0 ± 0.2 and -1.0 ± 0.2, respectively. Promotion with vanadium oxide increases a to 2.1 ± 0.2 and b to -0.7 ± 0.2. For CO_2 hydrogenation, addition of vanadium oxide decreases E_a from 17 ± 2 to 13 ± 2 kcal/mol. However, addition of vanadium oxide has no effect on a and b. Similar changes in rate parameters have been observed for TiOx on a Rh foil and for $Rh/V/SiO_2$ (39).

Selectivities of the clean and VOx covered surface are also presented in Table 6.2. The selectivity toward methane formation from CO decreases from 90 to 67 % upon promotion with 0.5 ML VOx, and the selectivities for ethylene, ethane, and propylene increase from 3.7, 3.3, and 1.6 %, respectively, to 17, 2.5, and 8.0 %, respectively. In contrast to CO hydrogenation, VOx promotion has no effect on the selectivity for CO_2 hydrogenation. With and without VOx present the selectivity to CH_4 is 99+%.

Table 6.2: Comparison between CO and CO_2 hydrogenation kinetics over TiOx and VOx covered Rh foil

	$CO + H_2$			$CO_2 + H_2$		
	Clean Rh	0.5 ML TiOx	0.2 ML VOx	Clean Rh	0.5 ML TiOx	0.5 ML VOx
CH_4 Act. Energy (kcal/mol)	24	17	13	17	17	13
H_2 Pressure Exponent	1.0	2.5	2.1	0.5	0.5	0.3
CO/CO_2 Pressure Exponent	-1.0	-0.3	-0.7	0.2	0.3	0.2
Normalized Rate	1.0	1.7	2.8	1.0	15.0	5.0

The effects of VOx promotion on the rate of CH_4 formation from CO and CO_2 over Rh presented here are similar to those reported earlier for TiOx. Levin et al. (71-73) observed a three-fold increase in the rate of CO hydrogenation, when a Rh foil was promoted with 0.5 ML of TiOx, and Williams et al. (78,79) observed a fifteen-fold increase in the rate of CO_2 hydrogenation, also for a TiOx coverage on Rh of 0.5 ML. Also relevant is the work of Van Santen et al. (39) who found that promotion of a Rh/SiO_2 catalyst with an amount of VOx sufficient to decrease the CO chemisorption capacity by 50% increases the CO hydrogenation activity of the catalyst four-fold.

Previous studies have suggested that the mechanisms for CO and CO_2 hydrogenation are similar (128). In both instances the critical step is cleavage of the C-O bond in adsorbed CO or a CH_xO ($x \leq 3$) species, the origin of adsorbed CO in the case CO_2 hydrogenation being the dissociation of CO_2 (129,130). The C_s or $CH_{x,s}$ species released by C-O bond cleavage of CO or CH_xO readily undergo hydrogenation to form CH_4. In support of this picture, it has been observed that adsorbed CO does not dissociate appreciably on Rh(111) surfaces (121) and that during temperature - programmed reduction of adsorbed CO by H_2, CH_4 and H_2O appear concurrently (39). Studies with Rh/SiO_2 indicate, as well, that the rate constant for CO dissociation is considerably smaller than that for CH_x hydrogenation (45).

The increase in CO methanation activity when Rh is promoted with VOx correlates very closely with the amount of deposited V present in the 2+ state, as can be seen by comparing Figs. 6.6 and 6.7. Since reduction of the deposited oxide proceeds inward from the metal-oxide adlineation (119), a significant fraction of the V^{2+} cations are expected to be present at the perimeter of the VOx islands comprising the overlayer. CO molecules can adsorb at these boundaries in such a fashion that the C end of the molecule is bond to an exposed Rh atom while the O end of the molecule is bound to a V^{2+} cation. Such bonding has been postulated earlier to facilitate cleavage of the C-O bond (43,51-55).

Thus, it is hypothesized that the observed increase in the methanation rate is attributable to the increased rate of CO dissociation caused by the presence of V^{2+} cations. Consistent with this interpretation are the AES and XPS observations that VOx promotion increases the concentration of surface carbon produced during CO hydrogenation.

The changes in the rate parameters for CO hydrogenation when Rh is promoted with VOx (see Table 6.2) can also be explained in the light of the postulated model. Williams et al. (79) have shown that greatly increasing the rate of dissociation of adsorbed CO by addition of an oxide promoter ultimately results in a shift in the rate limiting step from CO dissociation to hydrogenation of CH_x species. Such a shift causes an increase in the apparent dependence of the methanation rate on the partial pressure of H_2, and a decrease in the apparent dependence on the CO partial pressure.

The increase in the rate of CO_2 hydrogenation also correlates with the amount of V^{2+} present on the Rh surface, in a manner similar to that observed for CO hydrogenation. However, in contrast to CO hydrogenation, the maximum rate enhancement is much greater. Inspection of Table 6.2 also shows that the percentage of V^{2+} in a 0.5 ML VOx overlayer is greater following CO_2 than CO hydrogenation. The greater amount of V^{2+} in the former case can be attributed to a higher surface coverage by adsorbed H, a reducing agent that is more affective than CO in attacking VOx, since CO_2 adsorbs much more weakly than CO, and, hence, will not inhibit the dissociative adsorption of H_2 on Rh. V^{2+} cations are expected to enhance both the rate of CO_2 dissociation to CO and the rate of CO dissociation to C and O. The absence of a change in the H_2 and CO_2 partial pressure dependences of the rate of CO_2 methanation upon VOx promotion suggests that the rate limiting step is unaffected by the presence of the promoter.

To further emphasize the correlation between rate enhancement and reducibility, the data contained in Figs. 6.6, 6.7, and 6.8 are replotted in Fig. 6.9 as methanation rate versus V^{2+} XPS peak area for various oxide coverages. For CO_2 hydrogenation, the data

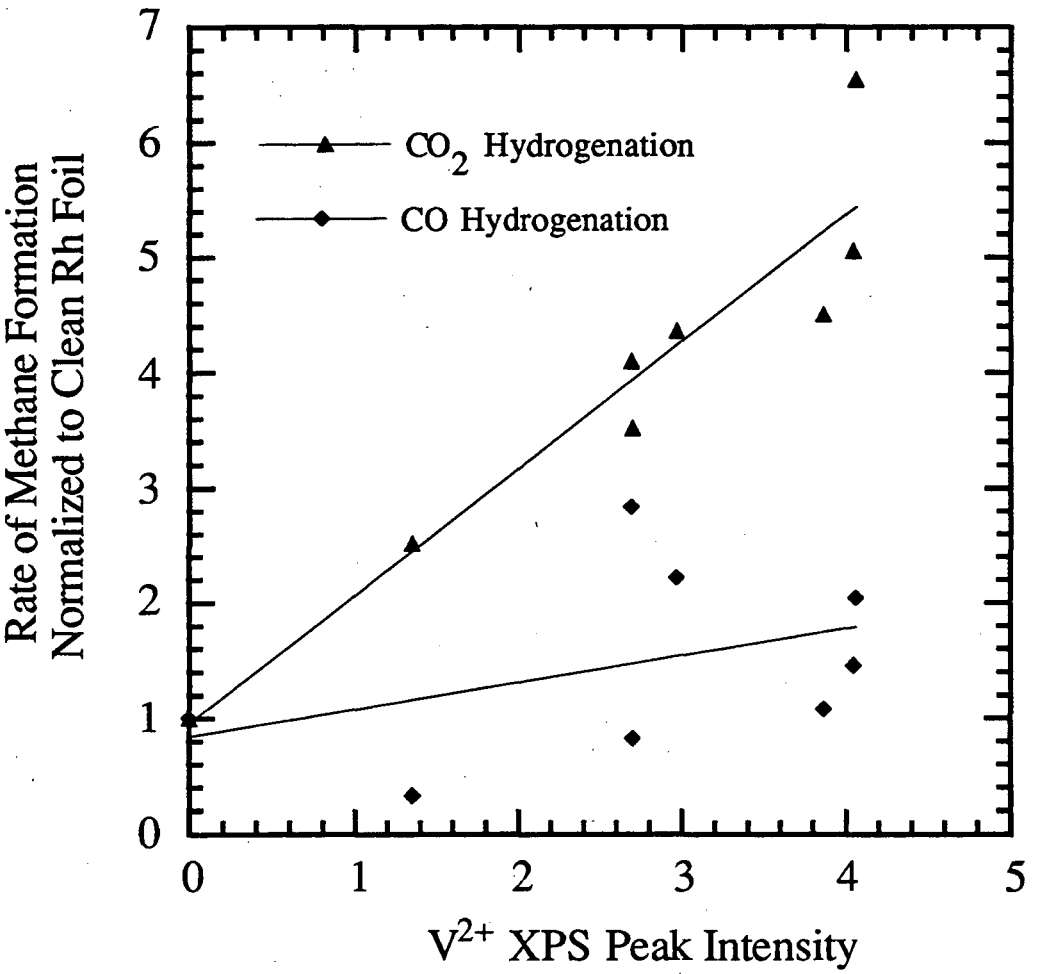

Figure 6.9: Rate of methane formation for CO and CO_2 hydrogenation as a function of V^{2+} XPS (513.8 eV) peak area for various vanadium oxide coverages on a Rh foil, r = 0.40 and 0.94, respectively.

fit to a linear function indicating that the degree of rate enhancement depends directly on the amount of reduced oxide. Although the CO hydrogenation data has more scatter, a qualitatively similar relationship exists between rate enhancement and oxide reducibility. The linear correlation of rate enhancement and oxide reducibility illustrated in Fig. 6.9 provides direct support for the often postulated mechanism (43,51-55) involving active site formation at reduced oxide sites of the oxide/metal interface and suggests that a redox interaction between the metal ion valence states (V^{2+} - V^{3+}) of the oxide promoter and the CO(a) reaction intermediates facilitates CO bond cleavage and leads to an increase in methanation rate. Assuming such a scheme is valid, the promoter ability of different oxides will depend not only on the number of reduced oxide sites but also on the redox potential of the metal ion valence pair.

6.4 Conclusions

Vanadia deposited on a Rh foil forms a two-dimensional overlayer at coverages below 1 ML. After oxidation, vanadium in the overlayer is present as V^{3+}. Titration of the O atoms present on the Rh surface reduces the V^{3+} cations in the overlayer to V^{2+}, the amount of V^{2+} cations passing through a maximum at a VOx coverage of 0.5 ML.

The deposits of vanadium oxide cause rate enhancements for CO and CO_2 hydrogenation. For CO hydrogenation, the rate maximizes at two times that of the clean surface rate at a coverage of 0.4 ± 0.2 ML. For CO_2 hydrogenation, the rate maximizes at 6 times that of the clean surface rate at a coverage of 0.6 ± 0.2 ML. For CO hydrogenation, the oxide promoter also causes a decrease in the activation energy, increase in hydrogen partial pressure dependence, and increase in selectivity to higher weight hydrocarbons. For CO_2 hydrogenation, the oxide has little effect on activation energy and

partial pressure dependences. The strong correlation between the amount of V^{2+} cations present and the rates of CO and CO_2 hydrogenation as a function of coverage, suggests that V^{2+} cations are responsible for increasing the rates of methane formation. It is proposed that V^{2+} cations promote the dissociation of CO_2 to CO_S and O_S, and of CO to C_S and O_S. The latter reaction, in particular, is hypothesized to be critical for the synthesis of methane from CO or CO_2.

Chapter 7

An XPS Study of Sub - Monolayer Transition Metal Oxides Deposits on Rh Foil: Influence of Rh on the Oxide Redox Properties

Abstract

XPS measurements of deposits of titanium, iron, zirconium, niobium, tantalum, and tungsten oxides on Rh foil are presented after exposure to oxidizing and reducing conditions. Multiple components are observed in the spectra indicating the presence of non - stoichiometric oxide deposits. A summary of published binding energy assignments for bulk and thin film oxides is compared with the observed spectra. Good agreement with the literature is found for the majority of peaks observed in the XPS spectra; however, for some components in the oxide overlayer spectra of zirconium, niobium, tantalum, and tungsten, no bulk oxide counterpart is known. Interaction at the oxide - metal interface

between the oxide and the substrate is suggested to result in the unique chemical properties observed in the oxide overlayer.

7.1 Introduction

Transition metal oxide thin films and surfaces are used in a variety of applications including as heterogeneous and electrolytic catalysts, coatings for mechanical and corrosion protection, and solid - state gas sensors. Depending on the valence state or stoichiometry, a transition metal oxide can exhibit a wide range of properties (131-133). For instance, stoichiometric TiO_2 is a semiconductor with a band gap of 3.1 eV, while TiO is an electrical conductor (133). Consequently, determining the chemical state of an oxide is crucial to understanding its behavior.

X - ray photoelectron spectroscopy (XPS) is commonly used to determine surface valence states. Despite the importance of valence in determining the properties of oxide thin films and surfaces, relatively few XPS investigations of these systems have been reported. A survey of reported XPS binding energies and oxidation state assignments for titanium, vanadium, iron, zirconium, niobium, tantalum, and tungsten oxides is presented in this article. A lack of consensus exists on the assignment of oxidation states from observed XPS binding energies, even for those oxides which have been studied most extensively. For example, binding energies reported for the Ti^{4+} oxidation state of titanium oxide range from 459.4 eV (134,135) to 458.4 eV (136) and for the assignment of Ti^{3+} range from 457.5 eV (137) to 455.7 eV (136). Since oxide samples are often insulating, disagreement in binding energy assignments can be partially attributed to surface charging. The approach in this work is to investigate oxide films which have been deposited on a conducting metal substrate to minimize charging effects. This method has

been applied in XPS investigations of oxide films of titanium, vanadium, aluminum, silicon, zinc, iron, rhenium, neodymium, and lead (138).

Deposition of thin film oxide overlayers on dissimilar metals creates an interface which plays a vital role in determining the chemical and physical properties of both components. In some cases, these properties will differ from those of either the bulk oxide or metal. For instance, the oxide - metal interface generated by deposition of sub - monolayer titanium (71-81) and vanadium (Chapter 6) oxide films on Rh has been demonstrated to lead to rates of CO and CO_2 hydrogenation which are several times greater than that of the metal or oxide alone. XPS measurements showed that the oxide overlayers of the vanadium (Chapter 6) and titanium (77) are non - stoichiometric, suggesting that valence state plays a role in determining the promoter ability of the oxide.

In this work, XPS spectra are presented for sub - monolayer deposits of titanium, iron, zirconium, niobium, tantalum, and tungsten oxides on Rh foil measured after oxidation, CO titration, CO hydrogenation, and CO_2 hydrogenation. This is one of the first reports of XPS measurements for deposits of zirconium, niobium, tantalum, and tungsten oxides on a dissimilar metal. The spectra of the oxide base metals are deconvoluted to determine the relative amounts of each valence state present. Oxidation state assignments are determined based on a comparison with reported binding energies for bulk and thin film oxides. Good agreement with the literature is found for the majority of peaks observed in the XPS spectra; however, for some components in the oxide overlayer spectra of zirconium, niobium, tantalum, and tungsten, no bulk oxide counterpart is known. The influence of bonding between the oxide deposit and the Rh substrate is postulated to stabilize oxide forms which have not been observed in bulk phases.

7.2 Experimental

A PHI ESCA 5300 was used for XPS and ISS measurements. It is equipped with a Mg and Al anode x-ray source, an He and Ar differentially pumped ion gun, a hemispherical analyzer, and a sample preparation cell. For XPS, the Mg anode (1253.6 eV) was used, and the hemispherical analyzer detector was operated at a 8.75 eV pass energy. The angle between the source and analyzer is 54.7 °. The coverage of the oxide deposits was determined using ISS. For ISS, an incident beam of He ions at 500 eV was scattered at an angle of 123.0 degrees and detected with the hemispherical analyzer operated at a 179 eV pass energy. The oxide overlayers were prepared in an adjacent preparation chamber which was maintained at a base pressure of 5×10^{-10} Torr. A transfer rod was employed to move the sample between chambers in vacuum. In the preparation chamber, an electron beam heater and alumel - chromel thermocouple were used to control and monitor the sample temperature.

Metals were deposited on a 1 cm^2 Rh foil that was 0.005 cm thick using an evaporator. The filaments used in the evaporator consisted of either a 0.020 to 0.040 in wire of the metal to be deposited in the case of W, Ta, Nb, and Zr or a 0.005 to 0.020 in wire of the metal to be deposited wound around 0.040in W wire in the case of Ti, V, and Fe. Currents of between 20 and 40 amps were necessary to give a deposition rates of approximately 1.0 ML/min, depending on the vapor pressure of the metal. A back pressure of 2×10^{-7} Torr of oxygen was present during evaporation in order to reduce carbon contamination. After metal deposition, the surface was oxidized at 1×10^{-6} Torr of O_2 at 350 °C for 5 min. To remove oxygen adsorbed on the exposed Rh surface and partially reduce the oxide overlayer, the sample was exposed to 10 L CO followed by temperature programmed desorption (CO titration).

From the preparation chamber the sample was transferred to an atmospheric - pressure isolation cell and exposed to reactant pressures up to 800 Torr. The temperature of the sample was maintained using an Research Inc. model 4085 radiative infrared spot heater that was focused through a quartz view - port and monitored using an alumel - chromel thermocouple. After treatment under atmospheric conditions, the sample was cooled to below 200 °C followed by evacuation to less than $1x10^{-6}$ Torr with a turbo-molecular pump. Evacuation required on average 3 min. The sample was then directly transferred to the analysis chamber under vacuum.

The XPS spectra were deconvoluted using the PHI ESCA 5300 software curve fit routine. The curve fit program allowed the peak position, height, width, and shape (Gaussian / Lorentzian) to be varied until the best least squares fit of the data was obtained. Peaks were added to the curve fit only when at least partially resolved in the experimental XPS curve. The binding energies of the fitted XPS peaks were assigned based on agreement with reported XPS data for reference compounds. Using this method, the error in the reported binding energy of the peaks is estimated to be ± 0.2 eV, and the error in relative intensity of the components is estimated to be ± 10 %.

7.3 Results

XPS measurements for each oxide have been made following oxidation in 10^{-6} Torr O_2 at 350 °C, CO titration (exposure to 10 L CO followed by a temperature programmed desorption), CO_2 hydrogenation, and CO hydrogenation. During CO_2 hydrogenation the reactant pressures were 190 Torr of CO_2 and 570 of H_2 Torr, and the reaction temperature was 250 °C. For CO hydrogenation, 253 Torr of CO was reacted with 506 Torr of H_2 at a temperature of 280 °C. Identical reaction conditions were used in

measurements performed of promotion by sub-monolayer oxide deposits of Rh foil (Chapter 8). All measurements presented are for deposits of 0.5 ML which is the coverage at which maximum rate enhancement of CO and CO_2 hydrogenation is observed.

7.3.1 Titanium

The titanium 2p XPS spectra of 0.5 ML oxide deposits on Rh are shown in Fig. 7.1. Four peaks are observed in the XPS spectrum. The peaks at 458.5 eV and 464.2 eV are assigned to Ti^{4+} (TiO_2), while those at 456.2 eV and 461.9 eV are assigned to Ti^{3+} (Ti_2O_3). Using these assignments, the titanium oxide film is determined to contain 11 % Ti^{3+} and 89 % Ti^{4+} after oxidation in 10^{-6} Torr O_2 based on a deconvolution and curve fit of the XPS spectrum in Fig. 7.1. Reducing the oxidized deposit by CO titration leads to an oxide overlayer containing 47 % Ti^{3+} and 53 % Ti^{4+}. After reaction, the originally oxidized deposit contains 27 % Ti in a 3+ oxidation state and 73 % in the 4+ oxidation state for CO_2 hydrogenation and 8.0 % in the 3+ oxidation state and 92 % in the 4+ oxidation state for CO hydrogenation.

The oxidation state assignments are based on comparisons with those reported in the literature for bulk titanium oxide and thin film samples as indicated in Table 7.1. The reported binding energies for the Ti^{4+} $2p_{3/2}$ oxidation state range from 459.4 eV to 458.4 eV. The peak observed at 458.5 eV to Ti^{4+} is within the range of those values reported in the literature. A survey of recent literature finds assignments for Ti^{3+} to binding energies of 456.3 eV, 456.2 eV, 456.8 eV, 456.5 eV, 457.5 eV, and 456.6 eV (see Table 1). Ti^{2+} has been assigned 454.7 eV, 454.8 eV, 454.9 eV, 455.0 eV, 454.6 eV in bulk and thin film titanium oxides. The XPS peak observed at 456.2 eV is in better agreement with the

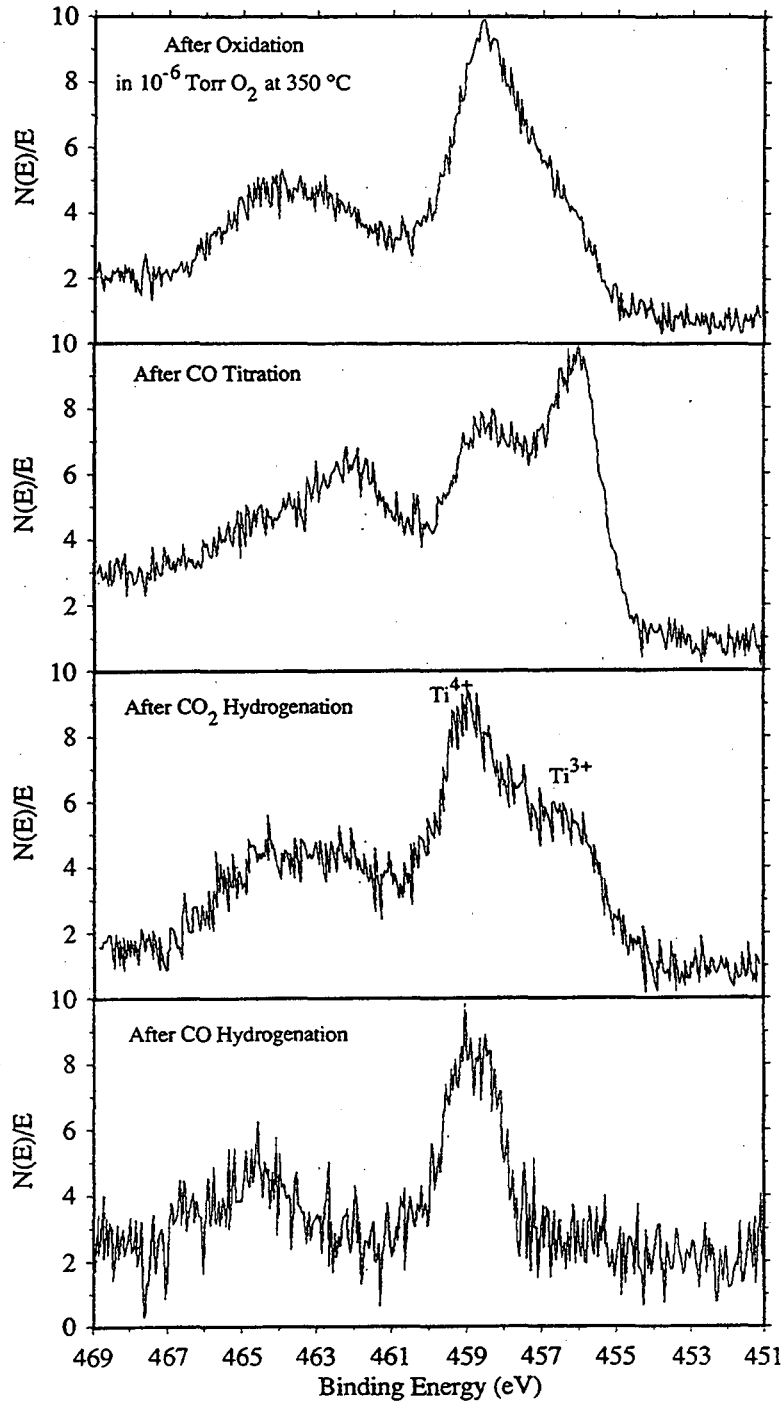

Figure 7.1. XPS spectra of the Ti (2p) region for a 0.5 ML oxide deposit on Rh foil measured after oxidation, CO titration, CO_2 hydrogenation, and CO hydrogenation (Ti^{4+} = 458.5 eV and Ti^{3+} = 456.2 eV).

Table 7.1: Summary of Oxidation State Assignments

Oxide	This Work				Literature			
TiOx	4+	3+		ΔE^{4-3}	TiO_2 (4+)	Ti_2O_3 (3+)	TiO (2+)	ΔE^{4-3}
	458.5	456.2		2.3	459.4[134,135], 459.2[148], 459.0[137], 458.9[102], 458.8[77,139,140], 458.7[141,143,144], 458.6-457.9[65,101], 458.52[22,66,145,146], 147, 458.4[136,142]	457.5[137], 456.9[135], 456.8[145], 147, 456.6[101], 456.5[65], 456.2[102], 455.7[77]	455.3[137], 455.0[65], 454.9[142], 454.8[147], 454.7[145], 454.6[66]	3.1[77], 2.7[102], 2.5[135], 2.1[65], 2.0[101], 1.7[145,147], 1.5[65]
ZrOx	4+	3+		ΔE^{4-3}	ZrO_2 (4+)	Zr_2O_3 (3+)		ΔE^{4-3}
	182.3	181.1		1.2	183.3[149,150], 183.2-181.9[151], 182.9[152], 182.8[153], 182.5[154], 182.2[155,156,144136], 181.9[156,157]	182.0[149], 181.7[153]		1.3[149], 1.1[153]
FeOx	3+	2+	0	ΔE^{3-2}	Fe_2O_3 (3+)	FeO (2+)	Fe (0)	ΔE^{3-2}
	711.5	710.0	707.8	1.5	711.4[158], 711.2[159], 710.9[160], 710.7-710.3[161]	709.9[158], 709.7[159], 709.4[160]	707.7[158], 707.0[139, 159]	1.5[158-160]
NbOx	5+	4+	3+	ΔE^{5-4}	Nb_2O_5 (5+)	NbO_2 (4+)	NbO (2+)	ΔE^{5-4}
	207.4	206.2	204.7	1.2	207.9[150], 207.8[162], 207.5[163,164], 207.4[165], 206.8[166]	207.3[150], 208.9[165], 205.3[167]	204.5[165], 203.7[167], 203.5[166], 202.8[163]	1.5[165,166], 0.6[150]
TaOx	5+	4+	3+	ΔE^{5-4}	Ta_2O_5 (5+)			
	26.3	25.4	24.3	0.9	26.8[164], 26.7[144,166], 26.2[150]			
VOx	+3	+2		ΔE^{3-2}	V_2O_5 (5+)	VO_2 (4+)	V_2O_3 (3+)	V(0)
	515.6	513.8		1.6	518.1[168], 517.6[169,161,144,162,143,136], 517.4[139], 517.0[173], 516.7[170], 516.6[140,172]	517.4[168], 516.5[172], 516.1[173]	515.6[168], 515.5[173]	512.7[172], 512.4[171, 174, 175], 512.3[143], 512.2[139]
WOx	6+	5+	4+	3+	WO_3 (6+)	WO_2 (4+)	W (0)	ΔE^{6-4}
	35.4	34.2	33.2	32.5	36.8[164], 36.3-35.6[161], 36.0[176,177], 35.8[150,166,178], 35.5[180], 35.0[179]	34.4[176], 32.5[180]	31.4[139]	3.0[180], 1.6[176]

literature assignments for Ti^{3+} than for Ti^{2+}. The greatest discrepancy for the assignment of the Ti^{3+} chemical state to a binding energy of 456.2 eV is with the 457.5 eV measurement of Carley et al. (137). However, a comparison of the difference in binding energies assignments for Ti^{4+} and Ti^{3+} (ΔE_b^{4-3}) of this work and that of Carley et al. demonstrates improved agreement between the two studies.

In a recent publication by Bardi (181), a summary has been presented of the relationship between reported titanium XPS measurements and oxide stoichiometry. Although the binding energy peak positions for Ti $2p_{3/2}$ ranging from 456 eV to 457 eV are in better agreement with literature assignments of Ti^{3+} (Ti_2O_3), Bardi suggests that Ti in this binding energy range is better assigned to a 2+ oxidation state based on oxide stoichiometries determined from O/Ti AES ratios. However, several authors (68) have shown that electron irradiation of titanium oxide films during AES experiments leads to chemical reduction due to loss of oxygen from the oxide. Additionally, AES sensitivity factors vary depending on the chemical environment. A sensitivity factor for oxygen determined from a known TiO_2 standard may differ from that applicable for the reduced oxide. Furthermore, determining stoichiometry from sensitivity factors requires knowledge of the relative mixture of Ti and O within the overlayer (83). In most instances, the relative distributions of Ti and O are not known. These factors make the assignment of composition and oxidation state based on the ratio of O to Ti AES intensities tentative. Bardi uses an electronic effect between Pt and TiOx to explain the approximate +1 eV discrepancy with assignments of Ti^{2+} in the literature (see Table 7.1); however, the origin of such an effect was not rigorously defined. If the 456 eV to 457 eV range of binding energies is instead assigned to Ti^{3+}, arguments involving electronic effects need not be invoked because of the good agreement with assignments in the literature particularly when variations due to charging effects are minimized by considering relative binding energies (ΔE_b).

Electron pair resonance (EPR) provides an independent method for identifying Ti^{3+}. In an EPR investigation of the reduction of Pt catalysts supported on TiO_2, Bonneviot et al. (25) obtain EPR spectra confirming the presence of Ti^{3+} ions. One of the Ti^{3+} EPR spectra had not been observed in bulk titania samples and was attributed to Ti^{3+} species located at the oxide - Pt interface. In analogous XPS studies of the reduction of Pt catalysts supported on titania (141), titanium XPS binding energies are observed that are in good agreement with those assigned to Ti^{3+} in Fig. 7.1.

7.3.2 Zirconium

XPS spectra of the zirconium $3d_{5/2}$ and $3d_{3/2}$ doublet are shown in Fig. 7.2. Peaks in the XPS spectrum positioned at 182.3 and 184.7 eV are assigned to the doublet for Zr^{4+}, $3d_{5/2}$ and $3d_{3/2}$ respectively. The peaks at 181.1 and 183.6 eV are assigned to the doublet for Zr^{3+}. These assignments for the oxidation states in zirconium oxide are found to be in excellent agreement with those reported in the literature as indicated in Table 7.1. In the XPS spectrum taken after oxidation, the primary peaks observed are positioned at the binding energies that have been assigned to Zr^{3+} doublet (181.1 and 183.6 eV). The overlap of these peaks does not account for the signal intensity observed at ~ 182 eV, requiring the introduction of the XPS peaks positioned at 182.3 and 184.7 eV that have been assigned to Zr^{4+}. The complete curve fit using these assignments for the positions of the oxidation states of zirconium gives 87 % Zr^{3+} and 13 % Zr^{4+}. In the spectrum observed after CO titration, the primary peaks are again those positioned at 181.1 and 183.6 eV; however, the intensity between these peaks, which corresponds to Zr^{4+} is a greater proportion of the total. A curve fit for the spectrum measured after CO titration gives 62 % Zr^{3+} and 38 % Zr^{4+}. Fig. 7.2 also shows the spectrum observed after CO_2 hydrogenation. In this spectrum, the primary peak is centered at a position of 182.3 eV,

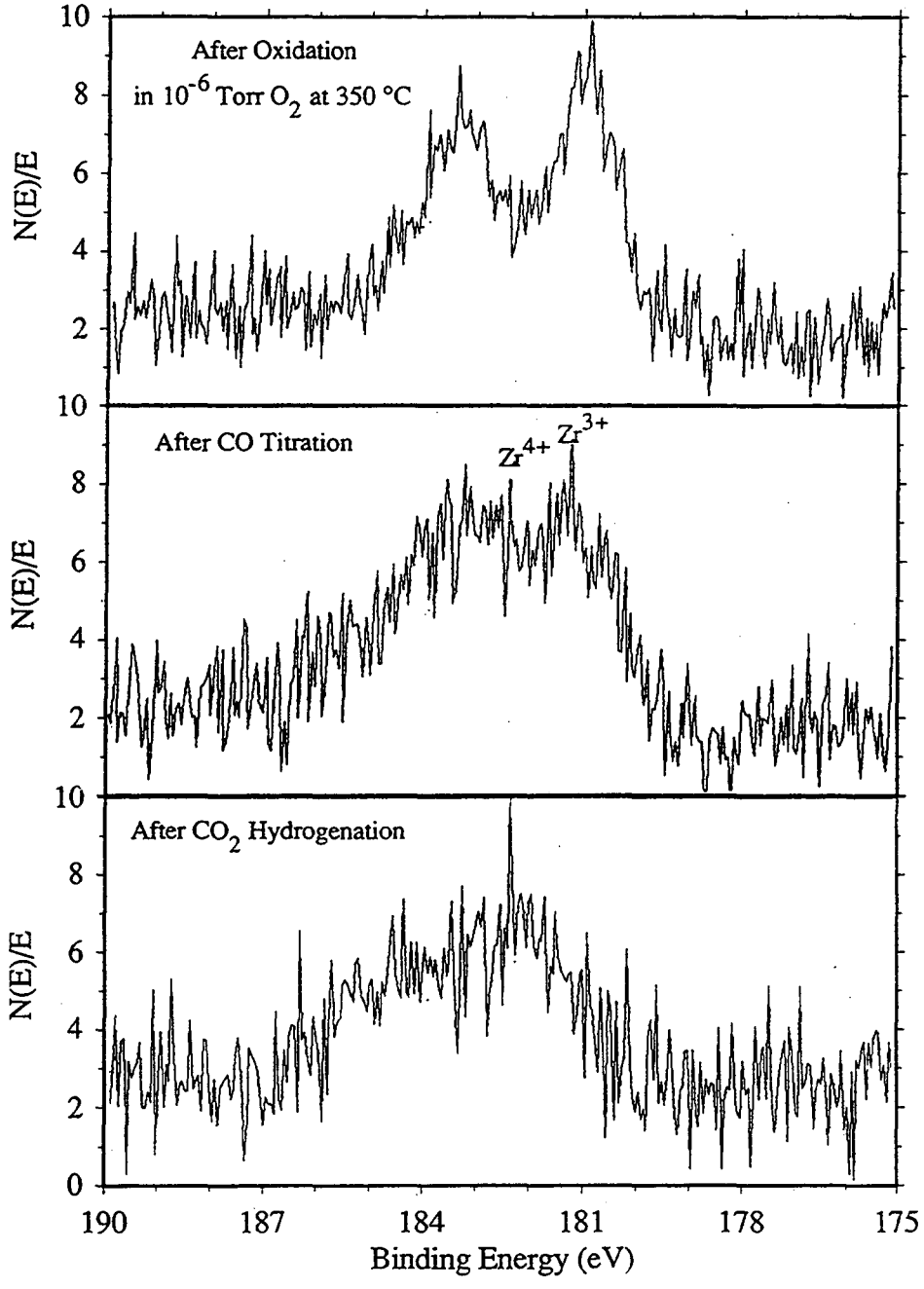

Figure 7.2. XPS spectra of the Zr (3d) region for a 0.5 ML oxide deposit on Rh foil measured after oxidation, CO titration, CO_2 hydrogenation, and CO hydrogenation (Zr^{4+} = 182.3 eV and Zr^{3+} = 181.1 eV).

which is the binding energy assigned to Zr^{4+} $3d_{5/2}$. Comparing this spectrum with that measured after CO titration and 10^{-6} Torr oxidation shows that the peak positioned at 182.3 eV in the CO_2 hydrogenation spectrum accounts for the overlap intensity observed in the other two spectrum. CO_2 hydrogenation leads to a deposit that contains 77 % Zr^{4+} and 23 % Zr^{3+}.

The presence of zirconium sub-oxides has been established in studies of the oxidation of zirconium surfaces. Investigations of the initial stages of oxidation of zirconium by Kumar et al.(149), Gonzalez et al.(152), and Morant et al.(153) have lead to identification of zirconium sub-oxides by XPS. In each of these studies, a Zr XPS peak has been observed with a binding energy and shift relative to ZrO_2 (ΔE_b) (see Table 7.1) which are in good agreement with the peak assigned in this work to Zr^{3+}. These authors suggest that this sub-oxide is Zr_2O_3.

7.3.3 Iron

The XPS spectra for a 0.5 ML iron oxide deposit are shown in Fig. 7.3. Features are observed from the $2p_{3/2}$ and $2p_{1/2}$ multiplet and from shake up peaks. For deconvolution, the $2p_{3/2}$ region from 715 to 705 eV was analyzed. The XPS peak observed at 711.5 eV is assigned to Fe^{3+}, at 710.0 eV is assigned to Fe^{2+}, and at 707.8 is assigned to Fe^0. The assignments for Fe^{3+} and Fe^{2+} are in good agreement with those from the literature tabulated in Table 7.1. The assignment of Fe^0 of 707.7 eV differs with the assignments in the literature by ~ 0.7 eV. The binding energy of 707.7 eV is in better agreement with that observed for iron carbide (708.1 eV (182)). However, no evidence for carbide formation is found in the C XPS region. Based on these assignments, 58 % Fe^{3+} and 42 % Fe^{2+} is observed after oxidation in 10^{-6} Torr O_2, 53 % Fe^{2+} and 47 % Fe^0 is observed after CO titration, 44 % Fe^{2+} and 56 % Fe^0 are observed

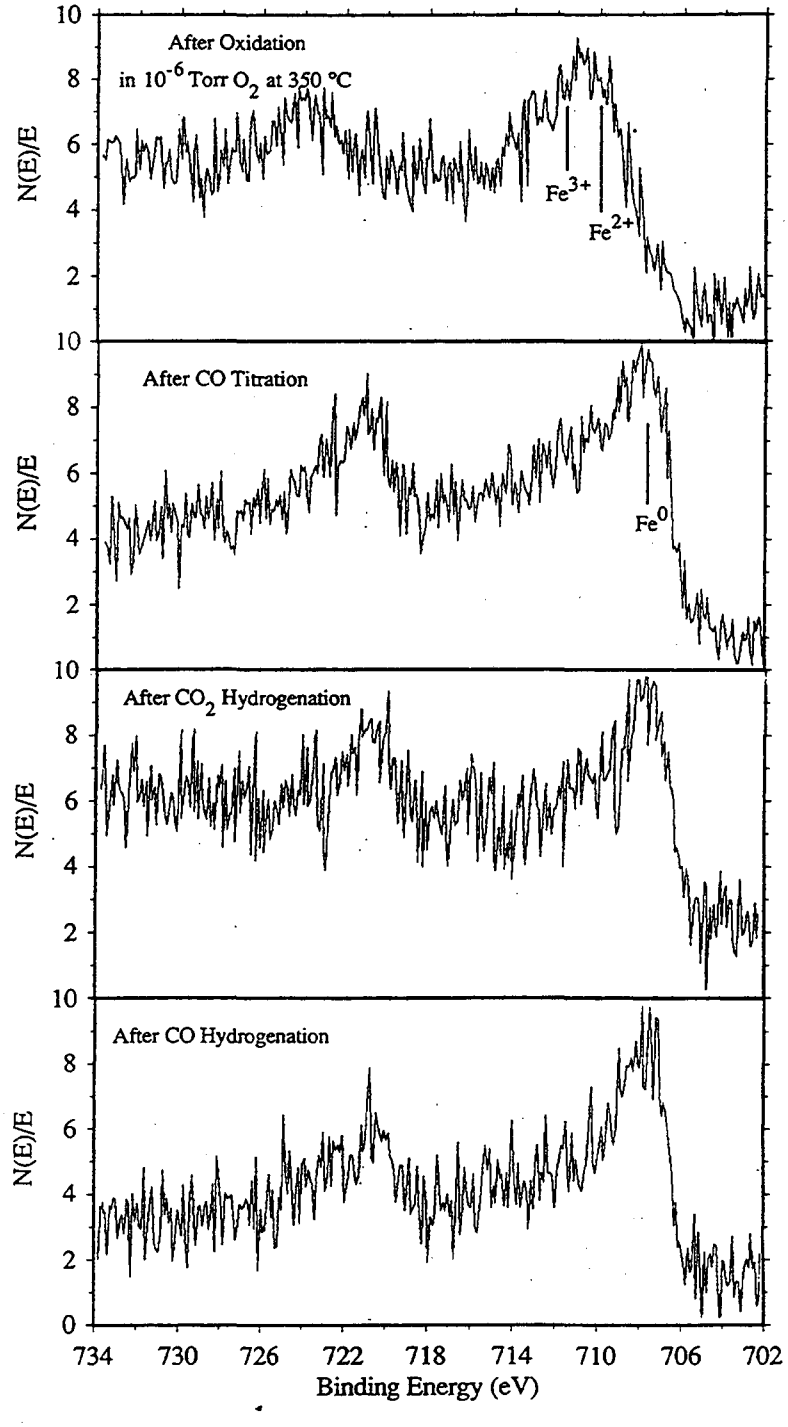

Figure 7.3: XPS spectra of the Fe (2p) region for a 0.5 ML oxide deposit on Rh foil measured after oxidation, CO titration, CO_2 hydrogenation, and CO hydrogenation (Fe^{3+} = 711.5 eV, Fe^{2+} = 710.0 eV, and Fe^0 = 707.8 eV).

after CO_2 hydrogenation, and 37 % Fe^{2+} and 63 % Fe^0 is observed after CO hydrogenation.

7.3.4 Niobium

The spectra for the 3d Nb region are shown in Fig. 7.4. Six peaks are observed corresponding to three sets of 3d doublets. The position of the $3d_{5/2}$ components are 207.4 eV, 206.2 eV, and 204.7 eV. To aid in determining the oxidation state of niobium sub-oxide associated with these peak positions, assignments of niobium oxide binding energies from the literature are organized in Table 7.1. The known oxides of niobium are Nb_2O_5 (+5), NbO_2 (+4), and NbO (+2). The range of literature assignments for the binding energy for Nb_2O_5 is 206.8 to 207.9 eV. In Fig. 7.4 the peak observed at 207.4 eV falls within the range of literature values for Nb_2O_5 and is therefore assigned a 5+ niobium oxidation state. The literature assignments for NbO_2 range from 205.3 to 207.3 eV, which leads to an assignment for the peak at a binding energy of 206.2 eV to Nb^{4+}. The range of literature assignments for NbO is 202.8 to 204.5 eV. In Fig. 7.4 the peak at 204.7 eV lies between the literature assignments for NbO_2 and NbO and is assigned to Nb^{3+}. Using these assignments, 87 % Nb^{4+} and 13 % Nb^{3+} are observed after oxidation in 10^{-6} Torr O_2. CO titration leads to an overlayer with 31 % Nb^{4+} and 69 % Nb^{3+}. After CO_2 hydrogenation 19 % Nb^{4+} and 81 % Nb^{3+} are observed, and after CO hydrogenation 60 % Nb^{5+}, 19 % Nb^{4+}, and 21 % Nb^{3+} are found.

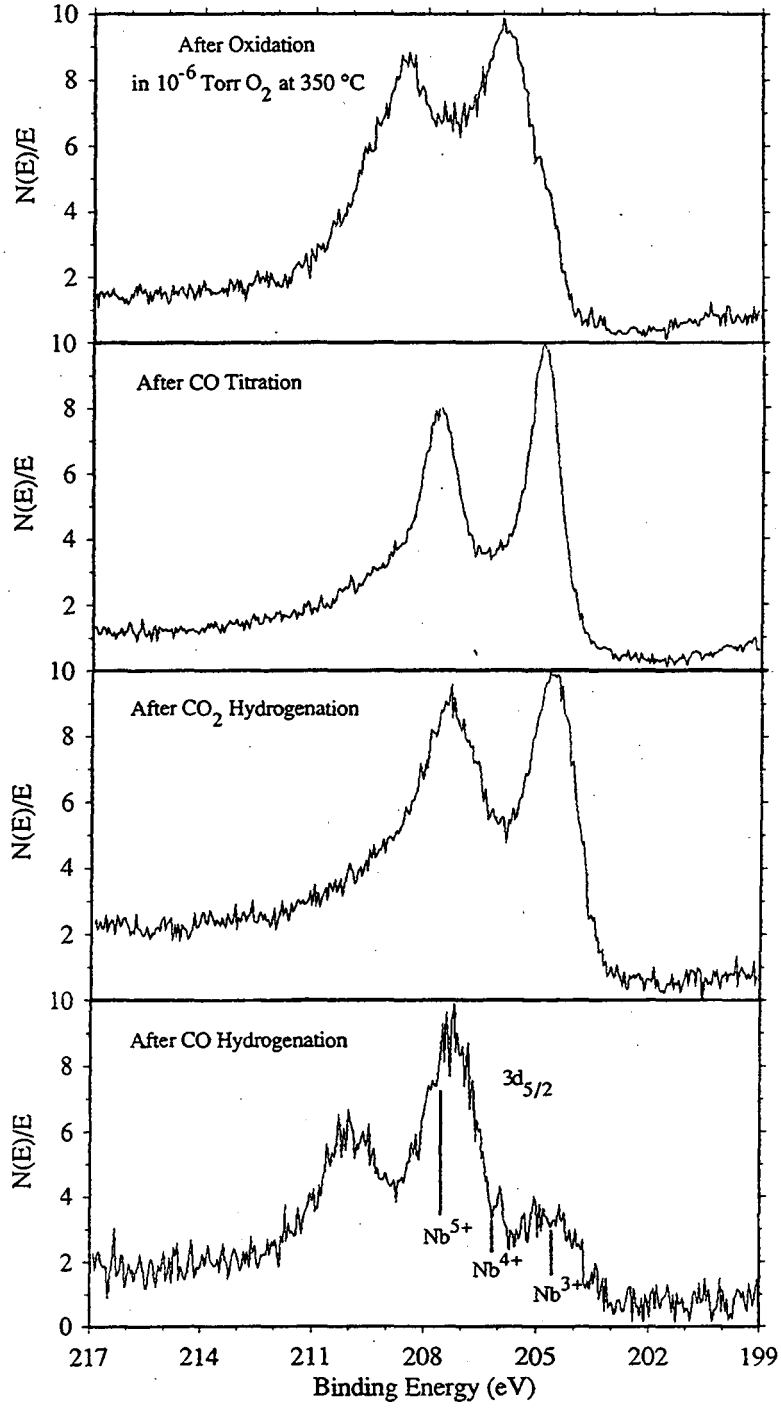

Figure 7.4: XPS spectra of the Nb (3d) region for a 0.5 ML oxide deposit on Rh foil measured after oxidation, CO titration, CO_2 hydrogenation, and CO hydrogenation (Nb^{5+} = 207.4 eV, Nb^{4+} = 206.2 eV, and Nb^{3+} = 204.7 eV).

7.3.5 Tantalum

The XPS spectra of the 4f doublet of tantalum for 0.5 ML oxide deposits on Rh foil are shown in Fig. 7.5. Like the spectra for niobium, six peaks corresponding to three sets of doublets can be identified. The binding energies of the three $4f_{7/2}$ peaks are 26.3 eV, 25.4 eV, and 24.3 eV. The only known bulk phase of tantalum oxide is Ta_2O_5. From the literature assignments of Ta_2O_5 given in Table 7.1, the peak positioned at 26.3 eV is assigned to Ta^{5+}. The assignment of the peaks at 25.4 and 24.3 eV is difficult considering that no reduced tantalum bulk oxide analog are known. To aid in making an estimate of the oxidation states for these binding energies, comparisons can be made to the assignments for niobium oxide. In a study of the core binding energies of Group IIIa, Vb, and VIb compounds, McGuire et al. (164) demonstrated a trend in the intrinsic chemical shifts of Nb, Ta, and W compounds. The plot of the binding energies of compounds of Nb versus analogous compounds of Ta resulted in a slope of 1.05. Therefore, based on the assignments determined for Nb, the peak in the tantalum spectra at 25.4 eV is assigned to Ta^{4+} and that at 24.3 to Ta^{3+}. A deconvolution of the spectra in Fig. 7.5 gives 77 % Ta^{5+} and 23 % Ta^{4+} after oxidation in 10^{-6} Torr O_2, 51 % Ta^{4+} and 49 % Ta^{3+} after CO titration, 42 % Ta^{4+} and 58 % Ta^{3+} after CO_2 hydrogenation, and 88 % Ta^{5+} and 12 % Ta^{4+} after CO hydrogenation.

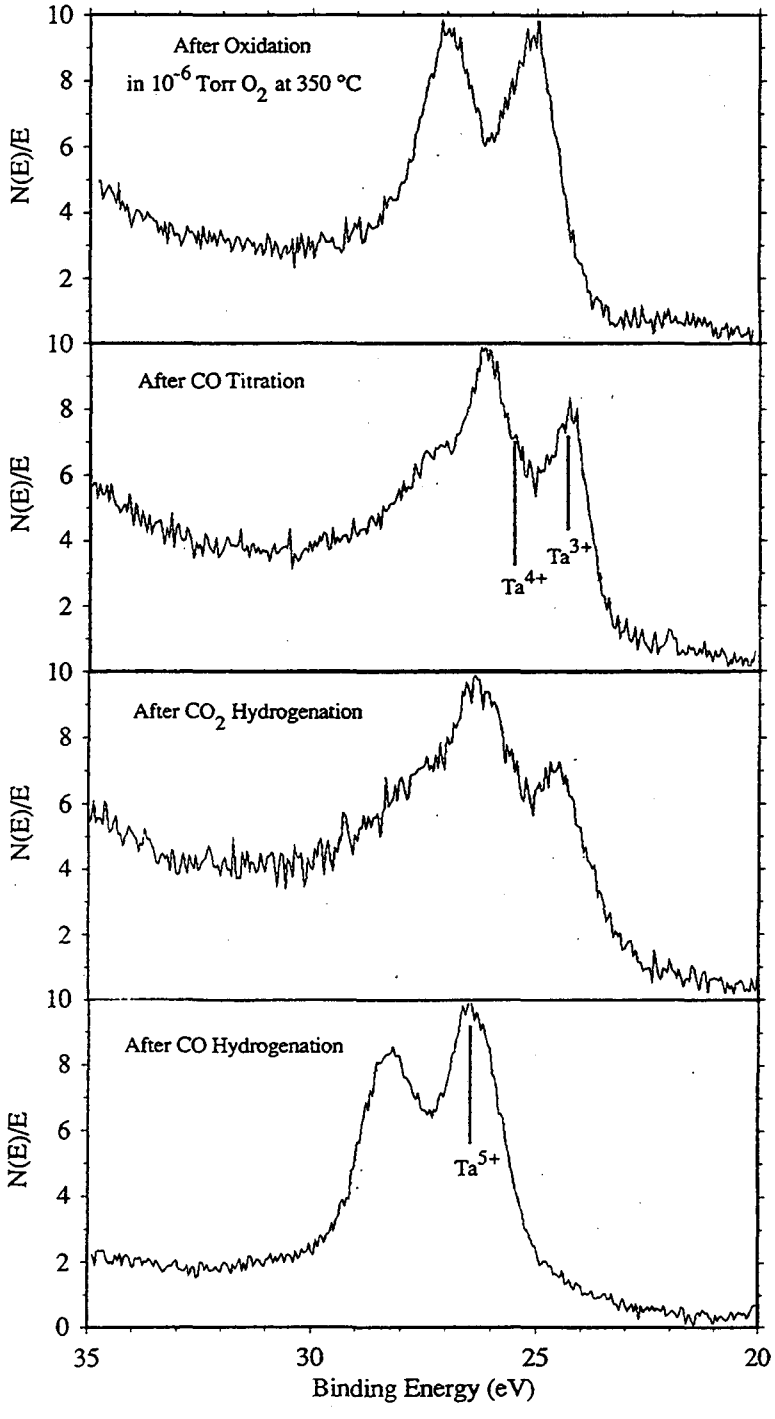

Figure 7.5: XPS spectra of the Ta (4f) region for a 0.5 ML oxide deposit on Rh foil measured after oxidation, CO titration, CO_2 hydrogenation, and CO hydrogenation (Ta^{5+} = 26.3 eV, Ta^{4+} = 25.4 eV, and Ta^{3+} = 24.3 eV).

7.3.6 Tungsten

XPS spectra of the W 4f region obtained from a 0.5 ML deposit of tungsten oxide on Rh foil are shown in Fig. 7.6. In order to obtained reasonable fits for these spectra, curves representing a total of five sets of doublets were applied in the deconvolution. The positions of the $4f_{7/2}$ doublets are 35.4 eV, 34.2 eV, 33.2 eV, 32.5 eV, and 31.9 eV. In the spectrum taken after oxidation in 10^{-6} Torr O_2 in Fig. 7.6, the curves positioned at 35.4 eV, 34.2 eV, and 33.2 eV are partially resolved. The fourth peak in this spectrum is a convolution of $4f_{5/2}$ doublets. After CO titration the primary peak is positioned at 33.2 eV. Its $4f_{5/2}$ doublet is at 35.4 eV. The primary peak in the spectrum taken after CO_2 hydrogenation is that positioned at 31.9 eV and its doublet at 34.1 eV. In addition, a shoulder is observed on the high binding energy side of these curves at 31.9 eV and 34.1 eV. The $4f_{5/2}$ doublets associated with the peaks at 31.9 and 34.1 eV are positioned at 32.5 eV and 34.7 eV , respectively. The known bulk oxides of tungsten are WO_3, $W_{18}O_{49}$, and WO_2. Literature values for the W $4f_{7/2}$ binding energies of these oxides are given Table 7.1. The range of literature assignments for W^{6+} in WO_3 is 36.3 to 35.2 eV. The peak at 35.4 eV is within this range and is assigned to W^{6+}. The range of binding energies found in the literature for WO_2 is 32.5 to 34.4 eV. This range encompasses the peaks observed at 34.2 eV, 33.2 eV, and 32.5 eV; however, the peak at 33.2 eV is in the best agreement with the majority of literature assignments of W^{4+} in WO_2 and is assigned to W^{4+}. With the peak at 33.2 eV assigned to W^{4+}, the peak at higher energy (34.2 eV) is estimated to correlate with the W^{5+} and that at lower binding energy (32.5 eV) is estimated to correspond to W^{3+}. An alternative estimate of the binding energies would be to assign each of these peaks to W^{4+}. This leaves the assignment of the peak at 31.9 eV. A binding energy of 31.9 eV is in fair agreement with the position of W $4f_{7/2}$ in tungsten carbides (31.5 eV (180) and 32.2 eV (164)). However, the position of the C XPS peak is not

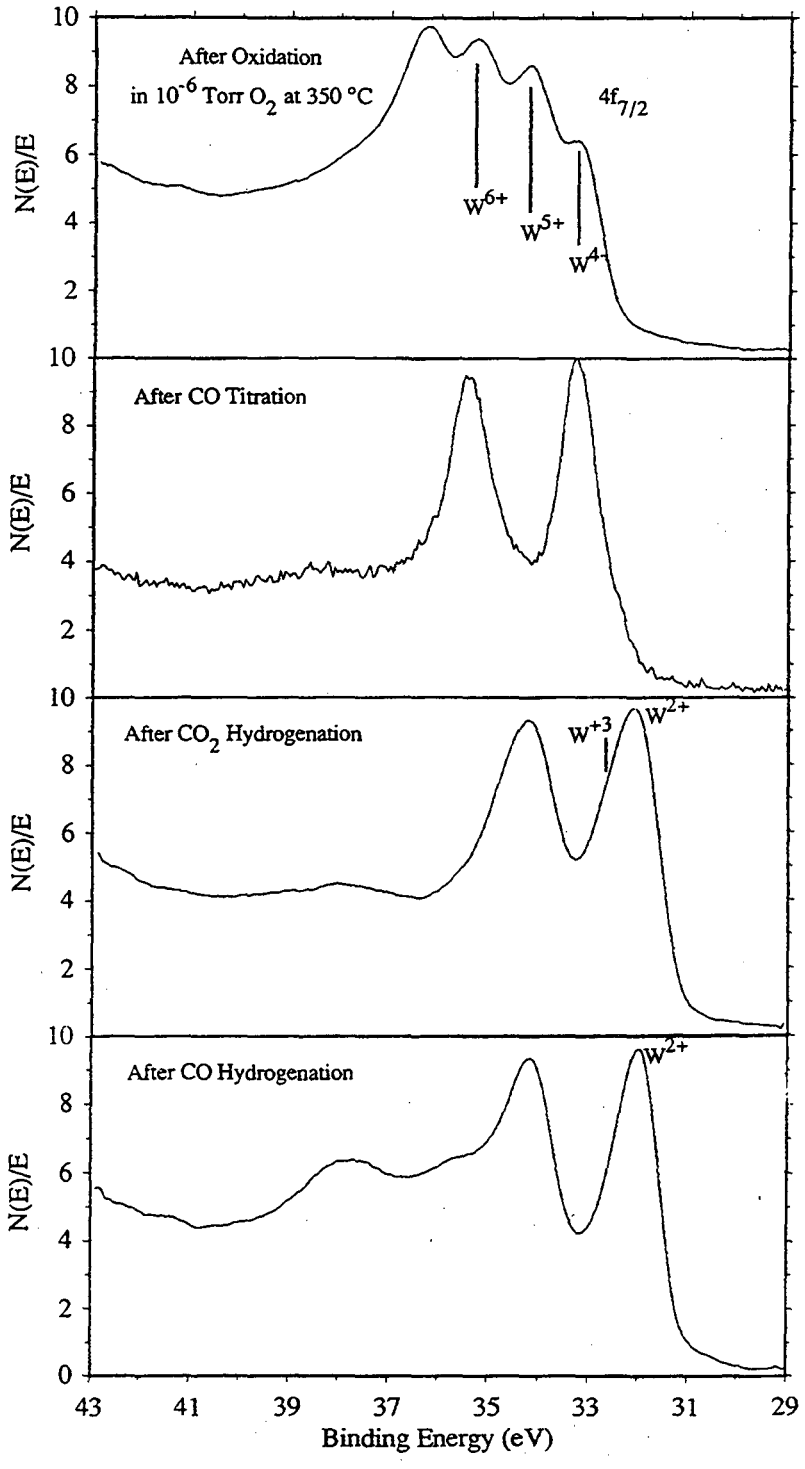

Figure 7.6: XPS spectra of the W (4f) region for a 0.5 ML oxide deposit on Rh foil measured after oxidation, CO titration, CO_2 hydrogenation, and CO hydrogenation (W^{6+} = 35.4 eV, W^{5+} = 34.2 eV, W^{4+} = 33.2 eV, W^{3+} = 32.5 eV, and W^{2+} = 31.9).

consistent with carbide formation. A binding energy of 31.9 eV could also possibly be assigned to W metal (139). However, the observation of a O XPS peak at 530 eV suggests the presence of tungsten oxide. Therefore, the peak at 31.9 eV is assigned to W^{2+} of a sub-oxide. From these assignments, a deconvolution of the spectra in Fig. 7.6 gives 26 % W^{6+}, 54 % W^{5+}, and 19 % W^{4+} after oxidation in 10^{-6} Torr O_2, 20 % W^{5+} and 80 % W^{4+} after CO titration, 69 % W^{3+} and 31 % W^{2+} after CO_2 hydrogenation, and 18 % W^{3+} and 82 % W^{2+} after CO hydrogenation. Using the alternative assignment of W^{4+} for the peaks at 34.2 eV, 33.2 eV, and 32.5 eV would effect the average oxidation state determined from the percentage of valence states an average of $\pm$ 0.4.

7.3.7 Rhodium

For each oxide deposit investigated, the Rh 3d XPS region was monitored after exposure to 10^{-6} Torr O_2 at 350 °C, CO titration, CO_2 hydrogenation, and CO hydrogenation. In each case the Rh binding energy remained constant at 307.3 eV. This binding energy corresponds to metallic Rh (139). Attempts were made at isolating the Rh at the oxide interface by increasing the angle between the sample and the detector. A change in the Rh XPS spectrum was not observed upon varying this angle. Consequently, no evidence is found for a net charge transfer between the oxide and the Rh substrate using XPS. Factors which could possibly mask charge transfer at the oxide - metal interface are delocalization of charge within the band structure of the substrate and convolution with the signal from the Rh sub - surface. Studies of Rh and Pt catalyst particles supported on transition metal oxides are inconclusive on the extent and direction of a net charge transfer between oxide and metal. Reports can be found in the literature of no measurable core level

binding energy shift relative to the metallic state and of negative shifts relative to the metallic state (6).

7.3.8 Oxygen

Oxygen XPS spectra have been acquired for each oxide deposit. As an example, the oxygen XPS spectrum of a 0.5 ML titanium oxide deposit on Rh foil is shown in Fig. 7.7 after exposure to 10^{-6} Torr O_2 at 350 °C, CO titration, CO_2 hydrogenation, and CO hydrogenation. The XPS O 1s curve contains a primary peak centered at 530.2 ± 0.2 eV and a shoulder positioned at 531.5 ± 0.3 eV. The peak at 530.2 eV is in agreement with the position of the O^{2-} ion in metal oxides (139). The peak at 531.5 eV closely matches assignments for hydroxyl groups ($H\text{-}O^-$) (139) and, also, O adsorbed to Rh (139). The relative amount of the $H\text{-}O^-$ is greater after CO and CO_2 hydrogenation than after oxidation and CO titration. The O XPS signal intensity has been used to determine the stoichiometry of the oxide deposits using sensitivity factors given in (139). The stoichiometry determined from the ratio of the O/M XPS intensity and from the oxidation states is in good agreement for titanium oxide; however, for the other oxides the relative oxygen content obtained using the sensitivity factors is greater than that expected given the observed oxidation states. For example, the stoichiometry of tungsten oxide after oxidation is determined to be $WO_{6.1}$ using sensitivity factors while using oxidation states the stoichiometry is $WO_{2.5}$. One difficulty in using sensitivity factors to determine stoichiometry is that a homogeneous distribution of the components is assumed (83) (see 7.3.1), and the reason for the over estimation of the oxygen content may be due to a preferential distribution of oxygen in the outer most surface layer of the oxide deposit relative to the metal cation.

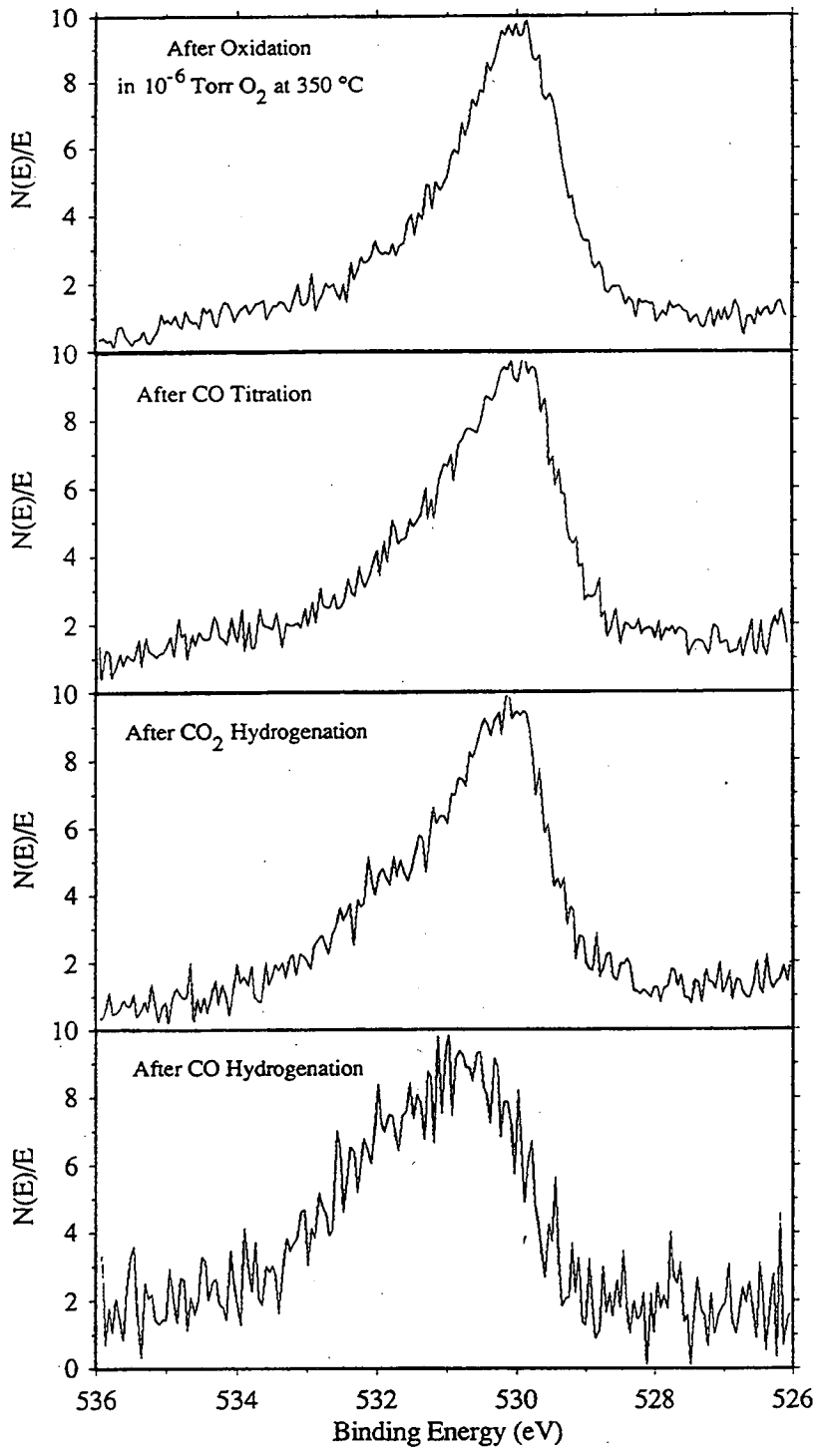

Figure 7.7: XPS spectra of the O (1s) region for a 0.5 ML titanium oxide deposit on Rh foil measured after oxidation, CO titration, CO_2 hydrogenation, and CO hydrogenation.

7.3.9 Carbon

The C 1s XPS region was monitored for each of the oxide deposits after oxidation in 10^{-6} Torr O_2 at 350 °C, CO titration, CO_2 hydrogenation, and CO hydrogenation. The amount of C XPS signal is negligible after oxidation and CO titration compared to that observed after CO_2 and CO hydrogenation. The spectra of the C region after CO_2 and CO hydrogenation for a 0.5 ML of titanium oxide on Rh foil is shown in Fig. 7.8. Only a single peak is resolved in each XPS spectrum. The position of the C XPS peak is 284.65 eV after CO_2 hydrogenation and 284.35 eV after CO hydrogenation. The two XPS spectra are similar except that the total C XPS intensity measured after CO hydrogenation is 3.1 times greater than that found after CO_2 hydrogenation. For each of the oxides, the C XPS intensity is greater after CO hydrogenation. ISS measurements taken after each reaction indicate that the carbon deposit fully covers the outer most layer of the sample. Consequently in order to reduce the underlying oxide, hydrogen must diffuse through a carbonaceous layer which is more extensive during CO hydrogenation than during CO_2 hydrogenation. This may be a factor which leads to the observation of a more reduced oxide overlayer after CO_2 hydrogenation than after CO hydrogenation for titanium, niobium, and tantalum oxides (see Fig. 7.1, 7.4, and 7.5). The 0.3 eV greater binding energy for the peak measured after CO_2 hydrogenation is consistent with the presence of a more hydrogenated carbonaceous layer (139).

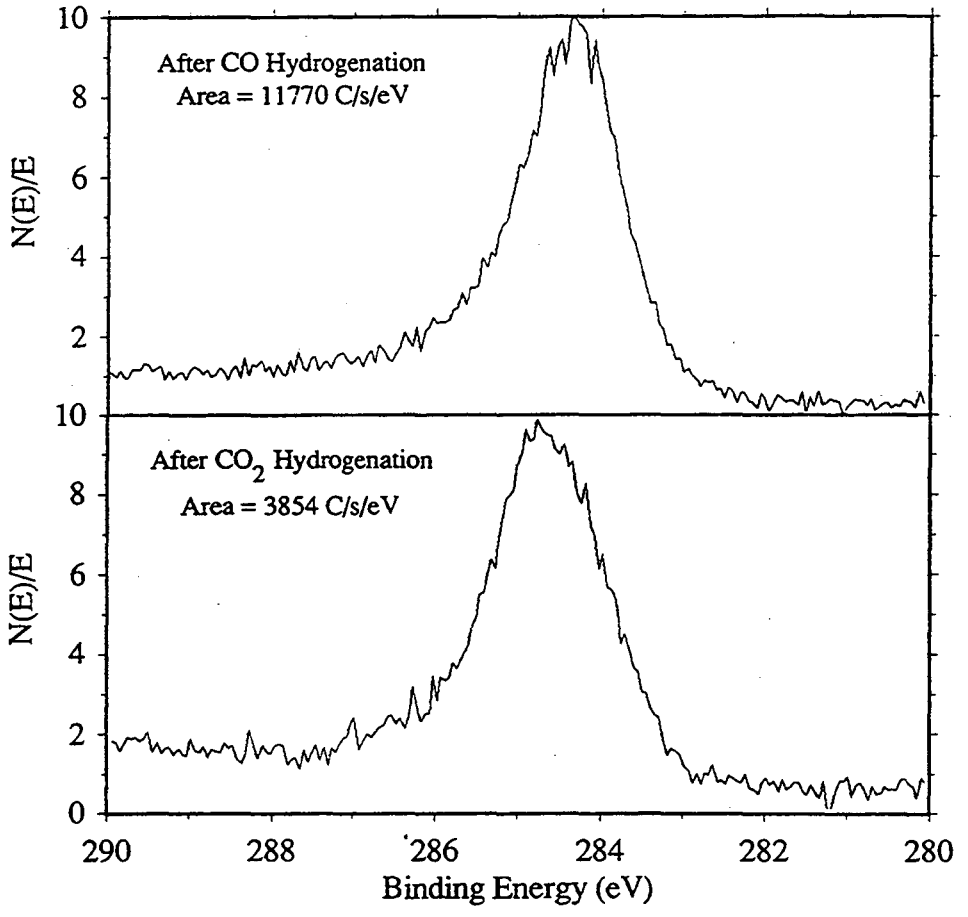

Figure 7.8: XPS spectra of the C (1s) region for a 0.5 ML titanium oxide deposit on Rh foil measured after CO hydrogenation, and CO_2 hydrogenation.

7.4 Discussion

The Rh substrate has been shown to influence the redox properties of the oxide deposits. Based on the Gibbs free energy of formation, the oxide phases expected to be observed after oxidation in 10^{-6} Torr O_2 are TiO_2 (889.5 kJ/mol), ZrO_2 (1037 kJ/mol), Ta_2O_5 (1912 kJ/mol), Nb_2O_5 (1905 kJ/mol), WO_3 (763.6 kJ/mol) and Fe_2O_3 (740.6 kJ/mol) (from ref. (183) at 298 K); however, for each of these oxides deposited on Rh foil, a partially reduced phase is found. Stable alloys are known to form between early transition metals such as Zr, Ti, Nb, and Ta and late transition metals such as Rh and Pt. The stability of these alloys, referred to as Engel - Brewer alloys, is attributed to overlap of filled orbitals of Pt and Rh metals with empty orbitals of Ti or Zr. Infinite dilution parameters (log (activity coefficient)), which give a measure of the strength of the isolated Rh-M bond, are -8.3 (Nb-Rh), -10.2 (Ti-Rh) and -12.7 (Zr - Rh), and Gibbs free energy of formation in kJ/gatom for some Rh and Pt alloys are -57 ($TiRh_3$), -75 ($TiPt_3$), -96 ($ZrPt_3$), -46 ($NbRh_3$) (184). The favorable thermodynamics for bonding between Rh and early transition metals suggests that the interaction between the transition metal oxide overlayer and the Rh substrate may play an important role in determining the chemical state of the oxide deposit. RhMOx (M = Nb, Ta, and W) alloys have been investigated with XPS by Nefedov et al. (162). The binding energies observed for the metal cations in the bulk oxides are of 207.8 eV for Nb (5+), 27.1 eV for Ta (5+), and 36.2 eV for W (6+). However, in the RhMOx alloys, the binding energies of these metal cations are observed to shift to lower values (206.7 eV for $RhNbO_4$, 26.0 eV for $RhTaO_4$, and 35.8 eV for Rh_2WO_6) indicating a decrease in oxidation state, similar to that observed in this work.

The importance of the substrate in determining the redox behavior of oxide deposits is further demonstrated by a study of Levin and coworkers (77). These authors investigated titania deposits on both Rh and Au substrates using XPS. For titania on Rh,

non - stoichiometric forms of the oxide were observed similar to those found in this study; however, when deposited on the Au substrate, stoichiometric TiO_2 was observed in agreement with predictions based on thermodynamic data of the bulk oxide.

Experimental evidence for direct bonding between a group 8 metal and transition metal oxides have been found by Haller et al. (185), using extended x-ray absorption fine structure spectroscopy (EXAFS) to investigate a hydrogen reduced TiO_2 supported Rh catalyst. These authors found a Rh-Ti bond distance of 2.53 - 2.56 Å which is within 0.12 Å of the 2.68 Å Rh-Ti bond in intermetallic compounds. Other investigators have also reported evidence for direct metal-metal interaction in transition metal oxide / Group 8 metal systems (186-189).

These considerations lead to the conclusion that the Rh foil substrate can stabilize reduced phases of the oxide deposits and that the driving force for reaction between the transition metal oxide and the Rh is a direct metal-metal bonding interaction similar to that found in Rh / M (M = Ti, Ta, Nb, W, and Zr) alloys.

Chapter 8

Promotion of Rh Foil Catalytic Activity by Deposits of Transition Metal Oxides

Abstract

Promotion by sub - monolayer quantities of metal oxides has been determined for CO hydrogenation and CO_2 hydrogenation over Rh foils. The metal oxides investigated include AlOx, TiOx, VOx, FeOx, ZrOx, NbOx, TaOx, and WOx. The coverage at which maximum rate enhancement occurs is approximately 0.5 ML for each oxide promoter. Titanium, niobium, and tantalum oxides are the most effective promoters and are found by XPS measurement to be stable in the highest oxidation states during reaction. The trend among the oxide promoters is attributed to the direct relationship between oxidation state and Lewis acidity. Bonding at the metal oxide / metal interface between the O - end of adsorbed CO and the Lewis acidic oxide is postulated to facilitate C - O bond dissociation and subsequent hydrogenation.

8.1 Introduction

Transition metal oxides have been found to dramatically alter the catalytic behavior of Group VIII metals (5-11). For Rh catalysts, oxide promoters can induce increases in overall conversion of several orders of magnitude for reactions involving hydrogenation of polar molecules such as CO, CO_2, and NO (11,33-37). Several explanations for oxide promotion have been introduced. Burch and Flambard (51) suggested that the active sites in the oxide promoted catalysts are located at the metal / metal oxide interface. Sachtler, Ichikawa and coworkers (55,56) extended this proposal by suggesting that a Lewis acid / base bonding interaction occurs between the oxygen end of the adsorbed CO and the oxide promoter at the oxide / metal interface.

The majority of investigations of oxide promotion have been performed using metals dispersed on high surface area supports. For these systems the amount of oxide promoter coverage is difficult to control. In our research a model catalyst is designed consisting of a Rh substrate on to which known coverages of oxide promoter are deposited. Catalytic activity is related to surface composition and structure using Auger electron spectroscopy (AES), x-ray photoelectron spectroscopy (XPS), ion scattering spectroscopy (ISS), and temperature programmed desorption (TPD). In previous studies, the promotion by titanium oxide of Rh foils was determined for CO hydrogenation (71-73), CO_2 hydrogenation (78,79), acetone hydrogenation (78), ethylene hydroformylation (80), ethylene hydrogenation (81), and ethane hydrogenolysis (81). Titanium oxide was found to enhance the activity of those reactions which involve hydrogenation of C - O bonds (CO hydrogenation, CO_2 hydrogenation, acetone hydrogenation, and ethylene hydroformylation). The maximum rate enhancement occurred at oxide coverages of 0.5 ML for each reaction.

In this chapter the study of oxide promotion of Rh foils is extended to include zirconium, iron, niobium, tantalum, and tungsten oxides. For each oxide maximum promotion is observed at approximately 0.5 ML. This coverage is identified with the maximum in number of oxide / metal interface sites. The oxides are found to promote CO_2 hydrogenation to a greater extent than CO hydrogenation. This is attributed to inhibition by the 3 to 4 times greater carbon deposit which is present during CO hydrogenation. The oxides which are found to be the most effective promoters (TiOx, TaOx, and NbOx) are stable in the highest oxidation states during reaction. The oxidation state is related to Lewis acidity using calculated electronegativities. Based on comparison with analogous organometallic compounds, a bonding configuration for adsorbed CO at the metal oxide / metal interface is proposed in which the C - end is bound to Rh and the O - end to the Lewis acidic oxide. This bonding is postulated to facilitate C - O bond dissociation and subsequent hydrogenation.

8.2 Experimental

Experiments were performed in a Varian UHV chamber equipped with a cylindrical mirror analyzer for AES, an EAI quadropole mass spectrometer, and an atmospheric-pressure isolation cell. Additional characterization of the catalyst samples were carried out in a PHI 5300 ESCA system equipped for x-ray photoelectron spectroscopy and ion scattering spectroscopy. The PHI 5300 ESCA was also equipped with an atmospheric-pressure isolation cell.

The Varian UHV chamber is evacuated by an oil diffusion pump and titanium sublimation pump to achieve a base pressure of 1×10^{-9} Torr. The sample, 1 cm^2 Rh polycrystalline foil 0.002-in thick, is attached to a manipulator through spot welds to

0.020-in gold support wires. An K type thermocouple is spot welded to the foil for temperature measurement. Prior to initiating a reaction, the foil is cleaned by high temperature annealing and sputtering to remove B, S contamination.

Metals were deposited on the Rh surface using an evaporator. The filaments used in the evaporator consisted of either a 0.020 to 0.040-in wire of the metal to be deposited in the case of W, Ta, Nb, and Zr or a 0.005 to 0.020-in wire of the metal to be deposited wound around 0.040-in W wire in the case of Ti, V, Fe, and Al. Currents of between 20 and 40 amps were necessary to give a deposition rates of approximately 1.0 ML/min, depending on the vapor pressure characteristics of the metal. A back pressure of 2×10^{-7} Torr of oxygen was present during evaporation in order to reduce carbon contamination. After metal deposition, the surface was oxidized at 1×10^{-6} Torr of O_2 at 350 °C for 5 min. To remove oxygen adsorbed on the exposed Rh surface, 2×10^{-7} Torr of CO was admitted into the chamber for 20 s, and the sample was then flashed to 400 °C. After preparation, an Auger spectrum was taken to determine the oxide coverage and to confirm the sample cleanliness. The bare Rh surface was given the same gas exposures before reaction to eliminate the possibility of ascribing rate enhancements to pretreatment effects. When necessary, the deposited oxide was removed by sputtering and annealing.

To perform a reaction, the sample was enclosed in a high-pressure cell, connected to a gas recirculation loop. The total volume of the reactor and recycle loop is 120 cm^3. H_2 and CO, or CO_2, purified through a trap maintained at 150K, were introduced into the loop, and argon was added when necessary to give a total pressure of 760 Torr. A metal-bellows pump was used to recirculate the gases at a flow rate of approximately 100 cm^3/min. The accumulation of reaction products in the loop was monitored with an HP 5890 II gas chromatograph equipped with an FID. A stainless steel 10 - ft. x 1/8 in column packed with 80/120 Carbopak B coated with 3% SP1500 was used for product

separation. All reactions were run at conversions of less than 5%. After reaction, approximately 10 min were required to return the UHV chamber to its base pressure.

The PHI ESCA 5300 was used for the XPS and ISS studies. It is equipped with a Mg and Al anode x-ray source, an He and Ar differentially pumped ion gun, a hemispherical analyzer, and a sample preparation cell. For XPS, the Mg anode (1253.6 eV) was used, and the hemispherical analyzer detector was operated at a 8.75 eV pass energy. For ISS, an incident beam of He ions at 500 eV was scattered at an angle of 123.0 degrees and detected with the hemispherical analyzer operated at a 179 eV pass energy. Before analysis, catalyst samples were prepared in an adjacent preparation chamber which was maintained at a base pressure of 1×10^{-9} Torr. A transfer rod was employed to move the sample between chambers in vacuo. An electron beam heater and a metal evaporation source were utilized to deposit oxide overlayers on a Rh foil surface in a similar manner as was described above for oxide preparation in the Varian UHV system. For reaction treatments of the surface, an atmospheric-pressure isolation cell was utilized. A transfer rod was employed to move the sample between atmospheric-pressure cell and the analysis chamber in vacuo.

8.3 Results

The coverages of the oxide deposits have been determined by measuring the oxide and Rh substrate AES intensities as a function of evaporation time. The breaks observed in the uptake curves are assigned to oxide coverages of 1.0 ML and used to calculate coverage calibration plots. The assignment of the coverage was confirmed by CO TPD measurements. Since CO does not adsorb appreciably to the oxide deposits, the TPD intensity becomes negligible at oxide coverages greater than 1.0 ML. The coverage

calibration curves, consisting of oxide coverage plotted as a function of Fe(651 eV)/Rh(302 eV) or Zr(113 eV)/Rh(302eV) AES ratios, are shown in Figs. 8.1 and 8.2 for zirconium and iron oxides. CO chemisorption has been used to determine the coverage for niobium, tantalum, and tungsten oxides. The coverage calibration for titanium oxide deposits is given in (76), for aluminum oxide in (73), and for vanadium oxide in Chapter 6. Each oxide exhibited a layer - by - layer growth mode for coverages up to 1.0 ML.

The effect of metal oxide deposits on the rate of methane formation from CO and CO_2 hydrogenation of a Rh foil is shown in Figs. 8.3 and 8.4. (The curves in Figs. 8.3 and 8.4 are added as a visual aid). The data is taken from (71-81) for titanium oxide, from (73) for aluminum oxide, and from Chapter 6 for vanadium oxide. For clean, unpromoted Rh foil, the rate of methane formation is 0.034 s^{-1} for CO hydrogenation at 280 °C in the presence of 253 Torr CO and 506 Torr H_2, and 0.19 s^{-1} for CO_2 hydrogenation at 250 °C in the presence of 190 Torr CO_2 and 570 Torr H_2. For CO hydrogenation, of the oxides studied TaOx has the greatest effect on the Rh foil catalytic activity. Addition of TaOx deposits to the Rh foil increases the rate of methane formation to a maximum of four times that of the clean surface at a coverage of 0.3 ML. As given in Table 8.1 the ordering of the oxides in promotion of CO hydrogenation from greatest to least is TaOx (3.9x), TiOx (3.0x), NbOx (2.5x), VOx (2.1x), WOx (2.1x), FeOx (1.7x), and AlOx (none). The increase observed in selectivity for higher weight hydrocarbons has the same ranking as the effect on rate of methane formation. The coverages at which the maximum rate enhancements are observed ranges between 0.3 and 0.5 ML. For coverages greater than 1.0 ML, the rate of methane formation decreases to less than that of the clean surface for all of the oxides except FeOx. The rate with deposits of FeOx increases to a plateau at approximately 2.0 ML where the rate, selectivity, and deactivation characteristics are similar to those observed over Fe foil (190) (see Fig. 8.5). (The curve in Fig. 8.5 is added as a visual aid). For AlOx, the rate

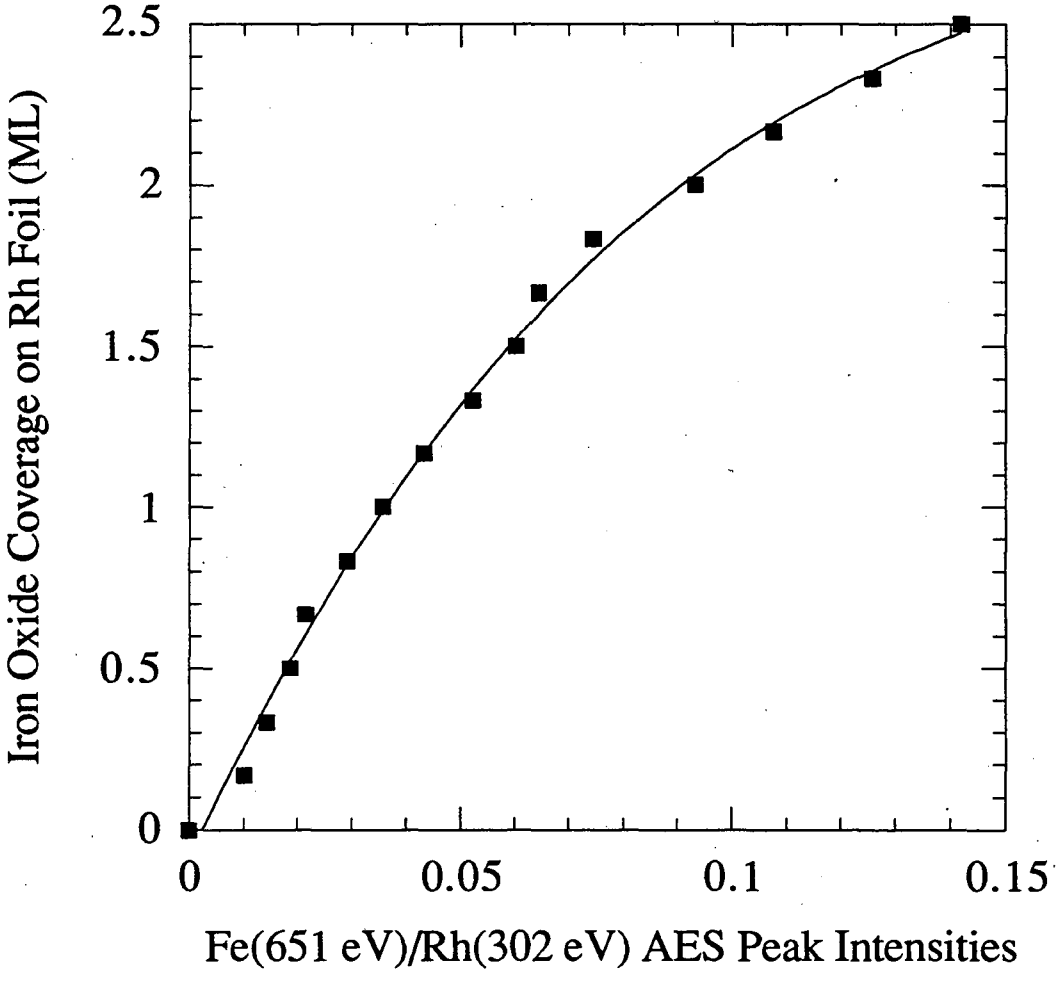

Figure 8.1: Iron oxide coverage on Rh foil plotted as a function of the ratio of Fe(651 eV)/Rh(302 eV) AES peak intensities (r = 0.99).

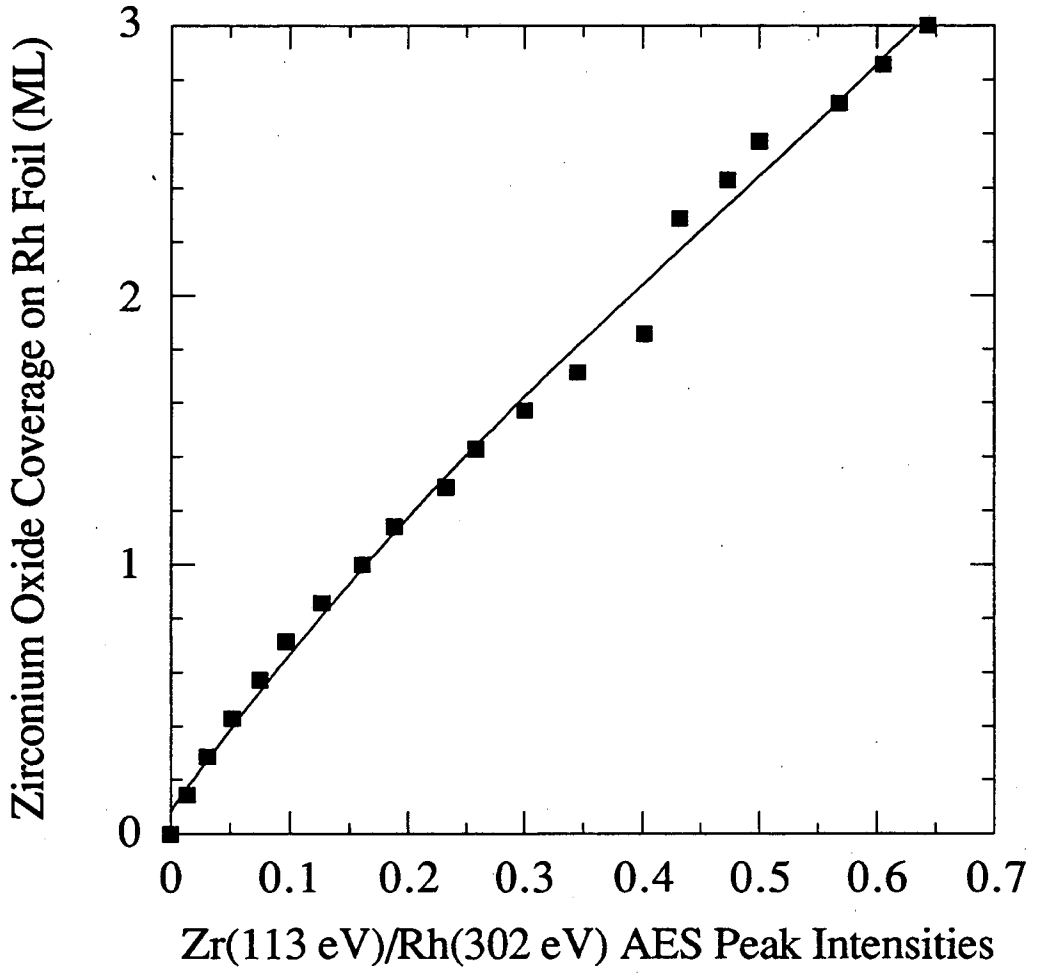

Figure 8.2: Zirconium oxide coverage on Rh foil plotted as a function of the ratio of Zr(113 eV)/Rh(302 eV) AES peak intensities (r = 0.99).

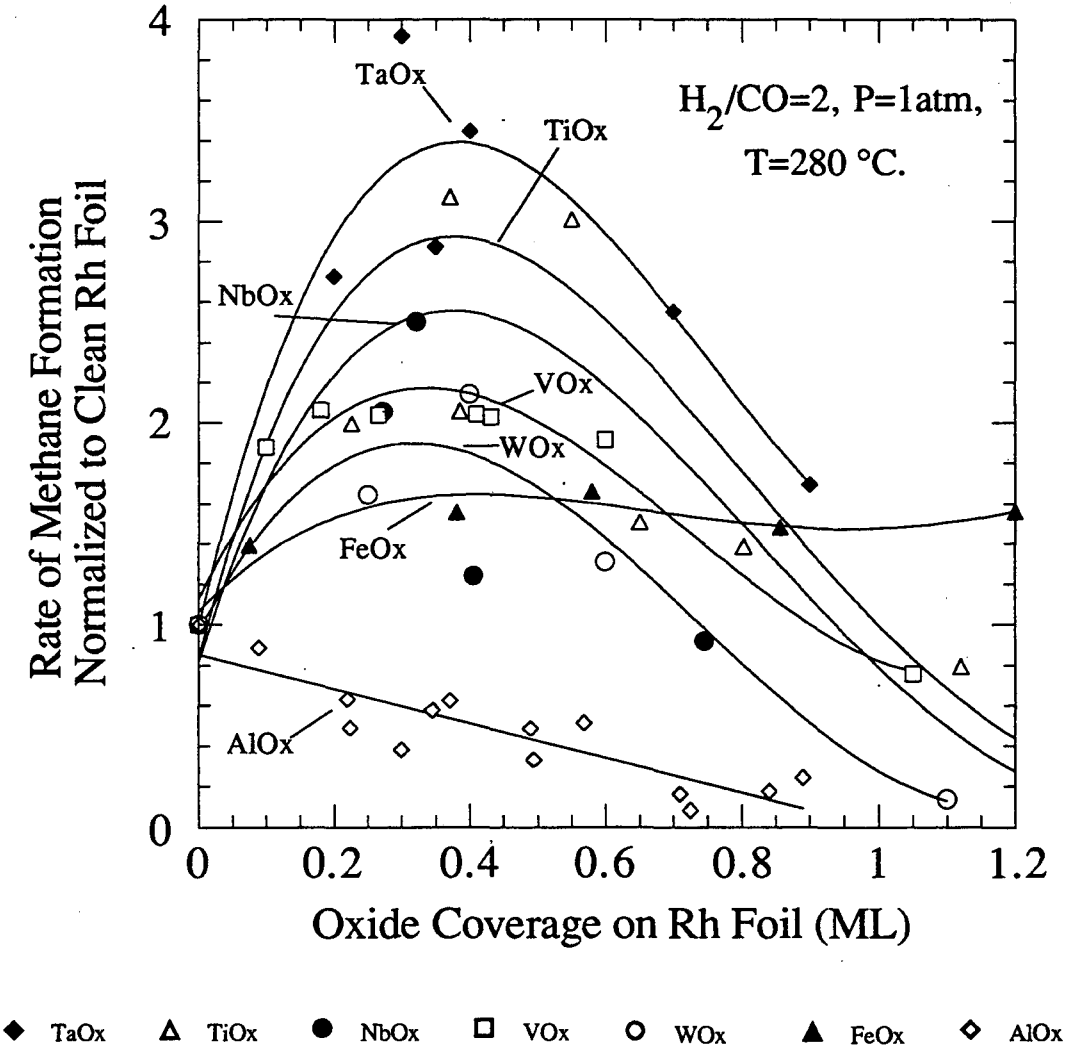

Figure 8.3: Rate of methane formation for CO hydrogenation plotted as a function of oxide coverage on Rh foil.

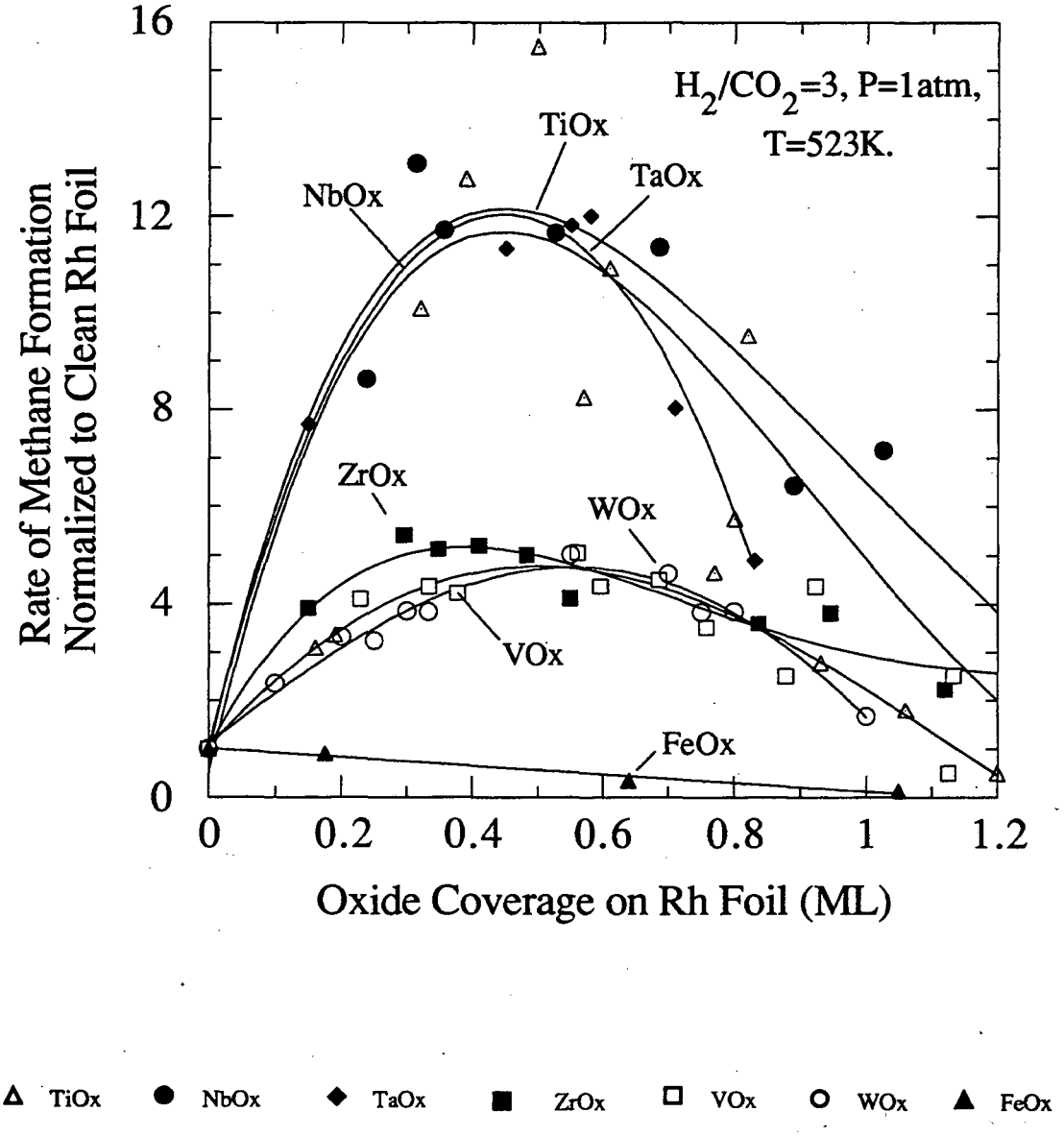

Figure 8.4: Rate of methane formation for CO_2 hydrogenation plotted as a function of oxide coverage on Rh foil.

Table 8.1: Comparison of promotion by 0.5 ML metal oxide deposits on Rh foil.

CO_2 Hydrogenation[1]		CO Hydrogenation[2]	
Oxide	Maximum Rate Enhancement	Oxide	Maximum Rate Enhancement
TiOx	15	TaOx	3.9
NbOx	13	TiOx	3.0
TaOx	12	NbOx	2.5
ZrOx	5.4	-	-
VOx	5.1	VOx	2.1
WOx	5.0	WOx	2.1
FeOx	0.0	FeOx	1.7

[1] H_2/CO_2=3, P=1atm, T=250 °C.

[2] H_2/CO=2, P=1atm, T=280 °C.

of methane formation decreases linearly with the amount deposited, indicating a geometric site blockage of the Rh catalytic sites.

For CO_2 hydrogenation the ordering of the oxides by effect on the rate of methane formation from greatest to least is TiOx (15x), NbOx (13x), TaOx (12x), ZrOx (5.4x), VOx (5.1x), WOx (5.0x), FeOx (none) (see Table 8.1). The extent of promotion is greater for CO_2 hydrogenation than for CO hydrogenation for all the oxides except FeOx. The oxide coverages at which the maximum rate enhancement is observed are between 0.4 and 0.6 ML, which is 0.1 to 0.2 ML greater than the coverage at maximum rate enhancement for CO hydrogenation. For coverages greater than 1.0 ML, the rate decreases to below that of the clean surface for all of the oxides except FeOx. A plateau in the rate of CO_2 hydrogenation for which the catalytic behavior is similar to that of Fe foil (190) is observed at a coverage of approximately 3.0 ML for multilayer deposits of FeOx on Rh foil (see Fig. 8.6). (The curve in Fig. 8.6 is added as a visual aid).

To determine the valence and stoichiometry of the metal oxide films, XPS measurements have been taken of the surface as prepared both before and after CO and CO_2 hydrogenation for coverages ranging up to 2.0 ML. The details of the XPS measurements, including spectra and oxidation state assignments, have been presented in Chapter 7. The average oxidation state measured of the oxide deposit prepared by oxidation with $1x10^{-6}$ Torr O_2 at 350 °C for 5 min before reaction compared with that measured after CO hydrogenation at 280 °C in the presence of 253 Torr CO and 506 Torr H_2 is shown in Fig. 8.7 for oxide coverages of 0.5 ML. For TaOx, NbOx, and TiOx the average oxidation state after CO hydrogenation increases compared to the valence state measured after oxidation in 10^{-6} Torr O_2, while for VOx, WOx, and FeOx the average oxidation state decreases after reaction. The oxidation state of aluminum oxide remains constant at the value of stoichiometric Al_2O_3 (3.0) before and after reaction. The ordering of the oxides in average oxidation state after CO hydrogenation from highest to

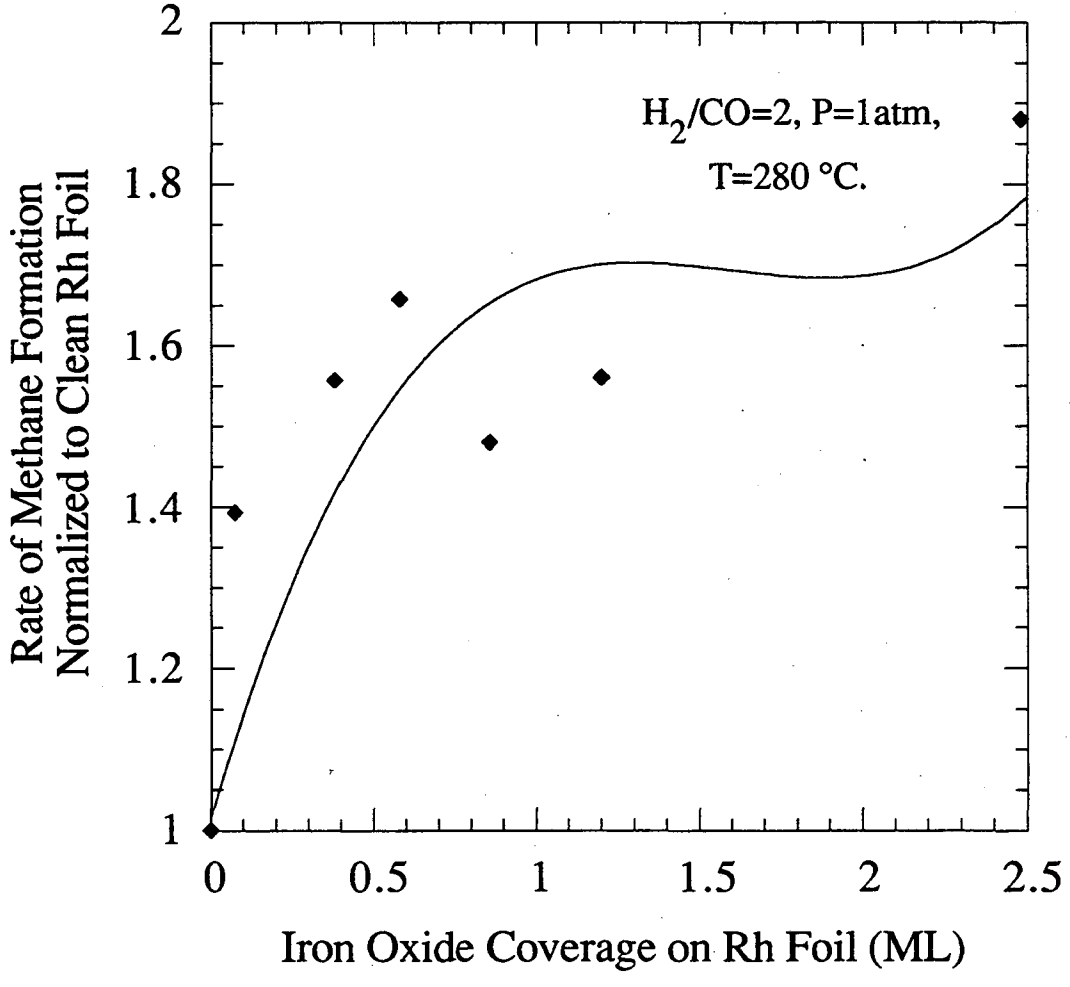

Figure 8.5: Rate of methane formation for CO hydrogenation plotted as a function of iron oxide coverage on Rh foil.

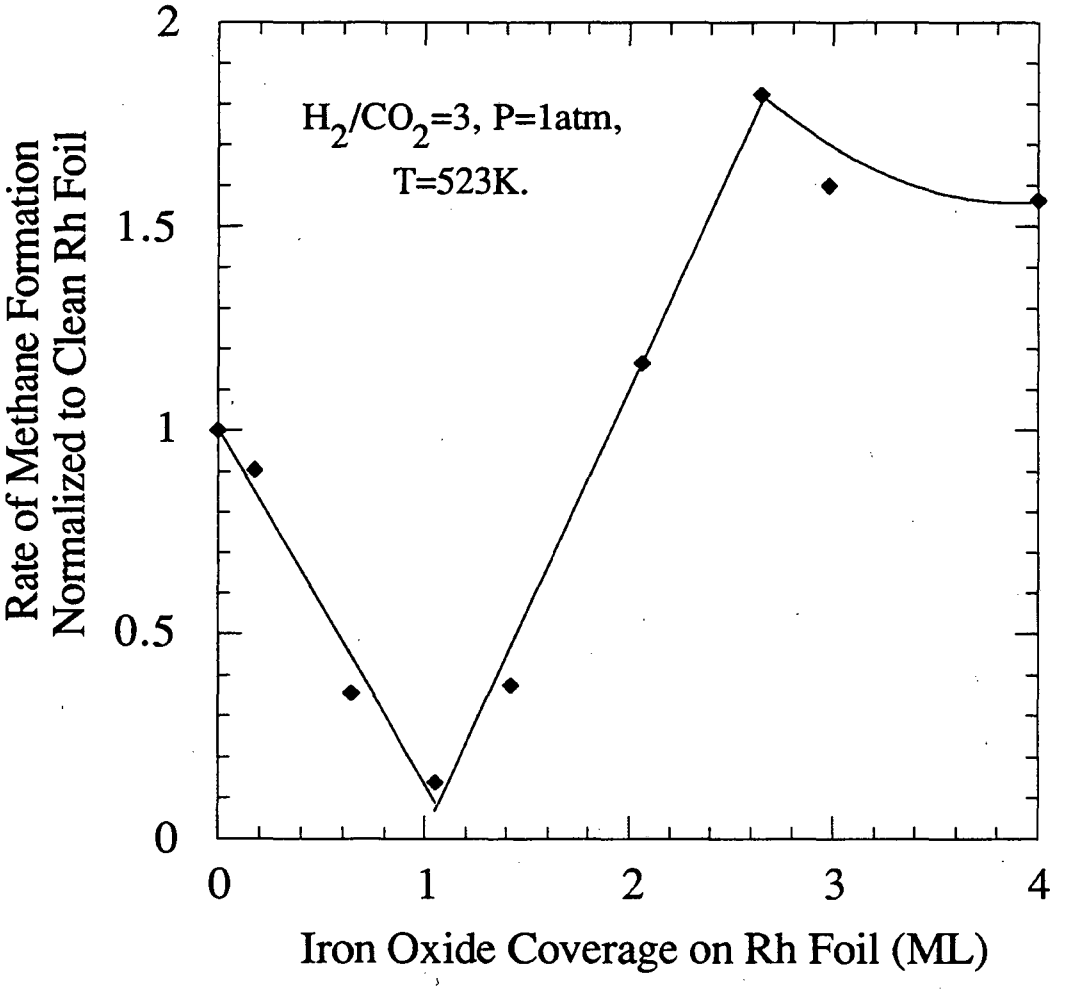

Figure 8.6: Rate of methane formation for CO_2 hydrogenation plotted as a function of iron oxide coverage on Rh foil.

lowest is TaOx, NbOx, TiOx, AlOx, VOx, WOx, and FeOx. The average oxidation state of each oxide before reaction (10^{-6} Torr oxidation) and after CO_2 hydrogenation at 250 °C in the presence of 190 Torr CO_2 and 570 Torr H_2 is presented in Fig. 8.8 for 0.5 ML oxide deposits. The average oxidation state after reaction is less than that measured after oxidation in 10^{-6} Torr oxygen for all the oxides except zirconium oxide. The ranking in average oxidation state after CO_2 hydrogenation from highest to lowest is ZrOx, TiOx, TaOx, NbOx, WOx, VOx, and FeOx. Comparing the oxidation states observed after each reaction shows that deposits of TaOx, TiOx, NbOx, and VOx after CO_2 hydrogenation are in reduced oxidation states relative to those found after CO hydrogenation.

The change in oxidation state as a function of oxide coverage has been measured for deposits of titanium oxide. Similar qualitative behavior is observed for the other oxides. Figure 8.9 shows the percentage of reduced Ti^{3+} of the 3+ / 4+ titanium redox pair measured as a function of oxide coverage after oxidation in 10^{-6} Torr O_2 at 350 °C and after exposure of the oxidized surface to 10 L CO followed by a temperature programmed desorption (CO titration). (The curve in Fig. 8.9 is added as a visual aid). After 10^{-6} Torr oxidation, the percentage of Ti^{3+} remains relatively constant at between 5 and 20%. CO titration leads to a reduction in the oxidation state of the titanium oxide overlayer that is highly dependent on coverage. The greatest reduction in oxidation state occurs at low oxide coverages. At 0.2 ML, 65% of the Ti is in the 3+ state after CO titration. However, as the coverage increases to 1.0 ML, CO titration has increasing less effect on the oxidation state of the oxidized overlayer. The coverage dependence of the oxidation state after CO and CO_2 hydrogenation is shown in Fig. 8.10. (The curve in Fig. 8.10 is added as a visual aid). As with CO titration, the overlayer is most reduced at low oxide coverges. The oxidation state of titanium after CO hydrogenation is greater than that found after CO_2 hydrogenation for each coverage investigated.

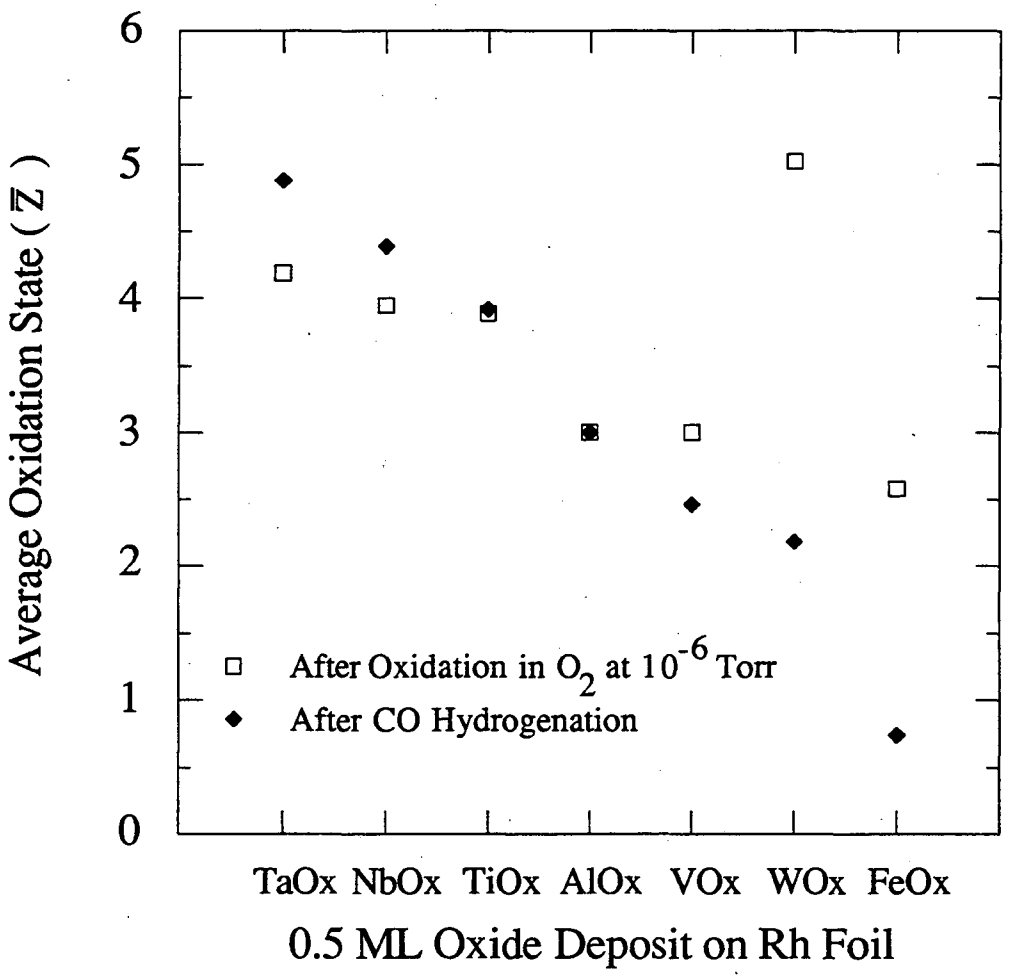

Figure 8.7: The average oxidation state for metal cations of the oxide deposits after $1x10^{-6}$ Torr O_2 at 350 °C for 5 min and after CO hydrogenation at 280 °C in the presence of 253 Torr CO and 506 Torr H_2.

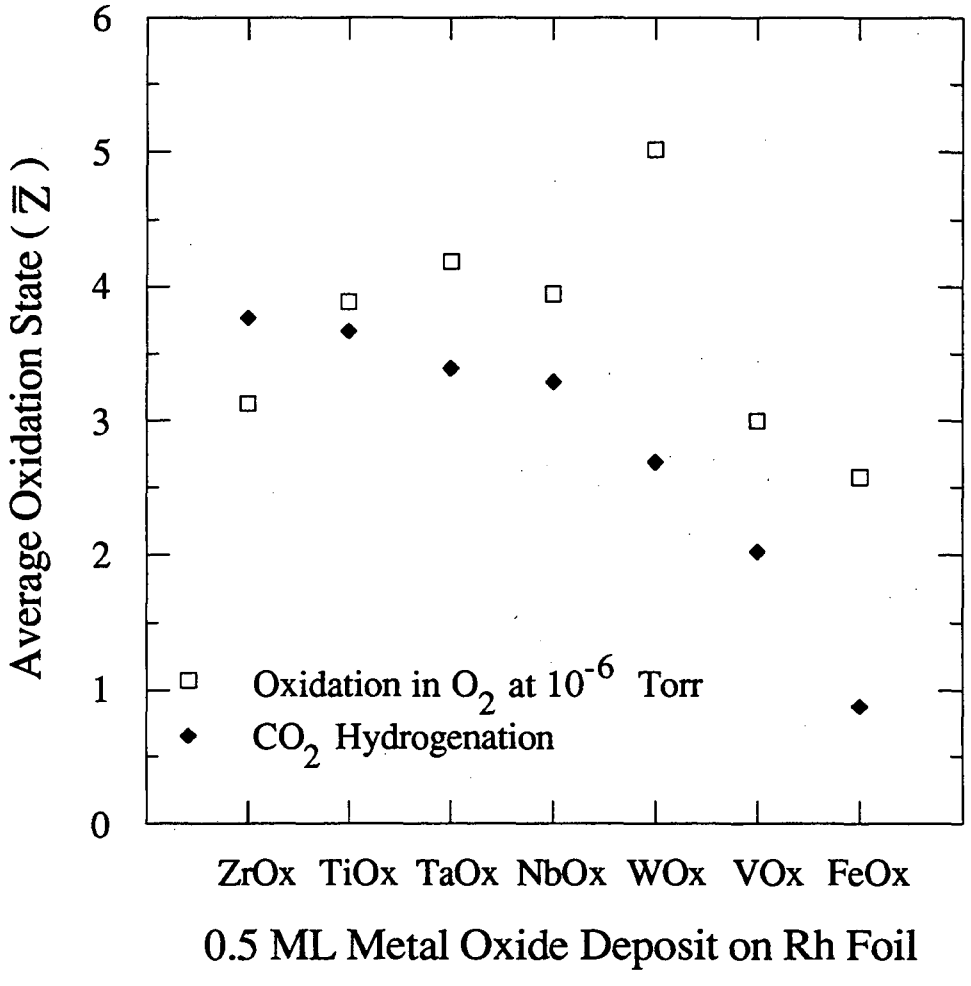

Figure 8.8: The average oxidation state for metal cations of the oxide deposits after $1x10^{-6}$ Torr O_2 at 350 °C for 5 min and after CO_2 hydrogenation at 250 °C in the presence of 190 Torr CO_2 and 570 Torr H_2.

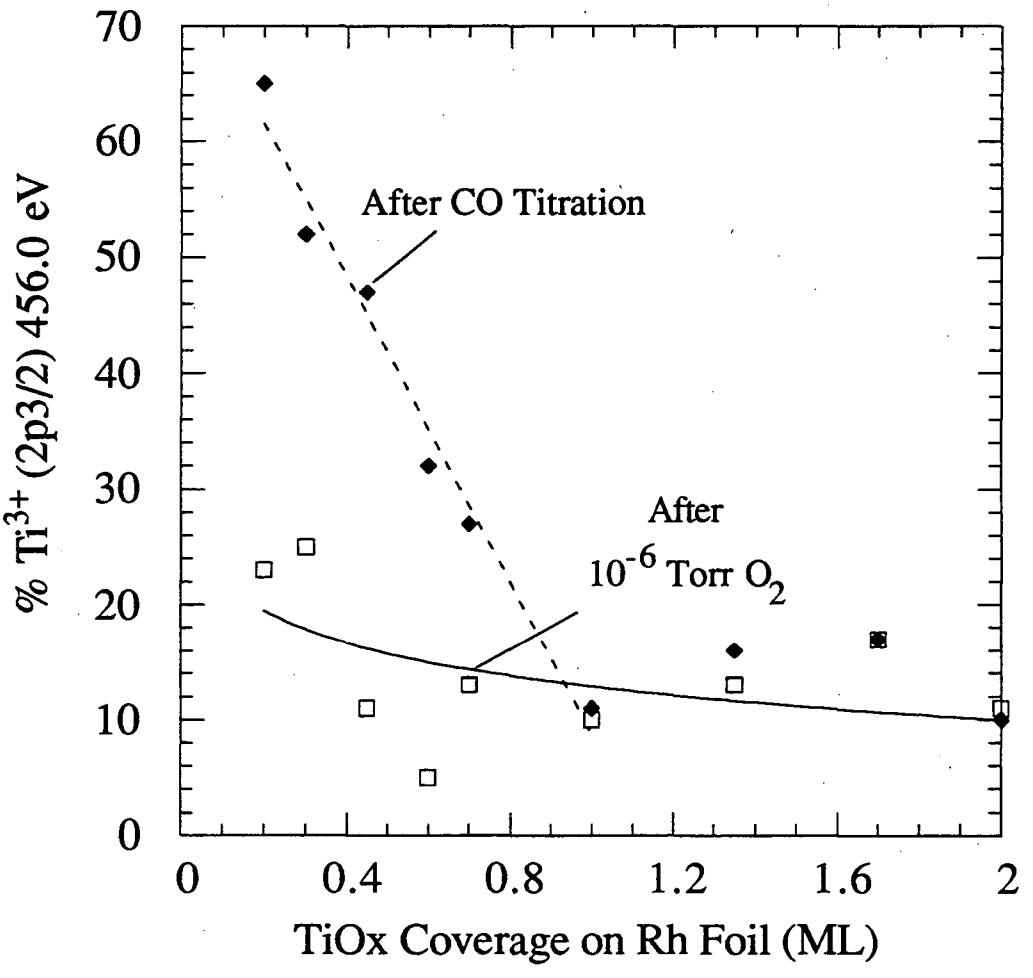

Figure 8.9: The percentage of Ti^{3+} after oxidation in 10^{-6} Torr O_2 at 350 °C and after CO titration plotted as a function of titanium oxide coverage on Rh foil.

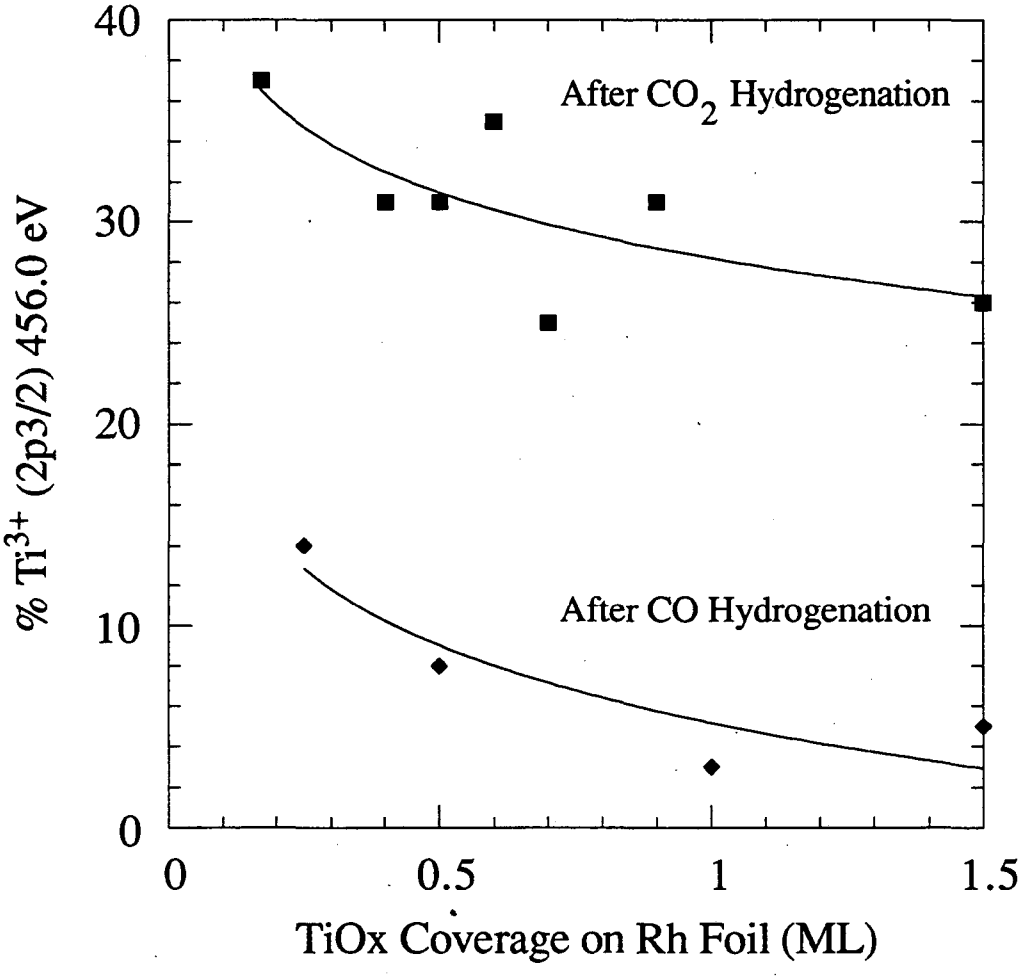

Figure 8.10: The percentage Ti^{3+} after CO and CO_2 hydrogenation plotted as a function of titanium oxide coverage on Rh foil.

8.4 Discussion

The mechanisms of CO and CO_2 hydrogenation over Rh both proceed through a rate determining step involving dissociation of a H_xCO ($x \leq 3$) surface intermediate (43-50). For CO_2 hydrogenation the H_xCO surface species is formed by cleavage of adsorbed CO_2 (33). Several investigators have shown that oxide promoters enhance the rate of C - O bond cleavage. In temperature programmed reduction (TPR) measurements, Sachtler and Ichikawa (43) report the simultaneous production of CH_4 and H_2O while annealing Rh/SiO_2 catalyst with a saturation coverage of CO in the presence of hydrogen. When the sample was promoted with MnOx, again CH_4 and H_2O were produced simultaneously during TPR but at a significantly lower temperature. These observations indicate that the MnOx promotes a rate limiting CO dissociation step for CO hydrogenation over Rh. The rate of CO dissociation has been shown to be enhanced in similar TPD and TPR studies of $VOx/Rh/SiO_2$ (39), Pd/TiO_2 and $TiO_2/Pd/SiO_2$ (44-48), Rh/TiO_2 (49), and $Ni/Ga/SiO_2$ (50).

The reducibility of the support, which has been demonstrated to be an important element leading to altered chemisorption properties after high temperature reduction of Rh catalysts supported on transition metal oxides (5-11), may also play a role in promoting CO dissociation. As a qualitative measure of the reducibility of the oxide deposits, the average oxidation state ($\overline{Z}$) measured after exposure to the reducing reaction conditions was subtracted from the average oxidation state of the film prepared before reaction by oxidation in 10^{-6} Torr O_2 ($\Delta\overline{Z}$). This qualitative measure of reducibility ($\Delta\overline{Z}$) is plotted as a function of change in Gibbs free energy at 298 K (ΔG) (183) for reduction of the most stable form of the bulk oxide to the elemental metal in Fig. 8.11 for CO hydrogenation and Fig. 8.12 for CO_2 hydrogenation. (The curves in Fig. 8.11 and 8.12

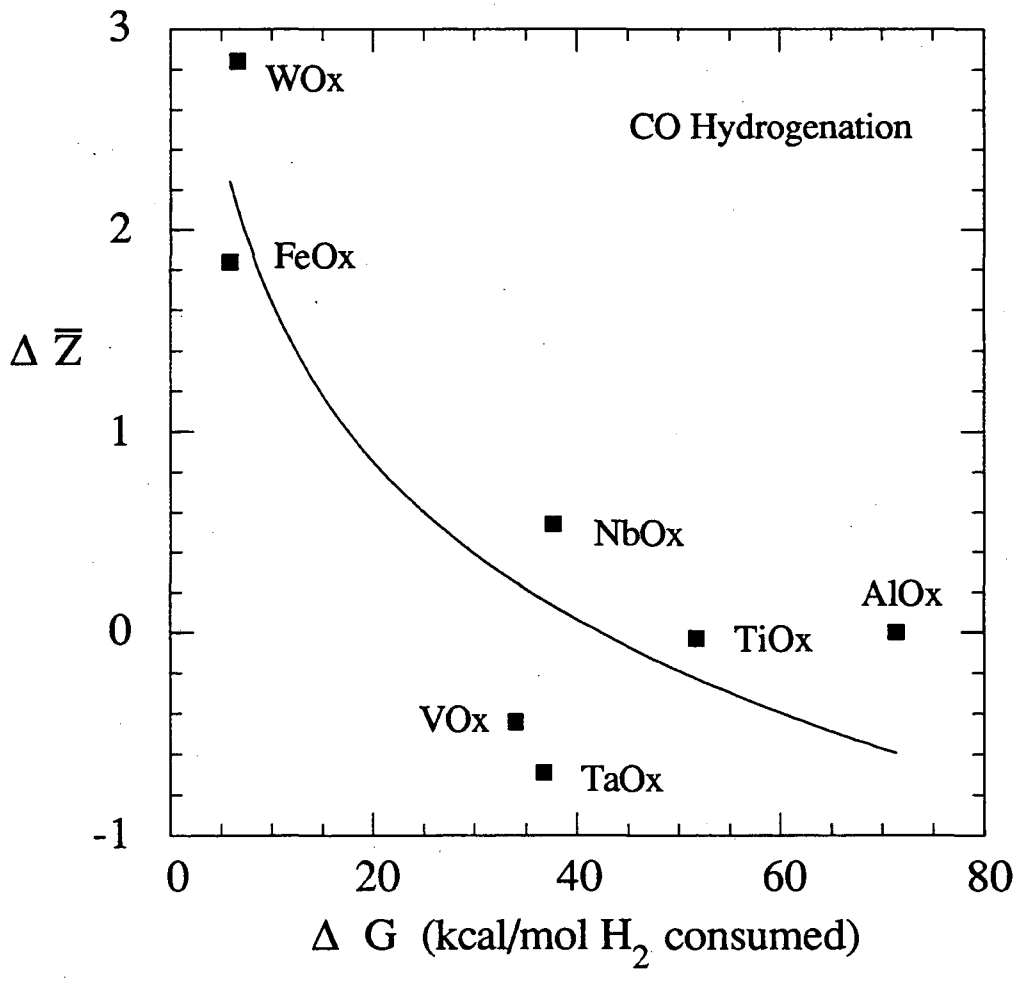

Figure 8.11: Reducibility ($\Delta\bar{Z}$) of 0.5 ML oxide deposits, the average oxidation state ($\bar{Z}$) measured after CO hydrogenation subtracted from the average oxidation state of the film prepared before reaction by oxidation in 10^{-6} Torr O_2 ($\Delta\bar{Z}$), plotted as a function of change in Gibbs free energy (ΔG) for reduction of the most stable form of the bulk oxide to the elemental metal.

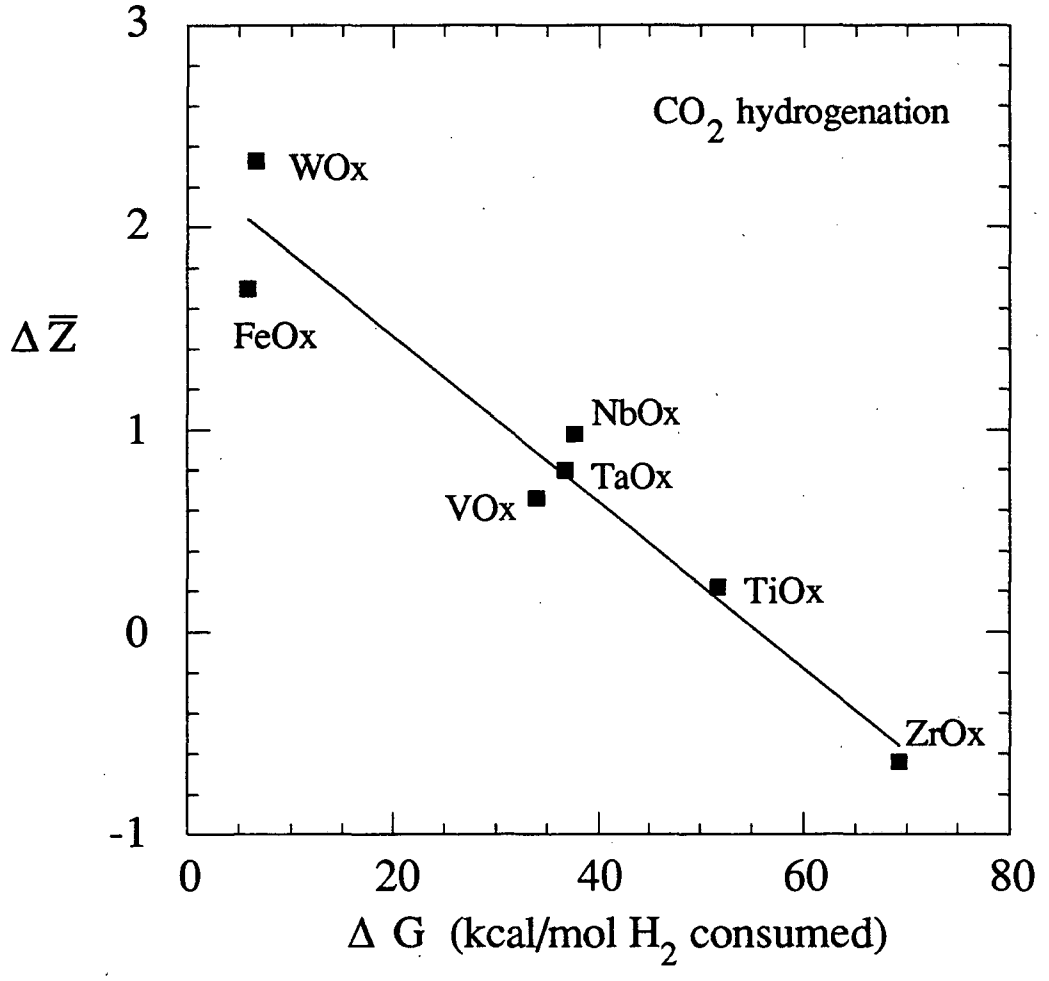

Figure 8.12: Reducibility ($\Delta\bar{Z}$) of 0.5 ML oxide deposits, the average oxidation state ($\bar{Z}$) measured after CO_2 hydrogenation subtracted from the average oxidation state of the film prepared before reaction by oxidation in 10^{-6} Torr O_2 ($\Delta\bar{Z}$), plotted as a function of change in Gibbs free energy (ΔG) for reduction of the most stable form of the bulk oxide to the elemental metal.

are added as a visual aid). The agreement between the qualitative measure of oxide reducibility and the Gibbs free energy change for reduction of the bulk oxide indicates that the difference in oxidation states before and after reaction ($\Delta\overline{Z}$) is a reasonable measure of relative reducibility. The reducibility of the oxide deposit is compared with oxide promotion in Figs. 8.13 and 8.14 for CO and CO_2 hydrogenation, respectively. No correlation between reducibility and rate enhancement is found. Although oxide reducibility is key in development of altered chemisorption properties, Figs. 8.13 and 8.14 clearly demonstrate that it is not the determining factor in oxide promotion.

While rate enhancement by the oxide deposits is not dependent on reducibility, a correlation does exist between the value of average oxidation state and oxide promotion. The trends among the oxides in average oxidation state measured after reaction are identical to the trends of oxide promotion with the exception of AlOx and ZrOx. This is demonstrated in Figs. 8.15 and 8.16 where oxide promotion is plotted as a function of oxidation state for CO and CO_2 hydrogenation, respectively. (The curves in Figs. 8.15 and 8.16 are added as a visual aid). For CO hydrogenation TaOx is stable in the highest oxidation state during reaction and causes the greatest degree of rate enhancement. For CO_2 hydrogenation, TiOx has the next highest oxidation state after ZrOx during reaction and gives the greatest degree of promotion. Iron oxide which is stable in the lowest oxidation state during reaction is the least effective promoter for CO_2 hydrogenation and the second least effective after AlOx for CO hydrogenation.

The XPS measurements show that both AlOx and ZrOx have unusual redox characteristics in comparison to the other oxides investigated. The oxidation state of the aluminum cation of AlOx remains at 3.0 before and after reaction. This is the oxidation state of the stoichiometric Al_2O_3. For each of the other oxides, oxidation states corresponding to non - stoichiometric forms of the oxide are observed. Consequently, the lack of rate enhancement by deposits of aluminum oxide may be attributed to the absence

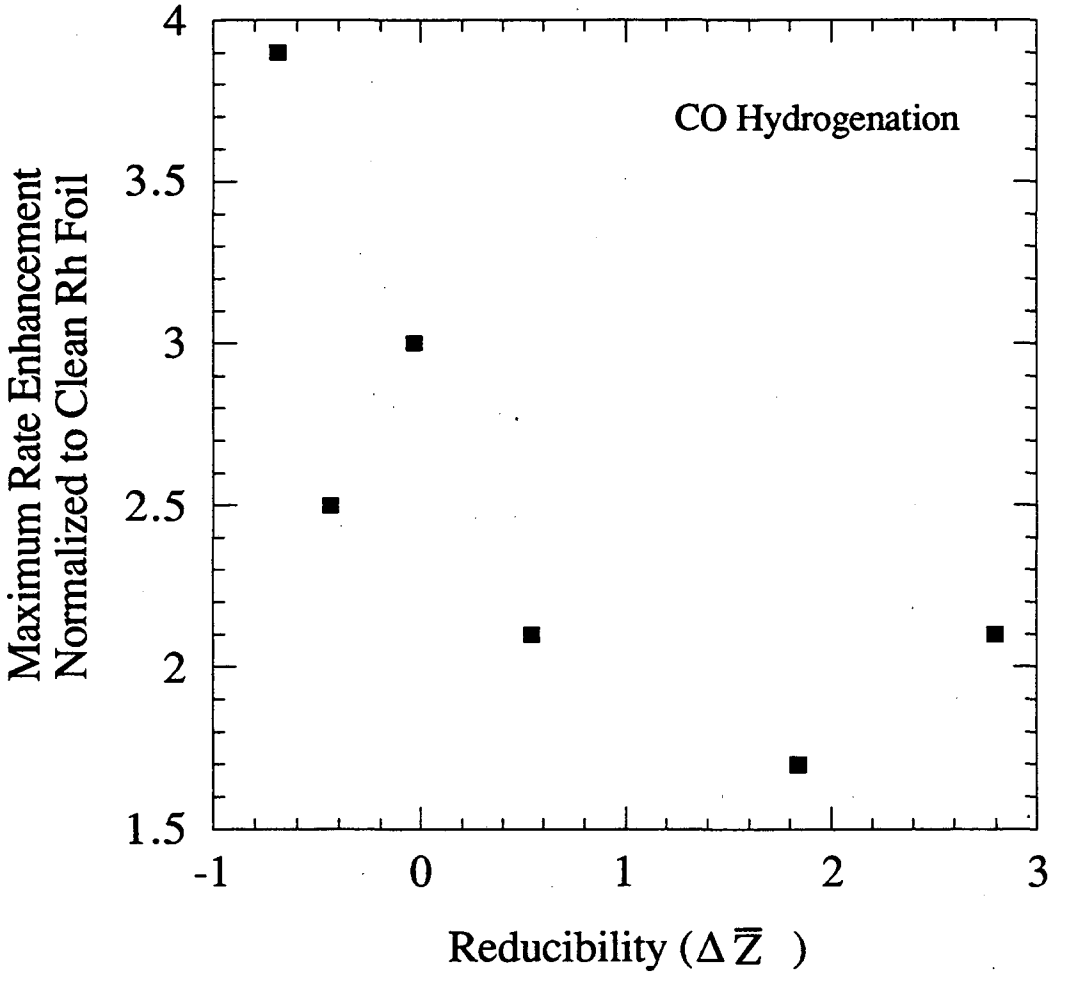

Figure 8.13: Maximum rate enhancement for CO hydrogenation plotted as a function of reducibility ($\Delta\overline{Z}$) for 0.5 ML oxide deposits on Rh foil.

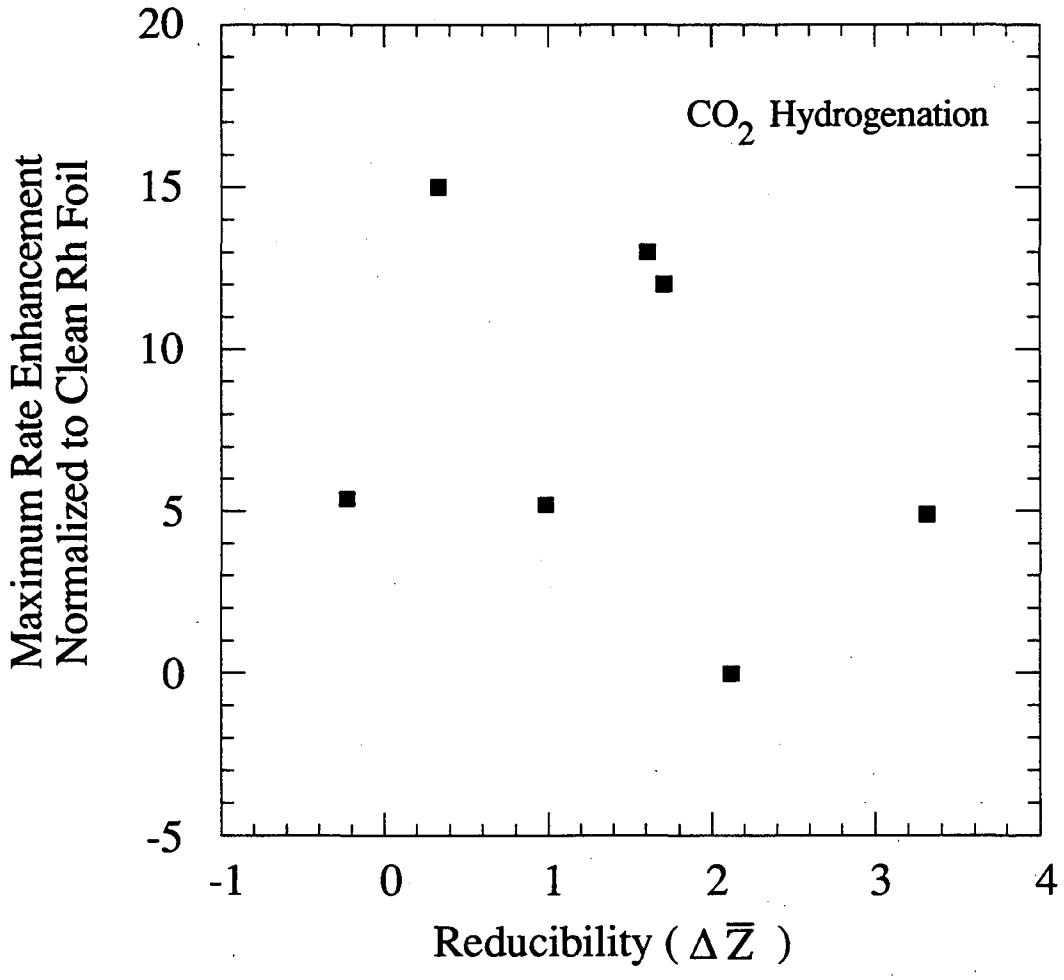

Figure 8.14: Maximum rate enhancement for CO_2 hydrogenation plotted as a function of reducibility ($\Delta\overline{Z}$) for 0.5 ML oxide deposits on Rh foil.

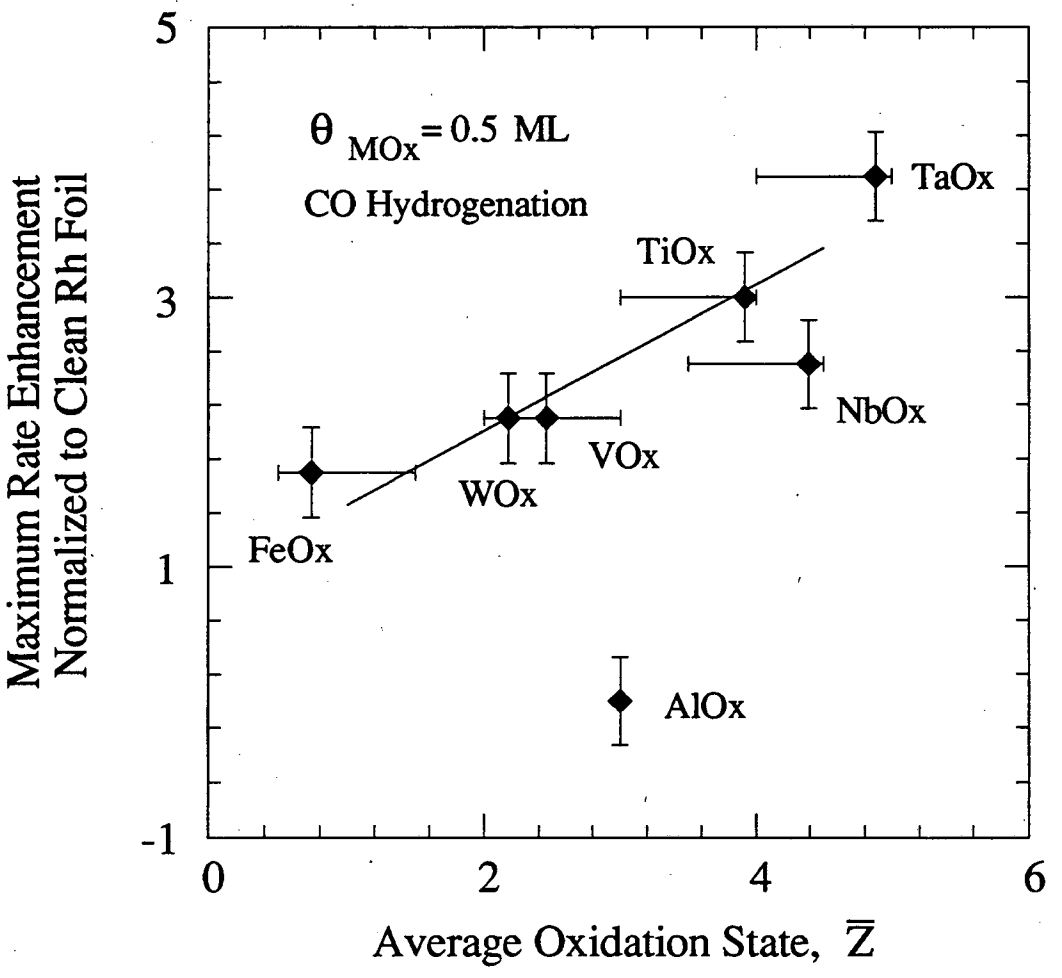

Figure 8.15: Maximum rate enhancement for CO hydrogenation plotted as a function of average oxidation state ($\overline{Z}$) for 0.5 ML oxide deposits on Rh foil.

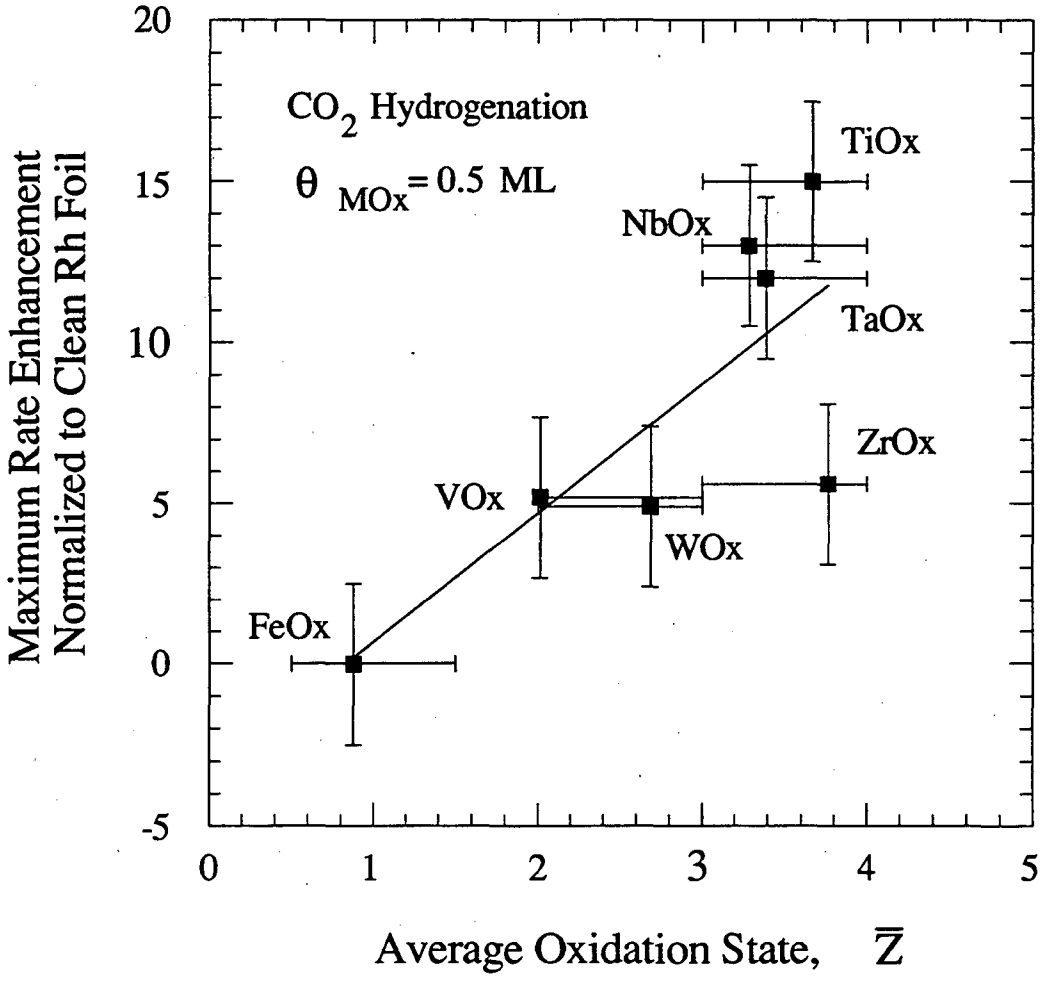

Figure 8.16: Maximum rate enhancement for CO_2 hydrogenation plotted as a function of reducibility ($\overline{Z}$) for 0.5 ML oxide deposits on Rh foil.

of non - stoichiometric defect sites in the oxide overlayer. Zirconium oxide is the only deposit studied in which the average oxidation state measured after CO_2 hydrogenation is greater than that observed after preparation in 10^{-6} Torr O_2 at 350 °C. This behavior is anomalous since CO_2 hydrogenation ($H_2/CO_2 = 3$) is a more reducing environment than 10^{-6} Torr O_2. Early transition metal oxides are known to form strong alloys with late transition metal (29). Of these one of the most stable is the alloy formed between Zr and Rh (29,184). The unusual redox properties of the deposits of ZrOx is likely due to the influence of bonding with the Rh substrate (see Chapter 7).

The study of the model catalyst allows the influence of oxide coverage on the reactivity of Rh foils to be systematically determined. This is a distinct advantage compared to studies of the supported catalyst where the decoration by deposits of oxide promoter of the catalytic metal particles is ill-defined. For each oxide Figs. 8.3 and 8.4 show that the maximum rate enhancement of CO and CO_2 hydrogenation occurs at oxide coverages of approximately 0.5 ML. A computer simulation of oxide island growth has been developed to aid in interpreting the significance of 0.5 ML coverages (74,75). From a given number of randomly selected nucleation sites, the criterion for island growth is nearest neighbor occupancy. The island growth simulation predicts that the percentage of sites located at the oxide / metal interface (or island perimeter) maximizes at a coverage of 0.5 ML, the coverage at which maximum rate enhancement is empirically observed. Thus, the island growth simulation is consistent with the conclusion that the active sites on oxide - promoted Rh surfaces are located at the oxide / metal interface.

The coverage dependence of the Ti oxidation state (% Ti^{3+}) for titanium oxide deposits is show in Fig. 8.9 after CO titration and in Fig. 8.10 after CO and CO_2 hydrogenation. CO titration involves exposure of the surface to 10 L CO at ambient temperature followed by temperature programmed desorption. Since titanium oxide does not adsorb CO, exposure to 10 L CO results in adsorption of CO to only the Rh sites of

the oxide / metal surface. During temperature programmed desorption, reduction of the oxide deposits by CO(a) requires migration of the adsorbate to the oxide / metal interface where reaction with the oxide to form CO_2(g) can occur. This process can be monitored by measuring the change in oxidation state of the oxide with XPS. Because CO(a) is a primary reaction intermediate, a similar mechanism of interaction to that involved in CO titration between the adsorbate and the oxide may occur during CO hydrogenation. In Fig. 8.17 the total XPS intensity of reduced Ti^{3+} formed after CO titration is plotted as a function of oxide coverage. The data in Fig. 8.17 is identical to that in Fig. 8.9 except that total amount of Ti^{3+} is plotted rather than the percentage. The plot in Fig. 8.17 is strikingly similar to those of rate enhancement versus coverage in Figs. 8.3 and 8.4. In each plot, a "volcano" shaped curve has a maximum at a coverage of 0.5 ML. The similar dependence of oxidation state and rate enhancement on oxide coverage supports the proposal that the active sites during CO and CO_2 hydrogenation are located at the oxide / metal interface.

Direct measurement of the oxide morphology has been attempted using scanning tunneling microscopy (STM). Wang et al. (119) investigated sub - monolayer titanium oxide films on a Rh(111) single crystal surface in UHV. Atomic height oxide islands of approximately 20 Å diameter were observed. As the coverage was increased, the density of islands increased while the dimensions of the islands remained approximately constant. As the coverage approached 1.0 ML, the islands began to coalesce particularly at step edges of the Rh substrate. Atomic resolution of the oxide islands could not be obtained; however, smaller scale (100 Å x 100 Å) images revealed the presence of enhanced STM contrast at the oxide island perimeter. This contrast was attributed to an increased electron density at the perimeter of the oxide deposits. An oxide periphery with an enhanced electron density is consistent with a mechanism in which CO(a) interacts with the oxide deposit at the oxide / metal interface and supports the conclusion that the

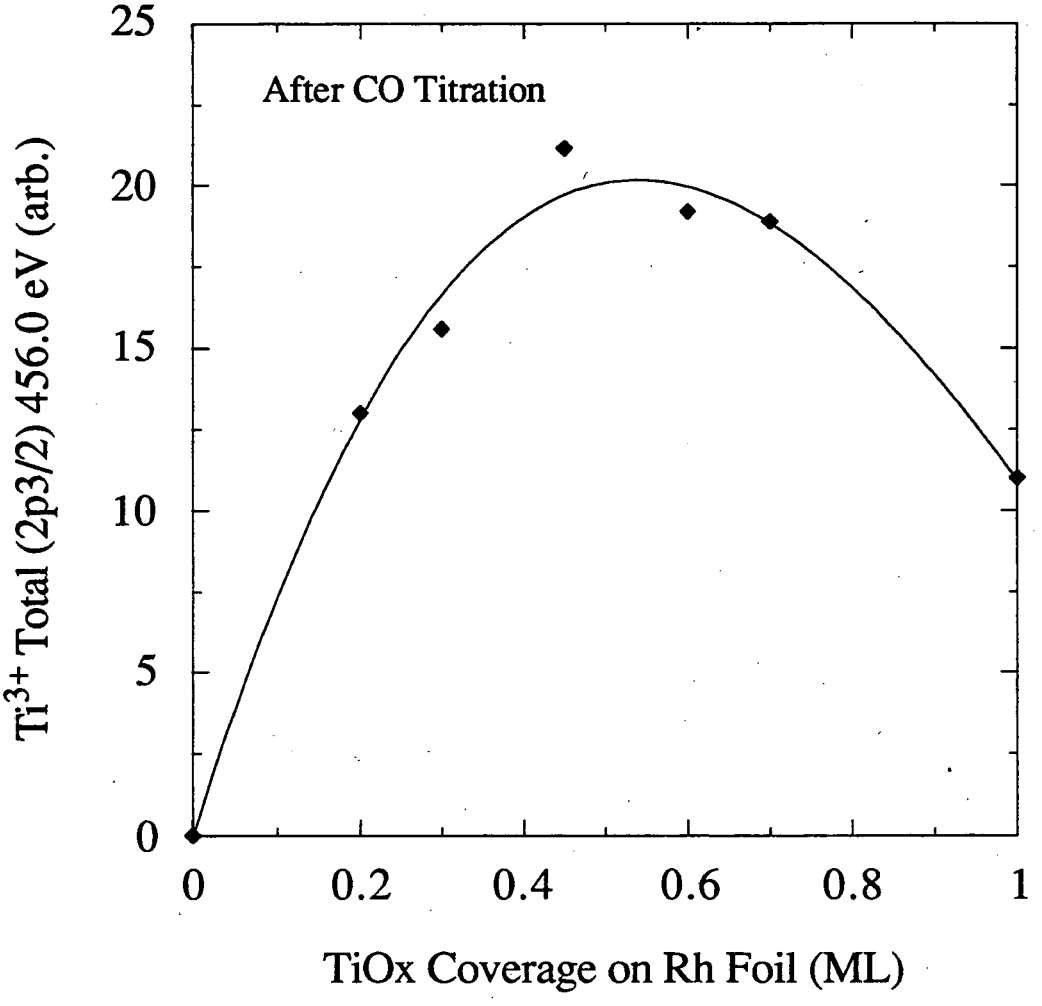

Figure 8.17: Ti^{3+} peak intensity after CO titration plotted as a function of coverage for titanium oxide deposits on Rh foil (r = 0.99).

perimeter of the oxide deposits provides sites with a structural and electronic configuration that leads to promotion of CO and CO_2 hydrogenation.

The primary difference between CO and CO_2 hydrogenation over Rh is the degree of carbon containing surface species present during reaction. The heat of adsorption (ΔH_{ad}) of CO to Rh is 29 - 32 kcal/mol (121-124) while that for CO_2 is significantly less at approximately 6 kcal/mol (79). Consequently, the carbon AES and XPS signal intensities measured after reaction are 3 to 4 times greater for CO hydrogenation than for CO_2 hydrogenation. The difference in the amount of carbon intermediates during reaction has a significant effect on the measured kinetic parameters. The partial pressure dependences and energy of activation for clean and oxide - promoted Rh foil have been measured for CO hydrogenation by Levin et al. (71-73) and for CO_2 hydrogenation by Williams et al (78,79). No change is observed in the kinetic parameters for CO_2 hydrogenation with the addition of titanium oxide to Rh foil. For CO hydrogenation, the CO partial pressure dependence increases from -1.0 to -0.3, the hydrogen partial pressure increases from 1.0 to 2.5, and the energy of activation decreases from 24 to 17 kcal/mol upon the deposition of TiOx to the Rh foil. These changes indicate a modification in the reaction mechanism. Kinetic expressions developed by Williams et al. (78) based on the H_2 and CO partial pressure dependences indicate that promotion of C - O bond dissociation by TiOx results in a shift in the rate limiting step for CO hydrogenation over Rh from CO(a) dissociation to hydrogenation of carbonaceous intermediates ($CH_x(a) + H_{4-x}(a) = CH_4(g)$). This shift in the rate limiting step for CO hydrogenation on the oxide promoted Rh foil results in a decrease in the promotion by TiOx relative to CO_2 hydrogenation for which no change is observed in the partial pressure dependences upon promotion with titanium oxide. These arguments provide a consistent explanation of the differences in promotion of CO and CO_2

hydrogenation which can be extended to explain the qualitatively similar behavior observed for the oxide deposits studied in this work.

Comparing the oxidation states observed after each reaction shows that deposits of TaOx, TiOx, NbOx, and VOx after CO_2 hydrogenation are in a reduced oxidation state relative to those found after CO hydrogenation. This is an apparent contradiction because the reaction mixture during CO_2 hydrogenation is more thermodynamically oxidizing than that during CO hydrogenation. However, during CO hydrogenation a 3 to 4 times greater carbon deposit is present. ISS measurements after CO hydrogenation indicate that the carbonaceous layer forms a contiguous layer which blocks the Rh metal and oxide deposit. The carbon deposit has been shown to limit access of hydrogen to the surface to such an extent that the rate limiting step during CO hydrogenation shifts to addition of H(a) to carbon intermediates (78). This lack of hydrogen at the oxide / metal surface may also kinetically limit the reduction of the oxide during CO hydrogenation.

The trends in oxide promotion match well with the ranking of the oxides in average oxidation measured after reaction as demonstrated in Figs. 8.15 and 8.16. Oxidation state (z) of an ion can be related to the electronegativity of the ion (χ_i) using the Pauling electronegativity of the element (χ_o) (191,192):

$$\chi_i = \chi_o(1 + 2z). \qquad (8.1)$$

The rate enhancement is plotted as a function of the electronegativity of the cation of the oxide in Fig. 8.18 for CO hydrogenation and in Fig. 8.19 for CO_2 hydrogenation. (The curves in Figs. 8.18 and 8.19 are added as a visual aid). Since electronegativity is proportional to Lewis acidity, the strong correlation in Figs. 8.18 and 8.19 between electronegativity and oxide promotion indicates that the important parameter determining rate enhancement by oxide deposits is Lewis acidity. The chemical significance of Lewis

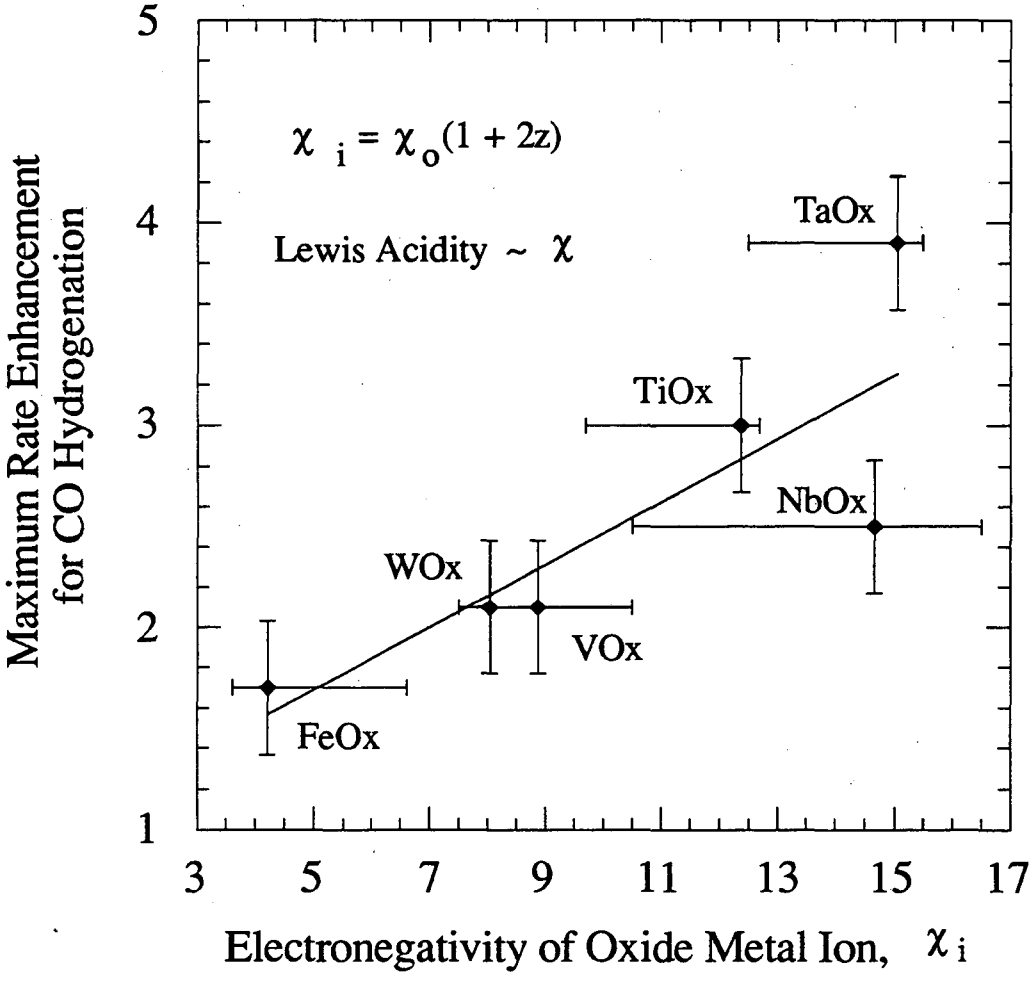

Figure 8.18: Maximum rate enhancement for CO hydrogenation plotted as a function of electronegativity (χ) for 0.5 ML oxide deposits on Rh foil.

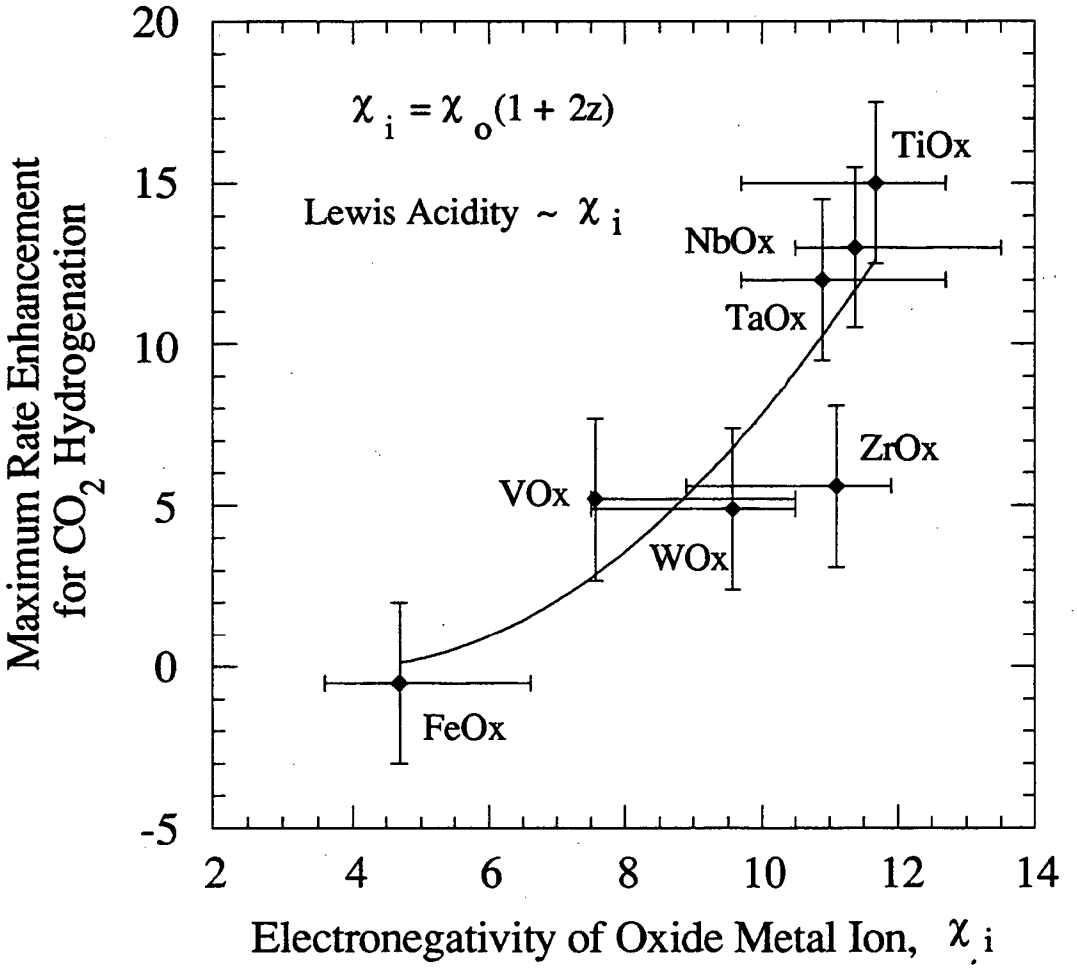

Figure 8.19: Maximum rate enhancement for CO_2 hydrogenation plotted as a function of electronegativity (χ) for 0.5 ML oxide deposits on Rh foil.

acidity in relation to promotion of CO and CO_2 hydrogenation can be better understood by considering C and O bonded carbonyl compounds (56). In these organometallic complexes the carbon-end of the carbonyl is bound to a late transition metal while the oxygen-end is bound to a Lewis acidic, early transition metals in a high oxidation state. The XPS measurements have shown that under reaction conditions the early transition metals titanium, tantalum, and niobium in the sub-monolayer oxide deposits on Rh foil are in high oxidation states. Therefore, a bonding scheme analogous to that observed in the C and O bonding carbonyl compounds would result in the carbon-end of the adsorbed CO bound to the Rh and the oxygen-end bound to the Lewis acidic early transition metal oxide in a high oxidation state. This type of bonding in the C and O bonded carbonyl compounds leads to a significant weakening of the CO bond as indicated by a lowering in CO stretching frequencies of up to 500 cm^{-1} (56). Substantial decreases in the CO stretching frequencies have also been observed in oxide promoted Rh catalysts (50,57-60). This leads to a scheme for promotion that builds upon elements which have been previously proposed by Burch and Flambard (51) and by Sachtler, Ichikawa and coworkers (43,55). In this scheme, adsorbed CO at the oxide / metal interface is bound simultaneously through its carbon-end to Rh and its oxygen-end to the Lewis acidic oxide stable in a high oxidation state. The bonding at the oxide / metal interface leads to a weakening of the CO bond which facilitates its dissociation and hydrogenation. The strength of the bonding at the interface depends on the Lewis acidity of the oxide which is determined by the oxidation state of the oxide base metal.

Chapter 9

Conclusions

9.1 Summary

The surface chemistry and catalytic properties of transition metal oxides deposited on Rh and Pt substrates have been investigated for coverages ranging from sub - monolayer to 5 ML. The oxide overlayers were prepared by evaporation and subsequent oxidation in an ultra - high vacuum environment and analyzed using the techniques of surface science (AES, TPD, XPS, ISS, and LEED). The influence of the oxide films on the CO and CO_2 hydrogenation activity of Rh and Pt foils was measured by enclosing the sample within an atmospheric reaction cell.

Titanium oxide films on Pt(111) form two ordered structures as observed with LEED and STM. The structure found after annealing in 1 x 10^{-6} Torr O_2 at temperatures ranging from 500 °C to 700 °C exhibits three - fold symmetry with a unit cell of 18.2 Å x 18.2 Å. XPS measurements indicate a TiO_2 stoichiometry. The three - fold symmetry of this titanium oxide film is similar to the (111) surface plane of nearly close - packed O^- ions

in rutile. After annealing in vacuum from 650 °C to 850 °C, the titanium oxide film forms a structure with a unit cell of 18.2 Å x 13.9 Å and a stoichiometry determined by XPS of Ti_4O_7. LEED and STM measurements indicate a similarity to partially reduced rutile $TiO_2(110)$. For annealing temperatures below 500 °C, the titanium oxide overlayers are disordered. Angle resolved XPS measurements of the disordered films indicate that reduced Ti^{3+} cations within the oxide overlayer are concentrated at the oxide/Pt(111) interface. Oxidation of the Ti^{3+} cations leads to a de-wetting of the oxide film.

Titanium oxide deposits on Pt foil lead to a significant enhancement of the CO and CO_2 hydrogenation over Pt foil. The rate of methane formation from CO_2 hydrogenation increases 31 times for a TiOx coverage of 0.2 ML for CO_2 hydrogenation, and the rate of methane formation from CO hydrogenation increases 17 times for a TiOx coverage of 0.4 ML. This degree of promotion is greater than that found on Rh foil in which the CH_4 rate enhancement is 15 times at a 0.5 ML TiOx coverage for CO_2 hydrogenation and 3.5 times at a 0.5 ML TiOx for CO hydrogenation. However, because the inherent activity for CO and CO_2 hydrogenation of Rh is several orders of magnitude greater than that of Pt, the methanation rate of the titanium oxide promoted Pt foil remains many times lower than that of Rh. The degree of titanium oxide promotion of the Pt foil is similar to that observed for supported Pt/TiO_2 catalysts indicating that the planar, TiOx/Pt foil model catalyst is representative of the high surface area supported system.

A series of transition metal oxides (including TiOx, VOx, FeOx, ZrOx, NbOx, TaOx, and WOx) were deposited on a Rh foil. The oxide coverage and growth mode was determined using AES, CO chemisorption, and ISS, and the oxidation state was determined using XPS. Each oxide exhibit a layer - by - layer growth mode and non - stoichiometric composition with multiple oxidation states. The oxidation states of the oxide films differ from those observed in bulk oxides treated at similar conditions. A bonding interaction, similar to that observed in Rh/M/O alloys, between the oxide deposit and Rh

substrate is postulated to stabilized the metal cations of the oxide in reduced oxidation states.

The oxide deposits strongly influence the catalytic activity of Rh foil. For CO hydrogenation each oxide investigated promotes the rate of methane formation over Rh foil. For CO_2 hydrogenation all the oxides except FeOx have a positive influence on activity. The coverage at which maximum rate enhancement is observed is approximately 0.5 ML for each oxide. No correlation is found between oxide reducibility and promoter ability; however, the degree of oxide rate enhancement scales with oxidation state. Titanium oxide, tantalum oxide, and niobium oxide are the most effective promoters and are stable in the highest oxidation states during both reactions (compared to VOx, WOx, and FeOx).

9.2 Scheme for Oxide Promotion

The most generally accepted scheme for transition metal oxide promotion of CO hydrogenation, first proposed by Burch and Flambard (51) and since invoked by several other authors (52-54), involves active site formation at the oxide/metal interface where CO dissociation is facilitated by interaction with oxide defect sites. A depiction of this scheme is given in Fig. 9.1. This work supports the proposal of active site formation at the oxide/metal interface. Maximum rate enhancement is observed at oxide coverages of 0.5 ML which are identified with the maximum in oxide perimeter, and XPS measurements indicate that each promoter oxide deposit has a significant number of defect sites which have been shown for TiOx to maximize at 0.5 ML (see Fig. 8.17). Sachtler et al. (43,55) extended upon the proposed scheme of Burch and Flambard (51) by suggesting that bonding at the transition metal oxide / metal interface is analogous to that observed in transition metal carbonyls interacting with a Lewis acid. In these systems, CO is

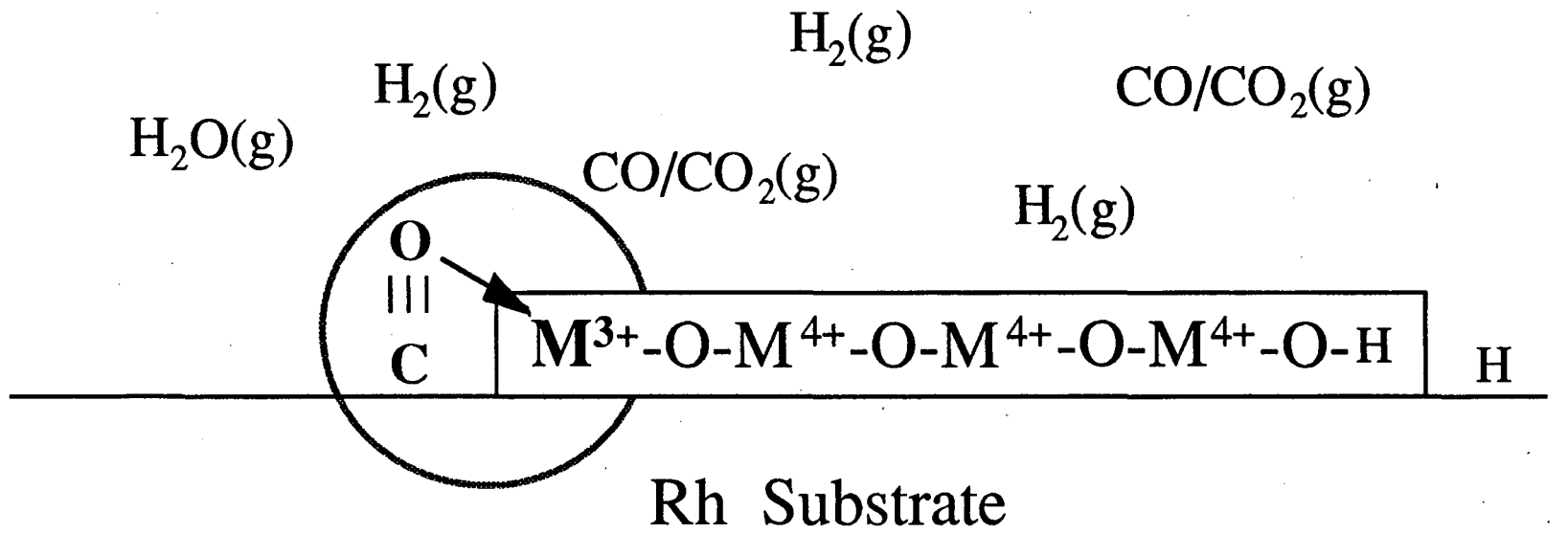

Figure 9.1: Scheme for transition metal oxide promotion of CO and CO_2 hydrogenation over Rh foil.

coordinated to the transition metal through the C atom and a Lewis acid, such as $AlCl_3$, interacts with the O atom. Sachtler et al. (43) found CO stretching frequencies in oxide promoted supported catalysts red shifted up to 500 cm^{-1} which is similar to stretching frequencies reported for the organo - metallic compounds (56).

In this work, the trend among the oxides in promoter effectiveness is shown to correlate with the oxidation state observed after reaction. Lewis acidity, a measure of ability to accept electrons in a chemical bond, is proportional to electronegativity. By relating the oxidation state of the oxide metal cation to electronegativity using the expression in 8.1, an approximate measure of the Lewis acidity of the oxide deposit is obtained. The agreement between cation electronegativity and oxide rate enhancement demonstrated in Figs. 8.18 and 8.19 indicates that Lewis acidity is a key factor in determining promoter effectiveness.

Given the demonstrated importance of oxide Lewis acidity, the negatively charged oxygen - end of a $H_xCO(a)$ ($x \leq 3$) (43-50) (a = adsorbed to Rh metal sites) surface species is postulated to form a Lewis acid - base bond with the positively charged metal cations at oxide defect sites. Once this Lewis acid - base surface complex forms, the C - O bond is weakened, and subsequent dissociation leads to oxidation of the metal cation and reduction of the carbonyl carbon atom. The redox cycle is completed when the oxide defect site is reformed by spillover of H(a) from the Rh metal to give a reduced oxide (MO_{x-1}) and $H_2O(g)$ (g = gas). The complete postulated mechanism of $H_xCO(a)$ dissociation is given by:

$$MO_{x-1} + H_xCO(a) \rightarrow H_xC(a) + MO_x$$

$$H_xC(a) + (4-x)H(a) \rightarrow CH_4(g)$$

$$H_2(g) \rightarrow 2H(a)$$

$$MO_x + 2H(a) \rightarrow MO_{x-1} + H_2O(g).$$

7.3 Implications and Limitations

There are several implications resulting from the above explanation of oxide promotion of bond breaking in polar molecules. The oxidation state of the oxide, which determines promotional character through its Lewis acidity, is influenced by the reaction environment (the oxidizing power of the reactant mixture) as well as the redox thermodynamics of the oxide. For a given reaction the effectiveness of the oxide promoter will depend on the match of the oxidation thermodynamics of the oxide with the redox potential of the reaction atmosphere. For example, tungsten oxide which is stable in the 2+, 3+ redox pair during CO and CO_2 hydrogenation causes less rate enhancement than titanium, tantalum, and niobium oxides which are stable in the higher 3+, 4+ redox pair that makes them better Lewis acids. However, under reaction conditions which are more oxidizing than that during CO and CO_2 hydrogenation, tungsten oxide would be stable in a higher redox pair (5+, 6+, for example) and be a more effective promoter than titanium, tantalum, and niobium oxides (which have maximum oxidation states of 4+, 5+, and 5+, respectively) if a similar promotion mechanism as that proposed for CO and CO_2 hydrogenation is applicable. Additionally, the oxidation state of the oxide at the oxide/metal interface is influenced by the metal substrate. In Chapter 4, Ti^{3+} of the titanium oxide film was found to be located at the oxide/Pt(111) interface, indicating that

bonding between the Pt and oxide deposit stabilized the reduced Ti^{3+} species. In Chapter 7, 0.5 ML oxide deposits of TiOx, ZrOx, TaOx, NbOx, and WOx on Rh foil were shown to be present in oxidation states inconsistent with those observed in the bulk oxides. Therefore, for a given reaction system and catalyst metal, Lewis acidity can be used to predict oxide promoter effectiveness by considering the influence of the reaction environment and metal - oxide bonding interactions on the oxidation state of the oxide.

The reactions which are found to be promoted by titanium oxide deposits on Rh foil are those which involve the hydrogenation of C-O bonds (75). Titanium oxide has also been demonstrated by Pande and Bell (37) to promote reduction of NO by H_2 and CO. This suggests that a Lewis acid / base interaction with an oxide promoter requires a polar or oxygen containing bond within the molecule. Consequently other reactions with molecules having polar functional groups (such as CN, CS, and NH) may also be affected by charge transfer at the oxide / metal interface, and the scheme presented here would predict that those oxides which are present in the highest oxidation states during reaction would be the most effective promoters.

Lewis acidic oxides promote reactions involving CO bond dissociation and hydrogenation to form hydrocarbons. For CO/CO_2 hydrogenation to form alcohols, basic oxides such as ZnOx and FeOx have been found to be the most effective promoters (43). By analogy to the mechanism presented for promotion with acidic oxides, a scheme for enhancement of alcohol formation may involve active sites at the oxide/metal interface where charge transfer from the basic cations of the oxide stabilizes the CO bond for alcohol synthesis.

The scheme presented for oxide promotion is fully consistent with the experimental observations; however, a direct measurement of CO bonded at the oxide/metal interface has not been made. Two possible techniques for probing adsorbed CO and the oxide perimeter are high resolution electron energy loss spectroscopy (HREELS) and STM.

With vibrational spectroscopes such as HREELS, the weakening of the CO bond can be monitored by measuring the shift in CO stretching frequency. This has been done using HREELS for CO adsorbed to MnOx promoted Ni(111) (57) and using infrared spectroscopy for CO adsorbed to oxide promoted supported catalysts (43,50,58-60). A limitation of HREELS is that the technique is not applicable in the pressure region of catalytic interest. A newly developed vibrational technique with which the solid - gas interface can be selectively probed at atmospheric pressures is sum frequency generation (SFG). STM has been employed to measure the morphology of titanium oxide deposits on Rh(111) in ultra - high vacuum (119). The STM images indicated the presence of uniform sized islands of approximately 20 Å in diameter. At the edge of the islands an enhanced STM contrast was observed that was tentatively assigned to reduced Ti^{3+}. Unfortunately, these promising experiments were discontinued before a quantity of images was accumulated allowing oxide coverage to be related to island morphology and before the presence of reduced Ti^{3+} at the island periphery could be more decisively confirmed. Continuing STM measurements in UHV and at elevated pressures and temperatures holds the greatest promise for further establishing the molecular details of oxide promotion.

Bibliography

1. G.A. Somorjai, *Chemistry in Two Dimensions* (Cornell University Press, 1981).
2. I. Lundstromm and C. Svensson, in: *Solid State Chemical Sensors* , eds. J. Janata and R.J. Huber (Academic Press, 1985).
3. G.R. Brubaker and P.B.P. Phipps, *Corrosion Chemistry* (American Chemical Society, Washington, D.C., 1979).
4. E. Cohen, in: *Modern Coating and Drying Technology* , eds. E. Cohen and E.B. Gutoff (VCH Publishers, 1992).
5. S.J. Tauster, S.C. Fung, R.T.K. Baker, and J.A. Horsely, Science, 211 (1981) 1121.
6. Catalytica Associates, Inc., *Metal - Support Interactions: Implications for New Catalyst Technologies* , (Multiclient Study 4184, 1984).
7. S.J. Tauster, Acct. Chem. Res. 20 (1987) 389.
8. A.T. Bell, in: *Catalyst Design - Progress and Perspectives*, ed. L.L. Hegedus (Wiley, New York, 1987).
9. R. Burch, in: *Hydrogen Effects in Catalysis*, eds. Z. Paal and P.G. Menon (Marcel Dekker, New York, 1988).
10. G.L. Haller and D.E. Resasco, Adv. Catal. 36 (1989) 173.
11. M.A. Vannice, Catal. Today 12 (1992) 255.

12. G.M. Schwab, J. Block, W. Müller, and D. Schultze, Naturwissenschaftern, 44 (1957) 582.
13. G.M. Schwab, J. Bolck, and D. Schultze, Angew. Chem., 71 (1958) 101.
14. G.M. Schwab, Adv. Catal., 27 (1978) 1.
15. Z.G. Szabó, F. Solymosi, and I. Batta, Z. Phys. Chem. N.F., 17 (1958) 125.
16. F. Solymosi, Catal. Rev., 1 (1967) 233.
17. S.J. Tauster, S.C. Fung, and R.L. Garten, J. Am. Chem. Soc., 100 (1978) 170.
18. M.A. Vannice and R.L. Garten, J. Catal., 56 (1979) 236.
19. D.N. Belton, Y.M. Sun, and J.M. White, J. Phys. Chem. 88 (1984) 5127.
20. D.N. Belton, Y.M. Sun, and J.M. White, J. Am. Chem. Soc. 106 (1984) 3059.
21. G. Gallaher, J.G. Goodwin, C.-S. Huang, and M. Houlla, J. Catal., 127 (1991) 719.
22. G. Munuera, A.R. Gonzalez-Elipe, J. Sanz, J.P. Espinos, J.C. Conesa, and J. Soria, J. Phys. Chem., 91 (1987) 6625.
23. M.T. Blasco, J.C. Conesa, J. Soria, A.R. Gonzalez-Elipe, G. Munuera, J.M. Rojo, and J. Sanz, J. Phys. Chem., 92 (1988) 4685.
24. L. Bonnevoit and G.L. Haller, J. Catal., 113 (1988) 96.
25. R.T.K. Baker, E.B. Prestridge, and L.L. Murrell, J. Catal., 85 (1983) 348.
26. A.G. Shastri, A.K. Datye, J. Schwank, J. Catal., 87 (1984) 265.
27. C. Dall'Agnol, A. Gervasini, F. Morazzoni, F.K. Pinna, G. Strukul, and L. Zanderighi, J. Catal. 96 (1986) 106.
28. W.K. Jozwiak, React. Kinet. Catal. Lett. 30 (1986) 345.
29. J.K. Gibson, L. Brewer, and K.A. Gingerich, Metall. Trans. A, 15 (1984) 2075.
30. L. Brewer and P.R. Wengert, Metall. Trans., 4 (1973) 83.
31. T. Iizuka, Y. Tanaka, and K. Tanabe, J. Catal. 76 (1982) 1.
32. T. Iizuka, Y. Tanaka, and K. Tanabe, J. Mol. Catal. 17 (1982) 381.

33. M.A. Henderson and S.D. Worley, J. Phys. Chem., 89 (1985) 1417.

34. F. Solymosi, A. Erdöhelyi, and T. Bánsági, J. Catal., 68 (1981) 371.

35. B. Sen and M.A. Vannice, J. Catal., 113 (1988) 52.

36. M.A. Vannice and B. Sen, J. Catal., 115 (1989) 65.

37. N. T. Pande and A.T. Bell, J. Catal. 98 (1986) 577.

38. K.J. Blankenburg and A.K. Datye, J. Catal., 128 (1991) 186.

39. T. Koerts, W.J.J. Welters, and R.A. van Santen, J. Catal. 134 (1992) 1.

40. T. Komaya, A.T. Bell, Z. Weng-Sieh, R. Gronsky, F. Engelke, T.S. King, and M. Pruski, J. Catal. in press.

41. T. Komaya, A.T. Bell, Z. Weng-Sieh, R. Gronsky, F. Engelke, T.S. King, and M. Pruski, J. Catal. in press.

42. J.C. Campuzano, in *The Chemical Physics of Solid Surfaces and Heterogeneous Catlysis* , eds. D.A. King and D.P. Woodruff (Vol. 3A, 389 Elsevier, Amsterdam 1990).

43. W.M.H. Sachtler and M.J. Ichikawa, J. Phys. Chem. 90 (1986) 4752.

44. E. Kikuchi, H. Nomura, M. Matsumoto, Y. Morita, Appl. Catal. 7 (1983) 1.

45. T. Mori, A. Masuda, H. Iimai, A. Miyamoto, R. Hasebe, and Y. Murakami, J. Phys. Chem., 87 (1983) 3648.

46. T. Mori, A. Miyamoto, H. Niizuma, N. Takahashi, T. Hattori, and Y. Murakami, J. Phys. Chem. 93 (1986) 109.

47. J.S. Rieck and A.T. Bell, J. Catal. 99 (1986) 262.

48. Y. Mori, T. Mori, A. Miyamoto, N. Takahashi, T. Hattori, and Y. Murakami, J. Phys. Chem. 93 (1989) 2039.

49. I. Mochida, N. Ikeyama, H. Ishibashi, and H. Fujitsu, J. Catal. 110 (1988) 159.

50. T. Shido and Y. Iwasawa, J. Catal. 137 (1992) 267.

51. R. Burch and A.R. Flambard, J. Catal. 86 (1982) 384.

52. M.A. Vannice and C. Sudhakar, J. Phys. Chem. 88 (1984) 2429.

53. J.S. Rieck and A.T. Bell, J. Catal. 99 (1986) 262.

54. M.E. Levin, M. Salmeron, A.T. Bell, and G.A. Somorjai, J. Chem. Soc., Faraday Trans. 1 83 (1987) 2061.

55. W.M.H. Sachtler, D.F. Shriver, W.B. Hollenberg, and A.F. Lang, J. Catal. 92 (1985) 429.

56. C.P. Horwitz and D.F. Shiver, Adv. Organomet. Chem. 23 (1984) 219.

57. Y.-B. Zhao and Y-W Chung, J. Catal. 106 (1987) 369.

58. B.J. Kip, E.G.F. Hermans, J.H.M.C. Van Wolput, N.M.A. Hermans, J. van Grondelle, and F. Prins, Appl. Catal. 35 (1987) 109.

59. J.C. Lavalley, J. Saussey, J. Lamotte, R. Breault, J.P. Hindermann, and A. Kiennemann, J. Phys. Chem. 94 (1990) 5941.

60. S. Boujana, D. Demri, J. Cressely, A. Kiennemann, and J.P. Hindermann, Catal. Lett. 7 (1990) 359.

61. C.T. Campbell, Adv. Catal. 36 (1989) 2.

62. S. Takatani and Y.-W. Chung, J. Catal. 90 (1984) 75.

63. K. Tamura, U. Bardi, and Y. Nihei., Sur. Sci. 197 (1988) L281.

64. H.R. Sadeghi and V.E. Henrich., J. Catal. 87 (1984) 279.

65. T. Sheng, X. Guoxing, and W. Hongli, J. Catal. 111 (1988) 136.

66. B.C. Beard and P.N. Ross, J. Phys. Chem. 90 (1986) 6811.

67. Y.-W. Chung, G. Xiong, and C.C. Kao, J. Catal. 85 (1984) 237.

68. R.A. Demmin , C.S. Ko, and R.J. Gorte, J. Phys. Chem. 89 (1985) 1151.

69. R.A. Demmin and R.J. Gorte, J. Catal. 98 (1986) 577.

70. R.A. Demmin and R.J. Gorte, J. Catal. 105 (1987).

71. M.E. Levin, M. Salmeron, A.T. Bell and G.A. Somorjai, J. Catal. 106 (1987) 401.

72. M.E. Levin, M. Salmeron, A.T. Bell and G.A. Somorjai, Faraday Trans. 1 83 (1987) 2061.

73. M.E. Levin, M. Salmeron, A.T. Bell and G.A. Somorjai, Surf. Sci. 195 (1988) 429.

74. M.E. Levin, Ph.D. Thesis, Department of Chemistry, University of Califonia, Berkeley, 1987.

75. K.J. Williams, Ph.D. Thesis, Department of Chemical Engineering, University of Califonia, Berkeley, 1991.

76. K.J. Williams, M. Salmeron, A.T. Bell, and G.A. Somorjai, Surf. Sci. 204 (1988) L745.

77. M.E. Levin, M. Salmeron, A.T. Bell, and G.A. Somorjai, Surf. Sci. 195 (1988) 429.

78. K.J. Williams, A.B. Boffa, M. Salmeron, A.T. Bell and G.A. Somorjai, Catal. Lett. 5 (1990) 385.

79. K.J. Williams, A.B. Boffa, M. Salmeron, A.T. Bell and G.A. Somorjai, Catal. Lett. 9 (1991) 41.

80. K.J. Williams, A.B. Boffa, M. Salmeron, A.T. Bell and G.A. Somorjai, Catal. Lett. 11 (1991) 77.

81. K.J. Williams, M. Salmeron, A.T. Bell and G.A. Somorjai, Catal. Lett. 1 (1988).

82. G. Ertyl and J. Kuppers, *Low Energy Electrons and Surface Chemistry* (Verlag Chemie, 1974).

83. D. Briggs and M.P. Seah, *Practical Surface Analysis: by Auger and X- ray Photoelectron Spectroscopy* (Wiley, 1983).

84. D.P. Woodruff and T.A. Delchar, *Modern Techniques of Surface Science* (Cambridge University Press, 1986).

85. S.M. Davis, F. Zaera, and G.A. Somorjai, J. Am. Chem. Soc. 104 (1982) 7453.

86. D. Jentz, Ph.D. Thesis, Department of Chemistry, University of Califonia, Berkeley, 1992.

87. R.G. Musket, W. McLean, C.A. Colenares, D.M. Makowiecki, and W.J. Siekhaus, Appl. Sur. Sci. 12 (1982) 143.

88. J.A. Venables, G.D.T. Spiller, and M. Hanbücken, Rep. Prog. Phys. 47 (1984) 399.

89. C. Argile and G.E. Rhead, Surf. Sci. 53 (1975) 659.

90. V. Maurice, M. Salmeron and, G.A. Somorjai, Surf. Sci. 237 (1990) 116.

91. G.H. Vurens, M. Salmeron, and G.A. Somorjai, Surf. Sci. 201 (1988) 129.

92. G.H. Vurens, V. Maurice, M. Salmeron, and G.A. Somorjai, Surf. Sci. 268 (1992) 170.

93. H.C. Galloway, J.J. Benítez, and M. Salmeron, Surf. Sci. 298 (1993) 127.

94. H.C. Galloway, J.J. Benítez, and M. Salmeron, J. Vac. Sci. Technol. A 12 (1994) in press.

95. W. Weiss and G.A. Somorjai, J. Vac. Sci. Technol. A 11 (1993) 2138.

96. W. Weiss, A. Barbieri, M.A. Van Hove, and G.A. Somorjai, Phys. Rev. Lett. 71 (1993) 1884.

97. D.M. Zeglinski, D.F. Ogletree, T.P. Beebe, and R.Q Hwang, Rev. Sci. Instr. 61 (1990) 3769.

98. Software by D.F. Ogletree (commercially available from RHK Technology, Rochester Hills, MI).

99. J.A. Horsley, J. Am. Chem. Soc. 101 (1979) 2870.

100. C.S. Ko and R.J. Gorte, J. Catal. 90 (1984) 59.

101. D.J. Dwyer, S.D. Cameron, and J. Gland, Surf. Sci. 159 (1985) 430.

102. C.M. Greenlief, J.M. White, C.S. Ko, and R.J. Gorte, J. Phys. Chem. 89 (1985) 5025.

103. R. Vanselow and M. Mundschau, J. Catal. 103 (1987) 426.

104. U. Bardi and P.N. Ross, J. Vac. Technol. A 4 (1984) 1461.

105. J.M. Herrmann, M. Gravelle-Rumeau-Maillot, and P.C. Gravelle, J. Catal. 104 (1987) 136.

106. V.E. Henrich and P.A. Cox, *The Surface Science of Metal Oxides* (Cambridge University Press, New York, 1994).

107. P.W. Murray, F.M. Leibsle, H.J. Fisher, C.F.J. Flipse, and G. Thorton, Phys. Rev. B 46 (1992) 12877.

108. G.E. Poirier, B.K. Hance, and J.M. White, J. Vac. Sci. Technol. B 10 (1992).

109. S.C. Abrahams and J.L. Bernstein, J. Chem. Phys. 55 (1971) 3206.

110. R.T.K. Baker, E.B. Prestridge, and R.L. Garter, J. Catal. 56 (1979) 390.

111. M. Sander and T. Engel, Surf. Sci. 302 (1994) L263.

112. G.S. Roher, V.E. Henrich, and D.A. Bonnell, Science 250 (1990) 1239.

113. E.J. Braunschweig, A.D. Logan, A.K. Datye, and D.J. Smith, J. Catal. 118 (1989) 227.

114. K.J. Blankenburg and A.K. Datye, J. Catal. 128 (1991) 186.

115. J.L. Falconer and A.E. Zagli, J. Catal. 62 (1980) 280.

116. E. Zagli and J.L. Falconer, J. Catal. 69 (1981) 1.

117. T.F. Mao and J.L. Falconer, J. Catal. 123 (1990) 443.

118. J.L. Robbins and E. Marucchi-Soos, J. Phys. Chem. 93 (1989) 2885.

119. H.C. Wang, D.F. Ogletree and M. Salmeron, J. Vac. Sci. Tech. B9(2) (1991) 853.

120. M.A. Vannice, C.C. Twu, and S.H. Moon, J. Catal. 79 (1983) 70.

121. D.G. Castner, B.A. Sexton, and G.A. Somorjai, Surf. Sci. 71 (1978) 519.

122. D.W. McKee, J. Catal. 8 (1967) 240.

123. B.E. Koel, D.E. Peebles, and J.M. White, Surf. Sci. 107 (1981) L367.

124. B.E. Koel, D.E. Peebles, and J.M. White, Surf. Sci. 125 (1983) 709.

125. F. Solymosi, I. Tombácz, and M. Kocsis, J. Catal. 75 (1982) 78.

126. S. Lars and T. Anderson, J. Chem. Soc. Faraday Trans. 1 75 (1979) 1356.

127. B.A. Sexton, A.E. Hughs, and K. Foger, J. Catal. 77 (1982) 85.

128. M.A. Henderson and S.D. Worley, J. Phys. Chem. 89 (1985) 1417.

129. J.S. Rieck and A.T. Bell, J. Catal. 96 (1985) 88.

130. E. Shustorovich and A.T. Bell, J. Catal. 113 (1988) 341.

131. O.T. Sorensen, in: *Nonstoichiometric Oxides* , ed. O.T. Soresen (Academic Press, NY, 1981).

132. H.H. Kung, *Transition Metal Oxides: Surface Chemistry and Catalysis* (Elsevier, NY, 1989).

133. F.S. Stone, in: *Chemistry and Chemical Engineering of Catalytic Processes*, eds. R. Prins and G.C.A. Schuit (NATO Adv. Study Inst. Series, 1980).

134. K.N. Rao, S. Mohan, M.S. Hegde, and T.V. Balasubramanian, J. Vac. Sci. Technol. A 11 (1993) 394.

135. J. Paul, S.D.Cameron, D.J. Dwyer, and F.M. Hoffmann, Surf. Sci. 177 (1986) 121.

136. V.I. Nefdov, Y.V. Salyn, , A.A. Chertkov, and L.N. Padurets, Zh. Neorg. Khim. 19 (1974) 1443.

137. A.F. Carley, P.R. Chalker, J.C. Riviere, and M.W. Roberts, J. Chem. Soc., Faraday Trans. I 83 (1987) 351.

138. G.H. Vurens, Ph.D. Thesis, Rifksuniversiteit Leiden (1989).

139. J.F. Moulder, W.F. Stickle, P.E. Sobol, and K.D. Bomben, in: *Φ Handbook of X-Ray Photoelectron Spectroscopy* 2nd ed. (Perkin-Elmer Co., Physical Electronics Division, Eden Prairie, MN, 1992).

140. L.Z. Zhao, S.H. Liu, D.H. Wang, and C.H. Pan, J. Electron Spectrosc. Relat. Phenom. 52 (1990) 571.

141. S.C. Fung, J. Catal. 76 (1982) 225.

142. D. Simon, C. Perrin, and J. Bardolle, J. Microsc. Spectosc. Electron 1 (1976) 175.

143. C.D. Wagner, W.D. Riggs, L.E. Davies, J.F. Moulder, and G.E. Mullenberg, in: *Handbook of X-Ray Photoelectron Spectroscopy* (Perkin-Elmer Co., Physical Electronics Division, Eden Prairie, MN, 1976).

144. V.E. Nefedov, D. Gati, B.F. Dzhurinskii, N.P. Sergushin, and Y.V. Salyn, Zh. Neorg. Khim. 20 (1975) 2307.

145. M.V. Kuznetsov, Ju.F. Zhuravlev, V.A. Zhilyaev, and V.A. Gubanov, J. Electron Spectrosc. Relat. Phenom. 58 (1992) 1.

146. J.P. Espinos, A.R. Gonzalez-Elipe, and G. Munurea, Appl. Surf. Sci. 62 (1992) 137.

147. S. Hofmann and J.M. Sanz, J. Trace Microprobe Tech. 1 (1982-83) 213.

148. J.M. Pan, U. Diebold, L. Zhang, and T.E. Madey, Surf. Sci. 295 (1993) 411.

149. L. Kumar, D.D. Sarma, and S. Krummacher, Appl. Surf. Sci. 32 (1988) 309.

150. D.D. Sarma and C.N.R. Rao, J. Electron Spectrosc. Relat. Phenom. 20 (1980) 25.

151. S. Harel, J.M. Mariot, and C.F. Hague, Surf. Sci. 269/270 (1992) 1167.

152. C.O. De Gonzalez and E.A. Garcia, Surf. Sci. 193 (1988) 305.

153. C. Morant, J.M. Sanz, L. Galan, L. Soriano, and F. Rueda, Surf. Sci. 218 (1989) 331.

154. N.K. Huang, H. Kheyrandish, and J.S. Colligon, Mater. Res. Bull. 27 (1992) 239.

155. T.L. Barr, J. Phys. Chem. 82 (1978) 1801.

156. T.L. Barr, J. Vac. Sci. Technol. 14 (1977) 660.

157. D. Majumdar and J. Chatterjee, Appl. Phys. 70 (1991) 988.

158. R.L. Kurtz and V.E. Henrich, Surf. Sci. 129 (1983) 345.

159. C.R. Brundle T.J. Chuang, and K. Wandelt, Surf. Sci. 68 (1977) 459.

160. N.S. McIntyre and D.G. Zetaruk, Anal. Chem. 49 (1977) 1521.

161. V.I. Nefedov, Y.V. Salyn, G. Leonhardt, and R. Scheibe, J. Electron Spectrosc. Relat. Phenom. 10 (1977) 121.

162. V.I. Nefedov, M.N. Firsov, and I.S. Shaplygin, J. Electron Spectrosc. Relat. Phenom. 26 (1982) 65.

163. D. Simon, C. Perrin, and P.C. Baillif, R. Acad. Sci. Ser. C 283 (1976) 241.

164. G.E. McGuire, G.K.K. Schweitzer, and T.A. Carlson, Inorg. Chem. 12 (1973) 2451.

165. R. Fountaine, R. Caillat, L. Feve, and M.J. Guittet, J. Electron Spectrosc. Relat. Phenom. 10 (1977) 349.

166. M. Shelef, L.P. Haack, R.E. Soltis, J.E. DeVries, and E.M. Logothetis, J. Catal. 137 (1992) 114.

167. M.K. Bahl, J. Phys. Chem. Solids 36 (1975) 485.

168. N.K. Nag and F.E. Massoth, J. Catal. 124 (1990) 127.

169. K. Hamrin, C. Nordling, and L. Kihlborg, Ann. Acad. Regiae. Sci. Upsal. 14 (1970) 70.

170. F.J. Gil-Llambias, A.M. Escudey, J.L.G. Fierro, and A. Lopez Agudo, J. Catal. 95 (1985) 520.

171. R. Larsson, B. Folkesson, and G. Schon, Chem. Scripta 3 (1973) 88.

172. J. Kasperkiewicz, J.A. Kovacich, and D. Lichtman, J. Electron Spectrosc. Relat. Phenom. 32 (1983) 123.

173. R.J. Colton, A.M. Guzman, and J.W. Rabalais, J. Appl. Phys. 49 (1978) 409.

174. M. Romand and M. Roubin, Anausis 4 (1976) 309.

175. Y.M. Shul'ga, V.N. Troitskii, M.I. Aivazov, and Y.G. Borod'ko, Zh. Neorg. Khim. 21 (1976) 2621.

176. P. Biloen and G.T. Pott, J. Catal. 30 (1973) 169.

177. F.P.J.M. Kerkhof and J.A. Moulijn, J. Electron Spectrosc. Relat. Phenom. 14 (1973) 453.

178. J.L. Walter and K.A. Lou, J. Mater. Sci. 24 (1989) 3577.

179. K.T. Ng and D.M. Hercules, J. Phys. Chem. 80 (1976) 2094.

180. R.J. Colton and J.W. Rabalais, Inorg. Chem. 15 (1976) 237.

181. U. Bardi, Catal. Lett. 5 (1990) 81.

182. I.N. Shabanova and V.A. Trapeznikov, J. Electron Spectrosc. Relat. Phenom. 6 (1975) 297.

183. D.R. Stull and H. Prophet (Project Directors), JANAF Thermochemical Tables, 2nd Ed. (U.S. Government Printing Office: Washington, D.C., 1971 and supplements, 1973 and 1975).

184. Susan Leonard, Ph.D. Thesis, Department of Chemistry, University of Califonia, Berkeley, 1991.

185. S. Sakellson, M. McMillan, and G. Haller, J. Phys. Chem. 90 (1986) 1733.

186. E.S. Shpiro, B.B. Dysenbina, O.P. Tkachenko, G.V. Antoshin, and Kh.M. Minachev, J. Catal. 110 (1988) 262.

187. H.R. Sadeghi and V.E. Henrich, J. Catal. 109 (1988) 1.

188. Z. Hu, H. Nakamura, K. Kunimori, and T. Uchijima, Catal. Lett. 1 (1988) 271.

189. R. Prins, J.H.A. Martens, and D.C. Koningsberger, in: *Structure and Reactivity of Surfaces* , eds. C. Moterra, A. Zecchina, and G. Costa (Elsevier, 1989).

190. D.J. Dwyer and G.A. Somorjai, J. Catal. 52 (1978) 291.

191. K.I. Tanaka and A. Ozaki, J. Catal. 8 (1967) 1.

192. R.T. Sanderson, *Chemical Periodicity* , (Reinhold, New York, 1960).

LAWRENCE BERKELEY LABORATORY
CENTER FOR ADVANCED MATERIALS
1 CYCLOTRON ROAD
BERKELEY, CALIFORNIA 94720